Politecnico di Torino

ScuDo

Scuola di Dottorato ~ Doctoral School

WHAT YOU ARE, TAKES YOU FAR

Doctoral Dissertation
Doctoral Program in Electrical, Electronic and Communications Enginering
(36.th cycle)

Fabrication and characterization of telecom quantum emitters in silicon for quantum technology applications

Greta Andrini

* * * * *

Supervisors
Prof. A., Rivetti
Prof. M., Rolo
Prof. M., Goano

Politecnico di Torino
June 27, 2024

This thesis is licensed under a Creative Commons License, Attribution - Noncommercial-NoDerivative Works 4.0 International: see www.creativecommons.org. The text may be reproduced for non-commercial purposes, provided that credit is given to the original author.

I hereby declare that, the contents and organisation of this dissertation constitute my own original work and does not compromise in any way the rights of third parties, including those relating to the security of personal data.

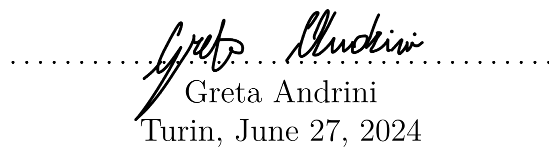

Greta Andrini
Turin, June 27, 2024

Summary

In recent decades, due to the presence of photoluminescence and electroluminescence from various optically active point defects, silicon has demonstrated the potential to integrate photon-emitting components with CMOS technology, despite its indirect band gap. However, it was only in 2020 that the first demonstration of single-photon emission in the infrared range and at cryogenic temperatures from the so-called G center was demonstrated, sparking renewed interest in luminescent centers within silicon for the development of next-generation technologies in the second quantum revolution. This result offered an enticing perspective to develop single photon sources emitting at telecom wavelengths. Moreover, these sources can be implemented in a host material with the highest available degree of maturity in processing and mass production, including industrially available techniques for manufacturing integrated photonics chips. The development and implementation of a complete silicon photonics integrated circuit for quantum computing applications would enormously benefit from the development of an industry-compatible deterministic single-ion implantation technique, allowing the manufacturing of monolithic devices equipped with multiple indistinguishable photon sources. This work provides an introductory discussion on single-photon sources as building blocks of quantum photonic technology, aiming to describe color centers in solid-state platforms, and providing the theoretical framework underpinning the experiments discussed. The addressed research questions are then contextualized through an overview of some of the significant optically active defects identified from the mid-70s up to the present, with a particular focus on the single-photon sources identified in silicon following the first demonstration in 2020. From the perspective of the concrete realization of second-quantum revolution devices, the core activity of this Dissertation is then discussed with a detailed description of the adopted methods to address the main manufacturing challenges in the realization of a well-established fabrication protocol for silicon-based quantum emitters. The ion-matter interaction mechanisms are discussed, along with the application of the ion implantation technique as a reliable industry-compatible fabrication technology for the realization of color centers. The role of radiation damage during the introduction of specific impurities into the crystal lattice is accurately investigated both in diamond, as a pioneering material in quantum technologies, and in silicon. An in-depth study in

diamond shows that, with high-temperature implantations it is possible to increase the vacancy density threshold required for the irreversible conversion of the diamond to a graphitic phase, thus enabling the achievement of higher-density ensembles, which constitutes a great advantage in the realization of quantum-enhanced sensing protocols. On the other hand, the focus on the radiation-induced intrinsic defects dynamics in silicon reveals an effective approach for the realization of recently discovered intrinsic interstitial quantum sources, named W centers. The use of single-photon sensitive microscopy at cryogenic temperatures enables the optical characterization of the emitters under study. In particular a systematic characterization of carbon-implanted high-purity silicon substrates enables the examination of the effects of post-implantation thermal treatment in the formation of intrinsic silicon defect complexes generated by the introduction of extrinsic atomic species. Along with the radiation damage, the delivery of single impurities and their conversion into stable single-photon sources are extensively covered. For the first fabrication challenge, the Ion Beam Induced Charge technique (IBIC) is explored as a post-detection technique for deterministic implantation. Notably, an experiment with a custom Si photodiode micromachined via FIB milling is proposed where the device is exploited as an integrated beam diagnostic tool for the real-time assessment of the beam spot size of the probe beam. The information on the size of a 2MeV Li+ ion micro-beam takes advantage of the spatial correlation between the induced charge pulse amplitude and the micro-structures through Charge Collection Efficiency (CCE) measurements. In contrast to the main techniques commonly adopted by the scientific community and based on the imaging of patterned standards, the proposed approach allows the qualification of the ion beam by the CCE mapping of the very same target of the ion beam analysis, avoiding possible limitations in the accuracy of the beam size estimation. Moreover, numerical simulations based on the Shockley-Ramo-Gunn model are carried out for data analysis, validating the interpretation of the experimental results as originating from the effects of the charge implanted during the FIB micromachining on the measured charge induction. Finally, the controlled activation of silicon color centers is explored. In contrast to statistical activation approaches based on conventional Rapid Thermal Annealing processes reported so far, a novel approach consisting of an ns heat transient in the annealing step, thus offering a practical off-equilibrium pathway for the occurrence of competitive processes in the formation of defective complexes in silicon is discussed. The interpretation of the experimental results, together with the strong non-stationarity of the technique, is then validated through a finite element analysis, which highlights the radically different defect engineering possibilities compared to conventional longer thermal treatments, thus paving the way to the direct and controlled fabrication of emitters embedded in integrated photonic circuits and waveguides.

Acknowledgements

I would like to express my gratitude to my supervisor, Prof. Angelo Rivetti, for giving me the opportunity to participate in such an interdisciplinary PhD program and for advising me through the challenges of the research career. I also would like to thank my co-supervisors, Prof. Manuel Rolo, and Prof. Michele Goano, for their valuable support throughout my research activities. They have been both very helpful in providing me with the necessary computational resources for the simulation activities, and Prof. Goano has always been available to clarify any doubts regarding my PhD career.

This work was supported by the QUANTEP project (Quantum Technology Experimental Platform), funded by the INFN CSN5 in the framework of the 2020 national call on quantum technologies. The simulation activities on novel radiation sensors have been carried out in the framework of the ARCADIA project funded by INFN CSN5 and have been supported by the ALICE 3 Timing Layers WG. The cryogenic workstation exploited in this Thesis work is part of the PiQuET (Piemonte Quantum Enabling Technology) infrastructure funded by Regione Piemonte (POR FESR 2014-2020), which is gratefully acknowledged.

My deepest gratitude goes to Prof. Jacopo Forneris for his availability, patience, and invaluable advice that were fundamental to the completion of my work and my scientific growth. I want to thank the entire Solid State Physics group at the University of Turin, especially the "Diamond" group led by Prof. Olivero. Without their help, the experiments presented in this Dissertation would not have been possible. I am grateful to have worked with them and learned a lot from them. I always felt included in a very united group with a pleasant working environment, which motivated me to pursue my PhD career. I especially thank Prof. Ettore Vittone for the precious scientific discussion concerning the IBIC technique and Dr. Sviatoslav Ditalia Tchernij for the countless clarifications and teachings regarding the experimental work.

I acknowledge the Quantum Optics group at the National Institute of Metrological Research (INRiM), led by Dr. Marco Genovese, for allowing me to carry out my experimental activities in their laboratories and for their valuable guidance and teachings during my time in the lab. I am particularly grateful to Dr. Paolo Traina, Dr. Ivo Pietro DeGiovanni, Dr. Ettore Bernardi, and Dr. Salvatore Virzì

for their support during my research.

Additionally, I would like to thank the ALICE 3 timing layer working group and the ARCADIA collaboration, particularly Prof. Lucio Pancheri and Marco Mandurrino, for their support and valuable teaching on the physics of electronic devices and their simulation.

I also acknowledge Prof. Matteo Cocuzza and Alessio Verna from DISAT, Politecnico di Torino, for giving me access to the ChiLab facility and assisting me in using the RTA Processing System.

Finally, I want to thank my family, Jacopo, and friends for their unwavering emotional and moral support throughout my journey.

Contents

Table of acronyms 1

Preface 4

1 Single-photon sources 6
- 1.1 Second-order autocorrelation function 8
- 1.2 Color centres 9
- 1.3 Experimental characterization of single-photon sources 14
  - 1.3.1 Hanbury-Brown Twiss interferometer (HBT) 14
  - 1.3.2 Time-Correlated Single Photon Counting (TCSPC) 16

2 Color centers in silicon 19
- 2.1 Properties of pure silicon 19
  - 2.1.1 Crystallographic structure and phonon properties 20
  - 2.1.2 Electronic properties 20
  - 2.1.3 Optical properties 22
- 2.2 Impurities and defects 26
  - 2.2.1 Contamination 26
  - 2.2.2 Intrinsic Impurities 27
  - 2.2.3 Common extrinsic defects 30
  - 2.2.4 Radiation-induced defects 32
  - 2.2.5 The W center 33
- 2.3 Carbon-related bands 35
  - 2.3.1 The C band 36
  - 2.3.2 The G center 36
  - 2.3.3 The T center 39

3 Methods 42
- 3.1 Confocal microscopy 42
- 3.2 Cryogenic PL measurements 46
  - 3.2.1 Piezo motion controllers 47
  - 3.2.2 Single photon detection 49

3.2.3 Experiment control and data processing 52
3.2.4 Cryostat 53
3.3 Mg-vacancy optical defects in diamond: a case study for cryogenic microscopy 54
3.4 Turin Ion implantation facility 63

4 Fabrication of color centers in silicon 67
4.1 Ion implantation 68
4.1.1 Interaction of ions with matter 68
4.1.2 Ion induced damage 73
4.2 Single-ion delivery 89
4.2.1 Ion Beam Induced Charge (IBIC) 89
4.2.2 An IBIC experiment for the in-situ measurement of the ion beam resolution 92
4.2.3 Numerical tool for device simulations 100
4.3 Color centers activation 106
4.3.1 Conventional thermal treatments 107
4.3.2 Off-equilibrium thermal processing 108

5 Monolithic Active Pixel Sensors (MAPS): a case study for device simulations 122
5.1 Time resolution in radiation detectors 123
5.2 The ARCADIA technology 124
5.2.1 MAPS without gain 125
5.2.2 MAPS with gain 139

Conclusion 145

Table of acronyms

TCSPC Time-Correlated Single Photon Counting

SPS Single-Photon Source

ZPL Zero Phonon Line

QKD Quantum Key Distribution

HBT Hanbury-Brown Twiss

TTL Transistor-transistor logic

SPAD Single Photon Avalanche Diode

SOI Silicon on Insulator Technology

BZ Brillouin Zone

VBM Valence Band Maximum

CBM Conduction Band Minimum

FCC Face Centered Cubic

CMOS Complementary Metal-Oxide-Semiconductor

CZ Czochraslki

FZ Float Zone

IC Integrated Circuit

EPR Electron Paramagnetic Resonance

DFT Desnity Functional Theory

Molecular Dynamics

MAPS Monolithic Active Pixel Sensors

LVM Local Vibrational Mode

LED Light Emitting Diode

PDF Point Spread Function

ATSM Agile Temperature Sample Mount

TEM Transmission Electron Microscopy

DCR Dark Count Rate

PDE Photon Detection Efficiency

DAQ Data Acquisition

RT Room Temperature

PL Photoluminescence

SNICS Source of Negative Ions by Cesium Sputtering

FIB Focused Ion Beam

IBIC Ion Beam Induced Charge

SRIM Stopping Ion Range in Matter

BCA Binary Collision Approximation

MD Molecular Dynamics

NV Nitrogen-Vacancy

ODMR Optically Detected Magnetic Resonance

CVD Chemical Vapor Deposition

RTA Rapid Thermal Annealing

CCE Charge Collection Efficiency

STIM Scanning Transmission Ion Microscopy

PIXE Particle-Induced X-ray Emission

SEM Scanning Electron Microscopy

BTE Boltzmann Transport Equation

DD Drift Diffusion

FE Finite Element

FD Finite Difference

TCAD Technology Computer Aided Design

MC Monte Carlo

MAPS Monolithci Active Pixel Sensors

FD-MAPS Fully Depleted Monolithic Active Pixel Sensors

WP Weighting Potential

MPV Most Probable Value

TOF Time of Flight

ENC Equivalent Noise Charge

Preface

Quantum technologies are a cutting-edge field that exploits specific properties of quantum mechanics to overcome classical limits. From secure communication networks to biosensors and computation, these technologies could result in revolutionary improvements in capacity, sensitivity, and speed capabilities. Among the most successful results is the field of Quantum Communications. Quantum cryptography, for instance, is an emerging technology that uses the time-bin encoding of individual fiber-coupled photons emitted from attenuated lasers for secure communication over long distances. Among several systems, quantum photonic states are preferred candidates to encode quantum information due to the lack of interaction with the external environment, making them robust against decoherence times. Single-photon sources based on attenuated laser or parametric-down conversion are well-rehearsed sources in currently available quantum communication protocols, but they cannot guarantee the "on-demand" delivery of photons with specific physical properties. Conversely, color centers in solid-state materials offer a promising alternative by providing the deterministic emission of fully polarized single indistinguishable photons, i.e., they can emit a single photon with a given wavelength and polarization when optically or electrically stimulated. For instance, diamond optical active impurities are pioneer systems in this field and among the most appealing candidates for solid-state implementation of quantum-enhanced sensing protocols and quantum processing devices at room temperature. However, the most known color centers emit visible light, and no class of defects has a currently known emission at wavelengths compatible with long-range optical fiber transport ($\sim$ 1500 nm). For this reason, the need to identify a more comprehensive set of quantum emitters and emerging new solid-state platforms for single-photon generation have rapidly changed the scenario of color centers. Recently, the demonstration of single photon emission in the near IR in silicon provides an intriguing silicon-native alternative and an enticing perspective for developing industrial-scale silicon-based single photon sources emitting at telecom wavelengths. Moreover, thanks to the high refractive index, the low spectral dispersion, and the compatibility with CMOS technology, Silicon Photonics paves the way for easy integration of complex optical systems, all working in the telecom C-band, with integrated electronic circuits. Therefore, in the direction of developing a complete silicon photonics integrated

circuit for Quantum Computation exploiting the linear optical quantum computing paradigm, the identification of suitable classes of telecom emitters in silicon and the ability to provide their deterministic placement to specific positions of a given optical circuit are essential.

Chapter 1 is dedicated to an introductory overview of single-photon sources from a theoretical point of view, supporting the experimental characterization in the following chapters. Moreover, it is intended to provide the relevant parameters and applications of color centers in quantum technologies, thus highlighting the primary research addressed questions in the landscape of solid-state quantum emitters. In **Chapter 2**, silicon's electron, optical, and structural properties are discussed with a major focus on its intrinsic and extrinsic lattice impurities and radiation-induced defects to provide the proper background for understanding the photoluminescence mechanisms in silicon. In particular, an insight into the main results of the renewed interest in silicon color centers provides an overview of the single-photon sources identified in silicon in the last few years, starting from the first demonstration in 2020. In **Chapter 3**, the technical details of the adopted methods for fabricating and characterizing color centers in silicon are described. On the other hand, the manufacturing process for the realization of silicon-based single-photon sources and the relative scientific challenges are thoroughly discussed in **Chapter 4**. In particular, the delivery of individual impurities in silicon wafers is addressed through the post-detection Ion Beam-Induced Charge (IBIC) technique for deterministic implantation. The quantum emitter creation yield is discussed in parallel; the efficient conversion of the silicon defects into stable single photon sources is tackled upon efficient thermal processing. Additionally, numerical simulations are reported as adjuvant technology for the design optimization of the target device in the deterministic positioning of single ions. Finally, **Chapter 5** is a case study that intends to stress the impact a complementary numerical modeling strategy could have in developing a controlled fabrication protocol for the realization of next-generation integrated quantum devices. The simulation activities covered are not strictly related to the tailoring of solid-state target properties; the depicted scenario is that of the innovative design of Fully Depleted-Monolithic Active Pixel Sensors (FD-MAPS) in the context of the INFN ARCADIA project.

Chapter 1

Single-photon sources

An ideal single-photon source (SPS) emits one photon with given physical properties per excitation pulse, such as wavelength and polarization. The efficient manipulation of quantum states of light is ensured by critical requirements of the ideal solid-state SPS that allow its exploitation in implementing quantum information processing protocols. These include [1]:

- a deterministic emission: the source must provide the on-demand delivery of only one photon per excitation pulse, avoiding multi-photon emission and with the photon being emitted shortly after the excitation;
- high emission count rate, meaning a short excited state lifetime, $\tau \sim$ ns;
- photostable emission without blinking or bleaching-like behavior;
- narrow Photoluminescence (PL) linewidth, i.e., ideally monochromatic emission, requiring low phonon coupling and negligible dephasing or spectral diffusion to exploit Fourier transform limited indistinguishable photons;
- fully polarized photons in absorption and emission channels;
- a two-quantum states system without a metastable shelving state that reduces the source's brightness.

Depending on the field of applications, different classes of emitters enable the implementation of specific quantum protocols, identifying the suitable trade-off between manufacturing advantages and associated drawbacks. For instance, high indistinguishability or near-infrared emission wavelength requirements can be relaxed in developing quantum-enhanced sensing protocols [2]. On the other hand, hyperfine coupling with nearby nuclear spins represents a crucial prerequisite in integrated photonic circuits for transferring quantum information between the electron spin of the single-photon source and the surrounding nuclear spins in the crystal lattice [3], [4]. Unless specific needs for long-distance communication must

be fulfilled, realizing solid-state quantum memories does not necessarily encounter particular constraints in visible (VIS) emission wavelengths. Conversely, emitting single photons within the telecom band in quantum processing systems utilizing commercial optical fibers is critical to minimize losses [5]. Furthermore, achieving quantum interference effects necessitates indistinguishable photons, which in turn require solid-state single-photon emitters with Fourier-transform-limited emission lines. Moreover, industry scale-compatible manufacturing processes together with a consolidated maturity of the material synthesis can constitute decisive factors in determining the suitable solid-state material platform; for instance, the development of a large programmable photonic processor, i.e., characterized by a large number of qubits, thus capable of processing higher complexity algorithms, could benefit from well-established technology such as silicon CMOS technology [6].

The commonly available platforms for single photon generation include:

- Faint lasers, also known as strongly attenuated lasers, operate with relatively low power (1mW [7]), using neutral optical filters until the single photon emission regime is statistically reached. While their emission can be deterministically controlled, they remain stochastic, and the emitted photons follow a Poisson distribution. Moreover, a considerable multi-photon component is typically present unless the number of zero-photon pulses is substantially increased (typical mean photon number per pulse $\sim$ 0,5 [8]).

- Parametric down-conversion is a process that utilizes the nonlinear characteristics of specific crystals. The method involves the use of a UV-pumping laser as an input, which results in the crystal producing entangled quantum states of light as an output. Typically, this approach generates heralded photons in pairs of single photons. However, being a second-order effect, the conversion process has a very small probability ($<10^{-6}$ [9]).

- Semiconductor quantum dots are reliable on-demand single photon sources based on heterostructures characterized by different band gaps, where the formation of discrete energy levels is observed due to the confinement of charge carriers in a volume comparable with the de Broglie wavelength. However, photostability is often among the main issues (bleaching and blinking phenomena heve been observed), and producing indistinguishable photons requires stringent fabrication strategies [8]. On the other side, they have a "tunable" emission wavelength characterized by high photon purity (>99% under resonant excitation)[8].

- Point defects in solid-state materials are bright (>Mcps emission rate), on-demand single photon sources that can operate at high temperatures. They are characterized by high quantum efficiency and provide photostable emission [8]. Notably, they offer an optimal interface between a solid-state medium

and photons, which are excellent "flying qubits" able to map the quantum state of a "stationary qubit" (represented by the electron and nuclear spin degree of freedom in the medium) onto a physical system. However, depending on the specific quantum protocol to be implemented, the availability of color centers with different emission properties implies the identification of a suitable trade-off between the manufacturing opportunities and the accompanying drawbacks. These last can include low creation efficiency, broad emission spectrum, low emission count rate, and cryogenic operational temperature. Moreover, optimized fabrication strategies, such as the controlled placement of single-photon sources registered to specific positions of a given optical circuit, their efficient optical activation, and their coherent control, are some of the prerequisites for the effective implementation of quantum technologies.

1.1 Second-order autocorrelation function

A criterion is thus necessary to quantify the non-classicality of the emitted photon statistics and determine if it is a single photon emitter. The method usually adopted consists of the measurement of the second-order autocorrelation function, traditionally referred to as $g^2(\tau)$, which quantifies the fluctuations of the electromagnetic field of a light beam. In particular, the function quantifies the probability of detecting a photon with a time delay τ, given the probability of detecting a photon at time t [1]. Therefore, the function evaluated at $\tau = 0$ provides the probability of detecting two photons simultaneously, which is impossible if a light source emits only one photon per excitation cycle. The ideal value for a quantum emitter should be indeed zero. The classical expression of the second-order autocorrelation is the following [10]:

$$g^2(\tau) = \frac{\langle I(t) \cdot I(t+\tau) \rangle}{\langle I(t) \rangle^2} \tag{1.1}$$

where $I(t) = E^*(t) \cdot E(t)$ is the electric field intensity and E(t) the electric field amplitude. Using the quantum theory, we can write the $g^2(\tau)$ in second quantization through photonic creation and annihilation operators as follows[10]:

$$g^2(\tau) = \frac{\langle \hat{a}^\dagger(t)\hat{a}^\dagger(t+\tau)\hat{a}(t)\hat{a}(t+\tau) \rangle}{\langle \hat{a}^\dagger(t)\hat{a}(t) \rangle^2} \tag{1.2}$$

Therefore, for a specific Fock state that fulfils the bosonic commutation relation, the correlation at zero time delay simplifies to:

$$g^2(0) = \frac{n(n-1)}{n^2} \tag{1.3}$$

Equation 1.3 clearly shows that when $n = 1$, $g^2(0) = 0$, which is the ideal scenario. In real-world experiments, the determination of this value is influenced by

factors such as background noise and dark counts from detectors. For this reason, a value below 0.5 (i.e., $g^2(0)$ when n = 2) is typically considered sufficient to verify the quantum nature of the source. However, the practical implementation of quantum protocols exploiting the interference of multiple indistinguishable photons cannot avoid the coupling of the emission properties with the crystal environment, thus highlighting the importance of achieving the highest possible signal-to-noise ratio along with the deterministic emission of indistinguishable photons.

1.2 Color centres

Color centers in solid-state materials are optically active defects occurring in the crystal lattice of semiconductors and insulators [11], [8]. Such defects can consist of missing atoms, also known as vacancies, atomic impurities, or a combination. Both intrinsic (vacancies, interstitials) or extrinsic configurations (i.e. related to alien atomic species in the crystal matrix) can result in optical transitions if the energy is delivered to the system through optical pumping or electrical excitation [12]. Color centers' electronic structure and photon emission are typically analyzed using a simplified model comprising an excited state, a ground state, and eventually, a shelving state to properly account for non-radiative transition pathways. For instance, the system can relax from the excited state to the ground state through a weakly allowed spin-flipping transition [13] or resonant energy-transfer processes involving neighboring lattice defects [14]. Therefore, a two-level or three-level system is commonly adopted to describe their emission dynamics (Figure 1.1) [1]. In

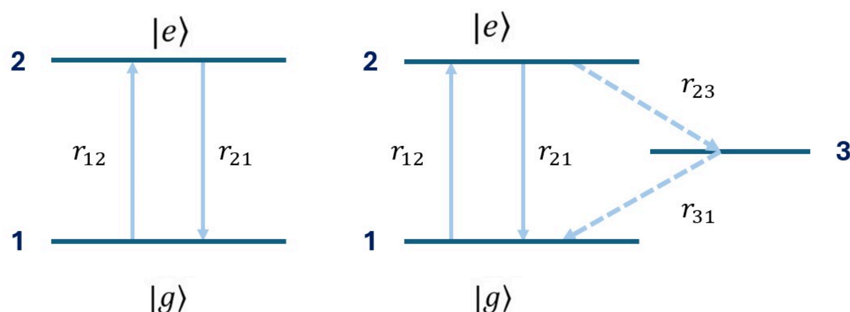

Figure 1.1: Schematic diagrams of two- and three-quantum state systems are shown in (a) and (b), respectively. The transition rates from level (i) to level (j) are denoted by $r_{i,j}$ where i,j=1-3.

both models, the ground state ($|g\rangle$) of the emitter under study is denoted as "1", while the lowest excited ($|e\rangle$) state is labeled as "2". Upon excitation, the system is promoted from the ground state to the excited state. Subsequently, when it relaxes back to the $|g\rangle$ state, one photon is emitted with a rate r_{21}. On the other hand,

the excitation rate, defined as r_{12} is proportional to the pumping power P:

$$r_{12} = \alpha \cdot P \tag{1.4}$$

Considering the occupation probability $n_1(t)$ and $n_2(t)$ of the ground and excited state, respectively, the following equations describe the population of the two levels [7]:

$$\begin{pmatrix} \dot{n}_1 \\ \dot{n}_2 \end{pmatrix} = \begin{pmatrix} -r_{12} & r_{21} \\ r_{12} & -r_{21} \end{pmatrix} \begin{pmatrix} n_1 \\ n_2 \end{pmatrix} \tag{1.5}$$

where the initial condition of the differential equations are set as follows:

$$\begin{cases} n_1(0) = 1 \\ n_2(0) = 0 \end{cases} \tag{1.6}$$

Therefore:

$$\dot{n}_2(t) = r_{12} - \lambda n_2(t) \tag{1.7}$$

where $\lambda = r_{12} + r_{21}$. The solution for the occupation probability of the excited state will thus be:

$$n_2(t) = n_2(\infty)[1 - exp(-\lambda t)] \tag{1.8}$$

where $n_2(\infty) = \frac{r_{12}}{\lambda}$, which refers to the excited steady state, assuming the optical pump (the laser) has been turned on long before. Since we are considering single photons, we can rewrite the intensities of the electromagnetic field in eq 1.1 using the emission probabilities n_1 and n_2. Therefore, the probability of emitting the first photon at a generic time t_0, considering the system already in the steady state, is described as follows:

$$I(t_0) = {r_{21}}^{\mathrm{R}} \cdot n_2(\infty) \tag{1.9}$$

where ${r_{21}}^{\mathrm{R}}$ is the radiative emission rate. The probability of emitting the second photon following the first emission at the time t_0 is instead defined as:

$$I(t_0 + t) = {r_{21}}^{\mathrm{R}} n_2(t) \tag{1.10}$$

Here, t denotes the time delay between the two emitted photons. Given that the first photon's emission brings the color center in its ground state, the probability of emitting the second photon is indeed proportional to $n_2(t)$, and it does not depend on t_0. Note that in the equation 1.1 the average is performed on t_0, thus:

$$\langle I(t) \rangle^2 = I(t_0)^2 = [{r_{21}}^{\mathrm{R}} n_2(\infty)]^2 \tag{1.11}$$

It follows that the second-order autocorrelation function for a two-quantum state system with one radiative transition from level 2 to level 1 is:

$$g^2(t) = \frac{n_2(t)}{n_2(\infty)} \tag{1.12}$$

Particularly, this last one leads to:

$$g^2(t) = \frac{n_2(t)}{n_2(\infty)} = 1 - exp(-\lambda t) \tag{1.13}$$

Furthermore, the parameter r_{21} can be determined by measuring the $g^2(\tau)$ under different optical power levels. The following relation specifically applies:

$$\lambda = r_{21} + \alpha P \tag{1.14}$$

It should be noted that, in off-resonance excitation (i.e., the energy of the laser pump is higher than the transition gap), r_{21} does not depend on the optical power since there is no stimulated emission. The resulting emission count rate is the combination of ${r_{21}}^{R}$ and any non-radiative decay rates, if present. The total decay rate would then be:

$$r_{21} = {r_{21}}^{\mathrm{R}} + {r_{21}}^{\mathrm{N}} \tag{1.15}$$

when the "R" and "N" denote the radiative and non-radiative nature, respectively. Its inverse, $\frac{1}{r_{21}} = \tau$, defines the system's lifetime, highlighting its connection with the emission rate of the colour centre and thus the aspect that makes this quantity an identifying characteristic of the emitter. At this point, we can introduce the quantum efficiency of the emitter as follows:

$$\eta_{\mathrm{Q}} = \frac{{r_{21}}^{\mathrm{R}}}{r_{12}} = \frac{{r_{21}}^{\mathrm{R}}}{{r_{21}}^{\mathrm{R}} + {r_{21}}^{\mathrm{N}}} \tag{1.16}$$

Making the $n_2(t \to \infty)$ explicit, from the solution of the differential equation system (1.5) yields:

$$n_2(\infty) = \frac{r_{12}}{r_{12} + r_{21}} \tag{1.17}$$

Consequently, the number of photons detected per unit time will be the product of:

- the probability of finding the system in the excited state ($n_2(\infty)$);
- the probability of having a radiative emission (${r_{21}}^{R}$);
- the probability of detecting a photon (i.e. collection efficiency η_{d})

Thus:

$$R = n_2(\infty){r_{21}}^{\mathrm{R}}\eta_{\mathrm{d}} = {r_{21}}^{\mathrm{R}}\eta_{\mathrm{d}}\frac{r_{12}}{r_{12} + r_{21}} = {r_{21}}^{\mathrm{R}}\eta_{\mathrm{d}}\eta_{\mathrm{Q}}\frac{\alpha P}{\alpha P + r_{21}} \tag{1.18}$$

The commonly adopted relation to fit the measurements of rate R versus pump power is the following [15], [14]:

$$R = I_{\infty}\frac{P}{P + P_{\mathrm{sat}}} \tag{1.19}$$

where I_∞ represents the maximum count rate when the emitter saturation occurs. Hereby, it can be directly derived that:

$$\begin{cases} I_\infty = \eta_\mathrm{d}\eta_\mathrm{Q}{r^\mathrm{R}}_{21} \\ P_\mathrm{sat} = \frac{r_{21}}{\alpha} \end{cases} \tag{1.20}$$

The quantum efficiency can be directly calculated if the detection efficiency is known. However, estimating factors like spherical aberrations that affect the collection efficiency of the objective lens can be a complex task. These aberrations can vary based on factors such as the focal depth, which differs among different color centers. Despite these challenges, the order of magnitude of η_d can be reasonably estimated. Finally, considering that the excitation probability is given by the product of the absorption cross-section by the incoming photon's flux, thus the parameter α is proportional to the absorption cross-section:

$$r_{12} = \alpha P = \frac{\alpha I}{h\nu} \tag{1.21}$$

where hν is the photon energy. For a complete description of the emission dynamics, sometimes a three-level model must be adopted, incorporating a non-radiative transition through a shelving state, as illustrated in Figure 1.1.b. Compared to the previously described model, this one includes a third metastable intermediate level, even though the radiative transition remains the one indicated by the solid arrow and involving the radiation decay rate r_{21}. The transitions characterised by the decay rates r_{23} and r_{31} are typically forbidden according to the electric dipole selection rules and occur through a non-radiative process known, for some systems, as intersystem crossing [13]. The equation system governing the emission dynamics (1.5) becomes:

$$\begin{pmatrix} \dot{n}_1 \\ \dot{n}_2 \\ \dot{n}_3 \end{pmatrix} = \begin{pmatrix} -r_{12} & r_{21} & r_{31} \\ r_{12} & -r_{21} - r_{23} & 0 \\ 0 & r_{23} & -r_{31} \end{pmatrix} \begin{pmatrix} n_1 \\ n_2 \\ n_3 \end{pmatrix} \tag{1.22}$$

where the initial conditions are:

$$\begin{cases} n_1(0) = 1 \\ n_2(0) = 0 \\ n_3(0) = 0 \end{cases} \tag{1.23}$$

Adopting the same approach of the two-level model, the resulting expression for the $g^2(\tau)$ is:

$$g^2(t) = \frac{n_2(t)}{n_2(\infty)} = 1 - (1 + a) \cdot exp(-\lambda_1 t) + a \cdot exp(-\lambda_2 t) \tag{1.24}$$

where a, λ_1, λ_2 are constants. In particular, λ_1 and λ_2 are the decay parameters directly connected to the characteristic times associated with the de-excitation of

the excited state and the shelving state. The first exponential term is responsible for the characteristic dip of the $g^2(\tau)$ at $t = 0$ in the case of single-photon sources and is similar to what is obtained for the two-level model (Figure 1.2, red curve). The second exponential term is due to the presence of the shelving state and determines the bunching effect, observable as an increase in above unity near the dip (Figure 1.2, black curve). The third state creates indeed an alternative decay channel compared to the radiative one, causing the radiative transition (measured by the function) to be delayed by a characteristic time corresponding to the system's re-initialization back to the ground state, from which the excitation and emission cycle can restart. The overall effect is, therefore, a temporal delay in photon generation linked to the decay dynamics through the third state. Additionally, assuming that the decay rate from level 2 to level 1 mediated by level 3 is negligible compared to the direct decay rate that constitutes the optical transition of interest, this implies that $r_{21} \gg r_{23}+r_{31}$, and consequently, we obtain the same relation found for the two-level model in 1.14, thus allowing to estimate the lifetime of the excited state adopting the same procedure.

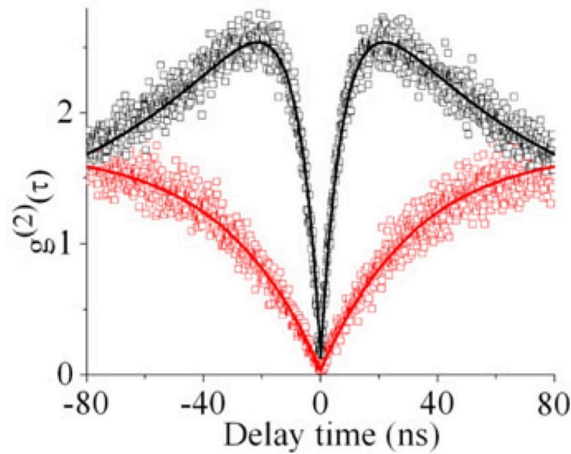

Figure 1.2: Example of a $g^2(\tau)$ function of a single NV center in artificial diamond described by a three-level model due to the presence of a shelving state, from [1]. The curve has been acquired below (red curve) and above (black curve) the saturation of the emission intensity, revealing the presence of the third state with a $g^2(\tau)>1$ for values near zero.

To conclude, the relevant parameters involved in the optical characterization of a solid-state single-color center are briefly discussed.

- The Zero Phonon Line (ZPL) represents the wavelength of photons emitted during a radiative transition between vibrational levels in the ground state. However, in the presence of a point defect within a crystal lattice, transitions

can be mediated by phonons, consequently leading to the emission of photons with lower energy, which are observed in the phonon sideband of the emission spectrum. The Debye-Waller factor parameter, which quantifies the portion of light emitted in the ZPL compared to the total emission of the color center, is a critical benchmark for evaluating the suitability of the source for quantum computation schemes involving matter qubits and linear optics. Moreover, the linewidth of the ZPL provides crucial insights into the indistinguishability of the emitted photons.

- The emission count rate refers to the speed at which photons are emitted and processed, directly influencing the device's overall performance. For this reason, it plays a pivotal role in evaluating the suitability of a single-photon source in quantum information transmission and processing applications where high-throughput data handling is essential in practical implementations of quantum information processing devices such as Quantum Key Distribution (QKD) systems.

- The emission intensity at saturation, representing the maximum photon count rate achievable when the emitter is fully saturated, is a reliable indicator of the source's brightness. When considered with the necessary optical power for excitation, this metric constitutes a quantitative parameter for assessing the performance of single-photon sources.

- A higher emission probability upon the defect excitation implies a higher quantum efficiency of the single-photon emitter. The latter is critical for evaluating how efficiently the emitter transforms excitation energy into emitted photons.

1.3 Experimental characterization of single-photon sources

This section illustrates the commonly adopted strategies for accessing the color center parameters described in the previous section. Chapter 3 will provide the experimental methods and a description of the implemented experimental apparatus in more detail.

1.3.1 Hanbury-Brown Twiss interferometer (HBT)

Figure 1.3 displays a single-photon-sensitive confocal microscope commonly employed to study the optical properties of color centers [16]. A common technique to analyze the emission statistics and differentiate the non-classical single-photon

emission from thermal or coherent light is the Hanbury-Brown and Twiss interferometer. The source light is directly sent onto a beam splitter, which divides the emission into two paths, each linked to a single-photon-sensitive detector [14]. The TTL pulse, corresponding to the detection of a photon produced by each detector, serves as the input signal for two separate acquisition channels of a time tagger. This module measures the coincidence time between the two signals, generating a histogram of events based on the time delay and representing the interferogram of the time differences between pairs of detection events at the two detectors. Specifically, the START channel is always the one from which the time delay is measured. Thus, detecting a photon in the START channel initiates an internal timer, which is then stopped upon the absorption of a second photon by the STOP detector. At this point, the time interval between the two events represents the input of the time-to-digital conversion operation, which generates a histogram of the measured delay events. This histogram directly reflects the second-order autocorrelation function $g^2(\tau)$, where the value at zero-time delay serves as a primary criterion for evaluating the non-classicality of the source. In particular, the measured histogram c(t) represents the second-order autocorrelation function upon the following normalization [7]:

$$g^2{}_{\exp}(\tau) = \frac{c(t)}{R_1 R_2 w T} \tag{1.25}$$

where R_1 and R_2 are the count rate of the two detectors, w is the bin width, and T is the acquisition time. A lack of event pairs recorded at t = 0 results indeed in an anti-bunching signature in the $g^2(\tau)$ histogram, indicating emission from an ideal single-photon source. As already anticipated, the measured signal is the sum of the emitted photons (i.e., the real signal, S) and the background (i.e., dark counts, reflected laser radiation, or non-classical spurious photoluminescence, B). Therefore, based on equation 1.1 the measured $g^2(\tau)$, indicated as $g^2{}_{\exp}(\tau)$ is defined as follows:

$$g_{\exp}{}^2 = \frac{\langle (S(t)+B(t))(S(t+\tau)+B(t+\tau))\rangle}{\langle S(t)+B(t)\rangle^2} \tag{1.26}$$

i.e.:

$$g^2(\tau) = \frac{\langle S(t)S(t+\tau)\rangle}{\langle S(t)\rangle^2} \tag{1.27}$$

Consequently, the measured function can be corrected according to the following relation:

$$g^2{}_{\text{correct}}(\tau) = \frac{g^2{}_{\exp}(\tau) + \rho^2 - 1}{\rho^2} \tag{1.28}$$

where $\rho = \frac{\langle S\rangle}{\langle S+B\rangle}$. Technical implications to remove the background and increase the signal-to-noise ratio include the utilization of highly pure substrates containing negligible contamination impurities, thus also limiting the introduction of partial

distinguishability in the collected photons. Additionally, the utilization of suitable optical filters allows for filtering out unwanted spectral components, such as the ones coming from both the elastic and inelastic scattering of the laser radiation with the sample surface. Furthermore, the integration of these single emitters into photonic structures has proved to be a successful approach for a significant improvement of their emission, in particular resulting in the enhancement of the photon-extraction-efficiency, such as for solid-immersion lenses or nanopillar [17], [18] and in the Purcell enhancement of their emission rate such as in the case of nanocavities [19].

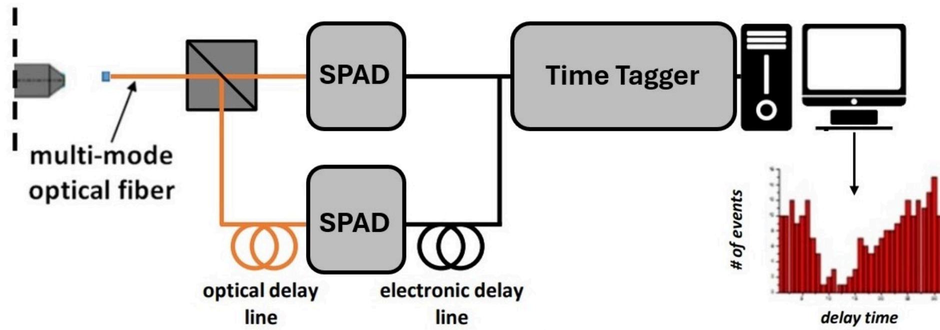

Figure 1.3: Schematic representation of a Hanbury-Brown-Twiss interferometer. The single photons are detected through two Single Photon Avalanche Diodes (SPADs), and the generated TTL pulses are sent to the Time Tagger to measure the coincidence time between the two signals.

1.3.2 Time-Correlated Single Photon Counting (TCSPC)

Time-resolved photoluminescence measurements offer an insight into the dynamics of optical excitation cycles. In particular, the time-correlated single photon counting (TCSPC) approach is typically used. The technique relies on the idea that the probability distribution for a single-photon emission following excitation gives the actual intensity distribution against time for all the emitted photons [20]. Thus, the time-resolved intensity profile of the emitter is retrieved by sampling the time of a single-photon emission following many periodic excitation pulses from a laser, collecting information concerning the emission dynamics over multiple excitation and emission cycles. As shown in Fig. 1.4, the creation of a histogram over several cycles involves the fluorescence stimulation employing a short laser pulse and the measure of the time interval between the excitation and the emission using a time tagger usually characterized by a time jitter in the order of tens of ps and a deadtime of few nanoseconds [21]. Generally, the width of the time bins aligns with the time tagger resolution of the order of a few ps. Since it is impossible to know the exact timing of decay events, a statistical expectation can only be predicted;

in fact, as well as for nuclear decay, the result in time-resolved fluorescence is a histogram showing the fluorescence decay profile reconstructed from many single photon events collected over many cycles. Figure 1.5 reports a schematic representation from [22] of start-stop times in time-resolved fluorescence measurements with the TCSPC technique. However, it is not necessary to do the TCSPC with single emitters. If the low probability of registering more than one photon per cycle is ensured, the histogram of photon arrivals still represents the time decay one would have obtained from a single shot time-resolved recording[22]. The reason for this approach comes from detectors and electronics' dead time of at least several nanoseconds (tens of μs for InGaAs detectors) after a photon event. During this period, they are unable to process another event. Because of these dead times, TCSPC systems are designed to register only one photon per excitation cycle. If the number of photons occurring in one excitation cycle is typically greater than one, the system may detect the first photon but miss subsequent ones. This would result in an over-representation of early photons in the histogram, known as "pile-up." Therefore, minimizing the likelihood of cycles with more than one photon is crucial. A rule of thumb can be applied for practical purposes: the average count rate at the detector should be no more than 1 to 5% of the excitation rate [22]. Thus, this requirement is important not to distort the histogram, thus affecting the lifetime of the color center under study, which can be determined through an exponential decay fit, and the $g^2(\tau)$ curves in HBT measurements as well.

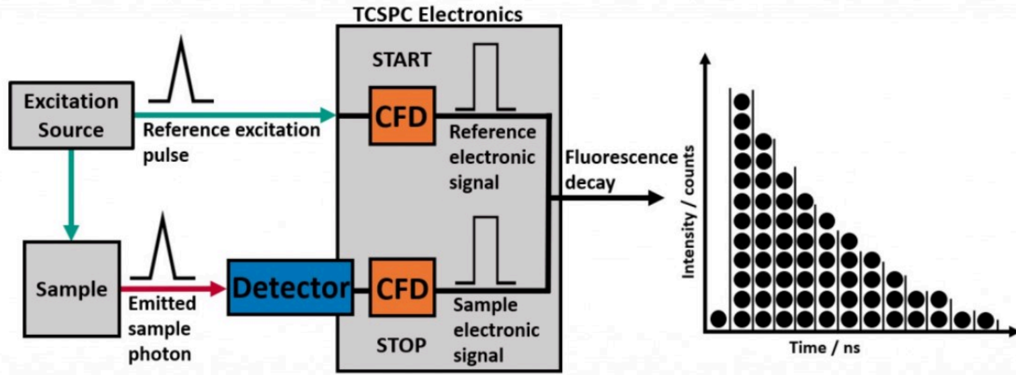

Figure 1.4: Schematic representation of a TCSPC setup with two inputs, reference START and sample STOP, producing a histogram of timed events, from [23].

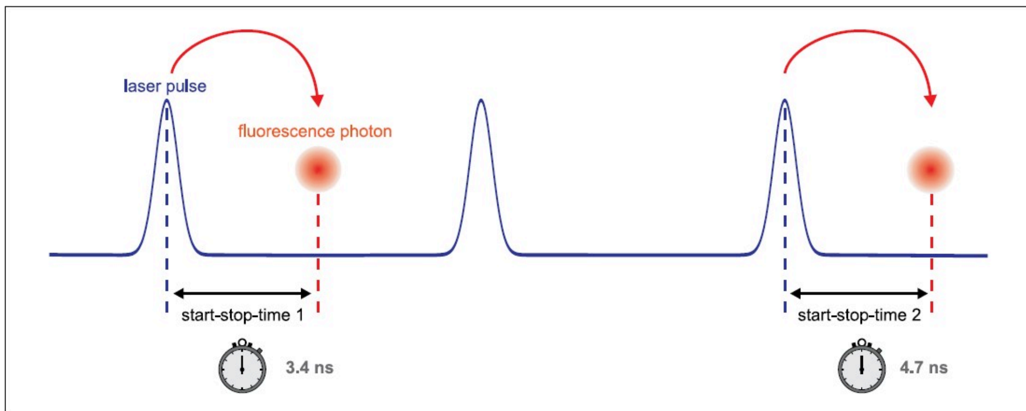

Figure 1.5: Start-stop times in time-resolved fluorescence using TCSPC. From [22].

Chapter 2

Color centers in silicon

This chapter will address the main features of silicon to provide the relevant background for understanding the photoluminescence mechanisms in this solid-state platform. The following sections will mainly discuss its electronic and optical properties with lattice impurities, both intrinsic and extrinsic, and radiation-induced effects, intending to go through some of the significant optically active defects identified from the mid-70s up to the present day. The chapter will end with an overview of the single-photon sources identified in silicon in the last few years, starting from the first demonstration in 2020. The discussion will thus provide an insight into the main results as part of the renewed interest for silicon color centers in the perspective of addressing the scalability challenges in quantum device fabrication protocols.

2.1 Properties of pure silicon

Silicon represents the 26% of the Earth's crust [24]. Well-established fabrication techniques have unlocked through decades the easy and cheap production of large crystals, reaching a very high purity and making silicon the most extensively used semiconductor in the microelectronics industry. Such a triumph directly results from its electrical, mechanical, and thermal properties. Silicon's electrical structure can indeed be easily tailored with the intentional introduction of donor and acceptor impurities, and the native occurrence of its insulator oxide (SiO_2) has made it possible to develop advanced and successful semiconductor wafer innovations such as the Silicon on Insulator (SOI) Technology [25][26]. Additionally, the device fabrication in silicon allows a wide operating temperature range (conventionally -55°C and 125°C), and silicon thermal and mechanical properties are well suited to using photo-lithographic techniques in the patterning of integrated circuits [25].

2.1.1 Crystallographic structure and phonon properties

Silicon is a tetravalent metalloid with atomic number 14. It can exist in a crystal form with a diamond cubic crystal lattice, e.g. with a Bravais lattice whose unit-cell basis contains eight atoms, two Si atoms at each lattice site and a lattice parameter of 0.543 nm, Fig. 2.1. The latter is constant in the 0 - 20 K temperature range, whereas decreases with increasing temperature, reaching a minimum for $\sim$ 120 K [27]. Consequently, in contrast to what is usually observed in other crystals, the negative thermal expansion may perturb the radiative transitions with an increase in the energy of emitted photons and be responsible for a blueshift of the characteristic optical lines. It is characterized by a density of 2330 kg$\times$ m^{-3}, corresponding to 5.0×10^{22} cm^{-3} atoms [27]. The Raman phonon energy, in the limit of low temperature, is 521 cm^{-2} [28]. Particularly, the phonon density of states in silicon at room temperature (300 K) is reported in Fig. 2.2, providing an idea of the involved energies responsible for redshifted radiative emissions in the case of phonon-assisted recombination.

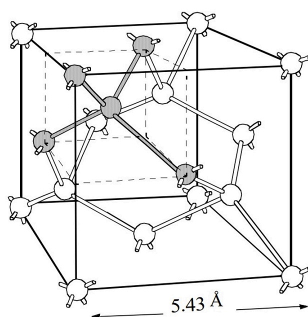

Figure 2.1: Crystal structure of silicon [29]

2.1.2 Electronic properties

The electronic configuration of silicon is [Ne]3s^{2}3p^2. It is an elemental solid where each atom is surrounded by four close neighbors, forming a tetrahedron. Each one shares four valence electrons with the neighbors, forming covalent bondings. In sp^3 bonded solids, the bonding and antibonding states generated from the four orbitals acquire dispersion in the crystal and generate eight sub-bands. The four corresponding to the bounding states are filled and called "valence band". The remaining four corresponding to antibonding states represent the "conduction band". Fig. 2.3 shows its electronic band structure and high symmetry points for the Brillouin Zone (BZ) in a face-centerd cubic lattice. The range of energies without electronic states across the whole BZ represents the band gap, which monotonically decreases from 1.170 eV at 0K to 1.125 eV at 300 K [27]. Since there are eight valence electrons in the primary unit cell of the solid, the four bands reported

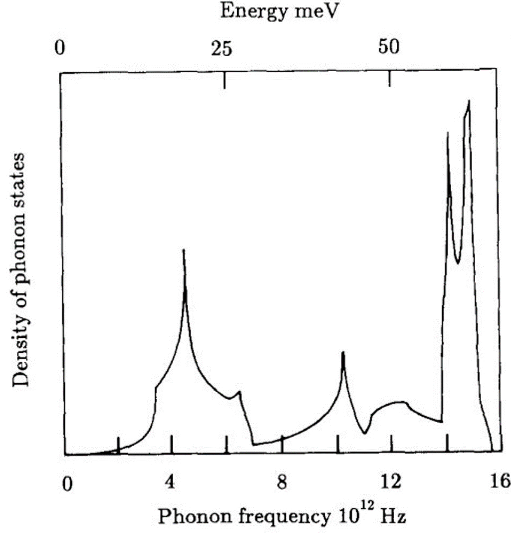

Figure 2.2: Density of phonon states of silicon calculated with the Born-Von Karman model for T = 300K [27][30].

in Fig. 2.3 and below zero are fully occupied. The Valence Band Maximum (VBM), representing the highest occupied state, is at the Γ point, whereas the lowest occupied one, i.e. the Conduction Band Minimum (CBM), is between the Γ and the X point, giving rise to an indirect bandgap. Moreover, in all the sp^3 bonded solids, the Valence Band has a minimum in Γ, which can be identified as the s-like state of the bonding orbitals originating from the interaction of sp^3 hybrids of nearest neighbor atoms. Additionally, since the hybridization involves one s and three p states, the top of the valence manifold at Γ corresponds to the p-like states of the bonding orbitals. Away from the Γ point, the states lose their s- or p-like character. Particularly, the VBM at k = 0 consists of a light hole band, a heavy hole band and a split-off band where $m_{lh} = 0.153m_0$, $m_{hh}= 0.537m_0$ and $m_{so}=0.29m_0$. The first two sub-bands are degenerate, whereas due to the spin-orbit interaction the energy of the third band is lower in k = 0 by Δ = 44 meV [27]. Since the Fermi level is in the middle of the bandgap in a pure crystal without impurities or intrinsic defects, at 0 K, all the electron states in the valence band are occupied, and all the states in the conduction band are empty. At room temperature, a few electrons may have enough energy to be thermally excited in the conduction band and create holes in the valence band. Electrons and holes recombination processes balance at thermal equilibrium, thus giving an average value of carriers per unit volume in pure or "intrinsic" silicon, typically referred to as n_i (T) for a given temperature. This means that n_i (T) electrons will be found per unit volume in the conduction band and the same hole concentration in the valence band. A generally accepted value for n_i (T) at room temperature is $1.45 \cdot 10^{10}$ cm^{-3} [25].

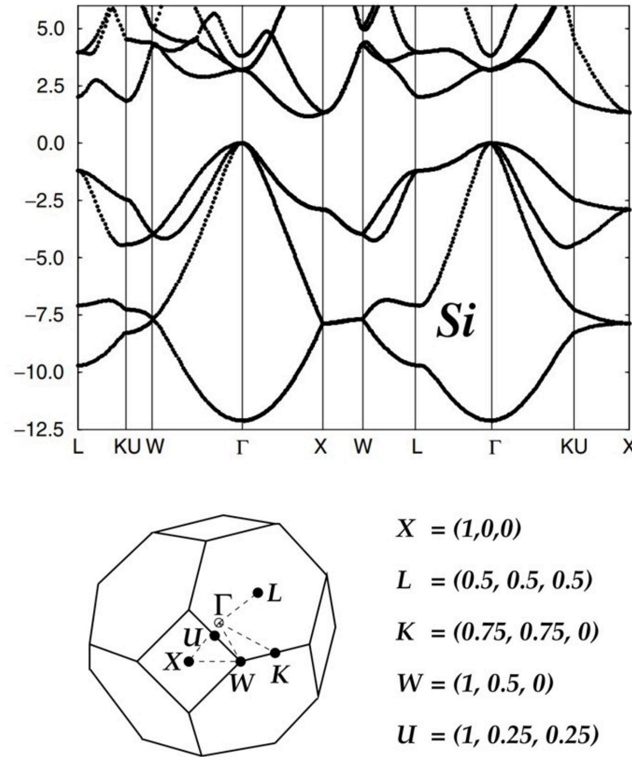

Figure 2.3: Band structure of silicon. The diagram below shows the band structure, which highlights the high symmetry points of the Brillouin Zone for the FCC lattice. The letters X, L, K, W, and U represent specific values expressed in units of $2\pi/a$, where a is the lattice constant. The symbol Γ denotes the center of the Brillouin zone. The energy scale is measured in electronvolts, where the zero point is set at the maximum of the Valence Band. [31]

2.1.3 Optical properties

Absorption

When an incident photon supplies energy to an ideal pure semiconductor, the primary electron excitation is a free electron-hole pair. In direct bandgap semiconductors, the energy absorption, if equal to the energy gap at a minimum, can directly promote an electron to the conduction band. Consequently, due to the electron decay back to the valence band, a photon emission occurs. Because silicon has an indirect band gap, meaning the electron and hole of the electron-hole pair have different wavevectors, the direct coupling of these states with the electromagnetic field cannot occur, and a third momentum-conserving particle, such as a phonon, must be involved. This also applies to the radiative recombination with the emission of one photon. Considering, thus, the population of phonon states at

high temperatures, the absorption of light quanta in silicon may have a significant width due to phonon-assisted processes. In the case of photons with considerably higher energy than the bandgap, the absorption coefficient is generally high, and the energy is absorbed within a few μm of the surface of the crystal, where a considerable out-of-equilibrium and steady-state concentration of electron and hole pairs are produced. In this regard, Fig. 2.4 displays the absorption coefficient for crystalline silicon versus the photon energy. Therefore, the excitation first results in the creation of free electrons and holes in the lattice. Additionally to free particle transitions, when the optical excitation occurs at adequately low temperatures, and the electrons are not too far from the holes, the Coloumb interaction gives rise to electron-hole pairs, which are coupled by small energy (14 meV for silicon [32]) and form what are called "free excitons". Since their energy no longer represents two independent particles, they provide the lower energy excitation in a semiconductor. For indirect semiconductors such as silicon, as long as the temperature is low enough to avoid their ionization, their lifetime can be long enough ($\sim$ 60 μs [32]) to allow the migration of free excitons and their trapping by lattice localized impurity atoms, thus forming what are known as "bound excitons". In other words, the energy of the free exciton is transferred to the point defect, promoting the latter to an excited state. Remarkably, among the different recombination processes responsible for extrinsic luminescence in silicon, bound exciton represents one of the most common mechanisms by which a shallow defect can emit a photon [27],[33]. The impurities in the crystal can increase the probability of recombination, effectively acting as traps for free exciton created with the absorption of photons during laser illumination and strongly localizing their wave function. Moreover, the properties of the emitted photons would be unambiguously dictated by the energy levels of the defect complex and related to the involved atomic species [27]. Conversely, photons with energy lower than the bandgap are not directly absorbed by a pure crystal. However, they can be absorbed by the optically active defects in the crystal matrix, thus avoiding any intermediate process in the energy transfer. Although this mechanism shows some advantages, such as the possibility of exploiting the polarisation of the exciting photons, the smaller oscillator strength can be too poor to produce a measurable signal. Regarding the intrinsic luminescence in silicon, Fig. 2.5 shows the dominant luminescence lines associated with the free exciton annihilation, which are assisted by the two-phonon emission of the transversal acoustic (TA, hν = 14.4 $\pm$ 0.2 meV), longitudinal optic (LO, hν = 56.2 $\pm$ 1 meV) and transversal optic (TO, hν = 58.0 $\pm$ 1 meV) modes [27]. The peak labeled 0 is the ideally forbidden zero-phonon transition occurring due to a slight deviation from a non-cubic environment.

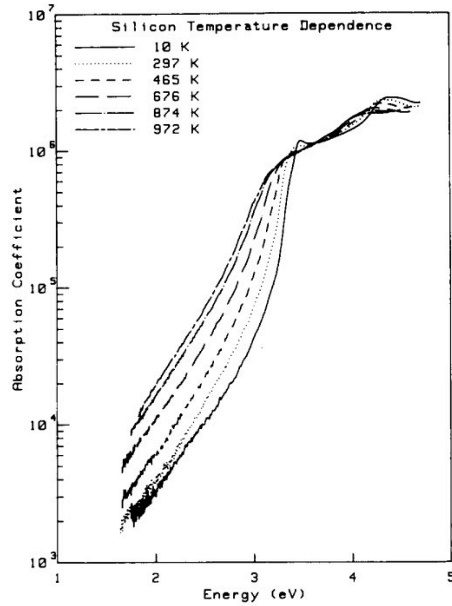

Figure 2.4: Optical Absorption coefficient of silicon as a function of the photon energy for chosen temperatures [34].

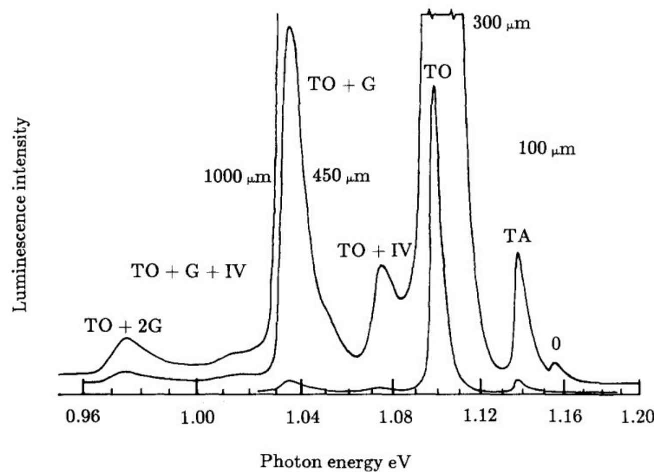

Figure 2.5: Intrinsic photoluminescence of Si at 26 K and displaying the phonon combinations involved, from [27]. The ratio of the relative intensities is temperature-dependent. G is the k = 0 optical mode. Four different values of slit width have been used (100 - 1000 μm).

Refractive index and reflection

The very high refractive index of silicon [35], n = 3.5 for $\lambda = 1.55$ μm, results in a crucial feature for the optical confinement required in the optical guiding, thus

allowing the realization of the interconnections between optical devices in photonic integrated circuits. It follows that the reflectance of silicon at normal incidence is very high, as displayed in Fig. 2.6. For photons characterized by energy lower than the band gap, the reflectivity R is approximately 30% of the incident light. On the other hand, for higher energy photons, up to the UV edge of the visible range, the reflectance increases; for instance, in the case of a green laser of 2.5 eV, roughly 40% of incident light is reflected [36]. On the one hand, these optical properties have unlocked the realization of a silicon-based integrated photonics platform, which has many advantages related to the host material, such as compatibility with the Complementary Metal-Oxide-Semiconductor (CMOS) electronic fabrication; on the other side, the high value of R can severely limit the extraction of light from color centers buried into the bulk due to the large portion of light reflected at the silicon-air interface. For this reason, a successful approach involves the optimal tuning of the fabrication parameters in manufacturing silicon color centers, such as the implantation energy used to introduce the atomic impurities at specific depths, to maximize the collection efficiency [37]. Synergically, the emission from the optically active point defects can directly be enhanced through the coupling with optical nanocavities, reaching even a 30-fold increase in the collected photoluminescence signal [38], [39].

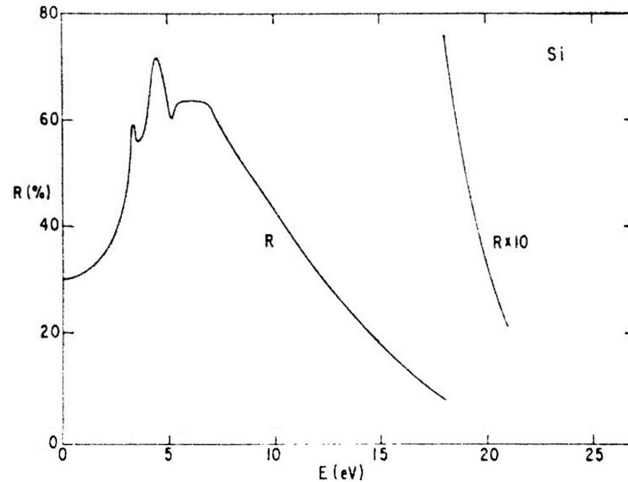

Figure 2.6: The reflectance R of Si for normal incident light as a function of the energy of the incident photon, from [36].

2.2 Impurities and defects

2.2.1 Contamination

The presence of impurities in artificially grown materials such as bulk silicon crystals can come from their presence in the polycrystalline seeding substrate, chemical elements in the crucible where the melted material is contained, or atomic species in the growth atmosphere. Two industrial processes commonly convert polycrystalline silicon into single-crystal ingots: crucible-pulling Czochralski technique (CZ) and crucible-free float zone growth (FZ). Although the FZ silicon is purer, 90% of the silicon production for the electronic industry is based on the crucible-pulled technique. This method was named after the Polish metallurgist Jan Czochralski and consists of a rotating seed crystal with the desired crystallographic orientation dipped in the molten silicon contained in a high-purity silica crucible. The pull rate and the melt temperature are adequately adjusted for the intended ingot diameter while the seed is withdrawn and rotated. During the lifting and the rotation, the silicon in the liquid-solid interface solidifies, creating a sizeable monocrystalline silicon. The process is usually performed in an inert atmosphere, such as argon. Active donor and acceptor impurities can also be added to the melt to dope the CZ crystals. However, the thermal dissolution of silica from the crucible represents the primary limit in the purity of the grown silicon, introducing a relatively large concentration of electrically inactive interstitial oxygen ($\sim$ 20 ppm) close to the solubility limit and eventually resulting in the impurity clustering when the crystal cools to room temperature. [40] The second major impurity in CZ silicon is carbon, with a typical concentration below the solubility limit ($\sim 10^{17}$ cm^{-3}) [41]). Substitutional carbon is also electrically inactive but can play an essential role in the kinetics of oxygen precipitation or indirectly in the impurity-gettering and wafer warping during processing. In this case, potential sources of contamination have been identified as either the polysilicon starting material or the graphite components used in the CZ pulling equipment during growth.[42].

On the other hand, the concentration of oxygen and carbon can be minimized down to $\sim 10^{16}$ cm^{-3} in the float zone technique where vertical melting is used. This type of silicon has a resistivity between 10 and 200 $\Omega \times$ cm and finds mainly application in semiconductor power devices. [43]. The seed with the desired crystal orientation is mounted on the tip of polysilicon where a contactless technique such as a halogen lamp furnace or RF heating coil is responsible for the melting of a very narrow region of the silicon, which is then moved along the crystal, converting the polycrystalline into single-crystal silicon [42]. The unpure silicon refinement results from the melted region where the impurity atoms diffuse towards the liquid area due to the segregation coefficient being smaller than the unity. The melted silicon thus resolidifies, leaving a trail of pure material. Unfortunately, from the mechanical strength point of view, the FZ silicon becomes more vulnerable to thermal stress

during device manufacturing. Therefore, slip dislocations and loss of geometrical planarity may represent severe limitations in IC device fabrication. A schematic representation of the single-crystal growth by float zone and Czochralski method is reported in Fig. 2.7.

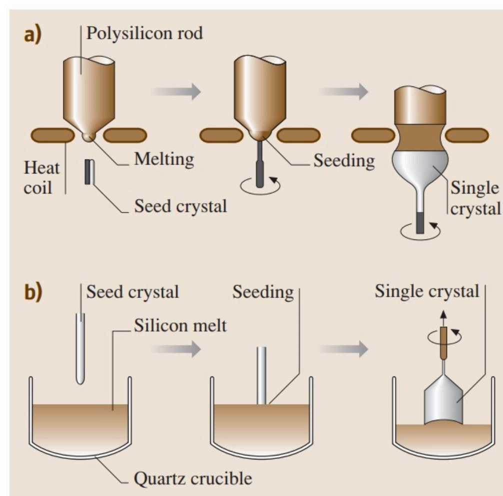

Figure 2.7: Schematic representation of the operational steps for the silicon single-crystal growth in the Float Zone a) and Czochralski b) method. From [42].

2.2.2 Intrinsic Impurities

Dominant intrinsic point defects in silicon are vacancy aggregates resulting in tiny holes known as voids, whose size is typically less than 150 nm, and silicon interstitial clusters, which, beyond a critical size, are responsible for the formation of a network of dislocation loops which generally extend for several microns [42]. The latter can especially represent a significant source of detrimental effects on the device's functioning, including increasing leakage currents or enhanced/retarded dopant diffusion [44], [45]. As reported by G. D. Watkins, the isolated vacancy has been detected upon MeV electron irradiation performed at cryogenic temperature through EPR measurements. It can exist in five different charge states (V^{2+}, V^{+}, V^{0}, V^{-}, V^{2-} and represents the first direct observation of a defect with "U-negative" properties, i.e. a defect that can traps two electrons or holes [46]. The V^{2+} traps two holes indeed, with the second more strongly bound than the first, indicating a net effect of the two carriers overcoming the Coulomb repulsion and being responsible for the reverse ordering of the levels in the band gap. The activation energy for the vacancy migration has been reported to be in the range of 0.18 eV - 0.45 eV, depending on the dominant charge state for each of the Fermi-level positions of the n-, p-type of high-resistivity silicon. For temperatures higher than $\sim$ 70 K for

n-type, $\sim$ 150 K for p-type and $\sim 200K$ in high resistivity material, the vacancies pair off with other defects in long-range diffusion processes, including interstitial oxygen, substitutional acceptors and donors, H_2 molecules and substitutional iso-electronic impurities such as Ge and Sn [47]. Figure 2.8 summarises the stability of isolated vacancies and the binding energy of vacancy-defect pairs upon 15-30 min isochronal annealing. Moreover, during ion implantation or other processes involving heavy particle damage, the kinetic energy of recoiling atoms can result in many displacements, promoting the aggregation of vacancies and originating divacancies, tri-vacancies, and 4-vacancies complexes, which are stable at room temperature and can act as nuclei or precursors of extended defects [48].

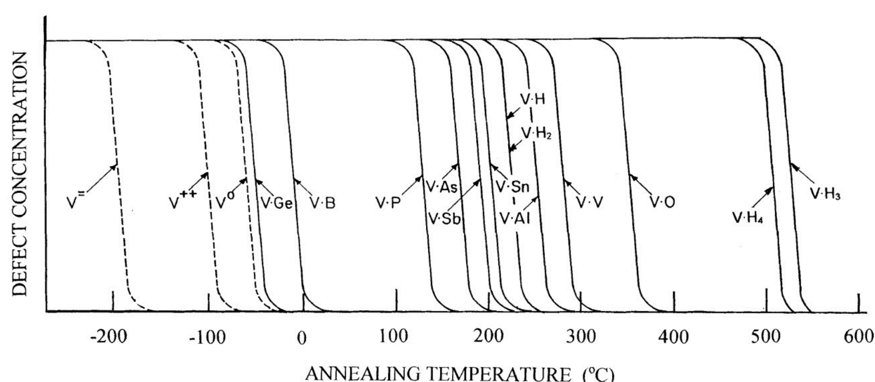

Figure 2.8: Schematic of vacancies and vacancies-defect pairs stability observed in 15-30 min isochronal annealing experiments [47].

As outlined in Chapter 4, ion implantation is a fundamental step in manufacturing silicon-based devices and fabricating silicon-based single photon sources. This process inevitably introduces self-interstitial defects, which are, in turn, responsible for the thermal enhanced diffusion of dopants when combined with subsequent thermal annealing and represent the building block of extended rod-like defects, such as rod-like 311 [49]. While the observation of the isolated self-interstitial remains elusive, and no Electron Paramagnetic Resonance (EPR) evidence at cryogenic temperatures under MeV electron irradiation has been reported either [47], pointing at the assumption of highly mobile defects even at 4 K, larger aggregates of self-interstitial (I_3, I_4) have proved to originate photoluminescence centers emitting at 1.0182 eV and 1.0398 eV, respectively known as W and X centers [50], [51]. The structure and the properties of the W emitter will be extensively discussed in one of the following sections. EPR and vibrational spectroscopy measurements have pointed out different silicon interstitial-related configurations, among them, reported in figure 2.9, the ones with Al, B, C, and H_2. In particular, the Si_i ejects the Al atom in the tetrahedra interstitial site, while the boron atom is placed between two silicon atoms, slightly off the bond-centered position. Similarly to the case of the vacancy, Si_i can be trapped by the H_2 molecule upon hydrogen implantation

or electron irradiation of silicon growth in hydrogen atmosphere [47]. Lastly, the moving Si_i produces a split configuration where carbon shares the lattice site with a silicon atom. The latter diffuses with relatively low activation energy (0.72-0.75 eV [52]) and is essential in forming another defect complex responsible for silicon's photoluminescence band at 769 meV. To provide an idea of the self-interstitial-related reactions, Fig. 2.10 displays the stability of different interstitial-related defects identified with EPR or vibrational spectroscopy measurements that would be observed upon 15-30 min isochronal annealing studies. The reported behavior outlines that the self-interstitial-related complexes have limited stability before, at a specific temperature, interstitial silicon atoms start migrating and are trapped by other impurities.

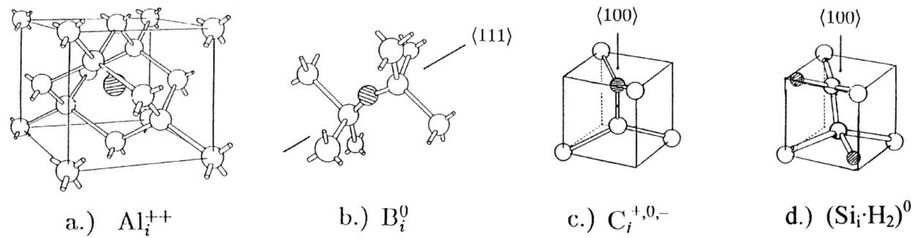

Figure 2.9: Common structural configurations of highly mobile interstitial silicon atoms trapped by atomic impurities. [47].

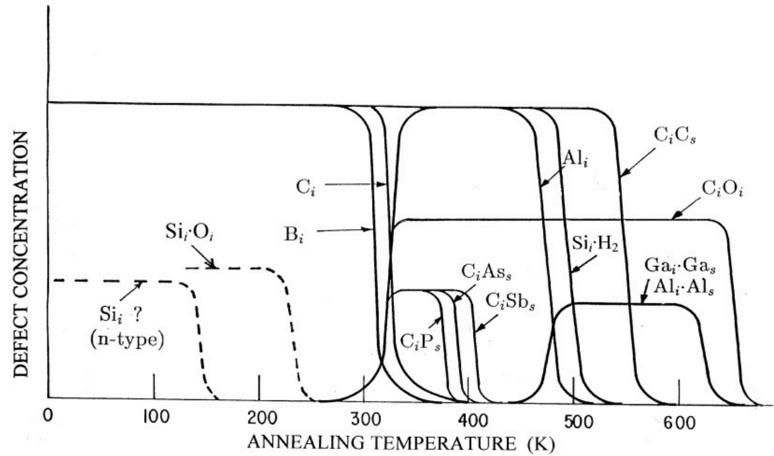

Figure 2.10: Interstitial-related defects evolution upon 15–30 min isochronal annealing from [47]. Each defect complex has limited stability before the interstitial silicon atoms start migrating and being captured from other atomic impurities.

In conclusion, both primary intrinsic defects in silicon, vacancies, and self-interstitials, are rapid diffusers. In particular, through indirect metal diffusion experiments in silicon, the product of the equilibrium concentration C_{eq} and the

diffusivity D of these intrinsic defects have been estimated for silicon interstitials and vacancies, respectively [42]:

$$C_{\text{eq}}D_{\text{I}} = 1.5 \times 10^{26} \times e^{(-4.95eV/kT)} \tag{2.1}$$

$$C_{\text{eq}}D_{\text{V}} = 1.3 \times 10^{23} \times e^{(-4.24eV/kT)} \tag{2.2}$$

where k is the Boltzmann constant, and T is the given temperature. Nowadays, different methods involving a very tight control over the crystal growth parameters permit the production of pure silicon free from interstitial defects. These techniques involve precise fabrication requirements such as the combination of nitrogen doping, fast pull rate, and subsequent high-temperature annealing ($\sim$ 1200°C) or even the complementary incorporation of Si interstitial and vacancies during the crystal growth [42]. Mainly, parameters such as the thermal history of the sample and the cooling rate have been intensely investigated, pointing out their importance in determining the size and the density distribution of vacancies and self-interstitials across the crystal. However, since this is beyond the scope of this thesis work, the experimental results and the theoretical model will not be discussed in these chapters.

2.2.3 Common extrinsic defects

Oxygen

The presence of oxygen in monocrystal silicon as a grown-in impurity has been previously discussed, especially in the case of Czochralski silicon. Interstitial isolated oxygen atoms in silicon form electrically neutral defects where the oxygen is bound to two neighbor silicon atoms. When the CZ silicon is heated, small aggregates of oxygen atoms acting as thermal donors are created. The maximum creation rate is reached at 450°C and is proportional to the fourth power of interstitial oxygen concentration [53]. These clusters can also significantly interact with other mobile defects, such as self-interstitial being captured at oxygen clusters [54]. Therefore, since CZ silicon lies for some time in this temperature regime when it cools from the melting point to room temperature, a general practice includes reheating the CZ silicon followed by a very rapid cooling to avoid the 450°C region. The characteristic vibrational mode at 1106 cm^{-1} ($\sim$ 9 μm) is typically used to detect the concentration of oxygen through absorption measurements [24]. Moreover, when oxygen originates self-complexes, it releases self-interstitials, which can make other species, notably carbon, mobile.

Carbon

Carbon can form several defect complexes in silicon, whose optical excitation results in a large variety of photoluminescence lines. As discussed in [27], it can couple with another carbon atom (969 meV band), one oxygen atom (789 meV band), one N atom (745.6 meV band), one Ga atom (875meV band), the four-lithium atom complex (1082 meV band), beryllium (1117 meV band) and various radiation damage centers. Other complexes with donors or acceptors are reported; examples include photoluminescence studies of Al-related defects in irradiated silicon [55]. As grown-in impurity, carbon is present in the substitutional lattice site, replacing one silicon atom. For this reason, proportionally to its concentration, it is also responsible for the lattice parameter contraction $\frac{\Delta a}{a}$ =6.5 $\times$ 10^{24} [27]. The diffusion energy of 3.15 eV is, in fact, indicative of impurities that are known to diffuse substitutionally [56], thus stating that carbon atoms occupy substitutional sites. This conclusion was also consolidated by the measured absorption bands in the infrared range (607 cm^{-1}) following theoretically predicted vibrational local modes of isolated substitutional carbon atoms. The absorption bands can shift instead to 830 cm^{-1} due to carbon precipitation and the formation of β silicon carbide if prolonged annealing ($\sim$ 100 hours) in the 1000-1250°C temperature range of silicon crystals with high carbon concentration is performed [27]. In this respect, the solubility of carbon near the silicon melting point is commonly accepted to be 4.5 $\times$ 10^{17} cm^{-3} and to decrease with temperature [57]. Moreover, in high oxygen-containing crystals that have been thermally processed in the 400-550°C temperature range, the high concentration of substitutional carbon has been identified as an inhibitor of oxygen clustering acting as thermal donors, resulting in the formation of carbon-oxygen complexes [58], [59], [60]. However, a silicon self-interstitial atom can easily displace the substitutional carbon C_s, creating a highly mobile interstitial carbon atom C_i. This interaction makes the presence of carbon a relevant aspect in the kinetics of the impurities that constitute point defects in silicon; for instance, it is responsible for the inhibition of transient enhanced diffusion of dopants, which are promoted by Si self-interstitials as well [61]. Interstitial carbon has been traditionally observed either by infrared absorption through its localized vibrational modes (930 cm^{-1} and 921 cm^{-1} [40], [27]), EPR [62], or its electronic transition at 856 meV in photoluminescence or absorption measurements. In particular, the absorption line reported at 855,9 meV would be the result of the excitation of an electron in the neutral charge configuration $(C_i)^0$, while the PL emission would result from the recombination of a weakly bound electron with $(C_i)^+$ [40]. In Fig. 2.11, the split interstitial structural configuration proposed by G. D. Watkins for the C_i center and displaying a C_{2v} symmetry is reported [62]. Being electrically active, it introduces a donor level at E_V+0.28 eV and an acceptor level at E_C-0.10 eV. Unlike substitutional carbon, interstitial carbon is highly mobile, and the measured activation energy for its diffusion is around 0.9 eV [63]. It is not stable at room temperature,

and thereby, it interacts with O_i, C_s, thus acting as a nucleation center for self-interstitials and complexes such as $C_i(S_i)$, $C_iO_i(S_i)$, and $C_sC_i(S_i)$ [64]. Considering that substitutional carbon acts as a trap for migrating interstitial carbon, the decay time for thermally activated trapping of C_i at C_s is inversely proportional to the carbon concentration of C_s atoms for a given temperature T [27]:

$$\tau = \frac{1.7 \times 10^{16} \times e^{(0.87eV/kT)}}{[C_s]} \tag{2.3}$$

where k is the Boltzmann constant.

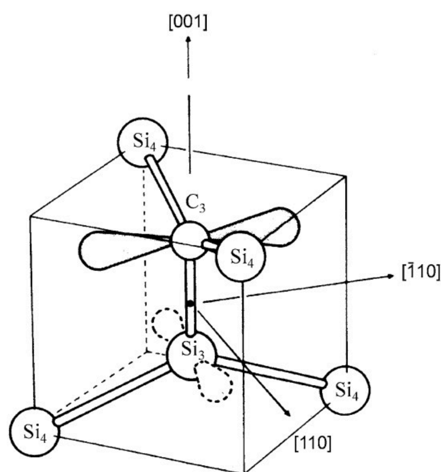

Figure 2.11: Split interstitial configuration of the positive charge state of the C_i center where the C and the Si are threefold coordinated. The captured free hole is represented as dashed, while Miller indices specify the main axes of the defect. [40].

2.2.4 Radiation-induced defects

As already anticipated, the formation of several optically active defect complexes has its origin in the radiation-generated excess of highly mobile interstitial silicon atoms Si_i, which arise from the stable displacement of silicon atoms during the radiation-induced damage of the crystal matrix, i.e., avoiding the complementary recombination with the created vacancies. The reactions in forming these systems critically depend on the irradiation temperature, the impurities in the silicon substrate, and the typology of damage [47]. Considering what has been previously discussed about vacancies and interstitial defects in silicon, depending on the temperature regime, the effects of the radiation process can evolve following different paths [27]. For instance, the storage of silicon samples at room temperature after low-temperature electron irradiations makes the interstitial carbon Ci

mobile and lets it complex with oxygen, if present, or substitutional carbon C_s. On the other side, for the same irradiation process, the photoluminescence signal related to carbon-based defects emitting at 969 meV, and promoted by the creation of interstitial silicon atoms, is halved in silicon samples irradiated at 100°C with respect to the case of room temperature irradiation; indeed the mean capture time of C_i at C_s sites is short compared to the irradiation time and the production rate of C_i is almost constant for temperature higher than 200 K, thus preventing the formation of the centers and self-interstitials [27]. When the irradiation process meanwhile takes place at a lower temperature but high enough for the C_i atoms to be sufficiently mobile, they complex with substitutional carbon or interstitial oxygen, thus originating the photoluminescence centers known as G and C centers, respectively. In irradiated Czocharlski silicon, the reorganisation of the metastable oxygen-vacancy pair O-V resulting from the trapping of mobile vacancies by the oxygen impurity atoms produces the so-called "A" center, which is a point defect characterized by vibrational absorption lines at 836 cm^{-1} 884 cm^{-1}. Since the irradiation with ions produces multiple damaged areas in the crystal matrix, complexes commonly produced upon room temperature irradiation and subsequent annealing are the 1040 meV band occurring at vacancy clusters and the W center (photoluminescence emission at 1018 meV) originating from interstitial silicon clusters [27]. The latter has been explicitly observed upon self-ion implantation [65], neutron irradiation [66], and melting and recrystallization mechanisms upon high-power laser annealing [67]. In 2022, the non-classical nature of the emitted light has been proved [50], thus unlocking the application of these common radiation damage centers in plenty of quantum prospectives based on intrinsic quantum emitters in silicon. For this reason, in the following section, its optical and structural properties will be carefully discussed.

2.2.5 The W center

The intrinsic complex known as W center is a tri-interstitial defect that occurs as a common radiation-induced defect in silicon [50], [49], [68] [69]. The evidence for an interstitial origin in many irradiated silicon devices strongly rules out any connection with intrinsic or extrinsic impurities thereby. Moreover, according to the latest Density Functional Theory (DFT) study [50], the structural configuration responsible for the below bandgap emission at 1018 meV and the relative localized vibrations is a tri-interstitial configuration. Indeed, based on the tight-binding approach [70], DFT calculations [71], and Molecular Dynamics (MD) [72], several structural models have been proposed to describe the W center. However, a tri-interstitial configuration resulted in being the most energetically favorable and advanced DFT calculations [50] has identified the I_3-V (Fig. 2.12) configuration out of the five potential candidate structural complexes as the suitable one to account for experimental results, including the very recently verified single-photon emission

[50]. The ground state of the neutral configuration of the defect is represented by a single resonant level 73 meV below the VBM. The ionization of the defect introduces an unoccupied charge transition level 0/+ of 55 meV above the VBM [50]. When the defect is photoexcited, the electron is promoted from the ground state to the lowest energy level close to a conduction state [50], while the created hole is localized in the defect (empty electronic level), which is, after the ionization, inside the silicon bandgap. Consequently, although this defect does not include electronic levels in the silicon bandgap, the below bandgap electronic transition results from the radiative exciton recombination. Fig. 2.13 displays the emission spectrum both at the ensemble and single level, where the bright Zero-Phonon Line (ZPL) emission at 1018 meV is visible together with the phonon sideband, including the Local Vibrational Mode (LVM) at 70 meV. Notably, the density of phonon states in bulk silicon, as presented in sec. 2.2, exhibits an evident absence of phonon states with energies beyond 60 meV. This observation implies that the mentioned LVM works as a distinctive feature to identify the presence of W emitters. Moreover, the LVM lies above the Raman frequency, in accordance with the hypothesis of a local strengthening of the chemical bonds, giving rise to resonant levels with the band extrema. In addition to the emission close to the Telecom O-band, a strong linear polarisation of the emitted light at the single emitter scale has been observed, thus offering another beneficial feature to exploit this single emission dipole in quantum information processing applications. In particular, the two orientations [110] and [$1\bar{1}0$] have been observed in SOI wafers upon 65 keV silicon implantation and subsequent flash annealing [50]. Finally, the average radiative lifetime of the excited state has been reported to be η = 34.5 ± 0.5 ns at the ensemble level [73]. On the other hand, values in the 3 - 30 ns range have been measured at the single defect level, probably affected by sample-related non-radiative recombination dynamics [50]. Even though the single-photon emission in silicon has only been demonstrated at cryogenic temperatures so far, with a maximum temperature of 50 K and the rapid decrease of the ZPL line, including the entire photoluminescence band, has been observed for increasing temperature at the ensemble level as well [69], successful examples of integration of this systems in the manufacturing of integrated photonic circuits have already been reported. To give some examples, the waveguide-coupled emission from ensembles of W centers fabricated in the intrinsic region of an electrically injected LED has been demonstrated in an all-silicon integrated chip [74], while, more recently, the coupling of the W PL signal to an SOI waveguide and microring resonators has stressed once more how silicon likely represents a potential platform for large-scale quantum technologies [75].

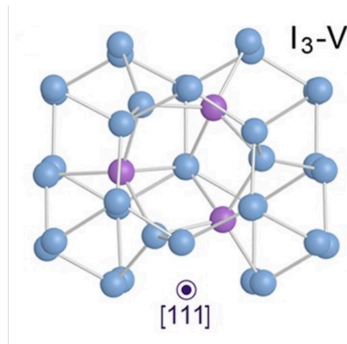

Figure 2.12: Tri-interstitial complex determined with DFT calculations in [50] and resulting as the most likely stable configuration addressable for the photoluminescence signal at 1018 meV in irradiated or self ion-implanted silicon samples.

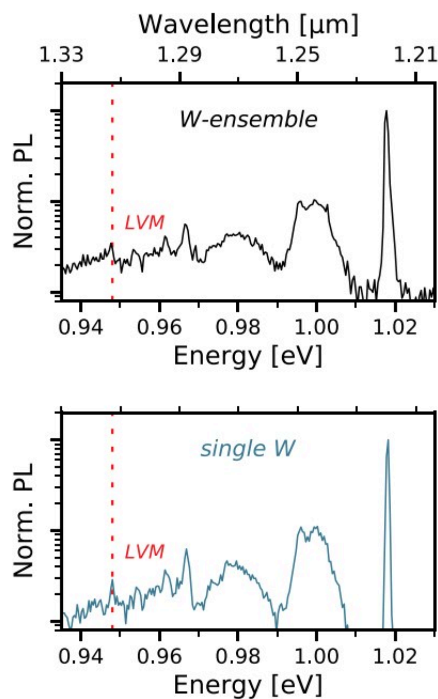

Figure 2.13: Emission spectrum acquired at 10 K under 532 nm excitation wavelength on a 65 keV Si implanted commercial SOI substrate both at the ensemble and single emitter level [50].

2.3 Carbon-related bands

Over the decades, several carbon-based optically active point defects have been revealed through photoluminescence or absorption spectroscopy in either electron-irradiated or ion-implanted silicon. The electronic transitions of these systems are

typically characterized by a pure transition, called zero-phonon line (ZPL), in the IR range, together with lower energy emission or absorption lines related to their LVMs. The following subsections will outline the substantial properties of three main defect complexes, the C, the G, and the T center, together with remarkable aspects that place them among the leading quantum systems for developing integrated quantum devices.

2.3.1 The C band

Room temperature radiation in carbon-doped and oxygen-rich silicon has been reported as responsible for forming photoluminescence centers containing one carbon atom and one oxygen atom [27], as theoretically predicted [76] and confirmed by isotope substitution experiments [77]. Figure 2.14 shows the typical photoluminescence band, generally called the C band, characterized by a ZPL at 0.79 eV and a phonon sideband including LVMs at energies hν = 64.5 meV, hν = 72.6 meV, hν = 138,1 meV, and hν = 145.3 meV according to [78]. The values agree with a recent in-depth theoretical characterization [76]. Figure 2.15 reports the carbon isotope effects on the zero-phonon line emission at 0.79 eV in ^{13}C riched silicon samples. Two components separated by 0.084 meV appear in correspondence of the ZPL. Although several studies have pointed to carbon among the impurities involved in the formation of the C band (789.4 meV) [79] [80], [81], [82], extensive investigations on the local mode replica spectrum have stated the lack of any isotope-related spectral shift or broadening of them, thus indicating that the carbon is not significantly involved in the local vibrational modes [83]. The C line would be ascribable to the neutral charge state of the C_iO_i interstitial neutral pair produced when an interstitial carbon atom C_i, resulting from the presence of radiation-induced interstitial silicon atoms, is trapped by an interstitial oxygen atom O_i [32]. According to what is reported in the literature, the center is thermally dissociated upon annealing in the 300-350°C temperature range. Around 20 minutes have been observed to be enough for dissociating the oxygen-carbon pair and letting the C_i migrate[80]. Such a defect complex commonly acts as a nucleation point for self-interstitials with the direct consequence that the destruction of the defect can occur by increasing the radiation-induced damage. Moreover, upon ns pulsed laser excitation and depending on the temperature, different values of the decay time have been reported for the C emission, ranging from 2.5 μs at 4 K [83] and 95 μs at 20 K [27].

2.3.2 The G center

The G center is a carbon-related point defect whose discovery in 2020 represents the first demonstration of single photon emission in silicon. This result has surged a strong interest among the scientific community, offering an exciting perspective to develop industrial-scale silicon-based single-photon sources emitting in

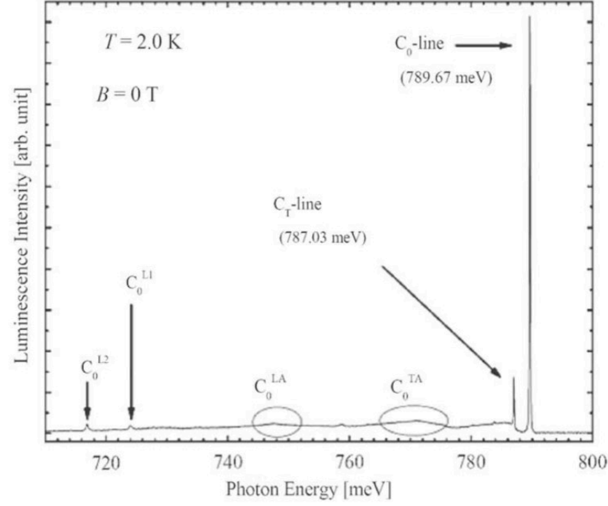

Figure 2.14: Photoluminescence spectrum of an ensemble of C centers acquired at 2.0 K on n-type Cz silicon irradiated with 1 MeV electron with a dose of 10^{18} cm^{-2}, without magnetic field and reported in [84]. Besides the ZPL transition at 789.67 meV, two phonon replica (C_0^{LA}, C_0^{TA}) and the local vibration modes (C_0^{L1}, C_0^{L2}) are visible.

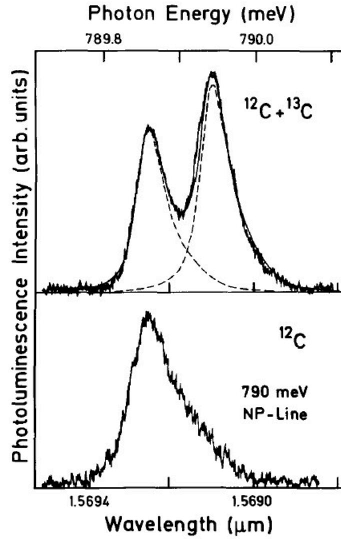

Figure 2.15: Isotope shift effects on the zero phonon line emission of the C center. In ^{13}C riched silicon, the fine structure reveals a doublet. The dashed line represents the deconvolution of the two peaks according to [77].

the telecom range. Indeed, as shown in Fig. 2.18, its emission spectrum is dominated by a ZPL emission at 0.969 eV (1279 nm) followed by a low-energy phonon

sideband. With respect to the latter, it is possible to observe two structured broad peaks at 0.950 eV (1305 nm) and 0.930 eV (1333 nm), corresponding to transverse acoustic (TA) phonons of the extrema of the phonon density states at the X and W points of the Brillouin zone and two sharp lines at 0.890 eV (1393 nm) and 0.825 eV (1503 nm), respectively called E and E' line, and representing two LVMs coming from the atomic vibrations in the defect itself [85]. The red curve represents the theoretically predicted spectrum according to the theoretical modeling of [86], where the longitudinal acoustic (LA) and optical (LO) phonons at the W and L points of the BZ have a less precise agreement with the band centered at 0.93 eV. Noteworthy is the suppression of the transverse optical (TO) phonon replica corresponding to the maximum phonon density states at the L point in the experimental data, probably due to selection rules. Finally, all these emissions overlap a broad background generated by the recombinations assisted by acoustic phonons [86]. As claimed by very recent theoretical calculations [87], the G center has at least three different configurations, where the one identified as "B configuration" and shown in Fig. 2.16 is responsible for the photoluminescence signal at 1279 nm. The suggested structure comprises two substitutional carbon atoms and an interstitial silicon atom bridging them, distorting from the <111> bond axis with a C_{1h} symmetry. The defect is bistable and, upon negative or positive charging, it can convert into the "A-configuration", which involves a $(C\text{-}Si)_i$ pair on a lattice site neighboring a substitutional carbon. The latter is not optically active and has an activation energy ranging from 0.15 eV and 0.21 eV [87]. Fig. 2.17 displays the many-electrons and single-electron energy levels of the C_sC_i bistable carbon pair in the B configuration, as reported by Gali's group in [88]. As evidenced, ^{1}A' is the ground state of the total electron configuration, and it is made of a fully occupied level (*a'*), which is resonant with the valence band, and an empty level (*a"*) in the bandgap. When an electron is promoted to the empty level, the hole level is promoted into the band gap, originating the excited states, ^{1}A" and ^{3}A".

As revealed by first principle calculations, the ZPL reports a fine structure with a splitting of $\sim$ 2.5 μeV, associated with the rotational levels of the interstitial silicon atom in the singlet excited state [88]. To optically access this rotational degree of freedom, the utilization of spinless, highly enriched ^{28}Si [82] for fabricating the G centers is needed. In this way, it is possible to remove the inhomogeneous broadening related to the heavier Si isotopes. In addition, the G center possesses a metastable triplet state active under optically detected magnetic resonance [89], delineating an appealing spin-selective singlet-triplet transition to implement a native qubit in silicon. In conclusion, even though the development and implementation of a complete silicon photonics integrated circuit for quantum computing applications is strictly related to the parallel advancement in the realization of an industry-compatible deterministic single-ion implantation technique, allowing the manufacturing of monolithic devices equipped with multiple indistinguishable photon sources, recent progresses from the fabrication [90] and technological point of

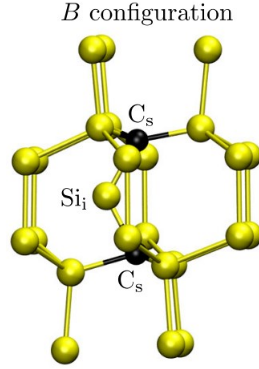

Figure 2.16: Visualization of the structural configuration known as "B configuration" theoretically identified in [88] and responsible for the photoluminescence signal at 1278 nm. The atoms are rearranged to form a structure that consists of two substitutional carbon atoms and one interstitial silicon atom in between them (C_s-Si_i-C_s).

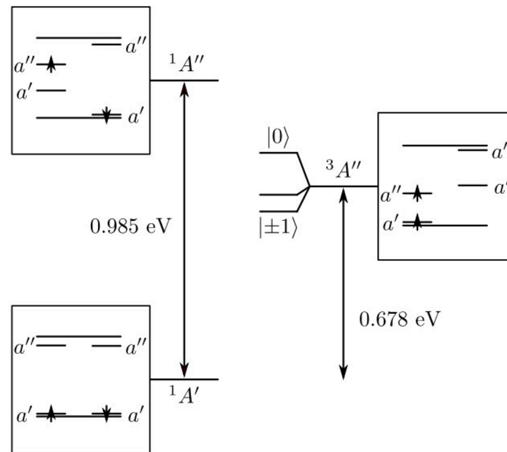

Figure 2.17: Many-electrons and single-electron energy level diagrams of the experimentally observed B configuration, from [88]. The optical transition between the two singlet states $^1A'' \rightarrow {}^1A'$ results in the 1279 nm emission line.

view, such as the integration of a single G center into a single-mode waveguide operating at its ZPL [91], has highlighted the potential of these systems for the manufacturing of quantum information processing devices.

2.3.3 The T center

The T center is another well-known carbon-based silicon defect isolated at the single-photon emitter level only in 2023 [92] and thus recently rediscovered for

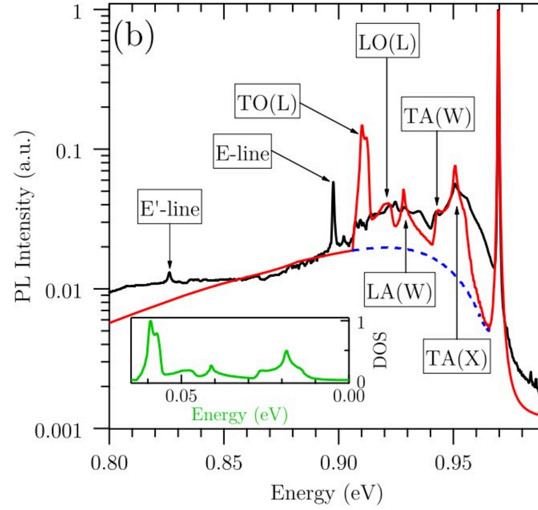

Figure 2.18: Theoretically predicted (red curve) and experimental (black curve) photoluminescence spectrum of an ensemble of G centers, acquired at 10 K upon 632 nm excitation wavelength on a 220-nm-thick silicon-on-insulator wafer, implanted with 36 keV C and a fluence of $2 \cdot 10^{14} cm^{-2}$, followed by a 20 s annealing at 1000°C, from [86].

quantum technology applications. The system has awakened renewed enthusiasm due to the possibility of storing quantum information through its spin. Recent first-principles computations indeed disclose that its emission in the technologically relevant O band splits under magnetic field [93]. The system has been suggested to form when substitutional carbon combines with C-H interstitials pair originated through ion implantation [94]. As shown in Fig. 2.19, the structure of the defective complex consists of two carbon atoms occupying a single silicon site where one is coupled to a hydrogen atom. [93]. New ab initio simulations by Daliah et al. [93] have identified two defect states; the first is represented by a state with both spin-up and spin-down degenerate levels at 300 meV below the VBM, whereas the second has a large splitting between spin-up state below the VBM and the spin-down state at the CBM. In Fig.2.20, the ground state is represented along with the excited one, which is made of an electron in a localized state and a hole from the highest-energy band edge state. The promotion of the electron originates a bound-defect exciton. The T center not only provides another promising photon-spin interface with a ZPL emission at 1326 nm (0.94 eV), thus supplying spin-selective optical transitions at the telecom O band and saturation intensity of 2 kcps [95], but it is also characterized by long-lived electron and nuclear spin lifetimes (2 ms and 1.1 s, respectively [96]) such as to consider the excitonic dynamics as an additional local quantum resource. On the other hand, it is characterized by a long radiative lifetime of 318 μs to the detriment of the high throughput demanded

in quantum information processing technology. Finally, it is readily susceptible to dehydrogenation, requiring exact fabrication conditions [93].

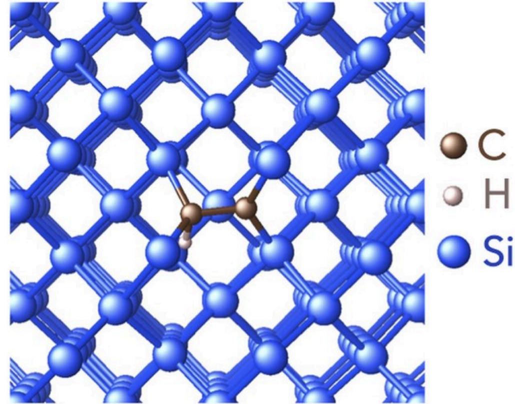

Figure 2.19: Visualization of the T center atomic structure where two bond carbon atoms occupy a single silicon atom site. The hydrogen atom is bound to one of the two carbon atoms. [93]

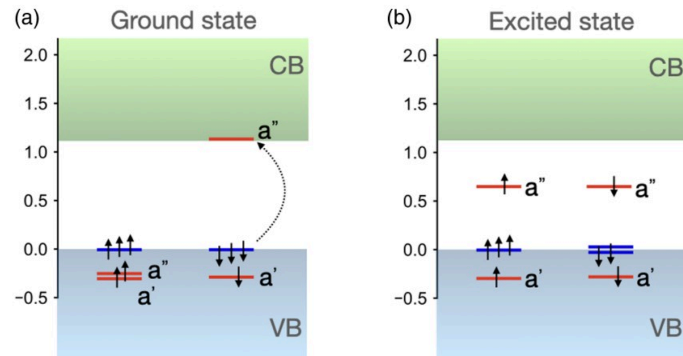

Figure 2.20: Energy levels of the two defect states identified in [96] through first principles computations for the ground and the excited state of the T center.

Chapter 3

Methods

This chapter addresses the technical details of the adopted methods for fabricating and characterizing color centers in silicon, which are described in the following chapters. For this reason, it is not intended to provide a complete discussion of the physical phenomena involved, which will be provided later, along with an overview of the results. I personally set up a cryogenic confocal microscope optimized for the IR range at the laboratories of the Italian National Institute of Metrology (INRiM). I received valuable support and teachings from the Quantum Optics group, which were crucial in implementing the experimental configurations discussed in Chapter 1. The setup validation involved thoroughly investigating the emission properties of preliminary reported Mg-based color centers in diamond and systematically characterizing them at cryogenic temperatures. My colleagues from the Solid State Physics group of the Physics Department greatly contributed in the optical characterization at room temperature. Our findings formed the basis of a journal article that we published in ACS Photonics in 2023 [15].

3.1 Confocal microscopy

Confocal microscopy represents a pivotal experimental technique in photoluminescence measurements for characterizing color centers both at the ensemble and single-emitter levels. The experimental configuration, which requires a light source with high intensity, was first patented by Marvin Minsky in 1957 [97]. However, its widespread adoption within the scientific community was only possible with the advent of suitable laser sources in the 80s. The operational characteristics that set it apart from conventional microscopy are [97]:

- a better lateral resolution improved by a factor of ~ 1.4 compared to that achievable with conventional microscopy;
- a depth resolution sufficient to allow optical sectioning; the "out of focus" information, constituted by photoluminescence from an optical section different

from the plane on which the excitation radiation is focused, is geometrically eliminated through a system of lenses and diaphragms, thus allowing the acquisition of an image representing a very thin section of the sample;

- high contrast due to the removal of the signal not originating from the considered focal plane.

A schematic representation of a confocal microscope is shown in figure 3.1.a. The main components are a light excitation source, an objective lens, a dichroic mirror, and an acquisition pinhole. The laser beam of the excitation source is focused to infinity by an objective and passes through a first pinhole represented by the core of the single-mode fiber, thus reproducing a point source whose rays are reflected by a dichroic mirror, allowing a second objective to focus them to a point within the sample's focal plane. The photoluminescence signal emitted by the color centers in the sample has a higher wavelength, so it is collected by the same objective and directed towards the dichroic mirror, where it is transmitted, thus reaching the core of the collecting fiber, which feeds the detector. The core of the optical fiber acts as a pinhole, geometrically blocking the radiation from planes different from the one where the laser was focused. In fact, despite the limited depth of field due to a high numerical aperture, the collection cone of the objective can include radiation from emitters that are at minimal distances ahead or behind the depth of the optical section under analysis. Choosing an objective with a large numerical aperture is essential to maximize the optical signal, ensuring high spatial resolution for detecting individual defects and a sufficient solid angle for efficient photoluminescence collection [98]. To make considerations on the collection efficiency of the radiation emitted by the sample under the isotropic emission assumption, valid in the case of color centers in bulk material or nanocrystals with a size smaller than the emission wavelength, we can consider the fraction of photons emitted in the solid angle Ω given by $\mathrm{F} = \Omega/4\pi$. Considering θ as the maximum angle relative to the optical axis within which photons can be collected, we can rewrite the considered fraction of emitted photons as follows:

$$F = \frac{1}{2}(1 - cos(\theta)) \tag{3.1}$$

Explicitly including the numerical aperture in the θ expression:

$$F = \frac{1}{2}\left(1 - cos\left(sin^{-1}\left(\frac{N.A.}{n}\right)\right)\right) \tag{3.2}$$

where n is the refractive index of the medium surrounding the emitters. Therefore, especially due to the refraction experienced by the radiation emitted by the sample at the semiconductor-air interface, which reduces the collection angle, the use of a large numerical aperture is essential. Finally, unlike conventional microscopy, of

which a schematic is shown in figure 3.1.b, the sample is not illuminated in "wide field" mode, but rather the laser radiation is focused and then raster scanned point by point, in order to obtain a "pixel by pixel" image of the optical section of the sample, namely a photoluminescence map. The latter can be realized by positioning the sample on a precision stage or performing a similar laser beam scan. The real

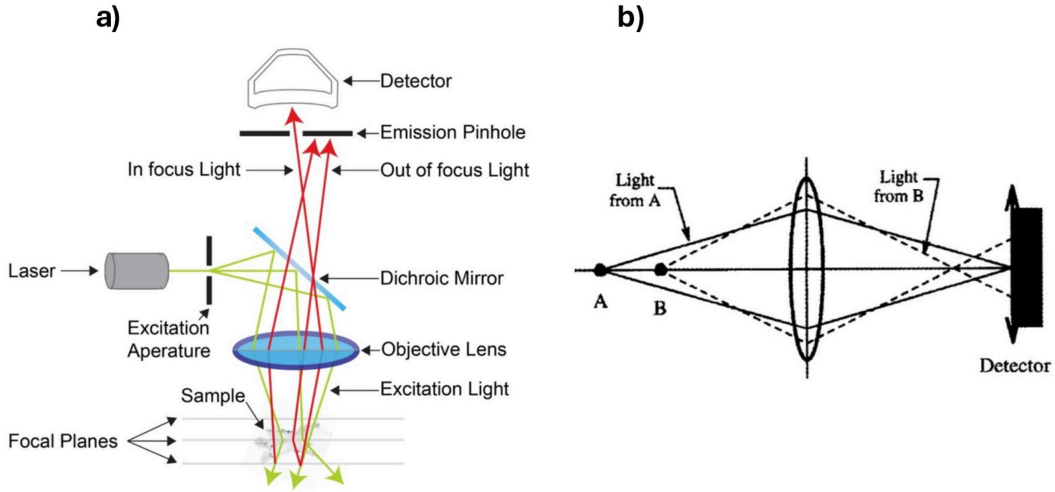

Figure 3.1: a) A schematic representation of a confocal microscope. The excitation radiation is depicted in green, while the red lines represent the photoluminescence originating from different optical sections of the sample. The term "confocal" is justified by three confocal points: the point-like excitation radiation source, the point where it is focused on the sample, and the collection point. b) A schematic representation of photoluminescence collected by a conventional microscope (from [97]). Unlike the confocal microscope, it is unable to discriminate depth; the signal recorded, intended as the integral of the intensity pattern obtained on the extended detector, following the photoluminescence emitted from a point belonging to the focal plane (point A), is the same as that obtained for a point not belonging to the focal plane (point B).

image of an ideally point-like source processed by any conventional optical system that requires the presence of an aperture, such as a diaphragm or a lens, can never be equally point-like; resolution is indeed limited by the diffraction of light. In the absence of aberrations and distortions, the resolution limit of the system is described by the Abbe equation:

$$d = \frac{0.61 \cdot \lambda}{N.A.} \tag{3.3}$$

where d is the resolvable feature size, and N.A. is the numerical aperture. The so-called Point Spread Function (PSF) allows quantifying how efficient an optical system is and is defined as the square of the amplitude h(ν). The latter represents

the transverse spatial variation of the image amplitude generated on the focal plane when the lens is illuminated by a perfectly point-like source [99]. Indeed, diffraction, combined with any aberrations, causes, at the focal plane, the formation of an image of the point-like source characterised by finite transverse dimensions. For a circular converging lens, in the absence of aberrations and under paraxial approximation, the PSF is represented by the Airy disk, and therefore its amplitude is given by:

$$h(\nu) = \frac{2J_1(\nu)}{\nu} \tag{3.4}$$

where:

- $J_1(\nu)$ is the first order Bessel function;
- $\nu = \frac{2\cdot\pi\cdot a\cdot r}{\lambda\cdot f}$ where a is the lens radius, f its focal length and r is the radial distance from the optical axis.

It is possible to calculate the intensity distribution in terms of the amplitude of the PSF, h(x,y), and the amplitude of the object's transmittance function, t(x,y), for each type of microscope. In particular, conventional coherent microscopy can be described as follows[97]:

$$I_{\mathrm{cc}} = |t \circledast h|^2 \tag{3.5}$$

Conversely, for conventional incoherent microscopy, the equation must be modified in:

$$I_{\mathrm{c,i}} = |t|^2 \circledast |h|^2 \tag{3.6}$$

Finally, for confocal microscopy, the following relation applies:

$$I_{\mathrm{c}} = |t \circledast h^2|^2 \tag{3.7}$$

The geometric response of a confocal microscope to a point-like object becomes hereby:

$$I_{\mathrm{cc}} = |h|^4 \tag{3.8}$$

Therefore, it can be concluded that the PSF, in the case of a circular aperture, in the absence of aberrations and under paraxial approximation, for a confocal microscope is given by the square of the Airy disk; the central lobe is, therefore, approximately 1.4 times narrower [100] than in the case of conventional microscopy, and the side lobes are more attenuated (figure 3.2). However, the definition of resolution is given in terms of the minimum distance necessary between two points (point sources) for them to be resolved by the optical system. For this reason, it is necessary to refer to the Rayleigh criterion, according to which the resolution threshold of two points occurs when the maximum of the Airy disk generated by one point coincides with

the first minimum of the Airy disk generated by the other. In the case of confocal microscopy, the Rayleigh distance is given by:

$$d = \frac{0.56 \cdot \lambda}{N.A.} \tag{3.9}$$

in contrast with conventional microscopy, where the minimum resolvable feature size is:

$$d = \frac{0.77 \cdot \lambda}{N.A.} \tag{3.10}$$

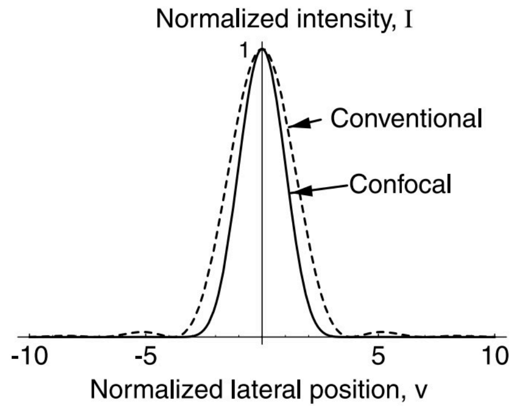

Figure 3.2: Conventional Airy disk (dashed line) compared with the image of a single-point object in a confocal system (solid curve). From [100]. The confocal image intensity sharpens at the central peak (~1.4 times) and is accompanied by weak side lobs.

3.2 Cryogenic PL measurements

Since single-photon emission in silicon has only been demonstrated at cryogenic temperatures so far, with a maximum temperature of 50 K (see sections 2.3, 2.2.5), part of this Thesis work has been devoted to the implementation of a single-photon sensitive confocal microscope working in the 4 K - 350 K temperature range to investigate the optical properties of the quantum emitters systematically. A schematic representation of the experimental setup for the measurement campaigns is reported in Figure 3.3. The PL analysis has been carried out using different CW 3B-class laser diodes providing continuous excitation wavelengths in the visible range coupled to a single-mode fiber that enters a PZO Poland 10x objective with (numerical aperture 0.22), through which they are focused to infinity. A dichroic mirror with a cutoff wavelength of 700 nm is used to reflect the excitation wavelength into a

vacuum-compatible Zeiss EC Epiplan-Neofluar 100x objective with a 0.85 numerical aperture and a working distance of 850 μm, which focuses the laser spot into a surface area of approximately 1 μm^2 on the sample plane. The objective temperature is responsively monitored through a Cernox sensor so that, eventually, a heating system helps in keeping the objective at room temperature. The same objective efficiently collects the emitted radiation, which feeds a Peltier-cooled InGaAs fiber-coupled Single Photon Avalanche Diode (SPAD) after passing through the dichroic mirror. In particular, through a near-infrared long pass filter (800 nm/1200 nm cutoff wavelength), the radiation of interest is selected and focused into the core of a multimode fiber (d = 50µm) using an achromatic doublet lens characterized by a 100 mm focal length and a 1050-1700 nm coating range ensuring an 80% of transmittance. For the spectral analysis of the emitted photoluminescence, the signal feeds a monochromator model Horiba iHR320 [101]. The latter is equipped with two diffraction gratings characterized by 1200 and 600 grooves · mm^{-1}, allowing the spectral exploration up to 2500 nm. The spectral resolution is less than 4 nm and results from multiple contributions, including the width of the monochromator's slits, the monochromator's transmission efficiency, and the intensity of radiation emitted by color centers. To achieve a good signal-to-noise ratio, the minimum acquisition dwell time per each acquisition wavelength is typically of the order of one or a few seconds. For every experiment, the sample was mounted on a dedicated sample mounter named Agile Temperature Sample Mount (ATSM) from Montana Instruments, where an integrated Cernox thermometer and heater provide reliable and responsive thermal control in the temperature's adjustable range. The sample mounter is fixed inside a cryostation vacuum chamber attached to the optical table. The dedicated sample mounter optimizes stage mechanical stiffness and rigidity while providing the thermal performance required for fast temperature changes in the whole temperature range. The declared temperature stability over approximately 2 hours is $<$50 mK (peak-peak), while the typical heating/cooling rate is 300 K/5 min. In addition, the specific material composition reduces thermal contraction to below 30 μm over the entire operating temperature range.

3.2.1 Piezo motion controllers

In the study of single photon emitters, the generation of photoluminescence maps, both on the xy plane (i.e., on the sample surface) and on the xz plane (where z denotes the direction perpendicular to the sample surface), requires nanometric precision. The sample is mounted on an XYZ vacuum and cryo-compatible piezoelectric system, which controls the nanometric positioning. Additionally, a stepper positioner enables coarser steps in the motion. The latter is represented by an Attocube Piezo Motion Controller ANC350 apparatus, which can be used in both "open loop" and "closed loop" modes. It allows simultaneous control of the three axes for sample manipulation by selecting appropriate actuators directly

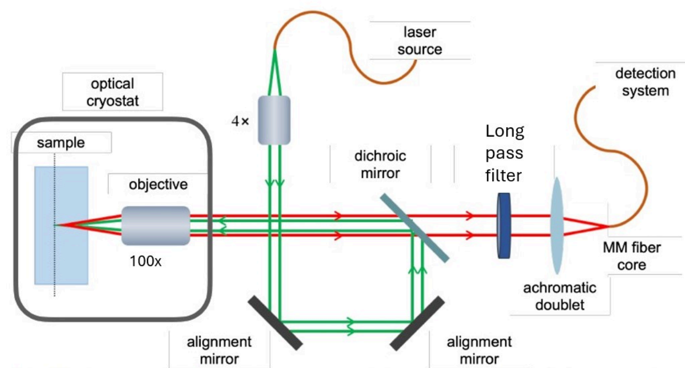

Figure 3.3: Schematic representation of the main optical elements composing the experimental photoluminescence setup adopted in this work. The sample is mounted on the sample holder of a cryostat inside the shielded vacuum chamber.

from the physical panel or via dedicated software provided by the manufacturer. It can be used in "stepping mode", where a variable voltage is applied to the piezoceramic material, resulting in motion consisting of numerous steps, the magnitude of which is determined by the amplitude of the applied signal. The elongation of the piezoceramic material can cover up to 5 mm through a suitable mechanical system. In the case of "fine positioning mode," a slowly variable DC potential is applied, utilizing the elongation of the piezoceramic material only once; therefore, the material properties limit the displacement, typically on the order of several micrometers. The frequency at which the signal is applied can be chosen within a range of 1Hz to 5kHz; the latter is proportional to the actuator's speed of movement. In particular, the micro-actuator used for the x and z axes is the Attocube model ANPx101/RES/LT/HV, compatible with high vacuum, with a voltage range from 0 V to 60 V and an operating temperature range from 1 K to 373 K. For the y-axis, the Attocube model ANPz102/RES/LT/HV micro-actuator is used, also compatible with high vacuum and having the same operating temperature range, with a total travel distance of 4.8 mm. The achievable resolution in an open loop operation with the mentioned voltages is approximately 1 μm for both systems. For the fine positioning of the sample, a modular Piezo Positioning Electronic ANC300 control unit is used, providing the suitable drive signals to actuate vacuum- and cryo-compatible Attocube systems positioners manually or under computer control. The ANC300 houses three ANSxyz100std Attocube open-loop nano-drivers working with a minimum tolerated pressure of $5 \cdot 10^{-11}$ mbar and offering a fine positioning range of 50x50x24 μm^3 at 300 K and 30x30x15 μm^3 at 4 K, corresponding to input voltage in the 0-60V and 0-150V range respectively. Therefore, a dedicated temperature calibration based on a common standard reference, such as a Transmission Electron Microscopy (TEM) mesh grid, was implemented before the experiment to verify the linearity between the applied voltage and the explored

range and find the suitable parameters for the automatization of the process in case of PL measurements at different temperatures. In this case, the resolution is nominally sub-nm, excluding any cross-talk effects.

3.2.2 Single photon detection

Infrared range

The photoluminescence radiation emitted by the sample in a single-photon regime is detected using a multimode fiber-pigtailed MPD PDM-IR/MMF50GI photon counting module, which includes a programmable frequency and pulse generator for precise detector gating, a dedicated front-end circuit for sensing photon avalanches, and a fast Active Quenching Circuit for quenching the detector's avalanche current and resetting the operative bias voltage. The system can operate in either free-running or gated mode with fine adjustable gate width operations. The core of this module is an InGaAs Single-Photon Avalanche Diode (SPAD) housed in the Detection Head and engineered for detecting near-infrared single photons up to 1700 nm. The detector has a 25 μm diameter active area, and it is mounted on the top of a three-stage Peltier cooler, which mitigates the device's primary source of internal noise consisting in a random Dark Count Rate (DCR) arising from thermally generated free carriers. Different key parameters can be easily configured through a PC software interface, including those used in this work:

- The internal trigger is an internally generated periodic waveform with a fixed and selectable frequency and a duty cycle equal to 50%. A TTL AUX OUT and/or a NIM AUX OUT can output the internal trigger to synchronize the PDM-IR module with other instrumentation. Moreover, a user-provided TRIGGER IN signal can be used to synchronize the GATE signal of the PDM-IR with a LASER source that cannot be triggered. For the measurements of this thesis work, an internal frequency of 1 MHz was adopted.

- The working temperature can be chosen among different regimes: high temperature (243 K), medium temperature (233 K), low temperature (229 K), and lowest temperature (225). In the latter case, a low ambient temperature is required for the module's thermal stability, and the DCR is the lowest possible. A low temperature has been generally set for the experiments with a typical DCR of 5kcps in a free-running regime.

- The SPAD performance can be regulated with the excess bias, defined as the difference between the SPAD bias voltage and its breakdown. As reported in Figure 3.4, the higher the Excess Bias, the higher the Photon Detection Efficiency (PDE). Since a higher Excess Bias implies a higher DCR, which, in contrast to the PDE, increases more than linearly, the best trade-off has been found for each measurement set-up.

- To avoid the avalanche re-triggerings of carriers that are trapped by deep levels in the junction's depletion layer and then released with a statistically fluctuating delay, the detector is kept off for a user programmable time, named hold-off time, T_{HO}, thus limiting the so-called afterpulse phenomenon. In contrast to high-quality silicon SPADs, the latter severely affects indeed infrared photon counting. Since the trapped carriers' decay times increase, the effect worsens at low temperatures. In particular, measuring the DCR as a function of the hold-off time can provide an idea of which can represent an ideal value (Fig. 3.5). Moreover, since typical values for InGaAs SPADs are of the order of tens of μs, around three orders of magnitude higher compared to silicon SPADs technology, the measured counting rate CR does not correspond to the actual value (CR_{HO}), which can be estimated as:

$$CR_{\text{HO}} = \frac{CR}{1 - CR \cdot t_{\text{HO}}} \tag{3.11}$$

- A TTL AUX OUT offers the possibility to interface and synchronize the PDM-IR with other instruments; the LVTTL output levels (0 - 3.3 V) allow to communicate with standard CMOS electronics and, in this case, are used to send the photon "click" signal to the counter.

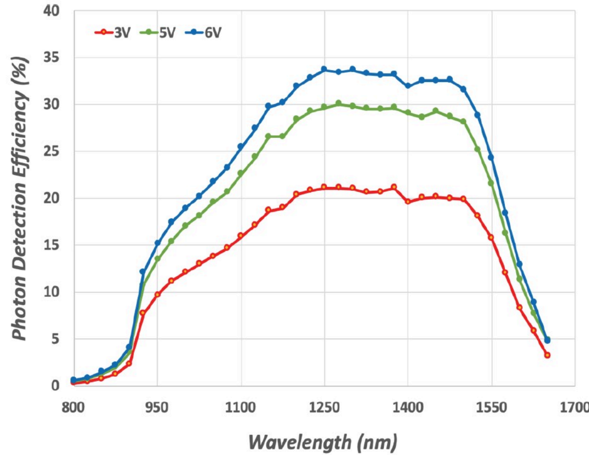

Figure 3.4: Photon Detection Efficiency (PDE) as a function of the photon wavelength. Different curves refer to different excess bias values. From [102].

In particular, the output signal from the detector is transferred via a coaxial cable terminated with a BNC connector to a multi-channel board that provides input/output combinations for data acquisition and generation (DAQ) from National Instruments. The latter is interfaced with the PC through a USB connection. In this context, the DAQ board acts as a counter with a temporal resolution of 10 ns

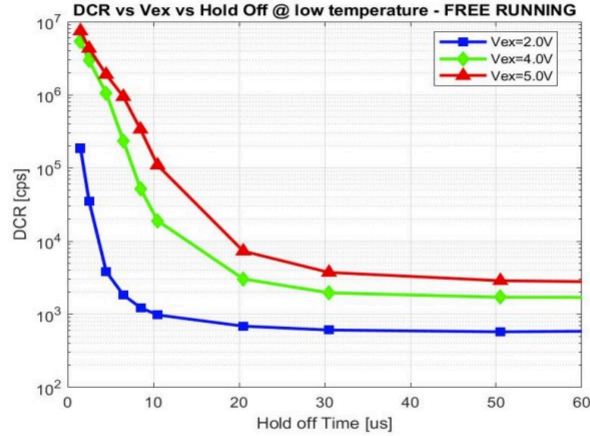

Figure 3.5: DCR as a function of the hold-off time for the free-running mode at three different excess biases. From [102].

[103], 32 channels, and possible voltage ranges for input signals of ± 0.2 V, ± 1 V, ± 5 V, ± 10 V.

Despite silicon SPADs are usually operated in free-running mode, where the devices are enabled immediately after the quenching of each avalanche, the InGaAs SPADs are preferably periodically enabled for a short time window called Gate with duration T_{ON}, i.e., the time the SPAD is turned on during each duty cycle. This regime is commonly preferred as it further reduces unwanted counts. Moreover, since high hold-off times are needed for reasonably low DCRs, the experimental saturation count rate is easily limited, as indicated in Fig. 3.11, thus flattening the signal intensity collected from different probed sample volumes. For this reason, the PL maps have been acquired in gated mode, where typical values of the parameters were T = 229 K, T_{ON} = 50 ns, T_{HO} = 20 μs, V_{excess} = 2 V. Conversely, since the monochromator's transmission efficiency is very low, its output port is fibre-coupled to the PDM-IR detector operated in free running mode to maximize the detector temporal predisposition to detect the incoming photons, thus maximizing the integrated signal over the chosen time interval.

Visible range

In the context of preliminary tests to verify the proper functioning of the experimental apparatus single-photon sources in the visible range have been used. Consequently, the photoluminescence radiation emitted from the sample in a single-photon regime has been detected using a SPAD, model SPCM-AQRH-14-FC (manufacturer: Excelitas). Thanks to an active quenching circuit, the dead time is 22 ns. The voltage pulse output generated is of TTL type, with a duration of (10 ± 2) ns and an amplitude of (2.2 ± 0.4) V. The detector achieves detection efficiencies

of 70% at a wavelength of 650 nm, with the active area being a circular region with a diameter of 180 μm. At the excitation wavelengths used in this case, the detection efficiency ranges from 10% to 20%. The photodiode is thermally stabilized using a double-stage thermoelectric system, ensuring a good signal-to-noise ratio and normal operation within a temperature range of 5°C to 70°C. The typical supply voltage is 5V, and the saturation threshold in terms of count rate is 37 Mcps. Moreover, the average dark count rate is less than 10^2 s^{-1}.

3.2.3 Experiment control and data processing

The entire instrumental apparatus is controlled through dedicated software called QUDI [104]. This software is a modular environment developed in Python, designed explicitly for experiments of confocal microscopy, quantum optics, and quantum computing. Its peculiarity lies in the "layered" structure of the code, which allows independent customization of the hardware part, experiment logic, and graphical interface. Each instrument is generally a commercial product interfacing with the PC through custom software, but the dynamics of the experiment require a specific combination and management of these instruments. QUDI allows handling information regarding the available hardware components and customizing the corresponding module while maintaining the same logic valid for any other quantum optics experiment using a confocal microscope. The modules are interconnected through a component manager. After launching within an Integrated Development Environment (IDE) such as PyCharm and using a single Python executable, start.py (see Figure 3.6.a), the component manager performs fundamental functions such as loading, error handling, reading configurations, and remote access to different components. This structure makes QUDI versatile, allowing for the design and addition of new modules for other experiments. The logic module (see Figure 3.6.b) is the only type of module configured to interact with others. It is the "layer" where function execution and synchronization of different devices are managed. Its main task is to convert inputs from the graphical interface into instructions for the hardware part. All procedural phases, from data acquisition to processing and memory allocation, are carried out in this module. The translation from logical language to language specific to the used component occurs at the lowest layer, which concerns hardware components. This is achieved using a function class, which is inherited by the hardware module. Within this class, the implementation of each function is replaced with that of the specific hardware component. Finally, through the Graphical User Interface (GUI) of the topmost "layer," created with the cross-platform Qt library, the user can interact with the experiment logic only at the input level and view data acquisition from multiple parallel processes (such as counts, photoluminescence map acquisition). It's worth noting that since the setup operates independently of the GUI, the latter cannot interact with the hardware module or process acquired data.

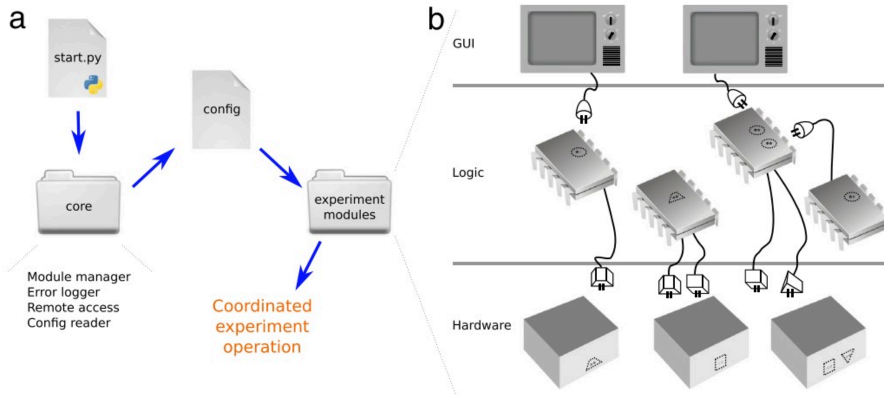

Figure 3.6: Schematic representation of the functional and structural design of the QUDI software from [104] a) In the process, the component manager reads the configuration file, creates a log file, and loads the modules designated in the configuration file. b) Relationship between the three categories of modules.

3.2.4 Cryostat

For the optical investigations of the silicon samples at cryogenic temperatures, a cryostation model CryostationS100 [105] (manufacturer: Montana Instruments) was used, as depicted in Figure 3.7.a, along with a schematic representation of the interconnections between the different devices comprising it (Figure 3.7.b). A Gifford-McMahon cryocooler recirculates a fixed helium gas source; the liquid helium is transported into the chamber where, following a free expansion, it is collected in gaseous form for subsequent compression. A variable-speed compressor (50/60Hz, 208-240VAC, 3.6kW), remotely controllable, compresses the helium. The control unit coordinates the station, which is connected to the PC via USB, allowing the apparatus to be managed through specific software. Thanks to this software, it is possible to manage the vacuum in the chamber, monitor pressure and temperature parameters, reach cryogenic temperatures, open the ventilation valve, and heat the chamber. Additionally, the system is constantly monitored to ensure its proper functioning and manage interfacing errors. The system is equipped with a series of dampers that absorb mechanical vibrations that could cause oscillation of the support to which the sample holder is fixed, relative to the optical bench, with an amplitude of less than 100 nm (peak-to-peak oscillation). The duration of the complete descent ramp is approximately 4.5 hours. A mechanical pump allows for a pressure value of approximately 2 Torr, where the system performs a test to check for any leaks. In case of a negative outcome, the compressor is activated, and the pressure drops to 10^{-4} Torr, representing the lower limit that the vacuum gauge can measure. Finally, a high vacuum (10^{-8} Torr) is achieved with cryopumping, necessary for descending to liquid helium temperatures.

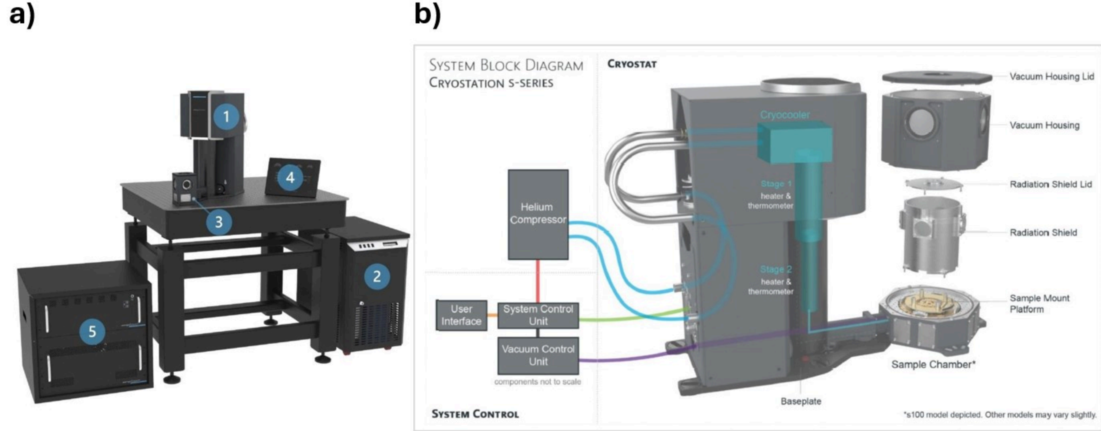

Figure 3.7: a) Cryostation: 1. Cryocooler, 2. Helium compressor, 3. Chamber and cryostat assemblable directly on the optical bench (4. Touchscreen user interface), 5. Control unit. b) Diagram of the connections related to the s100 cryostat station (manufacturer: Montana Instruments).

3.3 Mg-vacancy optical defects in diamond: a case study for cryogenic microscopy

The cryogenic confocal microscopy setup was preliminarily validated through the optical characterization of a known physical system emitting in the visible range. The customization of the experimental apparatus for telecom wavelengths was preceded by an investigation of the opto-physical properties of optically active Mg-based color centers in artificial diamonds. The section presents the results of the preliminary case study, which reveal the assessment of previously unreported physical properties of this class of emitters [15]. The systematic study is based on an exploratory report [106], which suggests the formation of optically active defects in artificial diamond emitting at 557.4 nm upon Mg implantation and annealing. These are part of novel classes of single-photon-emitting color centers with appealing features that have emerged in the last decade, in addition to the well-known and deeply investigated nitrogen vacancy center. Notably, the available experimental data indicate the realization of Mg-based color centers characterized by a high Debye-Waller factor, a sharp ZPL emission, high saturation intensity (>0.5 Mcps), and a short lifetime (2-4 ns). The optical properties of MgV centers were studied using a set of $2 \times 2 \times 0.5$ mm^3 IIa single-crystal diamond plates produced by ElementSix through a chemical vapor deposition process. The supplier classified the crystals as "electronic grade," indicating that the nominal substitutional N and B concentrations were below 5 ppb. The sample was fabricated employing ion implantation with 100 keV ^{24}Mg$^+$ ions at the IMBL laboratory (KU Leuven). Custom Al implantation masks were used to implant the sample on several 200 $\times$

200 μm^2 regions with varying fluences in the range of 5·10^9 - 5·10^{12} cm^{-2}. Subsequently, the sample underwent high-temperature annealing at 1200 °C for two hours at a pressure of about 10^{-6} hP, followed by an oxygen plasma treatment to reduce background fluorescence from surface contaminants.

Optical characterization at the ensemble level

Figure 3.8 shows the room temperature (RT) photoluminescence (PL) emission spectrum of the diamond implanted with the highest fluence of 5×10^{12} cm^{-2}. The spectrum was obtained using a confocal micro-Raman setup with a 532 nm excitation wavelength and a 21.6 mW optical power, achieving a resolution of less than 0.1 nm. The ensemble emission reveals several distinct spectral features:

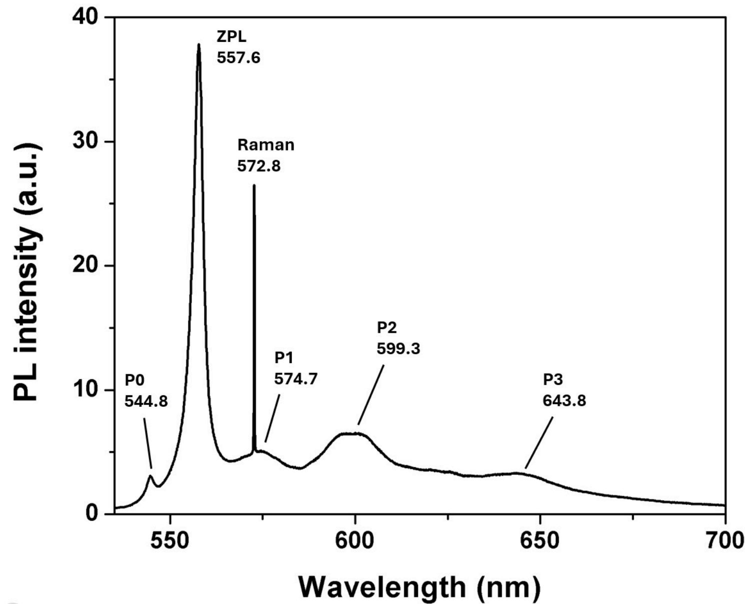

Figure 3.8: Room Temperature spectrum from an ensemble of MgV centers acquired on the 200x200 μm^2 region implanted with 5·10^{12} cm^{-2} upon 532 nm laser excitation.

- a very sharp emission at 572.8 nm representing the first order Raman scattering in diamond (1332 cm^{-2} Raman shift);
- an intense emission peak at 557.6 nm (2.224 eV; 3 nm FWHM), dominating the emission spectrum and in line with the early report where it is attributed to the ZPL of the MgV defect [106]. Additionally, theoretical prediction links the main emission to the Mg-related color center in its negative charge state [107];

- a group of less intense PL peaks are observed, with wavelengths centered at 574.7 nm (2.158 eV, referred to as “P_1” below), 599.3 nm (2.069 eV, P_2), and 643.8 nm (1.926 eV, P_3). These wavelengths are consistent with the phonon replica of the MgV center, as predicted in reference [107];

- an additional emission line at 544.8 nm (2.28 eV, referred to as "P_0" hereafter) showing higher emission energy compared to the MgV ZPL is present. The source of this feature remains unclear. Its association with Mg-related emission in n-type diamonds is questioned due to its detection in this study, where undoped and highly pure substrates were used. Additionally, there are no documented examples of irradiated or ion-implanted diamonds in the scientific literature to support its link to an intrinsic radiation-induced defect. This peak might be seen as either a distinct Mg-vacancy complex apart from the MgV center, similar to the 593.5 nm line in Sn-implanted diamond [108], or, less likely, as the expected ground-state splitting of the MgV defect. However, in the latter case, the observed splitting ($\sim$ 52 meV) would greatly surpass the expected value of 22 meV [107].

Further exploration into the temperature-dependent photoluminescence (PL) spectra spanning from 5 to 300 K, using 522 nm laser excitation, was conducted on the same MgV ensemble. This investigation was carried out using the single-photon sensitive cryogenic confocal microscope, which yielded two additional insights into the optical properties of this lattice complex. The first one concerns the MgV ZPL exhibiting a shift towards longer wavelengths as the temperature decreases. Figure 3.9 visualizes the phenomenon, where the central wavelength of the ZPL is plotted against temperature. The uncertainty associated with this shift was estimated to be around 0.2 nm based on the Gaussian centroid fitting parameter. At 5 K, the shift measured approximately 1 nm (558.4 nm) compared to the emission at room temperature (557.6 nm). This observation has not been documented yet in solid-state defects since the lattice parameter contraction is typically associated with a tightening of the chemical bonds and, thus, an increase in the emitted photon energy.

Secondly, the emission is primarily characterized by a new series of spectral features at low temperatures. Figure 3.10 shows the evolution of the spectrum for different temperatures in the 5-290 K range. These include a bright peak at 608.3 nm (2.038 eV, referred to as "L1" hereafter), with an intensity comparable to that of the MgV ZPL. This peak comes along with a set of weaker bands at 619.5 nm (2.001 eV, "L2"), 625.3 nm (1.983 eV, "L3"), and 652.3 nm (1.901 eV), which have been tentatively been interpreted as phonon replicas of L1. The spectral emissions at the ensemble level have been analyzed in the same implanted region to investigate the dependence of the emitted photoluminescence on the excitation wavelengths. To do so, three different excitation wavelengths have been used, adopting an optical power of $\sim$4 mW. Figure 3.11.a reports the spectra normalized to the optical power.

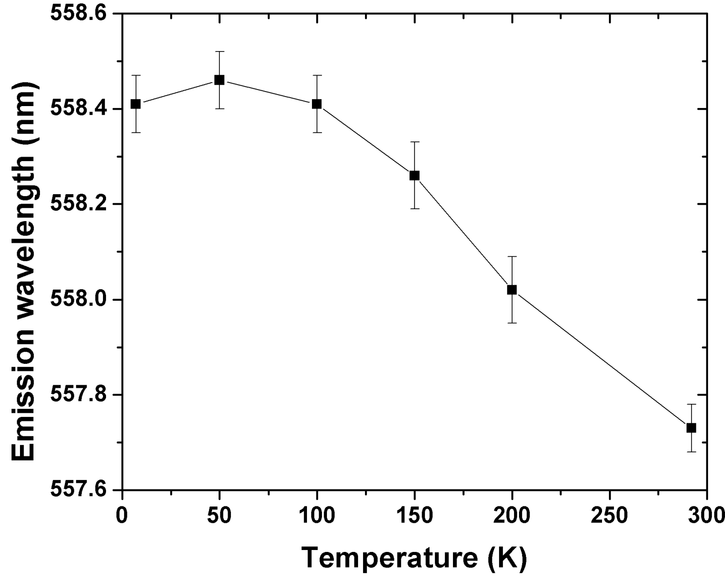

Figure 3.9: MgV center ZPL as a function of the temperature. The error bars were estimated from the uncertainty associated with the centroid parameter of the Gaussian fit.

For the sake of comparison, a set of emission spectra acquired at room temperature under five different excitation wavelengths are shown in Fig. 3.11.b, where the adopted optical power was 2.2 mW except for the spectrum acquired upon 522 nm laser (P_{laser} = 0.3 mW). Again, the spectra have been normalized to the optical excitation power. For each excitation wavelength, the presence of the ZPL along with the P_1-P_3 emission lines at room temperatures confirms that these features are related to photoluminescence (PL) characteristics in Mg-implanted diamond rather than Raman-related properties of the implanted host material. Moreover, it excludes any possible experimental artifacts, instead suggesting the observation of the theoretically predicted high tunability of the MgV system under different environmental conditions [107]. A 505 nm long-pass filter was adopted to properly filter the excitation radiation, except for the excitation spectrum acquired with a 522 nm laser. In the latter case, a 567 nm long-pass dichroic mirror was used, and the approximately 50% transmittance of the filter at 560 nm resulted in enough signal for observing the ZPL of the MgV center despite its reduced emission intensity. Additionally, when using the 522 nm laser, the first-order Raman scattering occurs at a wavelength of 561 nm, partially overlapping with the ZPL of the MgV center due to the resolution of the monochromator, thus preventing the direct comparison of the ZPL intensity obtained under a 522 nm laser and that observed at

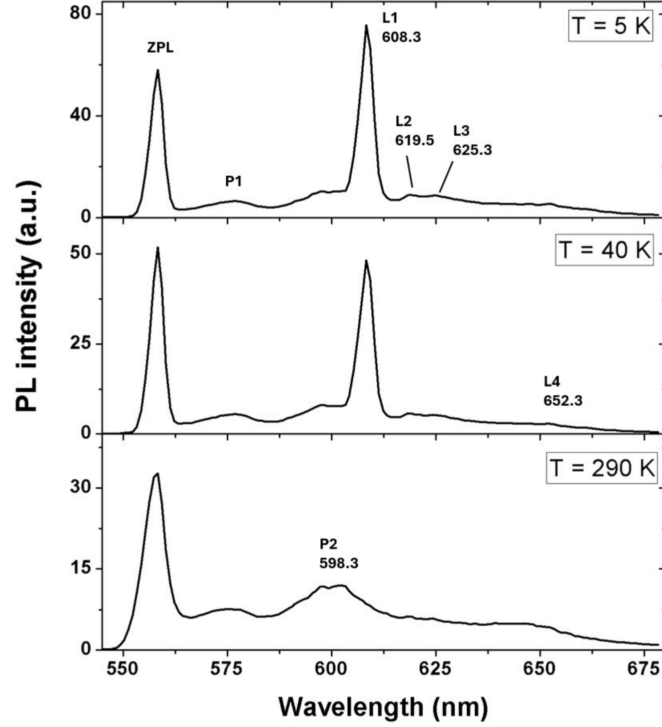

Figure 3.10: PL spectra acquired on a MgV ensemble under 522 nm excitation (excitation power of 3.7 mW) at a temperature of 5, 40, and 290 K.

other excitation wavelengths. Nonetheless, the overall intensity of the MgV ZPL shows a decreasing intensity for increasing excitation energies, probably promoting a conversion between different charge state configurations allowed in the diamond bandgap. This hypothesis is supported by the lack of observation of single emitters for excitation wavelengths lower than 510 nm. Moreover, the intensity of the MgV ZPL as a function of the excitation wavelength reported in Figure 3.12 and obtained through an in-depth and dedicated analysis performed with a supercontinuum laser (80 MHz NKT SuperK Fianum) characterized by a tunable emission wavelength with <10 nm bandwidth, confirms the maximum excitability of the centers upon 522 nm laser wavelength. The Raman-resonant excitation can indeed provide an effective tool to maximize the source intensity.

Optical characterization of single emitters

The optical characterization at the single-emitter level has been carried out at cryogenic temperatures via HBT interferometry, enabling the identification and analysis of single-emitting defects. Figure 3.13.a displays a PL spectrum acquired

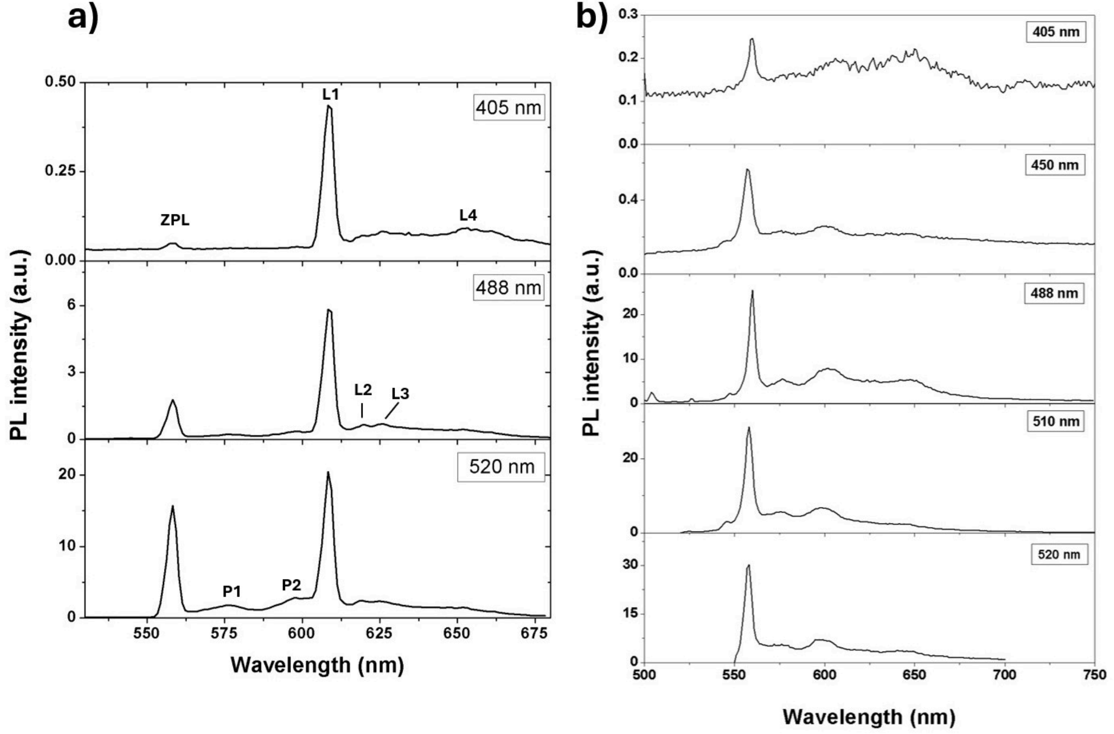

Figure 3.11: PL spectra acquired on an ensemble of MgV color centers a) at 5 K upon 405 nm (3.6 mW), 490.5 nm (4.0 mW), and 522 nm (3.6 mW) excitation wavelengths and b) at room temperature using) 405 nm (8 mW), 450 nm (2.2 mW), 490.5 nm (2.3 mW), 509.5 nm (2.2 mW), and 522 nm excitation wavelengths (0.3 mW).

from a single MgV emitter isolated at the outer edge of the 200x200 μm^2 Mg implanted region and highlighted by a white circle inf Fig. 3.13.b. The L1 emission observed at cryogenic temperatures in the case of ensemble measurements could not be identified at the single photon emitter level. However, the characterization at cryogenic temperature upon different excitation wavelengths did not successfully isolate a significant number of individual color centers, thus preventing the attribution of the L1 emission to a different structural configuration. The quantum nature of the emitted photoluminescence has been ensured by the measurement of the second-order autocorrelation function, showing the antibunching in correspondence with a null delay time (Figure 3.14.a) and a value of 0.467 ± 0.009 and 0.05 ± 0.01, respectively before and after background suppression, here entirely consisting of the first order and second-order Raman lines as visible in Fig. 3.13. The curve has been fitted according to the three-level system based on a preliminary and dedicated analysis carried out at room temperature under different optical power in the

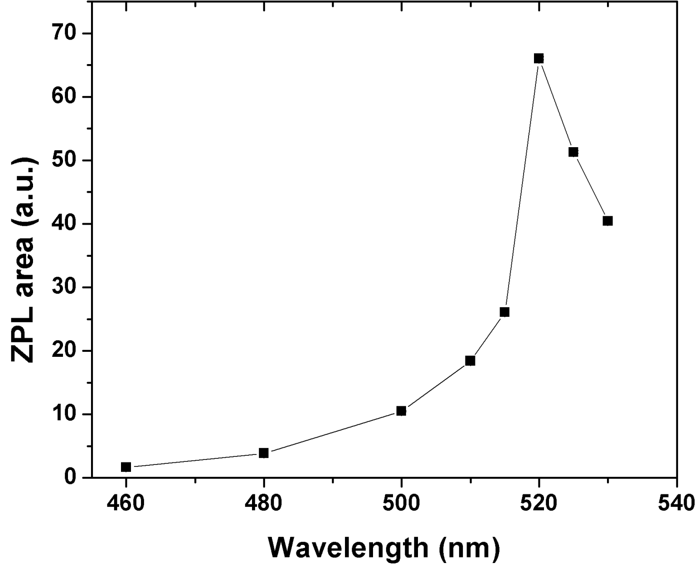

Figure 3.12: Integrated intensity corresponding to the area subtended by the ZPL peak as a function of the excitation wavelength. A supercontinuum laser (80 MHz NKT SuperK Fianum) with 10 nm width tunable emission wavelength and 50 μm optical power has been used. The background contribution was removed by taking a spectrum in a pristine region for each excitation wavelength.

0.20-0.52 mW range and highlighting a bunching effect suggesting the presence of a shelving state participating to the emission dynamics of the defect [15]. Therefore, the adopted model was:

$$g^2(\tau) = 1 - (1 + a) \cdot exp(-|\tau|\gamma_1) + a \cdot exp(-|\tau|\gamma_2) \tag{3.12}$$

where γ_1 and γ_2 are the reciprocal of the characteristic times representing the excited and shelving states' lifetime, respectively. The lifetime of the excited state can be indeed retrieved from the linear fit of the γ_1 parameter as a function of the adopted optical power and can be determined as $\tau = [\gamma_1(\text{P=0})]^{-1}$ (Figure 3.14.b). The lifetime of the excited state was determined to be (2.8 ± 1.1) ns, which is compatible with the results preliminarily obtained from a statistical analysis performed at room temperature on 15 individual MgV emitters and resulting in an average excited state lifetime of (2.4 ± 0.2) ns (Figure 3.15.a). The latter is, in turn, in good agreement with the explorative investigation reported in [106].

Both unique observations at cryogenic temperature, meaning the ZPL blue shift and the occurrence of additional spectral features, can be elucidated by considering recent theoretical predictions [107]. The first observation can be explained by

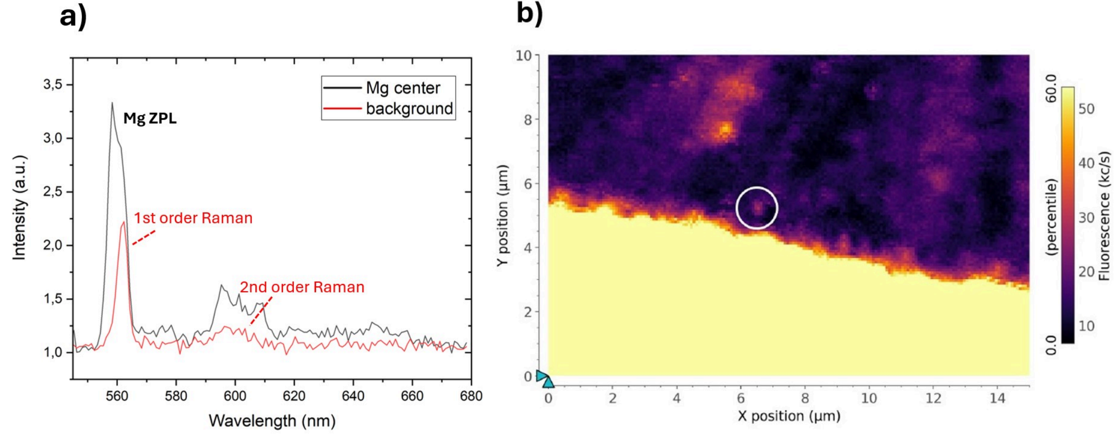

Figure 3.13: Investigation of single-photon emission at cryogenic temperature (7 K): a) Superimposed PL spectra acquired on a single MgV color center and on the pristine region under 522 nm excitation wavelength (P = 4.6 mW). b) PL maps showing the edge of the implanted region and a few sub-micrometer individual luminescent spots. The white circle refers to the individual emitter whose spectrum is reported in a).

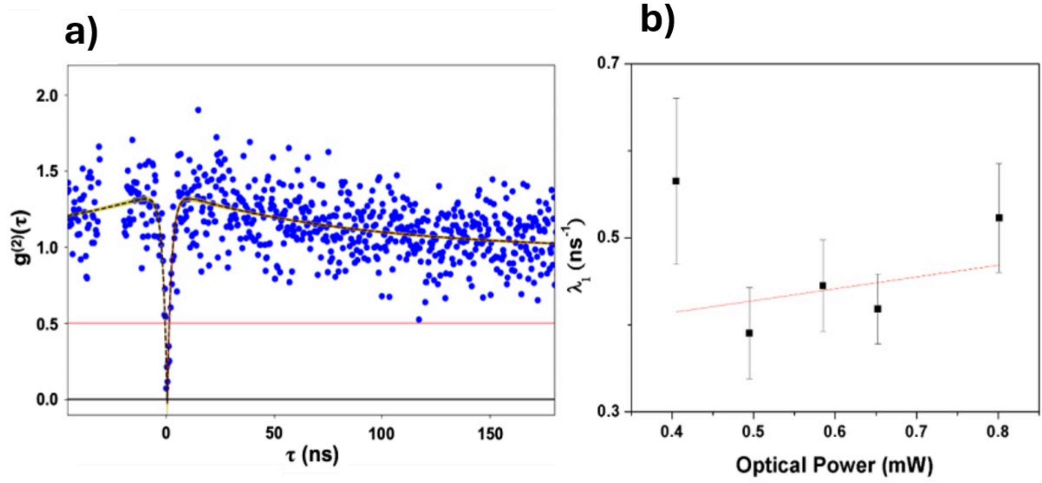

Figure 3.14: Investigation of single-photon emission at cryogenic temperature (7 K): a) second-order autocorrelation function acquired from the same emitter of Fig. 3.13 upon a power excitation of 0.7 mW. b) dependence of the γ_1 parameter on the optical excitation power.

considering the ZPL of MgV resulting from an emission doublet convolution. This interpretation aligns with theoretical predictions suggesting that this doublet arises from a split ground state [107] (Figure 3.16.a). The electronic structure of MgV al-

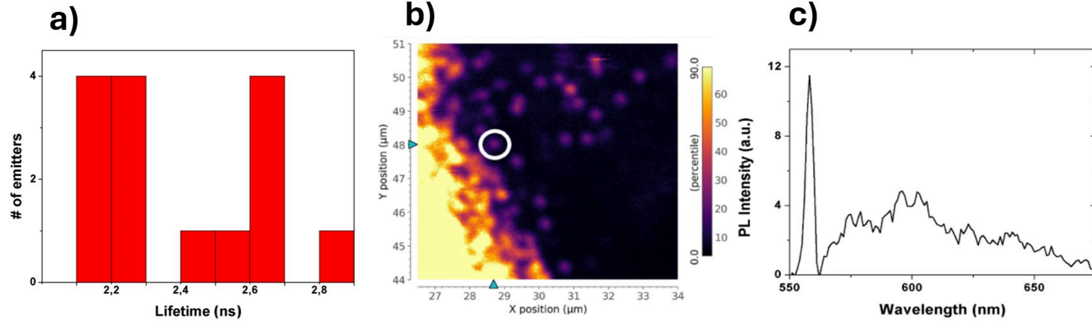

Figure 3.15: The excited-state lifetime distribution of 15 individual MgV centers at room temperature. b) A confocal microscopy map obtained using 1.0 mW of 522 nm laser excitation at the outer boundary of the region implanted with Mg^+ at a fluence of $5 \cdot 10^{12}$ cm^{-2}.

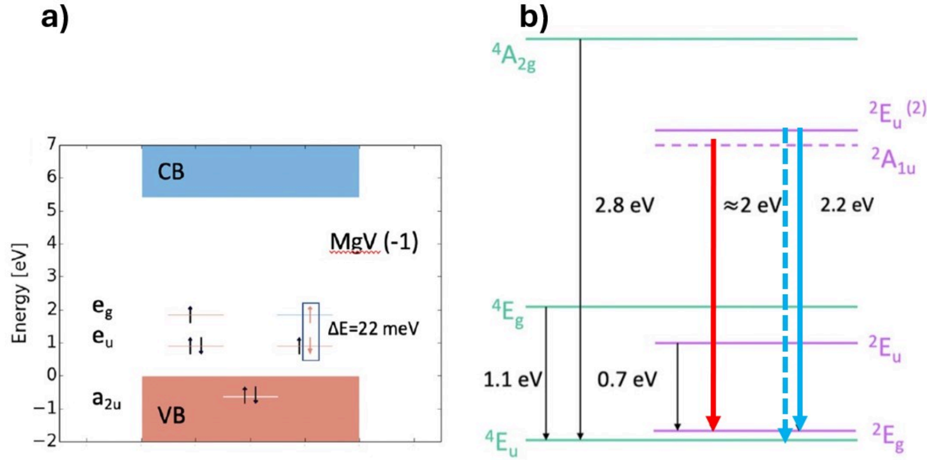

Figure 3.16: a) A diagram from [107] illustrates the electronic structure of MgV(-). It depicts the coexistence of two potential ground states, distinguished by a 22 meV gap, respective a corresponding spin-flip mechanism. b) A state energy diagram from theoretical investigations in [107] representing the electronic transitions where the relevant transitions have been highlighted with red and blue arrows. The purple levels refer to the doublet, while the green ones represent the ones of the quartet state.

lows two loosely separated spin states to coexist indeed, either of which can function as the ground state depending on temperature and external strain. In particular, the ground state splitting shows a decreasing energy gap with increasing compressive strain, corresponding to lower temperatures. Therefore, a higher occupation probability of the ^4E_u state would justify the observed blue shift (competitive transition process represented with blue arrows in Figure 3.16.b). However, further

investigation using high-resolution spectroscopy at cryogenic temperatures will be necessary to validate this hypothesis. Secondly, the energy of the L1 line aligns with the weakly allowed $^2A_{1u} \rightarrow {}^2E_g$ transition, which was predicted to be around 2 eV in [107] (Figure 3.16.b red arrow). The absence of this line at room temperature is consistent with its weakly allowed nature; indeed the approximately 185 meV energy gap between the $^2A_{1u}$ and the $^2E_u{}^{(2)}$states (the excited states involved in the ZPL and L1 transitions, both leading to the same final state ^2E_g as per [107] could be sufficient to favor the population of the latter through room temperature phonon-assisted processes, thereby suppressing the emission of the L1 line.

Outcomes

To conclude, the study carried out on the spectral features of MgV centers at cryogenic temperatures not only validated the experimental apparatus but also offered a consistent signature of the fabricated emitters with the systematic measurement campaign accomplished at room temperature (ZPL at 557.6 nm attributed to the$^2E_u{}^{(2)} \rightarrow {}^2E_g$ optical transition, 2.4 ns lifetime of the excited state and high saturation intensities in the 0.44-1.46 Mcps range [15]). Besides, the temperature-dependent behavior of this emission line revealed an unusual and counterintuitive blue shift, a phenomenon that has not been observed before in solid-state quantum emitters. In addition, previously unexplored emission properties are discussed, including the occurrence of a previously unreported line at 608.3 nm observable only at cryogenic temperatures; the latter provides experimental evidence in support of the theoretically predicted tunability of the system [107], opening up to exciting perspectives to develop quantum-enhanced sensing protocol with this class of emitters.

3.4 Turin Ion implantation facility

Most of the ion implantation processes, which will be described as part of the fabrication protocol for creating color centers in silicon, have been performed at the 100 keV ion implanter of the Solid State Physics laboratory at the Physics Department of the University of Turin. The implanter is equipped with two different beamlines, 0° and 20° (currently not operational). Fig. 3.17 displays a schematic representation of the top view of the multi-elemental ion implanter. It is characterized by a maximum terminal potential of 100 keV, and it has a Source of Negative Ions by Cesium Sputtering (SNICS), which is one of the most versatile ion sources for the production of a wide range of different ions, and thus for the exploration of new types of color centers in solid-state materials. The negative ions are generated by utilizing a Cs vapor, produced through a high-temperature reservoir where Cs is heated within the ion extraction chamber, between the sputter target (a solid cathode) and a hot conical ionizer with a positive potential [109]. Typically, the

cathode used in SNICS sources is a section of a copper rod coated with Cs, featuring a small cavity drilled along its axis and containing the powder with the desired element(s). The entire setup operates within high vacuum conditions. The Cs vapor from the reservoir diffuses into the space between the cold cathode and the heated ionizer; some of the Cs adhere to the cold cathode's surface, while some strike the hot ionizer and vaporize immediately, becoming ionized. The latter is then accelerated toward the cathode due to the applied electric field, causing atoms from the powdered sample to be sputtered out. Depending on the materials, some tend to sputter negative ions preferentially, while others release neutral or positive particles that gain electrons as they pass through the condensed Cs layer, resulting in negative ions. Because the entire ion source operates below ground potential and the extractor maintains a high positive potential relative to the entire ion source, the negative ions are accelerated and extracted from the source. Refer to Figure 3.18 for a schematic diagram.

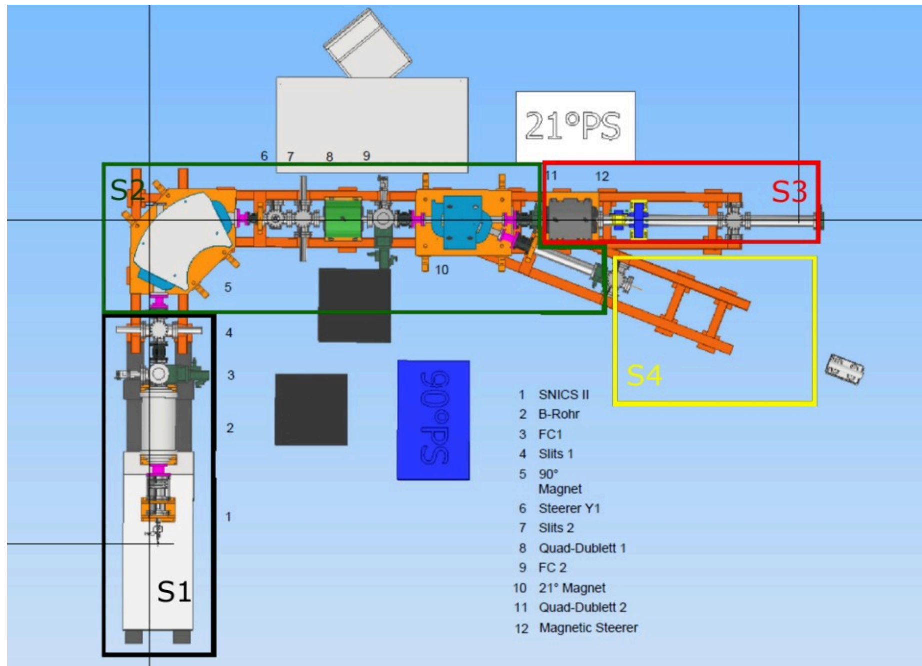

Figure 3.17: Scheatic representation of the components for the ion implanter setup (radiation chamber excluded) at the University of Turin Physics Department. S_1 refers to the source section, while S_2 is the analyzer magnet section. S_3 and S_4 comprise the two beamline sections, 0° and 21°, respectively.

Besides the ion source, an accelerator is distinguished by several fundamental components:

- acceleration stage: This component defines the type of accelerator and the range of operational energies, in this case up to 100 keV;

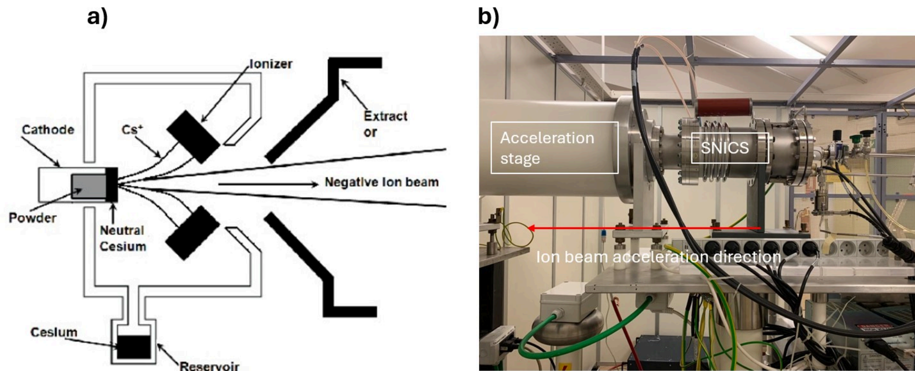

Figure 3.18: Schematic representation of Cs-based sputtering ion source a) together with the picture of the SNICS source and the acceleration stage at the To Ion implanter b).

- mass spectrometer: when different ion species are to be accelerated, efficient selection of masses at a specific energy is necessary. Tunable magnets are commonly used to achieve this purpose. Multiple ion species have been accelerated so far, including H, C, O, Mg, Si, MnO, Pb, and Sn;
- focusing elements: magnetic lenses, typically based on quadrupoles or octupoles, adjust the ion beam's divergence and direction;
- steerers: these elements allow the ion beam to be deviated by applying electromagnetic fields. They can be either magnetic or electrostatic.

Fig. 3.19 displays the irradiation chamber at the end of the 0° beamline in a class 10.000 cleanroom. Typical ion beam current values range from 10^{-12} and 10^{-6} A (depending upon ion type and charge state). For current measurements inside the irradiation chamber, a Faraday cup equipped with an electron suppressor plate and connected to a Keithley picoammeter is used. Two PI C-663.12 Mercury step motor controllers drive two PI VT-80 V6 vacuum-compatible linear stages (down to 10^{-6} mbar) to handle the Faraday cup alignment with the beam or the proper positioning of the sample holder. Dedicated control software and hardware include capabilities for monitoring operational parameters and controlling the beamline, providing the necessary interlock conditions. The same control software allows the handling of different valves, to enable the isolation of the different beamline sections, and Faraday cups to monitor the beam current. After the first set of quadrupoles, the beam is directed towards the second Faraday cup (FC2 in the schematic representation), which stops the beam in the irradiation chamber depending on the desired implantation fluence. A dedicated LabView interface permits indeed the setting of the required parameters to evaluate the recommended irradiation time and properly

drive the FC2, namely beam size, desired implantation fluence, and beam current in the irradiation chamber. The latter is indeed monitored as well. However, due to the minimum time interval required to insert the Faraday cup in the beamline, a minimum ion implantation fluence of 10^{10} cm^{-2} can be achieved. As described in the following sections, no collimation masks have been used for the ion implantation in silicon samples. Instead, a broad beam and custom Al masks have been adopted.

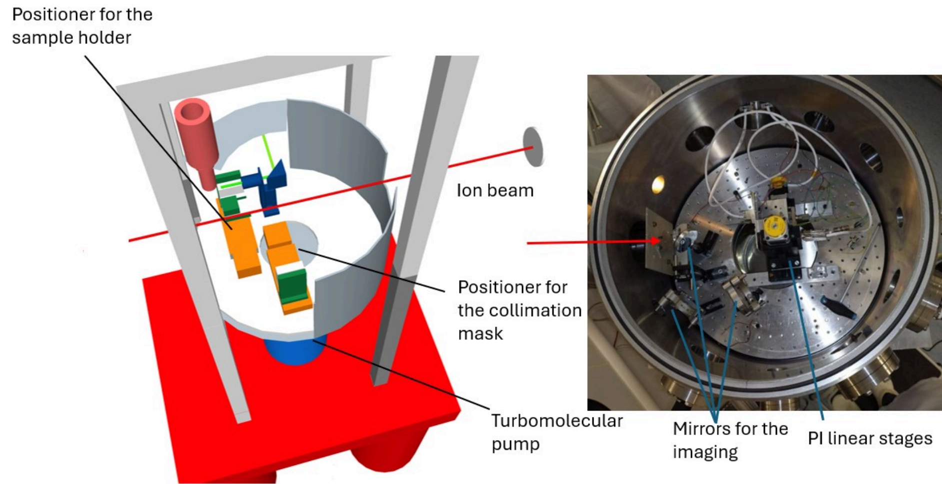

Figure 3.19: a) 3D view of the irradiation chamber at the end of the 0° beamline. b) Picture of the inside of the irradiation chamber.

Chapter 4

Fabrication of color centers in silicon

Today, established industry-compatible fabrication and processing techniques such as ion implantation and high-temperature thermal treatments are at the core of the fabrication of color centers in solid-state material, making the manufacturing process straightforward and efficient. Moreover, well-established technologies, such as focused ion beam (FIB) or masked implantation, can provide the controlled placement of emitters registered to nanoscale photonic structures. Such a process, however, involves additional **fabrication challenges**, namely the **delivery of individual impurities** and the quantum emitter **creation yield**. The results discussed in this chapter are the culmination of collaborative efforts involving the Solid State Physics group of the Physics Department, the Quantum Optics group of the INRiM Institute, researchers at the Laboratory for Ion Beam Interaction at the Ruđer Bošković Institute, the Turin branch of INFN, and the ChiLab of Politecnico di Torino. The development of silicon emitters was supported by colleagues from the Solid State Physics group, particularly those involved in keV ion implantation, using the Ion Implanter described in Chapter 3. These procedures were conducted based on the expertise of the Solid State Physics group, as evidenced by previous experiments involving MeV ion implantation, including the work I was involved in, which was eventually published in 2024 [110]. Additionally, I personally conducted research into the thermodynamic processes involved in creating solid-state emitters using conventional rapid thermal annealing, with the support of researchers from the Politecnico of Torino, and explored off-equilibrium strategies in the thermal processing of the implanted samples and their systematic optical characterization at the INRiM Laboratories. This study served as the basis for the Conference paper presented at the IEEE Photonics Society Summer Topicals Meeting in 2023 [111] and the publication in Communication Materials in 2024 [112]. Furthermore, we pursued a deterministic implantation approach using the Ion Beam-Induced Charge (IBIC) technique, which culminated in a publication in Vacuum in 2022 [113] in

collaboration with colleagues from the Ruđer Bošković Institute. The contribution of Prof. Ettore Vittone enabled us to employ additional numerical simulation tools to simulate the device's response to the ion beam.

4.1 Ion implantation

Ion implantation represents a reliable approach for introducing extrinsic impurities in the crystal matrix, and, as previously discussed, it is responsible for generating, at the same time, damage, i.e., vacancies and intrinsic defects. The following sections are intended to describe the ion-matter interaction mechanism and the application of ion implantation processes in fabricating solid-state color centers, along with the main manufacturing challenges.

4.1.1 Interaction of ions with matter

When an incident ion transits in the matter, it loses its energy through elastic and inelastic collisions with atoms of the target material. The energy deposition is described in terms of "energy stopping power", i.e., the energy loss of the particle per unit length $\frac{dE}{dX}$ and results from three concurrent contributions: the scattering with the nuclei, the interaction with the orbital electrons, and the radiative stopping powers [114]:

$$\frac{dE}{dX} = (\frac{dE}{dX})_{\text{nuclear}} + (\frac{dE}{dX})_{\text{electronic}} + (\frac{dE}{dX})_{\text{radiative}} \tag{4.1}$$

As the primary ion penetrates through the medium, it undergoes a series of interactions that excite or eject atomic electrons and gradually cause it to lose kinetic energy, decreasing its velocity. The electronic stopping power is associated with inelastic collisions, implicating the loss of a small fraction of the total energy of the primary ion per collision, negligibly deflecting the ion trajectory due to the high ion/electron mass ratio. However, since the primary ion undergoes a huge number of interactions with the bond electrons of the target material, the electronic interaction is responsible for losing most of the energy of a MeV ion passing through a material [115], [116]. At the end of its range, the ion's velocity slows to the point where nuclear interaction is the predominant phenomenon responsible for energy losses. Contrary to the interactions with bound electrons, the nuclear-stopping power involves the elastic scattering with the target nuclei, which is ruled by the Coloumb repulsion and causes a discrete energy loss with a considerable angular deflection of the ion trajectory. Finally, the radiative stopping power involves radiative processes such as Bremsstrahlung and Cerenkov radiation; however, since these last processes occur for high-energy particles (hundreds of MeV), this contribution can be safely neglected for the discussion in this Thesis work. Therefore, the path of the ion crossing the material is almost rectilinear except for the end

of its range, as displayed in Fig. 4.1. The interactions and the trajectories of fast ions can be investigated through the use of simulation codes based on Monte Carlo tracing techniques. One of the most widely used tools in material science is the Stopping Ion Range in Matter (SRIM) [117], a collection of software packages to calculate several features of the transport of ions in matter. This tool is based on the Binary Collision Approximation (BCA) method, which approximates the ion's travel through a material as a sequence of independent binary collisions with sample atoms [118], [119]. During these collisions, the ion is assumed to lose no energy when colliding with nuclei but experiences electronic stopping power while travelling a straight path between the collisions. The simulation of a significant number of ions displays mean observed values and their respective variances, including the ion range, the longitudinal and the lateral straggling, the energy loss, and the number of defects created per ion. In the BCA approach, the classical scattering integral is solved for the impact parameter of the incoming ion to treat a single collision between the incoming ion and a target atom (nucleus). The impact parameter b is defined as the perpendicular distance between the path of a projectile and the center of a potential field U(r) generated by an object that the projectile is approaching. Therefore, the relation between the impact parameter b and the scattering angle Θ in the center-of-mass coordinate system is defined as follows [120]:

$$\Theta = \pi - b = \int_{r_{\mathrm{m}}}^{\infty} \frac{1}{r^2\sqrt{1-(\frac{b}{r})^2-\frac{2U(r)}{E}}}\,dr, \tag{4.2}$$

where E is the incoming particle's energy, U(r) is the electrostatic potential and r_{m} is the minimum distance between the incoming ion and the target nucleus. The integration domain must be extended only over the interval in which the function is defined. The integral solution provides information about the angle and the energy loss of an ion after colliding with sample atoms and allows us to determine the difference between the energy of the ion before and after the collision. To obtain coordinates in the laboratory frame, the following transformation must be used:

$$tan(\theta) = \frac{M_2 sin(\Theta)}{M_1 + M_2 cos(\Theta)} \tag{4.3}$$

where M_1 is the mass of the incoming ion and M_2 is the one of the target atom. The kinetic factor, defined as $K(\theta) = \frac{E_{\mathrm{out}}}{E_{\mathrm{in}}}$ can be indeed written in the non-relativistic form and in the laboratory reference frame as follows [120]:

$$K(\theta) = \left\{ \frac{\sqrt{1-(\frac{M_1}{M_2})^2 \cdot sin^2(\theta)} + \frac{M_1}{M_2}\cdot cos(\theta)}{1+\frac{M_1}{M_2}} \right\}^2, \tag{4.4}$$

It is worth noting that the kinematic factor does not depend on the energy of the incident ion but only on the ratio of the two masses and the scattering angle θ.

Therefore, to solve the two-body scattering, the numerical integration takes the velocity and direction of an incoming ion as inputs and provides the new direction and velocity of both the ion and the recoil atom as outputs. In simulations, the target material is typically described by its elemental composition, density, and displacement energy threshold, and the damage that can be accounted for includes only interstitials, vacancies and substitutional atoms. Because electron interaction occurs continuously, it's impossible to consider each collision individually. In the Monte-Carlo simulation, the effect of these collisions is replaced by a mean value energy loss and deviation instead. On the other hand, due to their lower occurrence frequency, the interactions with nuclei can be taken into account one by one, allowing us to estimate their capability to deflect an ion's trajectory and create defects. Hence, the record of cases the software can process during the collision event is indeed the following:

- when an incident ion transfers a higher amount of energy to a target atom than the threshold, it can cause the target atom to break free from its position in the lattice. This creates a vacancy in the structure, and the target atom behaves like a projectile, causing defects. This phenomenon is commonly referred to as a damage cascade;
- if the energy transferred from the projectile (either a recoil atom or the original incoming ion) to the target atom is less than the threshold, the target atom is expected to return to its original site and release its kinetic energy as phonons;
- when a projectile has less kinetic energy than a threshold, it rests in an interstitial position and the kinetic energy is converted into phonons;
- lastly, a replacement collision can occur when a projectile has a kinetic energy below the threshold, but it causes the target atom to gain enough energy to leave the crystal lattice site.

In this scenario, the Monte Carlo method relies on the randomness of the distance and impact parameter of the subsequent colliding atom, which is sampled from a probability distribution that depends on the atomic density of the material. Consequently, such a method simulates an ion crossing an amorphous material, unlike the crystal BCA codes, which can also consider channelling effects [121]. However, the Monte Carlo BCA approach would still be a reliable method to simulate the ion passage in the material if the incident direction is not parallel to the high symmetry directions of the crystal.

At the end of the range, where the energy of the ion probe is smaller than that of the electrons of the material and the nuclear interaction is non-negligible, the energy of the incoming ion becomes comparable to that of the target's atoms, and the ion probe is said to be thermalised. Since the nuclear-stopping power significantly

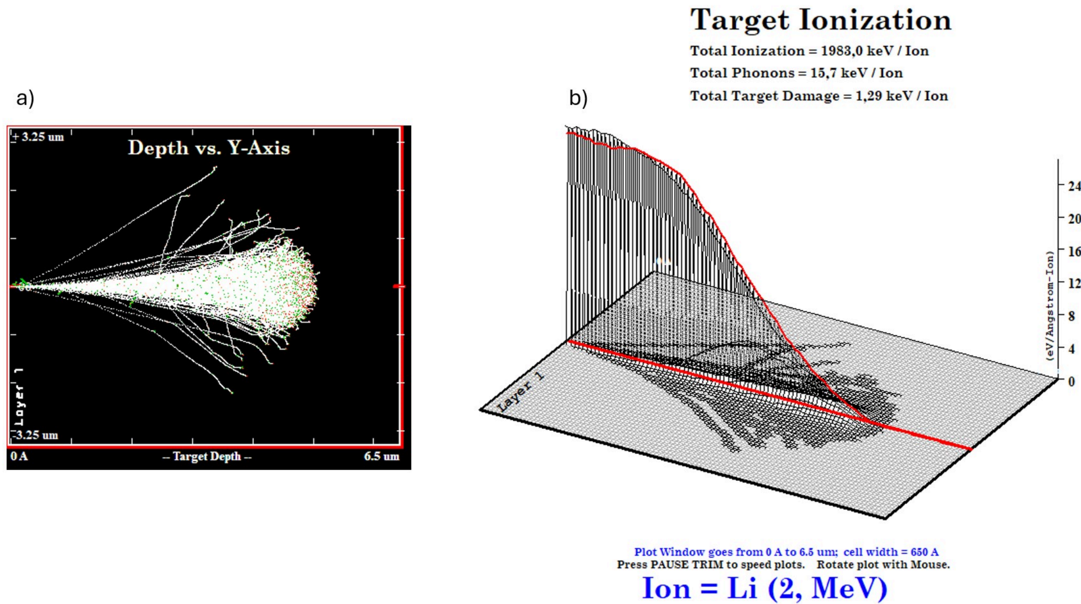

Figure 4.1: Example of a simulation output from SRIM [117]. a) X-Y collision plot of 2500 2 MeV Li ions crossing a 6.5 μm silicon substrate (ions enter the target material from the left side). Each track represents the path of the ion. b) 3D plot of the ionization map of the simulated tracks of the plot a). (Ions enter from the top side). The interactions have been calculated according to a detailed modeling of the damage, where the simulation keeps track of every recoiling atom until its energy drops below the lowest displacement energy of any target atom.

affects the energy of the projectile only at the end of the range, the electronic stopping power, which is, in good approximation, described by the Bethe-Bloch formula [122], defines the penetration depth, which can range from a few nanometers (keV) to tens of micrometres (MeV), depending on the energy of the projectile, as well as the mass and atomic number of both the entering ion and the target material. For instance, the ion range reduces with the mass of the projectile. At the same time, the interaction volume can vary from a few to hundreds of nanometers [123]. Since the ion probe's energy and mass dictate the ion range, the energy loss can be described as a function of the penetration depth by defining the Bragg's curve. The latter provides additional information regarding the density of ionized atoms of the target material along the incoming ion track. As incident ions cross the target material, they release energetic electrons (delta rays) that can travel a considerable distance from the primary ionization area along the ion track and subsequently lose their energy through the interaction with orbital atomic electrons, thus producing unbound electron-hole pairs. Consequently, when an incident MeV ion interacts with a semiconductor, a plasma volume of free electron-hole pairs surrounding the ion track originates. In particular, the latter is characterized by a submicrometer

radial extension where the energy of the delta rays defines the cone shape [124] and the Bragg's curve defines its density. From the perspective of creating individual color centers by means of ion beams, two main intrinsic limiting aspects must be considered in the development of the fabrication process. The interactions between individual atomic electrons cause fluctuations in the number and geometry of collisions, resulting in the dispersion of the ion beam both longitudinally and laterally. The distribution of energies of the initially monochromatic ions determines the distance each ion penetrates the material, called longitudinal struggling. On the other hand, the distribution of the transverse momentum acquired by the ions alters the ion trajectories and the stopping distances from the beam axes, which is defined as lateral struggling. Fig. 4.2 shows the ion distribution for the 2 MeV Li ion beam simulated in Fig. 4.1 where the SRIM code indicates the ion distribution as the ratio between the volumetric ion density ρ expressed in cm^{-3} and the ion fluence F, expressed in cm^{-2}. The result is thus the plotted quantity $\frac{\rho}{F}$ [cm^{-1}]. In particular, it can be noticed that the latter has a higher average lateral struggling (3.542 μm) compared to the 20 keV Li ion beam in the same silicon target (61.4 nm), thus further limiting in-plane accuracy in the ion positioning. Additionally, lower implantation energy is required to address the fabrication of shallow defects (<100 nm) in the case of quantum-enhanced sensors [125], quantum computation schemes based on solid-state color centers [95], [4] or their coupling with photonic structures [126]. Conversely, lower-energetic ions require higher-sensitivity readout electronics for the implementation of single-ion-implantation techniques [127], [128].

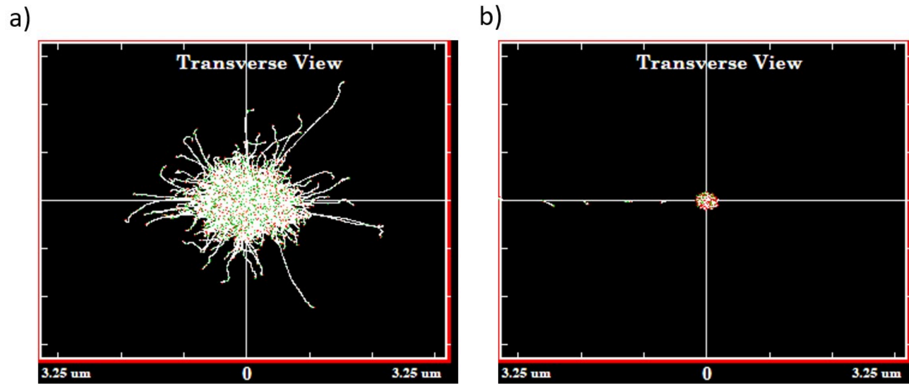

Figure 4.2: Example of a simulation output from SRIM [117]. a) Y-Z collision plot (transverse view) of the 2500 2 MeV Li ions crossing a 6.5 μm silicon substrate and simulated in Fig. 4.1. Each track represents the path of the ion. b) Comparison with the transverse view of 2500 20 keV Li ions crossing the same 6.5 μm silicon substrate. The interactions have been calculated according to a detailed modeling of the damage, where the simulation keeps track of every recoiling atom until its energy drops below the lowest displacement energy of any target atom.

4.1.2 Ion induced damage

Since two different solid-state material platforms have been used in this thesis work to address the main fabrication challenges in realising scalable quantum devices by means of ion implantation, the ion-induced damage for both diamond and silicon will be investigated in this section.

Diamond

Although the fabrication by means of ion implantation has been widely demonstrated for several classes of solid-state color centers, the incorporation of selected impurities in the crystal lattice goes parallel to the displacement of target atoms, i.e. the creation of lattice vacancies, interstitials, and simple complexes such as Frenkel pairs (vacancy and interstitial pair) [129]. Moreover, each incoming ion may have enough energy to cause further damage during its slowing down when it can initiate a chain reaction of atom displacements, which is known as a "damage cascade" or "thermal spike". As a result, hundreds or even thousands of vacancies can be created per incident ion [129] and at this damage density, the region under investigation (in proximity to the Bragg peak) can be assimilated more to an amorphous phase, then to a damaged crystal. Fig. 4.3 provides an idea of the entity of the displacement simulated in [130] and required to knock out the carbon atoms to a new position outside the diamond lattice. For example, if the displacement occurs in the <100> direction, 3Å displacement from the initial position results in the absolute minimum (16.5 eV) for the structural energy. The latter corresponds to the displacement of the atom, which leaves a vacancy and sits in a new interstitial position characterized by three-fold sp^2 coordination instead of the usual fourfold sp^3 one. This defect with a so-called “split-interstitial” configuration is called a Frenkel pair. MD studies on the minimum energy required to displace an atom from the lattice site permanently, previously mentioned as "displacement energy", was calculated to be 52 eV for off-axis directions [130], also confirmed with other computational methods [131]. The latter constitutes an important input parameter for calculating ion damage in diamonds through Monte Carlo simulation in SRIM.

For this reason, post-implantation thermal processing represents a reliable method to provide the kinetic energy necessary to recover the crystal matrix, promoting the recombination of vacancies with interstitial atoms and the integration of the extrinsic ion species in the defective structures. In this regard, as highlighted in the next section, particular attention indeed should be paid to the formation efficiency of these color centers, which heavily depends on the post-implantation activation process [132], [133], [134]. However, in the case of diamond, which undoubtedly stands as the pioneering of the solid-state platforms for quantum technologies, regardless of the thermal activation process, the cumulation of radiation-induced defects can represent an upper limit in the density of color centers achievable upon ion implantation. Consequently, the latter may result in restricting the possibility of realising

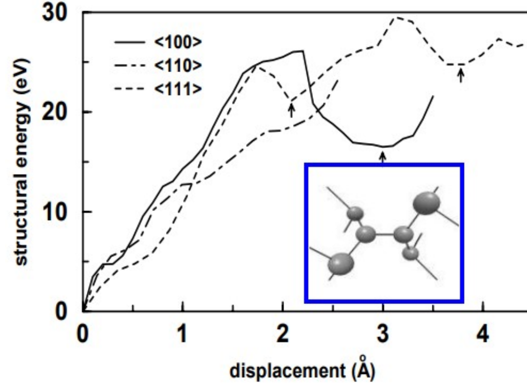

Figure 4.3: Calculated differences between the potential energy of the ideal diamond structure and that of the crystal when a C atom is displaced along the <100>, <110> and <111> crystallographic directions. From [130].

extremely sensitive high-spatial-resolution field quantum sensors based on high-density ensembles of color centers, where the sensitivity scales with the $\sqrt{N}$ and N is the number of quantum emitters [135]. In particular, the damage is induced by breaking the sp^3 bonds; when a sufficient concentration of damage is reached, the atomic reorganisation upon adequate conditions may result in the stabilisation of the sp^2 bonds, hence irreversibly converting the diamond into graphite. Since this threshold depends on the projectile energy and mass, the implantation temperature and fluence, unless heavily damaged diamond applications are targeted, such as in the case of electrically conductive microchannels [136], or electrodes [12], the identification of suitable implantation conditions to avoid the irreversible conversion of diamond into graphite is absolutely of primary importance. Although SRIM has some limitations, such as the fact that it does not consider defects created by precedent ions nor the cumulative damage events, the simulation tool allows us to estimate the ion implantation fluence responsible for the vacancy density regime above the "amorphization threshold." The latter is intended as the damage density for which the sp^2 bonds are thermodynamically preferred during the recovery of the crystal matrix upon post-implantation annealing. The vacancy density profile *p(z)* in SRIM is expressed as the mean number of vacancies created per incoming ion and depth unit, thus expressed as $[Vac \cdot ion \cdot \text{Å}^{-1}]$ (Fig. 4.4). Therefore, the maximum ion beam fluence F $[ion \cdot cm^{-2}]$ corresponding to the threshold volumetric vacancy density, i.e. ρ_{Vthr} $[Vac \cdot cm^{-3}]$ can be estimated as:

$$F_{\text{Vthr}} = \frac{p(z)}{\rho_{\text{Vthr}}} \tag{4.5}$$

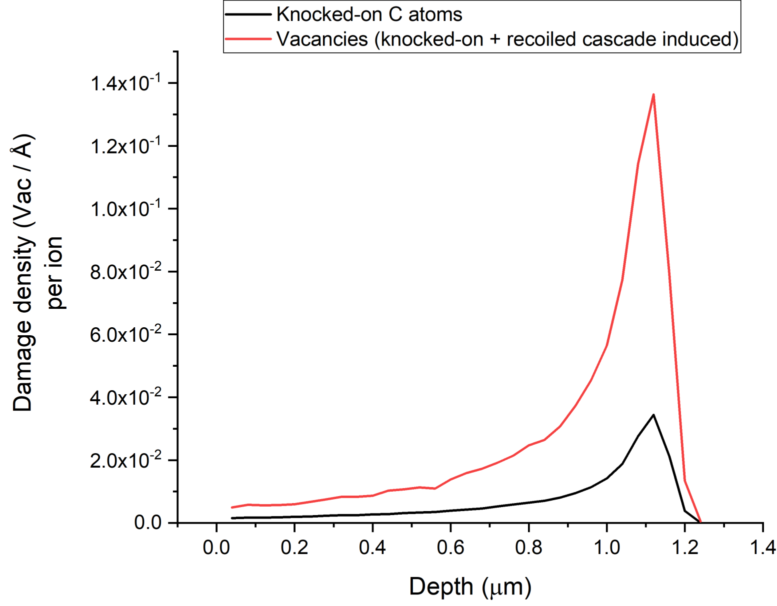

Figure 4.4: N^{2+} accelerated at 2 MeV into diamond. Damage profile: the black curve represents the vacancies directly caused by the incoming nitrogen ions, whereas the red one includes both ions and recoiled cascade-induced vacancies.

Ion implantation on a hot diamond substrate

As anticipated, the amorphization threshold depends on the ion species and energy. In particular, since graphite has a lower density than diamonds, the interested layer is not free to expand, and this effect is more pronounced as the layer lies deeper below the surface (MeV implantation energy). In other terms, a bigger "effort" is needed to turn a layer of amorphous carbon into graphite when the reconstruction of the sp^2 bonds experiences a mechanical pressure that can be in the order of several GPa [137]. For low-temperature implantation, i.e. $T_{impl} \leq$ room temperature, it has been reported that the diamond structure is irreversibly converted to a graphitic phase when the volume density of generated vacancies exceeds a value of about 10^{22} vac·cm^{-3} in the keV energy range [138] and $9{\cdot}10^{22}$ cm^{-3} in the MeV energy range [139]. For this reason, **part of this Thesis work was devoted to studying alternative experimental approaches** to unlock the fabrication of a high-dense ensemble of color centers upon ion implantation. In particular, using ion implantation on a hot diamond substrate, two main results have been achieved: the possibility to **increase the graphitization threshold** and, by assuming a linear dependence of the photoluminescence (PL) measured signal from the number of created color centers, a **higher formation efficiency** in the creation of Nitrogen-Vacancy (NV) centers in artificial diamond[110].

Featuring unique Opto-physical properties, the NV center has been extensively

studied over the past decade [140], [141]. This color center proved to be an appealing candidate for various applications in quantum computing [3], sensing, [142] and metrology [143], due to the coupling of its electronic spin to external interacting fields, the optical readout of its spin state based on PL intensity detection, and the availability of dynamic control protocols, which enable Optically-Detected Magnetic Resonance (ODMR) experiments. To develop field sensors with unprecedented sensitivity, several sensing schemes have been proposed that rely on high-density ensembles of NV centers, thus maximizing the signal-to-noise ratio [135] [2].

In this regard, the efficient fabrication of highly dense ensembles of color centers by implanting an artificial hot diamond substrate is reported. The sample used for the experiment is a $3 \times 3 \times 0.3$ mm^3 IIa Chemical Vapor Deposition (CVD) single crystal diamond produced by ElementSix and denominated "optical grade" due to its nominal concentrations of nitrogen and boron which are less than 1 ppm and 0.05 ppm, respectively. Fig. 4.7 shows the experimental configuration adopted for the ion implantation processes to implant well-defined regions of the same sample under different temperature conditions, thus enabling their homogeneous assessment and comparison. The sample was implanted with 2 MeV N^{2+} ions with four different fluences, namely $10^{15} cm^{-2}, 5 \cdot 10^{15} cm^{-2}, 10^{16} cm^{-2}$ and $2.5 \cdot 10^{16} cm^{-2}$. For each of the preceding implantation fluences, three different regions were implanted, varying the temperature at which the diamond substrate was held. Consequently, three different temperatures were adopted for the ion implantation, that is, $\sim$ 22°C (Room Temperature), 550 °C and 750 °C, while the sample was held in high vacuum ($\sim 10^{-7}$ mbar). Finally, to prevent the introduction of radiation damage to the crystal matrix at a too-high rate and hence allow for sufficient diffusion and recombination of vacancies during the implantation process, the ion current was adjusted $(5 \cdot 10^{-11} - 15 \cdot 10^{-11} A)$ to ensure that all ion implantations were performed within a well-defined one-hour timeframe.

Fig. 4.5 shows the volumetric vacancy density profiles obtained considering the vacancies damage profile reported in Fig. 4.4 and the equation 4.5 together with the graphitisation threshold of diamond for MeV ions [139]. The four implantation fluences operated for Sample #1 were chosen to be near the graphitisation threshold. Notably, the fluences of $1 \cdot 10^{15} cm^{-2}$ and $5 \cdot 10^{15} cm^{-2}$ resulted in a vacancy density profile below the graphitisation threshold, while the Bragg's peak of the vacancy density profiles associated with the $1 \cdot 10^{16} cm^{-2}$ and $2.5 \cdot 10^{16} cm^{-2}$ ion fluences rely above the graphitisation threshold at the end of the ion range, estimated to be 1 µm from the sample surface. Therefore, where ion implantation is performed by adopting these latter implantation fluences and at room temperature conditions, it is expected that a graphitic layer will irreversibly form after a thermal annealing process above 800 °C [139]. The optical micrograph reported in Fig. 4.6 display the different implanted areas for the "as implanted" sample, where it is evident that the two regions implanted at the highest implantation fluences at room temperature have been heavily amorphised due to the substantially different optical opacity with

respect the pristine region. The irradiated area implanted at $5 \cdot 10^{15} cm^{-2}$ also has the same damage entity. On the contrary, any regions implanted at temperatures of 550 °C and 750 °C do not present a particularly modified transparency with respect to the pristine diamond surface, thus excluding the apparent amorphization of the crystal lattice.

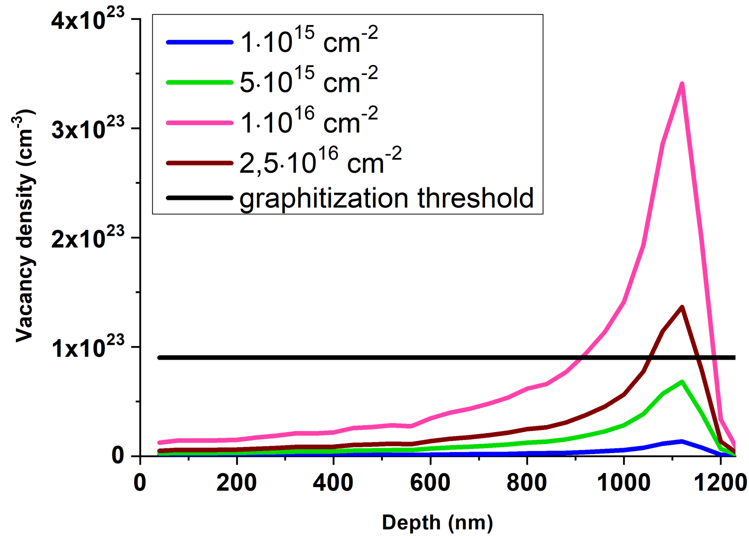

Figure 4.5: Vacancies density profiles corresponding to the ion implantation fluences adopted in the ion implantation process with 2MeV N^{2+}. The graphitisation threshold refers to MeV ions in diamond [139].

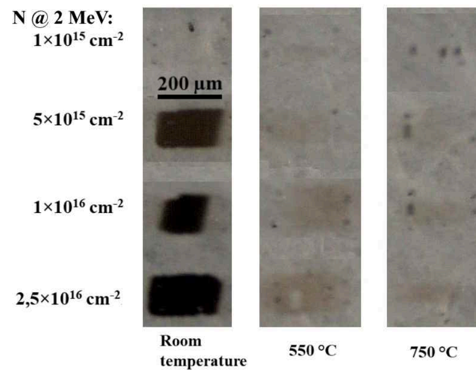

Figure 4.6: Optical micrograph of the "as implanted" sample, before the ex-situ thermal annealing.

Preliminary PL characterization was carried out after the ion implantation but before any subsequent thermal annealing process. The characterization was performed using confocal Raman spectroscopy with a Horiba-Jobin-Yvon LabRam

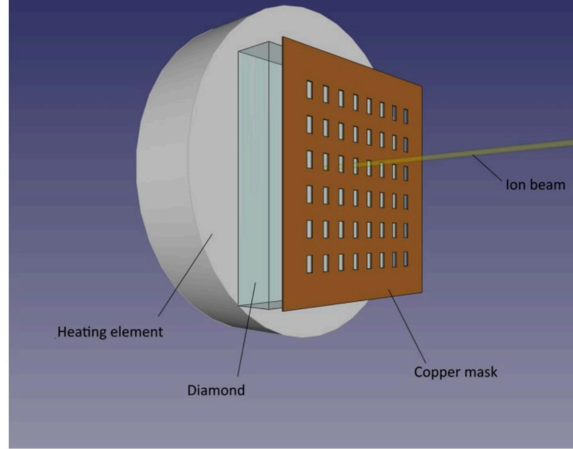

Figure 4.7: Experimental configuration adopted for ion implantation on a hot diamond substrate. The picture is not in scale. The diamond surface was implanted using an ion micro-beam with a diameter of about 10 µm. The beam was scanned over the surface through mask apertures using electromagnetic focusing and scanning.

HR-VIS instrument featuring a Peltier-cooled CCD detector array. A 532 nm laser focussed through a 20x air objective provided the excitation power of 21.6 mW [144]. Afterward, an additional annealing step was used to optically activate the NV centers in regions implanted at both room and high temperatures. The annealing process was performed ex-situ at 950°C for 12 hours (high vacuum, $\sim 10^{-6}$ mbar) to ensure that all irradiated regions were thermally processed equally. This duration was indeed chosen to be an order of magnitude higher than the one used during the fabrication process.

After the thermal processing, spectral characterization of the implated regions has been performed to assess the conversion of the nitrogen impurities into optically active NV centers. In particular, Fig. 4.8 shows a selected set of PL spectra acquired upon the same experimental condition, ensuring the same optical excitation power (21.6 mW) and collection efficiency for every analyzed region. To properly focus on the sample surface, the sample was mounted on a nanopositioner to be carefully positioned each time, maximizing the PL signal and thus ensuring a consistent PL analysis. The spectra reported refer to the three implanted regions (i.e., RT, 500°C and 750°C) with the highest implantation fluence, namely $2.5 \cdot 10^{16} cm^{-2}$, and for each one, three spectral features can be distinguished:

- the first-order Raman scattering at 572.6 nm (1332 cm^{-1} shift under 532 nm excitation wavelength);
- the ZPL of the neutral charge state (NV^0) at 575 nm and its phonon replica

at higher wavelengths;

- the ZPL of the negative charge state (NV^-) at 638 nm and its phonon replica at higher wavelengths.

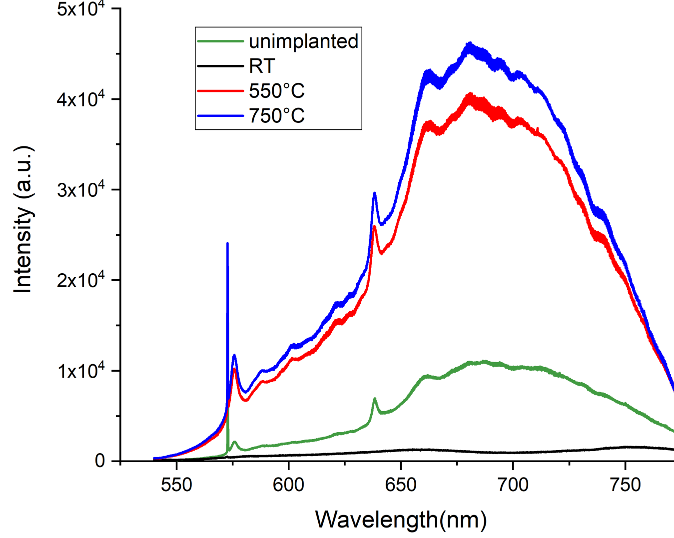

Figure 4.8: PL spectra acquired after the ex-situ thermal annealing at 950 °C (12 h) for the regions implanted with a fluence of $2.5 \cdot 10^{16} cm^{-2}$ at room temperature (black line); 550°C (red line) and 750°C (blue line). The green curve shows the spectrum acquired on a pristine region of the sample. A 532 nm excitation wavelength with P = 21.6 mW was used.

To compare the PL signal associated with the different regions, the PL spectrum of each was integrated over the spectral region related to the NV emission in the 560-750 nm range, as reported in Fig. 4.9. Moreover, since the experimental conditions were preserved during the spectral investigation of the different implanted regions and no other spectral features different from the NV emission were observed in the considered PL spectra, we can assume that each PL integrated signal is proportional to the NV concentration in the investigated volume ($\sim 2\mu m^3$ for the adopted setup).

Fig. 4.10 shows the integrated PL signals plotted against the relevant experimental parameters, i.e. ion fluence and implantation temperature for the "as implanted" sample (a) and after its thermal treatment with 12 hours annealing at 950°C (b).

Consistently to what reported in literature [145], [146] where a limited quantum efficiency caused by a "self-absorption" process is reported for high density of created NV centers, in the "as implanted" spectral analysis, a more intense emission is evident from the regions implanted at the lowest fluence among the adopted fluence range, i.e. $1 \cdot 10^{15} cm^{-2}$. Besides this, the regions implanted at higher temperatures

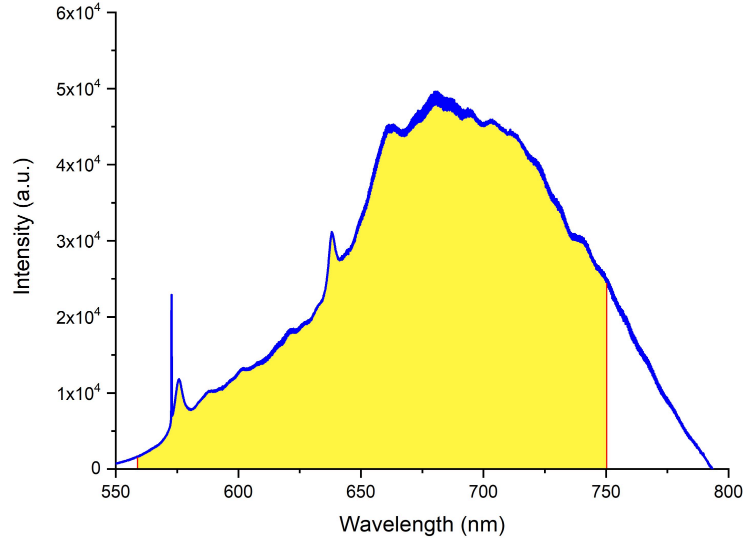

Figure 4.9: PL spectrum from an ensemble of NV centers acquired in the region implanted at room temperature with a fluence of $1 \cdot 10^{16} cm^{-2}$. The region highlighted in yellow and delimited by the red lines in the 560-750 nm spectral range corresponds to the integrated signal.

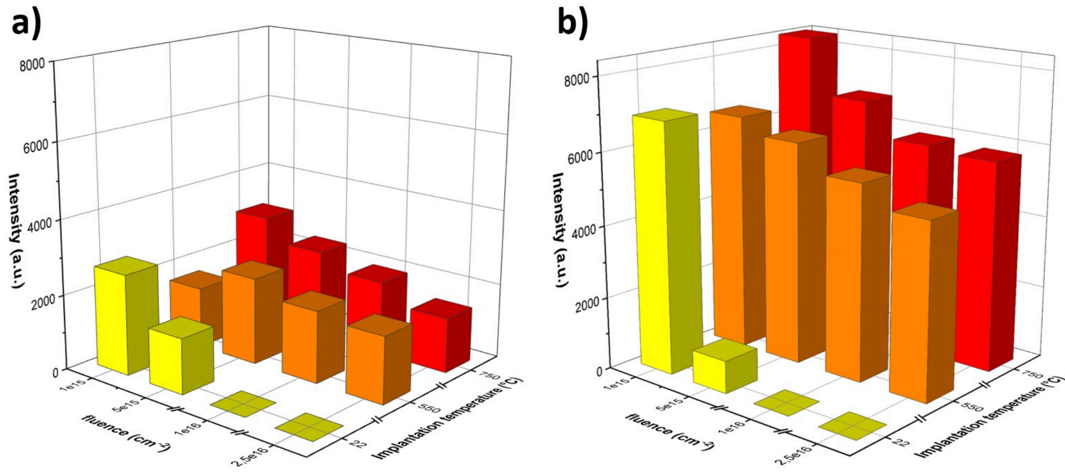

Figure 4.10: Histograms of intensities obtained as shown in Fig. 4.9 for each implanted region at different annealing steps: a) pre-annealing, b) after 12 h annealing at 950°C.

are characterized by a higher PL signal with respect to their room-temperature counterparts. The effect of in-situ annealing is even more pronounced looking at the

highest implantation fluences ($2.5 \cdot 10^{16} cm^{-2}$, $1 \cdot 10^{-2} cm^{-2}$); the lack of PL emission from the NV centers at room temperature is perfectly consistent with what is commonly verified for fluences above the graphitisation threshold [136]. Secondly, the regions implanted at 550°C and 750°C resulted in the in-situ recovery of the crystal matrix and, consequently, in the increase of the graphitisation threshold, which is justified by the evidence of the spectral emissions of the NV as already reported in Fig. 4.8.

Outcomes

To conclude, the study of the PL signal from NV centers fabricated on a hot diamond substrate has highlighted two main aspects. For implantation temperatures of 550°C and 750°C, an **increase in the graphitisation threshold** for values above $3.5 \cdot 10^{23} cm^{-3}$ (Fig. 4.4) is observed. In this way, the substrate can accommodate a higher number of ions before irreversibly graphitizing, thus **allowing for the fabrication of a larger ensemble of color centers to increase the system's sensitivity**. Moreover, for the same implantation fluences, a progressively **increasing PL intensity at increasing implantation temperatures** indicates an **increase in the creation efficiency of NV centers upon N implantation**. The latter assumes a linear dependence in the total measured PL intensity on the number of fabricated optically active defect complexes. In particular, comparing the PL from the implanted area with the lowest fluence ($1 \cdot 10^{15} cm^{-2}$) at room temperature and 750°C, the formation efficiency is estimated to be 26 % higher in the case of ion implantation on a hot diamond substrate. The latter result agrees with a previous study on the in-situ optimization of co-implantation and substrate temperature for fabricating NV centers in artificial diamond [147]. Finally, although the original NV concentration of the sample is not well determined, and the producer indicates upper limits for the nitrogen concentrations (<1ppm), it is possible to provide an upper limit to the creation efficiency as follows. According to the scientific literature [148], the typical concentration of the native substitutional nitrogen in "optical grade" diamonds is below 0.5 % of the native substitutional nitrogen, thus indicating an upper limit of 5ppb of NV and corresponding to $\sim 9 \cdot 10^{14}$ cm^{-3}. The not-implanted areas in our sample should correspond to the abovementioned specifications, and their fluorescence did not change significantly after the thermal annealing steps (no recombination of vacancies with the substitutional nitrogen). Since the spectra consisted only of NV centers fluorescence (as reported in Fig. 4.8), it was possible to normalize the acquired spectra to obtain an estimation of the creation efficiency for each of the implanted areas. Therefore, by integrating the spectra acquired from a reference not implanted region and the region implanted at $1 \cdot 10^{15}$ cm^{-2} after 12 h of thermal annealing at 950°C, in the same way we did for all the data in our work, we obtained that the fluorescence in the implanted area increased respect to the not implanted one by a factor of 5.6. This results in

a concentration of NV centers of $\sim 5{\cdot}10^{15}$ cm^{-3}.

Silicon

As already discussed in 2.2.5, the W center is an optically active tri-interstitial radiation-induced defect complex in silicon, and it is characterized by a sharp emission line (ZPL) (< 0.1 nm [50]) at 1218 nm (1.018 eV)). Therefore, looking at silicon as a promising solid-state platform for integrated solutions in **single-photon device fabrication indispensably requires the parallel study of these intrinsic defect complexes**. Besides this, the recent isolation of the W center at the single-emitter level unlocks a promising perspective for the **development of integrated silicon photonics based on native defects**. Nevertheless, it is still crucial to develop the technological capability to control their placement in high-purity silicon substrates based on mature ion implantation techniques that can deliver single impurities with high spatial resolution. So far, the scientific community has worked on the optimization of W-center PL emission by creating self-interstitial defects in silicon through self-ion implantation [65], i.e., Si^+ implantation in silicon. However, the growing interest in the scientific community in creating new types of silicon-based single photon sources poses **the need to understand the role of the radiation damage occurring during the ion implantation processes commonly adopted for introducing the different impurities into the silicon lattice**. With this aim and the spreading enthusiasm about the possibility of developing large-scale quantum photonics devices based on the recent advances regarding the carbon-based G center [90], [91], in this Thesis work, **the suitability of ion implantation for creating W centers and their optical properties are investigated involving C keV ion implantation** followed by multiple rapid thermal annealing processes [111].

Self-interstitial defects in silicon upon carbon implantation

For the following study, a set of seven 3x3 mm^2 nominally identical pieces has been cut from a commercially available float zone n-type silicon wafer. The samples have been homogenously implanted with a fluence of $2 \cdot 10^{14} cm^{-2}$ and consequently thermal processed with a PID-controlled SSI SOLARIS 150 Rapid Thermal Processing System, which uses high-intensity visible radiation to heat single wafers for short process periods at precisely controlled temperatures. Seven different temperatures were chosen to perform the thermal treatment of the different samples: 320°C, 365°C, 400°C, 450°C, 500°C, 700°C, and 1000°C. Fig. 4.11 displays the temperature profile of the annealing process carried out in a 300 Standard Cubic Centimeter per Minute (SCCM) total flow of N_2 where a temperature ramp rate of $\sim$ 65°C/s was used. Thus, the opto-physical properties of the processed substrates were explored through a systematic characterization performed at cryogenic temperature via the

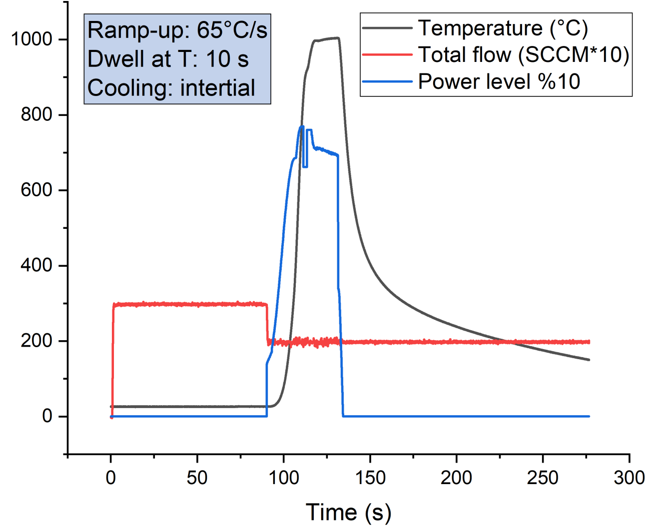

Figure 4.11: Temperature profile of the Rapid Thermal Annealing performed with an SSI SOLARIS 150 Rapid Thermal Processing System. The plateau temperature is 1000°C. The process has been performed in a total flow of 300 Standard Cubic Centimeters per Minute (SCCM) of N_2.

fiber-coupled single photon-sensitive confocal microscope exhaustively described in the previous chapter. The diffraction-limited focused excitation spot on the sample surface was produced using a 488 nm laser diode whose penetration depth in silicon ($\sim 150nm$ [34]) is sufficient to provide efficient optical excitation to the volume of created defects upon 36 keV C^- ions with a penetration depth of $\sim$ 100 nm according to SRIM simulation [117]. Combining a 700 nm long-pass dichroic mirror and an 800 nm long-pass filter, the spectral range of interest was selected for investigation. The signal emitted from the samples is collected through the core of a multimode optical fiber coupled to an InGaAs single-photon avalanche detector (MPDPDM-IR / MMF50GI). Finally, the spectral features were systematically analyzed by means of a Horiba iHR320 monochromator, providing a spectral resolution estimated as $\leq$ 4 nm. Fig. 4.12 displays the PL spectra acquired at 10 K after the 20 s RTA treatments at different annealing temperatures. From the spectral analysis, it is possible to distinguish:

- a bright emission at 1217 nm corresponding to the W ZPL;
- a structured phonon sideband at higher wavelengths;
- a weak signal at 1307 nm, consistent with the expected emission related to the Local Vibrational Mode (LVM) at 70 meV ($\sim$ 1308 nm).

These spectral features unequivocally identify the presence of W emitters, according to what was already discussed in section 2.2.5. Conversely, although varying

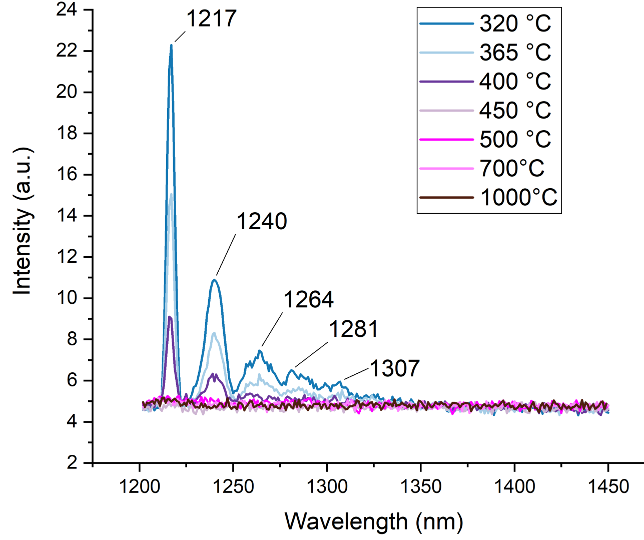

Figure 4.12: PL spectra acquired at T=10 K in the carbon implanted regions upon 488 nm excitation for different annealing temperatures. The optical power was 4.41 mW.

processing temperatures and the introduction of carbon impurities through ion implantation, unlike in other investigations on Silicon On Insulators (SOI) substrates [149], no spectral features linked to carbon-based G centers (section 2.3.2), were detected at any stage of RTA processing.

Moreover, the intensity of the emitted signal gradually decreases at increasing annealing temperatures, suggesting a progressive recovery of the crystal lattice and, consequently, the thermally induced dissociation of the interstitial clusters of highly mobile silicon atoms. In particular, from the annealing data, we can estimate the deactivation energy of the centers by fitting the Arrhenius plot reported in Fig. 4.13 with the function [65]:

$$ln(I) = \frac{E_{\mathrm{D}}}{R} + ln(k), \tag{4.6}$$

where I is the PL intensity, E_{D} is the deactivation energy, R is the gas constant, and k is a constant whose value is connected to the dissociation process of the W centers. The dissociation energy resulted in $E_{\mathrm{D}} = (0.90 \pm 0{,}11)eV$, where the error is calculated, propagating the error of the slope obtained from the fit. The latter perfectly aligns with the values reported in optimizing W emission upon self-ion implantation [65] and with dedicated studies on the activation and deactivation energies of these systems [150]. Unfortunately, the lack of data for lower temperatures did not allow the estimation of the activation energy.

As described in section 3.2, the sample is mounted on a dedicated platform for the precise control of the local temperature. Therefore, as reported in Fig. 4.14, the

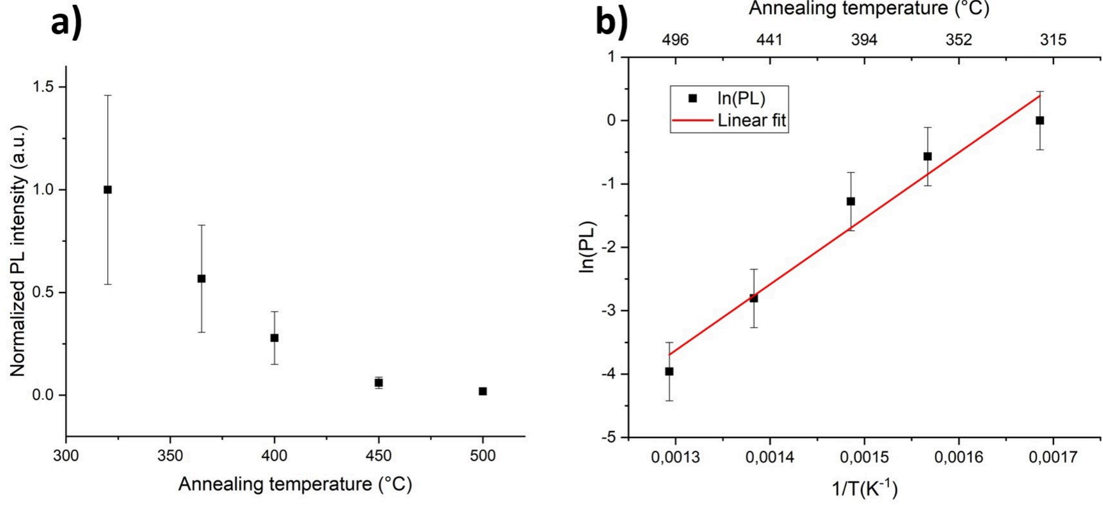

Figure 4.13: PL intensity as a function of the annealing temperature for 5 different n-type float zone silicon samples implanted with $2 \cdot 10^{14} cm^{-2}$ and subsequently thermally treated with a Rapid Thermal Annealing processing system, a). The Arrhenius plot of the data is reported in b). Since the integrated PL intensity measured for the 450°C annealing was the last significantly different from the background signal, only a subset of the measured data, referring to the 320°C-500°C range, was selected to estimate the deactivation energy. The data have been fitted according to a straight line y = mx+q where the extrapolated parameters are m = 10400 ± 1300 K and q = -17 ± 2.

temperature dependence of the PL signal was investigated. The intensity strongly decreases with increasing temperature until it becomes negligible for temperatures above 70 K. An analysis of the integrated signal in the 1210-1220 nm range, corresponding to the ZPL transition of the W center, particularly highlights a shift of around 10 K in the "knee" value for the temperature dependence of the PL with respect to a recent study on the optimization of the optical properties of W quantum emitters upon self-ion implantation (Fig. 4.15).

So far, the experimental data presented were intrinsically limited by the resolution of the monochromator (∼ 4 nm), which was, in turn, limited by the optical efficiency of our setup. Additional measurements have thus been performed to optimize the acquisition parameters to further improve spectral resolution. In this way, the ZPL emission wavelength was investigated as a function of the measurement temperature, qualitatively revealing a redshift of around 2 nm in the 10-90 K explored range (Fig. 4.16).

Finally, to access a comprehensive overview of the damage-induced intrinsic defects created during the introduction of the carbon impurities, the lifetime of the excited state has been measured using a 532 nm PicoQuant pulsed laser diode

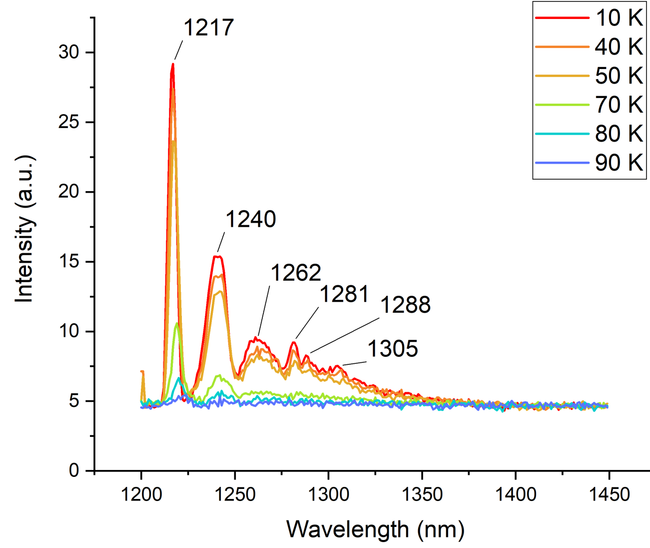

Figure 4.14: Temperature dependence of the PL from an ensemble of W centers fabricated on an n-type float zone silicon upon 36 keV C- ions with a fluence of $2 \cdot 10^{14} cm^{-2}$ and subsequently thermally processed with a Rapid Thermal Annealing at 320°C.

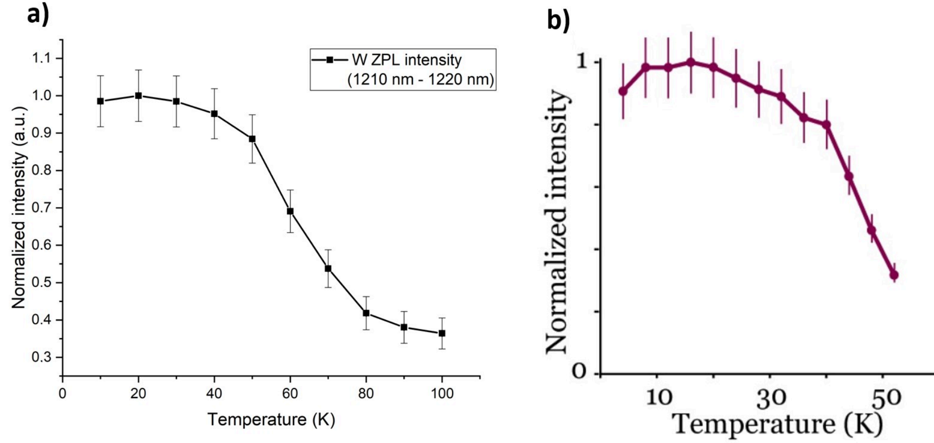

Figure 4.15: On the left, the temperature dependence of the PL intensity measured on an ensemble of W centers fabricated in a n-type float zone silicon upon 36 keV C- ion implantation (fluence $= 2 \cdot 10^{14} cm^{-2}$). The error bars have been calculated with Gaussian error propagation, assuming a Poissonian distribution for the measured PL counts. On the right, the PL intensity temperature dependence for W centers fabricated upon 80 keV Si implantation on a p-type bulk silicon sample from [65].

with a 20 MHz repetition rate and 20 ps pulse width. The optical power used was 2.5 mW. As already discussed in section 1.3.2, the time-dependent intensity

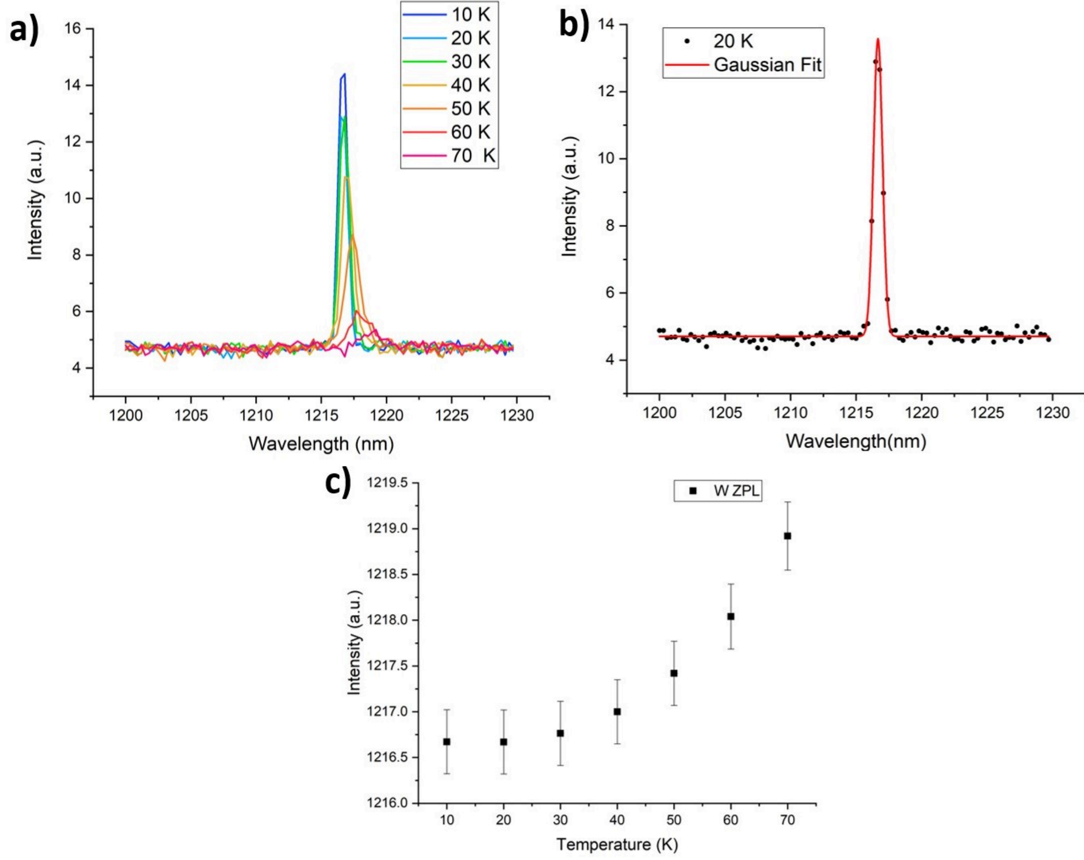

Figure 4.16: Redshift of the W ZPL. a) PL spectra acquired at different temperatures from an ensemble of W centers in the sample implanted with 36 keV C$^-$ ions and subsequently annealed with an RTA process at 320°C. b) Example of Gaussian Fit for estimating the ZPL in the case of PL spectrum acquired at 20K where $\lambda =$ 1216,670 $\pm$ 0.005 and FWHM = 0.498 $\pm$ 0.008 nm. c) The dependence of the W center ZPL on the temperature adopted during the PL measurements. The error bars were calculated through the sum of squared errors, considering the uncertainty associated with the Gaussian centroid fitting parameter and the resulting HWHM.

profile of multiple excitation and emission cycles can provide information on the characteristic time of the quantum source. Here, the time-dependent PL emission has been fitted with a bi-exponential decay (Fig. 4.17) where one decay parameter, corresponding to the shorter decay time, allows the decoupling of fast components, such as the laser reflection, from the lifetime of the excited state. In particular, the excited state lifetime was quantified as (18.8 ± 0.3) ns. The result is slightly below the one reported at the ensemble level [65], although it remains within the variability identified at the single emitter level (10 ns - 35 ns) [50]. Finally, Fig. 4.18 displays the FWHM estimated from the Gaussian fit of the W centers emission

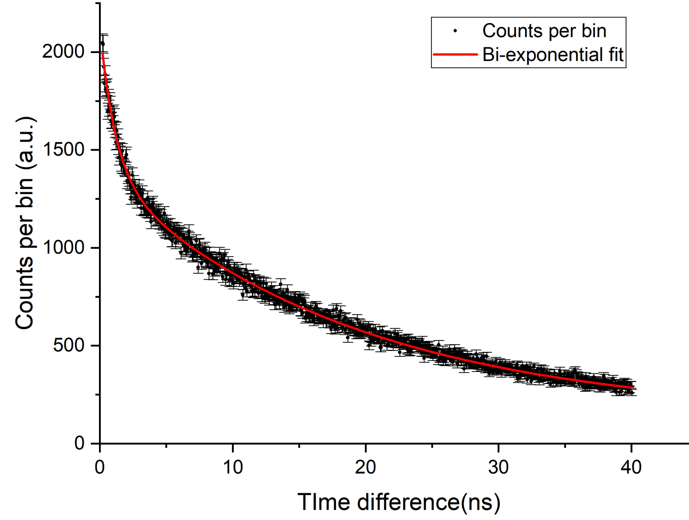

Figure 4.17: Emission lifetime against a trigger laser pulse acquired at 10 K from an ensemble of W centers of the sample implanted with 36 keV carbon ions and thermally processed at 320 °C. A bi-exponential has been used to evaluate the excited state lifetime, according to the commonly adopted physical model [151].

at the ensemble level as a function of the temperature; the spectral resolution of the monochromator limits the measured values, thus allowing to set an upper limit on the emission linewidth and qualitatively observe the temperature behavior. However, the value measured at 10K verifies that the monochromaticity of the emission is in line with the values reported in the literature upon the introduction of pure crystal damage. [74].

Outcomes

In conclusion, the emission enhancement at 1218 nm for the lowest considered annealing temperatures demonstrates that **the radiation damage introduced upon keV ion implantation effectively promotes the formation of the W centers**. Moreover, the optical characterization of the ensemble level carried out through the evaluation of benchmark parameters, such as the transition lifetime or the emission linewidth, has confirmed that **the quality of the fabricated emitters is consistent with what has already been reported in the scientific literature** on the optimization of the PL from W centers upon Si implantation. This indicates, in parallel, the **G centers' poor formation efficiency under RTA post-implantation treatment in high-purity samples** where the low native carbon concentration probably limits their formation.

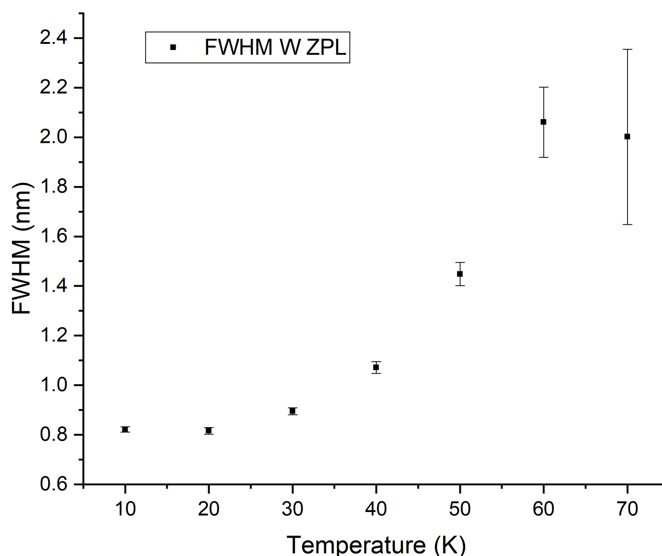

Figure 4.18: FWHM of the W ZPL as a function of the temperature. The error bars were estimated from the uncertainty associated with the Gaussian σ fitting parameter.

4.2 Single-ion delivery

Among the main fabrication challenges in the realization of large-scale single-photon devices by means of ion implantation is undoubtedly the delivery of individual impurities at each implantation site. In particular, deterministic implantation requires controlled fabrication strategies, which are currently investigated in the scientific community based on either pre- or post-detection techniques, i.e., either the preparation of the accelerating system for the delivery to the target of one single ion or the detection of the signal generated by the single ion that has been delivered to the target. The Ion Beam Induced Charge technique will be discussed in the following sections as a post-detection technique for implementing a deterministic approach to implant single impurities in silicon.

4.2.1 Ion Beam Induced Charge (IBIC)

The term Ion Beam Induced Charge dates back to the '90s, and it refers to a scanning microscopy technique that uses MeV ions to probe the fundamental electronic properties of semiconductors and devices. As discussed in the context of ion-matter interactions, the strike of a MeV ion in a semiconductor material is responsible for generating a plasma volume of free electron-hole pairs surrounding the ion track. The electric response can be read as an electrical signal at the front-end electronics, originating from the induction of the carriers moving inside

a medium permeated by an electric field and belonging to a system of sensing electrodes. The latter, in general, depends on

- the ionization profile, i.e., the Bragg curve, which depends on the ion mass, energy, and structural composition of the target material;
- the mechanism responsible for charge pulse formation, which is determined by the electric field geometry and the charge carriers' transport properties.

For this reason, measuring the induced charge at the device's electrodes can retrieve valuable information on the device's electronic properties by utilizing a probe ion beam with defined energy and mass. Moreover, the method can particularly benefit from the raster scanning of a focused ion beam across the sample surface [152]. The electronic features can be indeed punctually investigated when a micrometer or a sub-micrometer resolution is achieved jointly with the tuning of the experimental parameters, such as the ion probe energy. The induced charge, which provides the experimental observable, is typically mapped as a function of the position. Two different configurations can be set up for the experiment: front and lateral IBIC. The frontal geometry is commonly adopted for generating two-dimensional Charge Collection Efficiency (CCE) maps [113], while in the lateral configuration, keeping the same ionizing profile, it allows the study of the charge collection properties, namely mobility, diffusivity, and depletion region width, as a function of the depth [153]. Additionally, a waveform digitizer with sub-nanosecond time resolution allows the study of the time evolution of the induced signal in the so-called Transient IBIC [154]. In wide band gap semiconductors, such as diamond or silicon carbide or in the depletion region of p-n junction or Schottky diodes, the relaxation regime is fulfilled [155] and the semiconductor resembles a capacitor; since the carriers live a very long time compared to the time needed to level off a disturbance, e.g., an excess electron concentration δn, and recover the charge neutrality, a non-zero electric field is responsible for the carriers drift towards the collection electrodes and for the generation of the induced signal under their motion until they "land". Since, in most devices, the saturation drift velocity is significantly less than the speed of light, the charge induction can be described in purely electrostatic terms, neglecting any additional contribution related to magnetic effects due to the motion of charge carriers. This means the electric field is instantaneously propagating along the whole device's thickness [156]. Assuming that the excess charge carriers generated are insufficient to perturb the semiconductor's electric field, the induced charge at the electrodes can be determined by the Shockley-Ramo theorem [157], [158]. The latter was further generalized to partially depleted devices by Gunn in 1964 [159] and states that the current flowing between ground and the generic i-th electrode induced by a q-moving charge with arbitrary arrangements of conductors and space charges is:

$$i_{\mathrm{i}} = -q \cdot v_{\mathrm{d}} \cdot \frac{\delta E}{\delta V_{\mathrm{i}}} \tag{4.7}$$

where v_d is the velocity of the moving charge. The latter is connected to the drift electric field generated by all the potential applied to the structures, according to the relationship:

$$\overrightarrow{E_{\text{drift}}} = \mu \cdot \overrightarrow{v_{\text{d}}} \tag{4.8}$$

where μ is the carrier mobility, whereas $\frac{\delta E}{\delta V_{\text{i}}}$ is the Gunn's weighting field and is given by the derivative of the electric field with respect to the voltage V_i of the i-th electrode, while all other electrodes are held at a fixed potential. It is worth stressing thus that the signal is not the result of the charge arriving at the electrode but the induced charge resulting from the movement of the carriers in an electric field. The relation has been generalized for any semiconductor junction upon arbitrary polarisation conditions[160]. The total induced charge Q_i induced at the i-th electrode can be obtained by integrating the eq.4.7 over the collection time, meaning the time a carrier needs to reach the electrode. Additionally, considering a continuous inducing distribution of excess free carriers generated at t=0, it is possible to express the total induced charge at the i-th electrode as [161]:

$$Q_{\text{i}} = -q \int_0^t dt' \iiint_\Omega \rho(r,t) \cdot \overrightarrow{v_{\text{d}}}(\overrightarrow{r}) \cdot \frac{\delta E(\overrightarrow{r})}{\delta V_{\text{i}}} \, d^3r \tag{4.9}$$

where Ω is the semiconductor volume, and the excess free carrier concentration ρ is evaluated by solving the associated continuity equation [162]. Therefore, the carriers' mobility, diffusivity, and lifetime, as well as the electric field's intensity and geometry, determine the induced charge pulse described in eq. 4.9. However, it is worth noting that the eq. 4.7 and 4.9 have been obtained based on the superposition principle, i.e., on the linearity of the differential equations for the electrostatics and the charge transport; consequently, only light ion probes can be described since plasma delay or funneling effects when heavy ions are used are not properly taken into account in the Schokley-Ramo-Gunn approach. They are usually indeed treated with numerical methods [163]. Finite element methods can be used for moderately complex devices. For the physics-based modeling, two main ingredients are used: Poisson's equation to describe the relation between the electric field and the charge density and the carrier dynamics to account for the proper response of the charge carriers to the electric field [164]. The electrostatic potential of the semiconductor volume Ω is hereby defined as:

$$\nabla^2 \Phi(\overrightarrow{r}) = -\frac{\rho(\overrightarrow{r})}{\epsilon} \tag{4.10}$$

where ϵ is the dielectric constant of the semiconductor and

$$\rho(\overrightarrow{r}) = q[N_{\text{D}} - N_{\text{A}} + p(\overrightarrow{r}) - n(\overrightarrow{r})] \tag{4.11}$$

is the charge density, including the contribution of acceptors N_A and donors N_D distributions and free electrons $n(\overrightarrow{r})$ and holes $p(\overrightarrow{r})$. To obtain the electron and hole densities, the relative continuity equations must be solved:

$$\frac{\delta n}{\delta t} = \nabla[D_{\mathrm{n}}\nabla n(\overrightarrow{r}) + \mu_{\mathrm{n}}E(\overrightarrow{r})n(\overrightarrow{r})] - \frac{\Delta n}{\tau_{\mathrm{n}}} \tag{4.12}$$

$$\frac{\delta p}{\delta t} = \nabla[D_{\mathrm{p}}\nabla n(\overrightarrow{r}) + \mu_{\mathrm{p}}E(\overrightarrow{r})n(\overrightarrow{r})] - \frac{\Delta p}{\tau_{\mathrm{p}}} \tag{4.13}$$

being $\tau_{\mathrm{n,p}}$ the lifetime of free electrons and holes and the Shockley-Read-Hall (SRH) terms linearized (lifetime approximation [164]). Assuming ohmic contacts (Γ_0) at the electrodes and semiconductor/insulator interfaces at the boundaries (Γ_{i}), $\mathrm{n}_0(\overrightarrow{r},\mathrm{t}) = \mathrm{N}_{\mathrm{D}}$ and $\mathrm{p}_0(\overrightarrow{r},\mathrm{t}) = \mathrm{N}_{\mathrm{A}}$ $\forall$ t and $\overrightarrow{r} \in \Gamma_0$, where $\mathrm{n}_0(\overrightarrow{r})$ and $\mathrm{p}_0(\overrightarrow{r})$ are the carrier concentration at the equilibrium. Conversely, $\overrightarrow{n}\cdot \nabla\mathrm{n}(\overrightarrow{r},\mathrm{t}) = \overrightarrow{n} \cdot \nabla\mathrm{p}(\overrightarrow{r},\mathrm{t}) = 0$, $\forall$ $\overrightarrow{r}$, $\mathrm{t} \in \Gamma_{\mathrm{i}}$, being $\overrightarrow{n}$ the normal vector to the boundary surface $\delta\Omega$.

4.2.2 An IBIC experiment for the in-situ measurement of the ion beam resolution

As previously discussed, MeV probe ion beams represent a powerful resource for characterizing semiconductor materials and devices. Additionally, they are an appealing and versatile tool for modifying and functionalizing solid-state materials. Equally important is the single-defect engineering developed in the last decades, which relies on the controlled introduction of individual dopants by ion implantation [165]. The latter, along with the functionalization of materials at the nanoscale [166], has significantly benefited from the steady improvements in the focusing and collimation of ion beams. Indeed, the availability of **tools for accurately controlling the beam size** and **its resolution** becomes crucial in processing involving the employment of MeV beams whose spot sizes approach the nanometre scale. So far, STIM (Scanning Transmission Ion Microscopy) and PIXE (Particle-Induced X-ray Emission) are the main techniques commonly implemented by the scientific community. Since they rely on the imaging of patterned standards to access the beam resolution [167], e.g., TEM grids, a **dedicated reference standard typically different from the sample to be processed is required**. Moreover, a **separate measurement system** and ion currents ranging from nA (as for PIXE) to fractions of fA (as for STIM or other single-ion detection techniques) are needed. To overcome these possible limitations to the accuracy of the beam size estimation at sub-μm scales and in the perspective of **practical and automated functionalization processes** when high positional accuracy and precision are demanded, a new method for **the evaluation of the resolution of low energy micro beams has been investigated in this Thesis work**. Specifically, the **sample target is exploited as a diagnostic tool for the real-time assessment of the ion beam resolution**. The proposed case study assesses the possibility of gaining spatial information on the size of a 2 MeV Li+ ion micro-beam by realizing a dedicated IBIC experiment. In particular, the in-situ measurement of the ion beam

resolution is discussed based on a new concept of spot size monitor represented by a Si photodiode nano machined via FIB milling. CCE measurements on the machined structures revealed, in fact, a spatial correlation between the induced charge pulse amplitudes and the micromachined structures, which were used to estimate the resolution of the probing beam. For the experiment, a *TO-5 packaged S1223* Si PiN photodiode by Hamamatsu was used [168]. The reverse engineering through capacitance-voltage measurements allows us to infer an almost constant donor concentration $\sim 7 \cdot 10^{13} cm^{-3}$. Conversely, the spreading resistance profiling revealed a 0.6 μm thick p+ layer with a maximum acceptor concentration of $2 \cdot 10^{19} cm^{-3}$. During a preliminary experiment using a MeV proton beam focussed at different incident angles, the dead layer thickness was measured by Angle-Resolved IBIC [169] and resulted in 180 nm. To properly mill the active area of the photodiode, the borosilicate cover window of the TO-5 packaging was removed. The diode milling was performed by scanning a 30 keV Ga+ focused ion beam across the diode surface, corresponding to an ion current of around 10 nA and an upper limit in the beam resolution of 100 nm. The fabricated sample resulted in the cross-shaped structure reported in Fig. 4.19.a, acquired with Scanning Electron Microscopy (SEM) and showing several individual square hollows together with additional alignment triangles. A picture of the tilted sample (52°, Fig. 4.19.b) was also acquired to evidence the selective removal of ~ 4 μm of material and verify the formation of sharp hollow sidewalls within the <100 nm FIB spatial resolution. To verify the compatibility of the milling process with the IBIC protocol, the current voltage characteristic of the diode was acquired before and after the fabrication procedure. From Fig.4.20, it is evident that the micromachining left almost unaffected the forward current, while an increase of the leakage current under reverse bias from ~ 1 nA to ~ 200 nA was registered. Nevertheless, this value did not hinder the IBIC measurements since the signal-to-noise ratio and the preserved signal quality from a pristine region proved to be compatible with the IBIC investigation.

Photocurrent analysis

Under photocurrent analysis, a preliminary assessment of the response to the micro-machined structure was explored. In particular, a 445 nm excitation laser with 2 mW power was used, and the laser-induced current was mapped as a function of the position of the incident beam in a custom confocal microscopy setup, exploiting the <100 nm positional accuracy in the sample positioning and a ~ 1 μm laser spot size upon focussing on the sample surface through a 100x 0.95 N.A. air objective. The photocurrent was measured with a 6487 Kithley picoammeter, and Fig. 4.21.a reports the typical photocurrent map of a 100x100 μm^2. From Fig. 4.21.b the intensity drop of the photocurrent signal is visible in correspondence with the 3 μm and 1 μm side FIB-machined hollows; the large numerical aperture of the confocal microscope objective causes indeed the strong defocusing of the laser beam

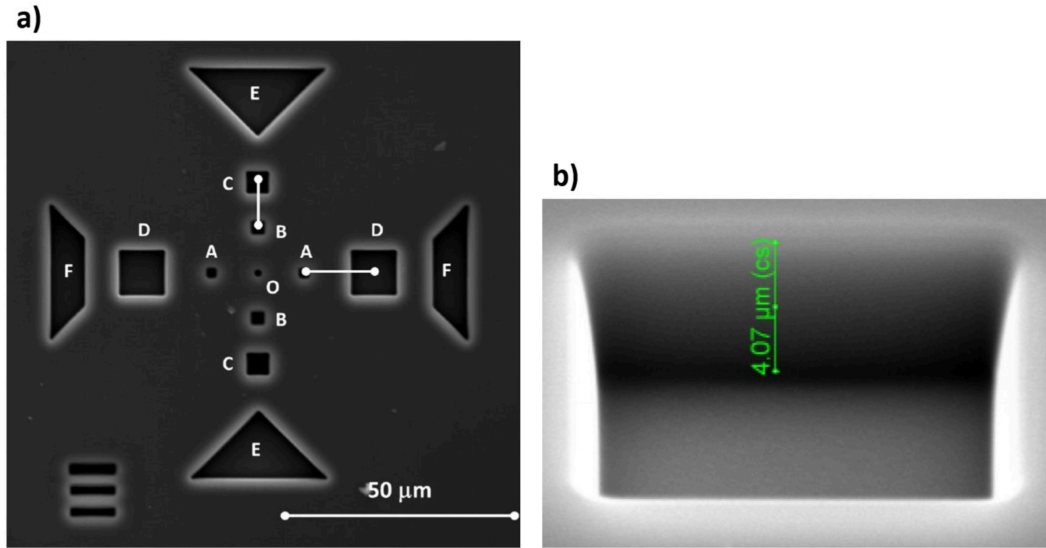

Figure 4.19: a) SEM image of the diode displaying the set of FIB-machined hollows. The nominal sizes of the square edges are 1 μm (O), 2 μm (A), 3 μm (B), 5 μm (C) and 10 μm (D). The distance of the centers of the structures O-A, O-B, B-C is 10 μm; A-D is 15 μm. The distance of the vertices of C-E and the edges of D-F is 10 μm. b) Cross section of a 10x10 μm^2 hollow sidewall in the 52° tilted sample.

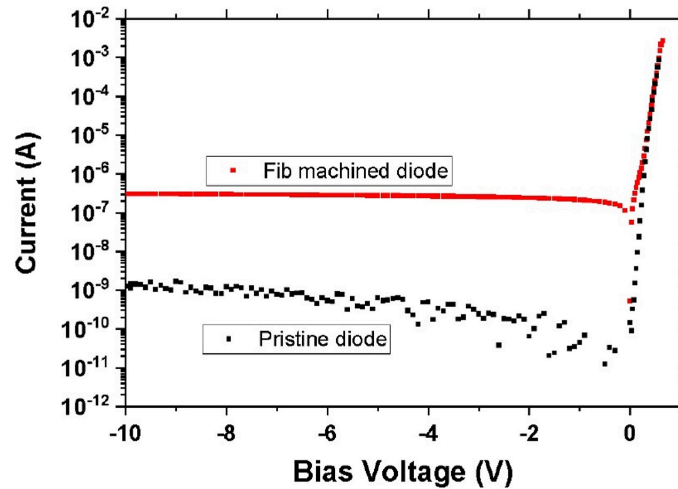

Figure 4.20: Current-voltage characteristic of the FIB-milled diode before and after the fabrication process.

cone with respect to the focal plane whose spot size is estimated to be $\sim$ 26 μm at a depth of 4 μm (fig. 4.22). Based on the regression of the data fitted with error and complementary error functions, the sudden drop of the signal was exploited to

obtain the beam spot size, which resulted in a FWHM = (0.8 ± 0.4) μm from the first derivative of the fitting curve, consistently with the value reported for other PL experiment carried out on the same experimental setup [16]. The procedure represents the commonly adopted analysis to estimate the beam spot size based on reference mesh grids [167].

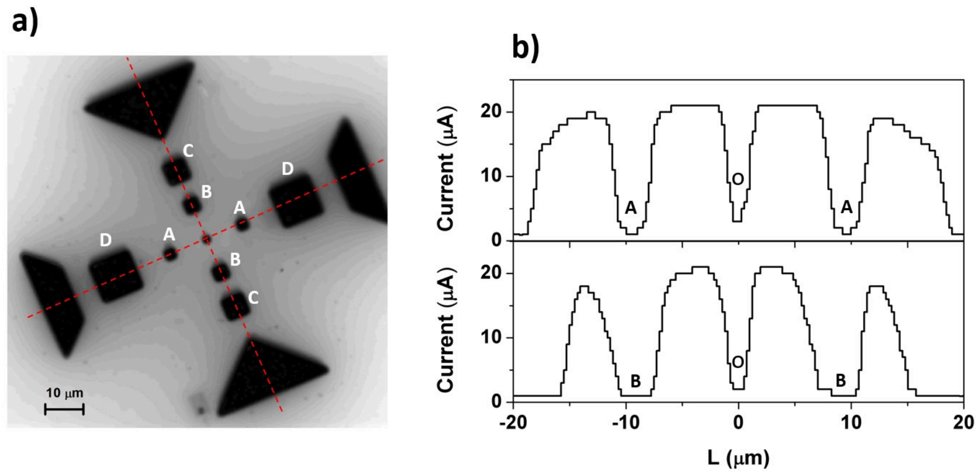

Figure 4.21: a) Photocurrent map of 200x200 μm^2 The measured photocurrent at each map pixel was encoded in a greyscale scale. b) Photocurrent 1-D profiles extracted from the two symmetry axes of the FIB-machined device, highlighted in red in fig a). L represents the distance from the central hollow.
The letters refer to the FIB-milled structures as labeled in the SEM picture in Fig. 4.19

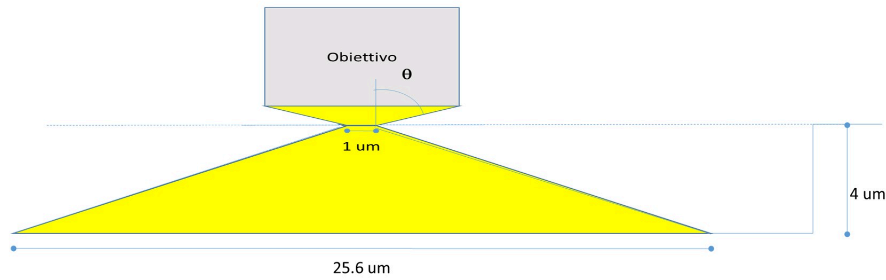

Figure 4.22: Strong defocusing of the laser beam with respect to the focal plane, resulting in a spot of ∼ 26 μm in correspondence of the FIB-milled hollows. Due to the edges of the hollows, most of the light gets scattered and absorbed, leading to a decrease in the intensity of the photocurrent.

Ion beam microscopy

Before the IBIC measurements, the estimation of the beam spot size was investigated following a conventional procedure among the scientific community represented by the Scanning Transmission Ion Microscopy (STIM) based on a standard reference consisting of a 400 mesh copper grid. The STIM and IBIC measurements were carried out at the Laboratory for Ion Beam Interactions of the Ruđer Bošković Institute, where a combination of fine apertures and magnetic quadrupoles enable the focusing of the ion beam, achieving a micrometer spatial resolution. A 2 MeV Li^+ micro ion beam was raster-scanned over the sample surface, being the penetration depth in silicon compatible with the depth of the FIB-milled hollows (fig. 4.23), thus allowing the investigation of their complementary volume.

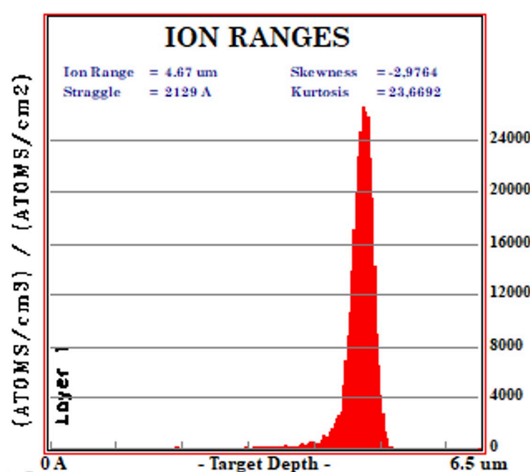

Figure 4.23: Average projective range of 2 MeV Li ions in Si calculated with SRIM. 2500 events have been simulated in 6.5 μm Si substrate. The interactions have been calculated according to a detailed modeling of the damage, where the simulation keeps track of every recoiling atom until its energy drops below the lowest displacement energy of any target atom.

A standard charge-sensitive electronic chain processed the charge pulse generated by each incident ion, including:

- an AMPTEK 250, which is an ultra-low noise (<100 electrons rms at room temperature) charge-sensitive preamplifier for a wide range of detectors with capacitance from less than one to several thousand picofarads. It has a fast rise time (2.5 ns at 0 pF), allows both positive and negative signal processing, and for optimization across various applications, users can choose the input field effect transistor, which is external to the package.
- an ORTEC 570 general-purpose amplifier for energy spectroscopy with all types of detectors characterized by low-noise (<5μV for unipolar output,

shaping time $\geq$ 2 μs, coarse gain $\geq$ 100) and wide gain range (continuously adjustable from 1 to 1500)

Fig. 4.24 displays the IBIC-induced charge pulses spectra resulting from the aforementioned electronic chain and acquired from a pristine region of the FIB-machined photodiode under different biasing conditions, displaying a FWHM of 32 keV for 14.5 bias voltage ($\sim$ 4 channels), close to the resolution estimated in [168], herby confirming the compatibility of the FIB-milling process with the IBIC investigation. Moreover, the electrostatic conditions discussed in this work (i.e., 2.7 V reverse bias) correspond to an induced charge pulse height of channel $\sim$230, corresponding to a signal-to-noise ratio of $\sim$8 with respect to the noise floor at channel $\sim$30. The SPECTOR data acquisition system allows storing each event along with its ion beam coordinates [170]. The STIM map of a 400 mesh copper grid is illustrated in Figure 4.25. On the right, the extrapolated 1-dimensional profiles are reported, corresponding to the highlighted yellow region on the left map. These profiles have been fitted using a combination of error and complementary error functions indicated by the dashed red line. The beam spot size was hence quantified (2.3 $\pm$ 0.6) μm from the first derivative of the fitting curve. Fig. 4.26 reports the CCE maps

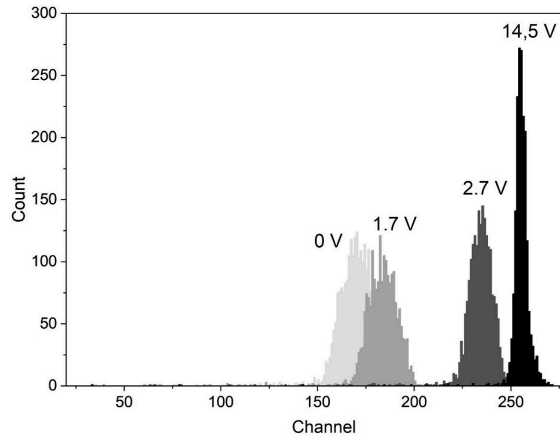

Figure 4.24: Charge pulses spectra acquired from a pristine region of the FIB-machined photodiode under different biasing conditions. For 2.7 V reverse bias, an induced charge pulse height of channel $\sim$230, corresponding to a signal-to-noise ratio of $\sim$8 with respect to the noise floor at channel $\sim$30, is observed. The CCE spectrum reveals an FWHM corresponding to 32 keV in full depletion condition.

acquired under 0 V (a) and 2.7 V reverse bias voltage (b). Based on the assumption that electrons and holes are completely collected when generated in the pristine depletion region, these latter have been obtained from the IBIC maps, dividing the median channel of each pixel by the peak channel corresponding to the signal collected in the pristine region. A greyscale was used to encode the signal. By doing

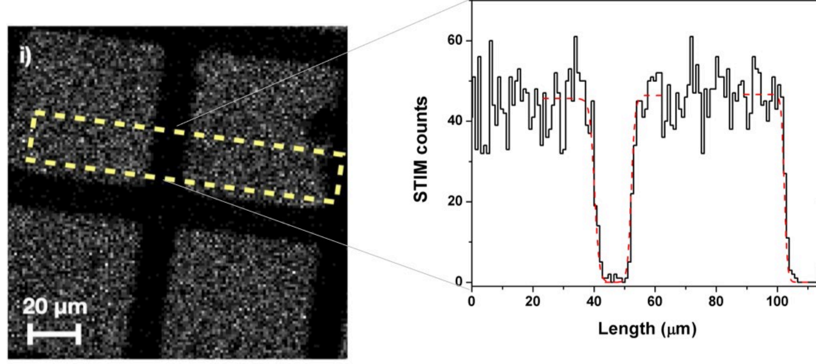

Figure 4.25: The image on the left displays the STIM (scanning transmission ion microscopy) map of a 400 mesh copper grid acquired using a 2 MeV Li focus ion beam. The image on the right shows the profile (black line) of the STIM counts from the highlighted yellow region in the left picture. The red dashed lines represent the corresponding sigmoid fitting curves.

so, it is possible to distinguish the shapes of the FIB-milled hollows. The lines highlighted in color and running along the symmetry axis of the squared hollows represent the CCE 1-D profiles plotted on the right of the maps. In contrast, the color scale identifies the value of the CCE for each pixel (0.4 μm and 0.23 μm side for 0 V and 2.7 V, respectively). At the edge of the hollows, an abrupt decrease in the signal is observed, such as in the case of the photocurrent analysis. However, quite unexpectedly, the signal significantly recovers its amplitude in the center of the hollows. Moreover, the visibility of the peak turns out to be dependent on the applied bias and the hollow size. An in-depth investigation of the reasons behind this behavior has been carried out through the use of finite element analysis and will be discussed in the following section. For the regression of the data, this time, a combination of error and complementary error functions together with Gaussians enables replicating the trend at the edges of the hollows and the peaks at the center (red curves). Again, the ion beam size was estimated through the FWHM of the first derivative of the erf's and erfc's functions. Two values were obtained for the vertical and horizontal 1-D profiles, (1.6 ± 0.2) μm and (1.97 ± 0.10) μm, respectively. The slight discrepancy is in line with the non-uniform CCE distribution in the center of the hollows, and considering the smallest one, 1μm side, which allows setting up an upper limit of 1-2 μm to the ion beam.

Outcomes

Taking into consideration the ultimate resolution limit determined by the lateral straggling of ions in the target substrate [117], the observed results are expected to scale with the ion beam size. Likewise, being the surface-related modification

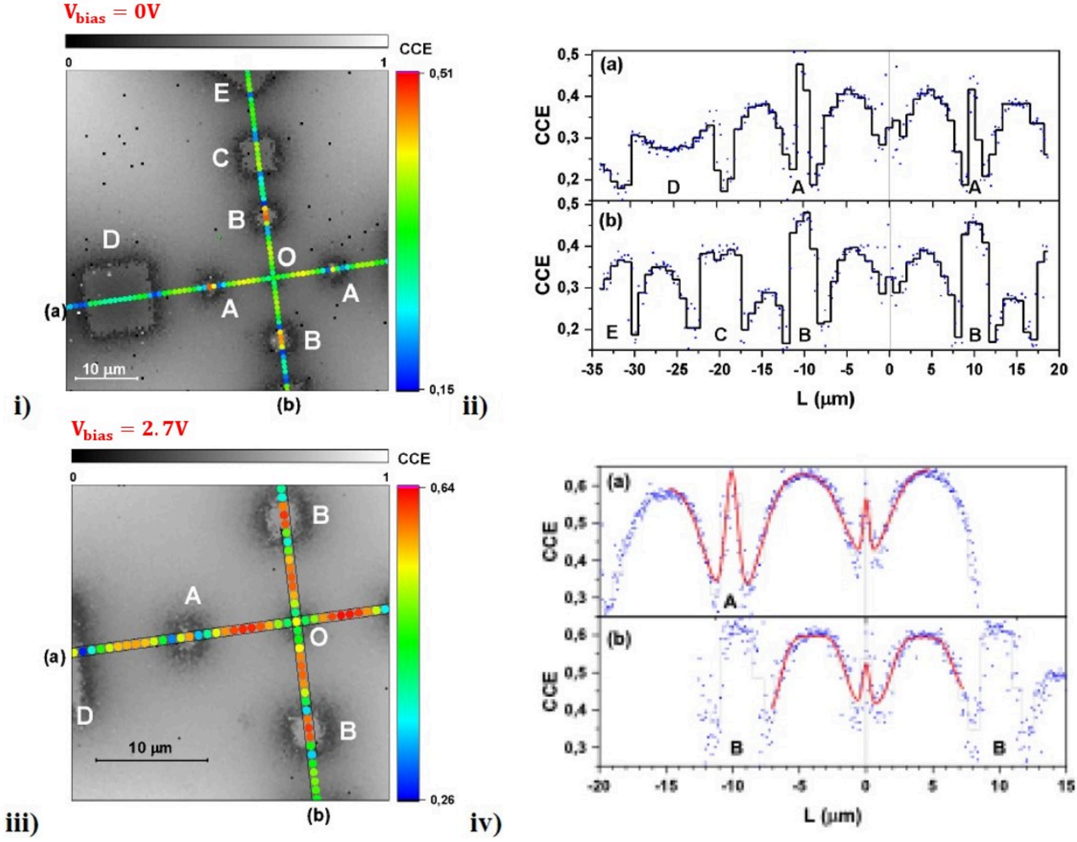

Figure 4.26: IBIC map of 47 × 47 μm^2 acquired using a 2 MeV Li ion beam from the FIB-machined device under 0 V (i) and 2.7 V (iii) bias conditions. The letters refer to the structures labeled in Fig. 4.19. The map displays the median IBIC signal of the pixels in the top grayscale. The colored markers along the two perpendicular stripes (a and b), which are 0.8 μm wide, indicate the median IBIC signal. The color scale on the right shows the range of the IBIC signal distribution, with the minimum and maximum values representing the 1st and 99th percentile of the distribution for the pixel in stripes (a) and (b). The plot on the right (ii and iv) displays the median IBIC profiles extracted from each individual pixel in the stripes (a) and (b). The abscissa L represents the distance from the central hollow. The red curve fits the experimental data with a combination of error and complementary error functions.

of the internal electric field lines more pronounced at lower energies, the spatial dependence of the CCE would be particularly enhanced in the keV range, which is the energy range of interest in recent deterministic ion implantation experiments [128], [90]. Furthermore, utilizing IBIC methods on nm-thick hollows may benefit from the lack of a separate reference standard and the associated limitations, such as the lack of X-ray production for PIXE (Particle-Induced X-ray Emission) or the

sensitivity to elastic scattering with the grid edges for STIM (Scanning Transmission Ion Microscopy), thus avoiding to invalidate the accuracy of beam resolution assessment. In confirmation of this, the beam size estimated from the IBIC profiles was lower than the STIM analysis, thus suggesting that the method could offer higher accuracy in estimating the actual value. The suggested approach can serve as a reliable technique for testing the spatial resolution of ion microbeams in experimental settings. This could prove to be particularly valuable in applications where precise in situ monitoring is required, such as deterministic ion implantation, micro-radio dosimetry, or micro ion lithography [171], [172], [173].

4.2.3 Numerical tool for device simulations

Numerical modeling is a powerful tool that provides access to several quantities that allow the understanding of the devices' behavior and the optimization of their electrical characteristics. As anticipated, modeling an actual device relies on defining a geometry domain and a suitable set of physics-based differential equations representing the dedicated transport model. Maxwell's equations provide the precise framework for electromagnetics, while an accurate model of carrier transport would necessitate a comprehensive quantum description of electrons and holes in the context of wavepackets. Therefore, the system of equations representing the core of the simulation that will be discussed is based on a semiclassical approach represented by the two continuity equations deriving from the standard Boltzmann Transport Equation (BTE) and Poisson's equation, forming the so-called Drift Diffusion (DD) model. The latter, made of two non-linear and one linear equation in four variables, must be necessarily simplified to implement a computer program. For this reason, the Partial Differential Equations (PDEs) are usually discretized in space and time domains to transform them into ordinary differential equations (ODEs). Doing so divides the device geometry into a grid of nodes, and the dynamic transitions are treated as a sequence of quasi-stationary states. Consequently, for each node of the grid, the discretized version of the DD model is used, and the physical quantities are expressed as functions of their nodal values. Two schemes are commonly adopted for discretizing the equations, namely Finite Element (FE) and Finite Difference (FD). Without going into much detail, starting from the Poisson equation in the well-known form (eq. 4.10), it can be demonstrated that a matrix equation is obtained [164]:

$$A \cdot \Phi = f \tag{4.14}$$

where A is the matrix containing the nodal values and opportune weighting functions, whereas Φ and f are the column vectors of the discretized potential and the known term of the PDE, respectively. This latter equation thus represents the discretized Poisson's equation using the FE scheme [164], where the unit elements are the triangular control regions defined by three nearby grid nodes (Fig. 4.27).

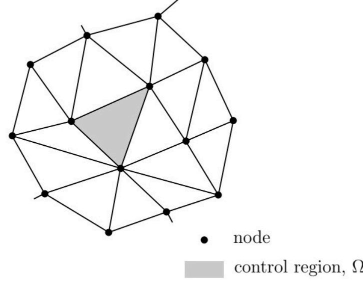

Figure 4.27: Bidimensional representation of Finite Element (FE), from [174]. All physical quantities refer to a control triangle formed by three nearby nodes.

In the following sections, Finite Element Analysis will be reported in the context of the IBIC technique, unlocking the physical investigation of the experimental evidence reported in section 4.2.2. This technology would indeed undoubtedly aid in handling the design optimization of a dedicated radiation sensor for the response signal produced by keV ion implantation, thus representing a powerful and potentially consolidated approach for the **design optimization of the target** itself as a **solid-state particle sensor** for the **deterministic positioning of single ions**.

Simulation of the IBIC signal

To understand the reasons behind the experimental evidence reported in section 4.2.2, simulations of induced charge have been conducted using the COMSOL 3.5a software based on the IBIC theoretical model [161], [175]. The diode electrostatics were determined by solving Poisson's and continuity equations starting from the previously evaluated doping profile using the spreading resistance profiling [168], Fig. 4.28. The boundary conditions normally used to simulate semiconductor devices were applied [162]: Dirichlet-type conditions for the fixed voltage at the top and back (grounded) contacts and homogeneous Neumann conditions on the insulating sidewalls of the hollow. Besides this, due to the Ga ions implanted during the Focused Ion Beam implantation, the bottom of the hollows are assumed to be electrically charged, consequently requiring inhomogeneous Neumann-type boundary conditions:

$$-\overrightarrow{n} \cdot \overrightarrow{D} = \sigma \tag{4.15}$$

where $\overrightarrow{n}$ is the unitary vector normal to the semiconductor surface, $\overrightarrow{D}$ is the displacement vector, and σ the surface charge density. It is worth noting that the value of this surface charge σ was assumed as a free parameter for the finite element simulations. Finally, FIB-induced structural stress affecting the transport and recombination dynamics of the semiconductor has not been considered, and a carrier lifetime of tens of μs, along with a conventional expression for the carrier

mobilities, were adopted. Conversely, at the hollows' edges, an infinite recombination velocity was assumed justified by the micromachining damage. Fig. 4.29

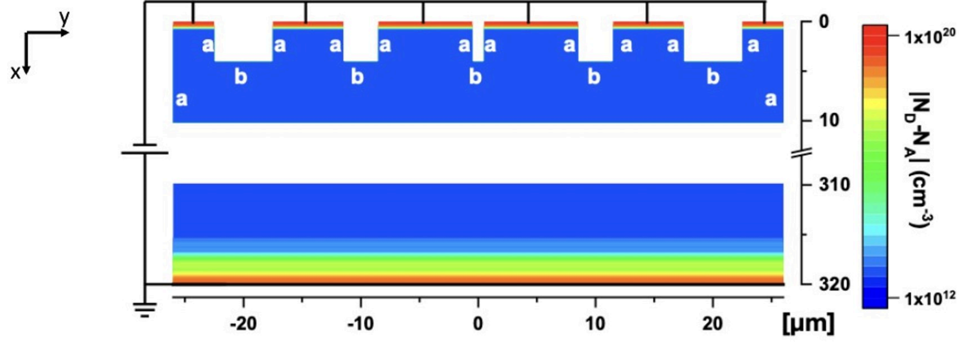

Figure 4.28: The figure shows a two-dimensional scheme of a diode, with hollow squares labeled according to Fig. 4.19. The contour plot shows the absolute doping concentration, represented by the color scale on the right. "ND" indicates the donor concentration, while "NA" indicates the acceptor concentration. At the bottom of the hollows, the various types of boundaries of Poisson's equation are identified by "a" (homogeneous Neumann boundary condition) and "b" (inhomogeneous Neumann boundary condition for taking into account a surface charge density). The diode is reverse polarised with the bottom electrode grounded.

exhibits the contour plot of the Gunn potential described in eq. 4.7 for $\sigma = 0$ and $\sigma = 16$ nC cm^{-2} under 0 V applied bias. The latter was fixed at $\sigma = 16$ nC cm^{-2} based on the better agreement between the simulated CCE profiles and the experimental ones displayed in Fig. 4.26. It is evident that for $\sigma = 0$, Gunn's weighting potential (Φ) is at its maximum at the top electrode but almost non-existent beneath the hollows. Therefore, since the induced signal is determined by the difference in Φ between the initial and final position of the moving charges, and the device collects holes, if these latter are generated at the bottom of the hollows and subsequently drift to the top sensitive electrode, they contribute to charge induction [161]. Worthy of particular attention is that the equipotential lines at the base of the hollows are quite widely spaced when the value of σ is equal to zero. This suggests that the electric field strength in this area is comparatively low. Oppositely, when a surface charge $\sigma = 16$ nC cm^{-2} is simulated at the bottom of the hollows, the lines gather densely, resulting in more significant contributions to the induced signals from the minority carriers.

Instead of solving the equations 4.12 and 4.13 to substitute the current density in eq. 4.9 and thus evaluating the induced currents at the electrodes, a more efficient method can be exploited to directly calculate the CCE at the i-th electrode and as a function of the charge generation point. The method relies on the utilization of Green's function to solve the non-homogeneous continuity equation for the excess

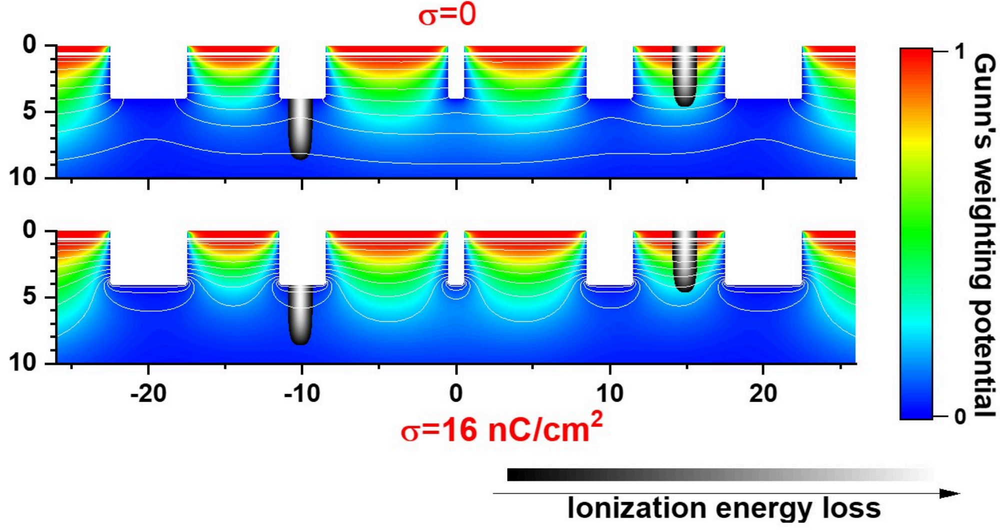

Figure 4.29: Contour plot of Gunn's weighting potential evaluated with COMSOL simulations for two different surface charges, $\sigma = 0$ on the top and $\sigma = 16$ nC cm^{-2} on the bottom. The device profile includes the hollows C, B, O, B, and C (see labels in Figure 4.19). The white lines represent the electrostatic potential at null bias voltage. The ionization profile of incident 2 MeV Li ions is represented in a greyscale plot on two positions: onto the surface and the bottom of the hollow structure B (see labels in Figure 4.19).

charge carrier concentration. It was formulated by T. H. Prettyman [176] and proposed by E. Vittone [161] as a tool to simulate the charge pulses induced by the drift and the diffusion of excess charge carriers in IBIC experiments with partially depleted semiconductor devices, under routinely adopted assumptions for semiconductor devices' analysis. If the semiconductor operates in steady-state mode, meaning the charge generated by the radiation interactions does not significantly perturb the electric field, the continuity equations can be decoupled from Poisson's equation. Additionally, due to the lower excess carrier concentration compared to the number of trapping and recombination centers and the shorter trapping time compared to the transit time, the generation and recombination terms can be linearised [176]. Under these assumptions, the equation for excess carrier within the semiconductors is obtained by adding a source term G to the second member of equations 4.12 and 4.13:

$$G = \delta(r - r')\delta(t) \tag{4.16}$$

which is chosen to be an impulse of unit charge for mapping charge pulses [177]. In this way, the charge collection efficiency is determined as:

$$\eta_{\mathrm{n/h}} = Q_{\mathrm{e/h}}(t)/q \tag{4.17}$$

where q is the charge of a single carrier, and Q is the induced charge determined by equation 4.9. Therefore, it is worth noting that the charge collection efficiency is represented by Green's function for the electron/hole continuity equations (4.12, 4.13). In this way, it can be demonstrated that an adjoint continuity equation can be constructed since the excess carrier continuity equation involves linear operators. By doing so, a point-like electron excess carrier concentration generated at t_0 and position x_0 is characterized by a temporal evolution of the total charge collection efficiency represented by the equation [177]:

$$\frac{\delta n^+}{\delta t} = -\mu_\mathrm{n}\overrightarrow{E}\nabla n^+ + \nabla\cdot(D_\mathrm{n}\nabla n^+) - \frac{n^+}{\tau_\mathrm{n}} + {G_\mathrm{n}}^+ \tag{4.18}$$

where n^+ is the adjoint electron concentration, and ${G_n}^+$ is the adjoint generation term to be determined, imposing suitable physical constraints. For instance, if it is selected to be [177]:

$${G^+}_\mathrm{n} = \mu_\mathrm{n}\nabla\Phi\cdot\nabla\Phi_\mathrm{k} \tag{4.19}$$

where the variable Φ represents the potential of the semiconductor volume, as determined by the equation 4.10, and Φ_k is the weighting potential solved by the Poisson equation when the electrodes connected to the selected circuit k are held to a unit potential, while all other electrodes are grounded. A similar expression can be derived for the holes with the same interpretation. Hereby, to determine all the pulses a detector can produce for a selected circuit and charges at discrete locations, the time-dependent adjoint continuity equation can be solved. In this regard, Figure 4.30 shows the simulated electrons and holes contributions to the total CCE obtained with the adjoint equation for a null bias voltage and considering two different surface charge densities, $\sigma = 0$ on the left and $\sigma = 16$ nC cm^{-2} on the right. In particular, the induced charge profiles have been simulated by considering the contribution of any carrier generated along the trajectory of ions scanning along the y-direction, representing the direction parallel to the surface. The ion beam is directed towards the nominal position at y = ξ, and the resulting electron-hole generation profile Γ can be obtained by convolving the SRIM-normalized ionization energy loss profile S(x,y) with the Gaussian profile G(y,ξ), which is centered at y = ξ. Therefore:

$$\Gamma(x,y,\xi) = \int dy'\cdot G(y-y',\xi)\cdot S(x,y') \tag{4.20}$$

Being the depth of focus of the ion microbeam focusing system typically much larger than the depth of the hollows (4 nm) [152], the beam shape Γ(x; y; ξ) can be assumed to be unaltered regardless of the incident position. To estimate the induced charge profile, the generation profile Γ is then integrated over the entire semiconductor volume by the CCE, resulting in:

$$P(\xi) = \int dx \int dy\cdot CCE(x,y)\cdot\Gamma(x,y,\xi) \tag{4.21}$$

The graphs at the bottom of figure 4.30 display the simulation results adopting a bias voltage of V = 0 and a Gaussian beam with FWHM = 0.5, 1, 2.0 μm. The contribution of electrons to the induced charge is only slightly affected by the surface charge introduced by the Ga ions machining at the bottom of the hollows. On the other hand, holes effectively drift to the top electrode due to the electric field induced when $\sigma = 16$ nC cm^{-2}. This results in a higher CCE beneath the hollows. Moreover, in light of the observations mentioned above, it can be concluded that in the former case, the amount of induced charge collected when the ion hits the hollow is low. On the other hand, in the case where $\sigma = 16$ nC cm^{-2}, the profiles show peaks at the center of the hollows. These peaks are in good agreement with the experimental profile shown in Fig. 4.26, where IBIC peaks are visible at the O, B, and C hollows. Finally, the appearance of peaks at the central 1×1 μm^2 hollow in both the experimental and simulated profiles for different FWHM provides an upper limit of 2 μm for the FWHM of the ion microbeam.

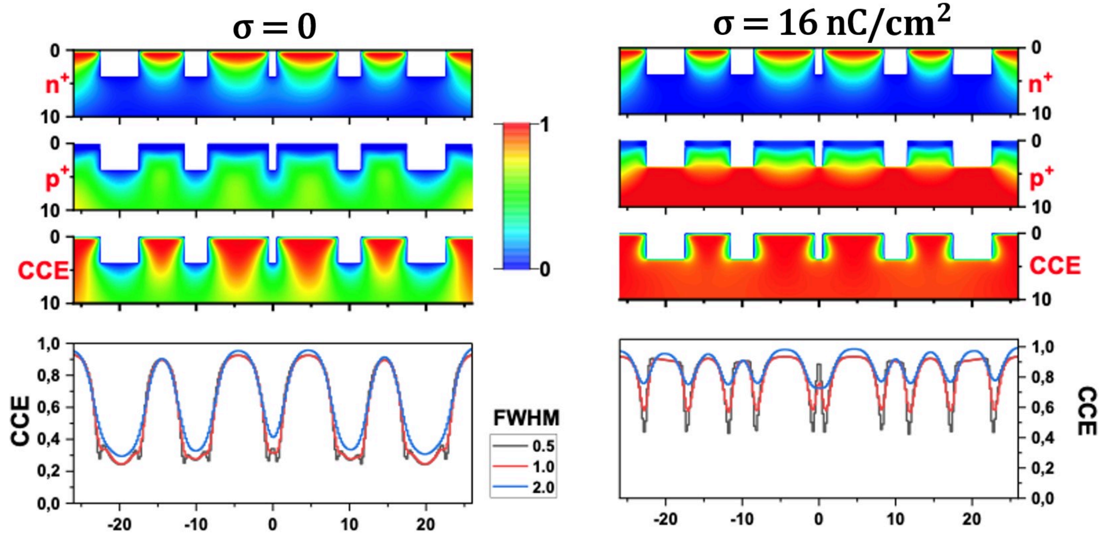

Figure 4.30: Simulated electrons n$^+$ (top), holes p$^+$ (middle) contributions to the total CCE maps (bottom). The depicted structures are C, B, O, B, and C, labeled according to Fig. 4.19. The surface charge at the bottom of the hollows is assumed to be zero ($\sigma = 0$) on the left and $\sigma = 16$ nC cm^{-2} on the right. The bias voltage is null, and the plots at the bottom are the induced charge profiles calculated from the above CCE maps and the ionization profiles reported in Fig. 4.29. The profiles have been calculated for different values of the centroid of the Gaussian beam, characterized by different FWHM (black, red, and blue curves). All maps and graphs use μm as the unit of measurement.

Yet another proof of the estimated surface charge is reported in Figure 4.31, showing the simulated induced charge profiles at a bias voltage of 2.7 V along the

(a) and (b) stripes, as in the experimental profiles reported in Fig. 4.26. A Gaussian ion beam with FWHM = 1.0 μm is assumed, and qualitatively good matching is achieved between the simulated profiles and the experimental results. The IBIC signals are indeed low at the hollow sidewalls due to high surface recombination velocity, whereas they recover as the charge density increases in the centers of the hollows. It is worth noting that even at zero bias voltage, the surface charge creates an effective electric field that spreads throughout the region being tested by the ions, as shown in Fig. 4.29 and 4.30. Increasing the reverse bias voltage does not indeed significantly improve the movement of carriers produced under the hollows towards the sensitive electrode despite the widening of the depletion layer.

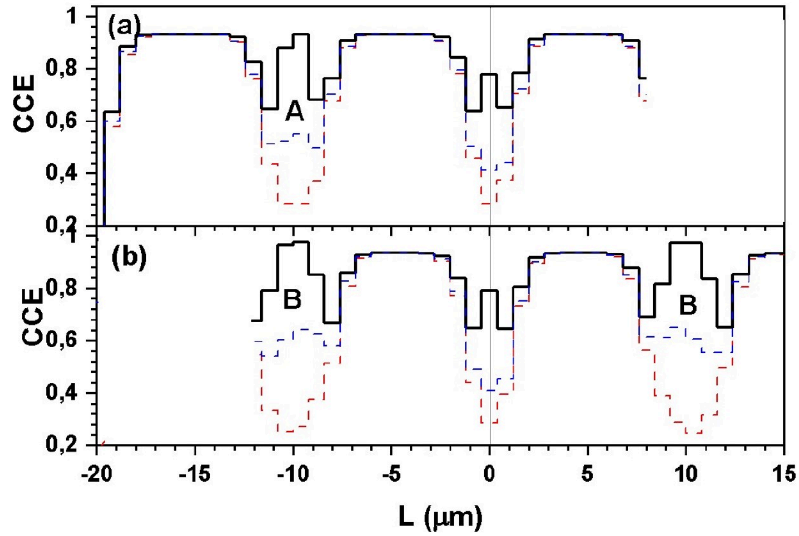

Figure 4.31: Simulated IBIC profiles corresponding to the experimental ones reported in Fig. 4.26 along the (a) and (b) stripes. The bias voltage is 2.7 V, and a Gaussian ion beam with FWHM = 1 μm is adopted. Different surface charge values have been chosen: dotted red line: $\sigma = 0$, dotted blue line: $\sigma = 1.6$ nC cm^{-2}, continuous black line: $\sigma = 16$ nC cm^{-2}. The abscissa represents the distance from the central hollow.

4.3 Color centers activation

The lack of any spectral characteristics associated with carbon-based optically active defects in Figure 4.12 has raised inquiries regarding the most efficient method for generating G centers in high-purity silicon substrates. The kinetic factors involved in the defect evolution thermodynamic pathway, such as activation and

subsequent deactivation at higher annealing temperatures, may prevent the conversion of introduced impurities into stable telecom emitters when using conventional stationary thermal treatments lasting longer than a few seconds (i.e., Rapid Thermal Annealing or furnace annealing). However, the successful implementation of many indistinguishable individual color centers in technology applications will require reliable manufacturing methods. For instance, an in-depth investigation of the microscopic processes occurring during the annealing step is still crucial to overcome the limitations recently highlighted [178] in realizing large-scale arrays of G emitters.

4.3.1 Conventional thermal treatments

Based on the information provided in section 2.3.2, it is clear that the formation of the G center requires two distinct processes. Firstly, the accommodation of C atoms at substitutional lattice sites, and secondly, the creation of interstitial Si atoms. Annealing treatments particularly enhance the migration of the latter and their recombination with the lattice vacancies, thus suppressing their concentration. On the other hand, radiation-induced damage within the crystal promotes the creation of highly mobile interstitial Si. Moreover, the thermal energy provided to the substrate through thermal treatment favors the accommodation of C atoms into substitutional lattice sites. In this regard, the common fabrication protocols adopted in the scientific community since 2020 are summarised in table 4.3.1. The production of the G center has been typically reported in carbon-rich samples ($[C] > 10^{16} cm^{-3}$), obtained either by Czochralski synthesis or by carbon ion implantation or even commercially available Silicon on Insulator (SOI) substrate where the device thickness is typically Czochralski silicon [86], [37], [149], [179]. Subsequently, the substrate is usually processed by conventional thermal annealing and eventually irradiated with protons to provide supplementary interstitial silicon atoms to increase the fabrication process efficiency. Notably, the carbon ion implantation step can be replaced by silicon implantation or single proton irradiation, making the introduction of carbon unnecessary if the native carbon concentration in the substrate is already sufficiently high [90]. As a confirmation, experimental protocols for fabricating this class of emitters were reported under carbon [180] and silicon [90] implantation without the need for a post-implantation thermal treatment. Extensive investigations on the annealing-dependent dynamic in the formation of the G center upon RTA treatment have identified the above-mentioned annealing as the main limiting factor in fully exploiting the promising properties of these systems in the scalable manufacturing of large-scale quantum devices. A schematic view of the commonly adopted experimental procedure is reported in Fig. 4.32, highlighting how the identification of these single-photon sources relies on a purely statistical approach based on purposedly lowering the creation yield. Except for

manufacturing processes where nanofabricated implantation masks or FIB Technology are involved [90], the thermal processing is exploited to reduce the defect density to a single-emitter regime. Moreover, together with a progressive dissociation of the defects evidenced by the decreasing density of quantum emitters, the signal-to-noise ratio of the individual identified emitters has demonstrated a direct connection with the duration of the annealing as well, favoring a longer process to minimize the contribution of the background [178]. Further, the broadening of the ZPL emission, a benchmark in the quality evaluation of the quantum source, has been associated with the duration of thermal treatment after introducing the carbon impurities via ion implantation [178]. The progress dissociation of the defects can be explained, bearing in mind the migration energies of substitutional and interstitial carbon discussed in section 2.2.3, which are 3.15 eV and 0.9 eV, respectively. Thus, the disaggregation of the G centers would firstly go through a conversion of the optically active "B configuration" into the optically inactive "A configuration" with an activation energy of only 0.16 eV [87], i.e., lower than the diffusion activation energy (see section 2.3.2 for more details), and the subsequent stochastic release of interstitial carbon atoms C_i [178]. Proof of the escaping of carbon atoms is the compatibility of the thermal destruction energy of the emitter with the migration energy of C_i [178]. An experimental confirmation of this phenomenon is offered by Secondary Ion Mass Spectrometry (SIMS) measurements of post-annealed samples, which reported a maximum concentration of carbon at both the top and the bottom interfaces [178].

Besides this, a recent theoretical study has pointed out that higher energy structural configurations are kinetically preferred in the temperature region where the G center exists since the defects break up before transforming into the lowest configuration energy [87]. Therefore, the kinetics factor prevents the formation of the theoretically predicted most stable configuration, named "C configuration", which has been calculated to have an activation energy much higher (1.2 eV) with respect to the dominantly occurring bi-stable "A" and "B" configurations (0.3 eV) [87]. Being the activation energy of the C configuration even higher than the silicon band gap, the "C" configuration can not be formed upon non-radiative recombination of electron-hole pairs either. Additionally, the activation energy required to transform the "A" ("B") configuration into the "C" one resulted in much higher energy than the one required to anneal out the carbon-pair defect [87].

4.3.2 Off-equilibrium thermal processing

Since the duration of thermal treatment must be carefully considered, as it can affect the evolution and stabilization of the G center in relation to other defective complexes, in this section, new fabrication strategies that involve dynamic annealing are being explored as a potential alternative to conventional thermal processing. Evidence supporting this claim is found in the lower temperature recorded for the

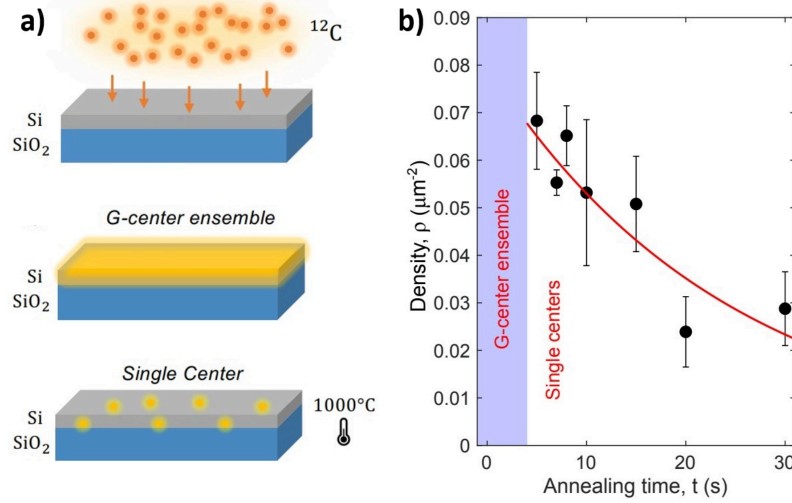

Figure 4.32: Commonly adopted fabrication protocol to create single G emitters with a standard commercial SOI wafer. The implantation results in the formation of a G-center ensemble, and the creation of single-color centers involves rapid thermal annealing for the controlled decrease of the emitter's density. a) Picturesque representation of the process from [178], b) Measurements of the emitters density as a function of the annealing duration ($T_{plateau}$ = 1000 °C) from [178].

Ref	Substrate native C concentration	Ion implantation
[86]	220 nm commercial SOI	C 36 keV $10^{14} cm^{-2}$
[37]	220 nm commercial SOI	C 36 keV $5 \cdot 10^{13} cm^{-2}$
[180]	$< 10^{16} cm^{-3} (1 ppma)$	C 5.5 keV 10^{12} cm^{-2}
[149]	commercial SOI Soitec	C 36 keV $5 \cdot 10^{13} cm^{-2}$
[90]	$> 10^{16} cm^{-3} (1 ppma)$	Si 40 keV $10^{9} cm^{-2}$
[179]	commercial SOI	C 8 keV 0.3 to 300 $10^{11} cm^{-2}$

Ref	Annealing	Co-implantation
[86]	1000°C 20 s (RTA)	500 keV to 2 MeV protons
[37]	1000°C 20 s (RTA)	No
[180]	No	No
[149]	1050 °C 20 s (RTA)	No
[90]	1000 °C 60 s (RTA)	No
[179]	1000 °C 20 s (RTA)	0.3 to 300 $10^{11} cm^{-2}$ protons

Table 4.1: Commonly adopted fabrication protocols for the G center.

annealing out of the W center (400 °C [65], [111]) and G center (250 °C [27])

following conventional rapid thermal annealing, in contrast to the peak temperature estimated in ns-pulsed ion implantation [181]. Additionally, the combination of non-equilibrium processes with μs-long high-power laser along with surface functionalization based on organic molecules has led to the creation of a highly dense ensemble of G centers by promoting the incorporation of carbon atoms above their solubility limit [182]. Therefore, in the perspective of single-defect engineering, in this Thesis work, the fabrication of G centers upon **more responsive thermal annealing** is discussed to exclude a limiting purely statistical approach. **To compensate** for the limitation previously discussed, i.e., the **poor creation yield**, the **loss of photon indistinguishability** [178], the **activation strictly dependent on the native concentrations of the silicon substrate impurities** (see table 4.3.1), the non-invasive and localized efficient activation of G centers in silicon is reported upon high-power ns-pulsed laser processing in C-implanted float zone silicon.

Sample processing

In preparation of the experiment, a sample was cut from a commercial float zone (FZ) silicon wafer (carbon concentration $< 5{\cdot}10^{14} cm^{-3}$) uniformly implanted with 36 keV C^{-} ions at $2 \cdot 10^{14} cm^{-2}$ fluence to introduce the carbon atoms impurities. Based on the lack of observation of spectral features related to the bi-carbon defects in Fig. 4.12, off-equilibrium fabrication strategies were investigated as a valid alternative to access the dynamics of the G defect complexes. In particular, the adopted approach relies on fast heat transients delivered by a focused Q-switched ns-pulsed Nd:YAG 532 nm (second harmonic) Laser Cutting System *EzLaze3* by *New Wave research* characterized by a pulse duration of 4 ns and a repetition rate of 5 Hz. A train of 5 lasing pulses was used to anneal $7x7\ \mu m^2$ regions locally, avoiding any additional thermal treatment besides the one under consideration. A schematic view of the adopted experimental configuration is reported in Fig. 4.33. The primary lens system focuses the source, which is then collimated by an aperture measuring 2.75x2.75 mm^2. Additional X-Y shutters allow to manipulate the beam size from a minimum of $\sim 3x3\ \mu m^2$ up to $50x50\ \mu m^2$. The maximum energy is 0.6 mJ for a 4 ns laser pulse duration, resulting in a maximum power density of 1.32 $MW{\cdot}cm^{-2}$. Moreover, the pulse undergoes further focusing on the sample by a 20x magnification objective. Finally, the sample is mounted on an X-Y μ-positioner with 25 μm sensitivity. Energy densities in the 0.58-1.16 $mJ{\cdot}cm^{-2}$range were selected for the experiment.

The non-stationarity of the process is represented by the heat transient displayed in Fig. 4.34, which is significantly faster than the temperature profile reported in Fig. 4.11. The latter was simulated by finite element analysis using COMSOL 3.5a, where a two-dimensional model with cylindrical symmetry reported in Fig. 4.35

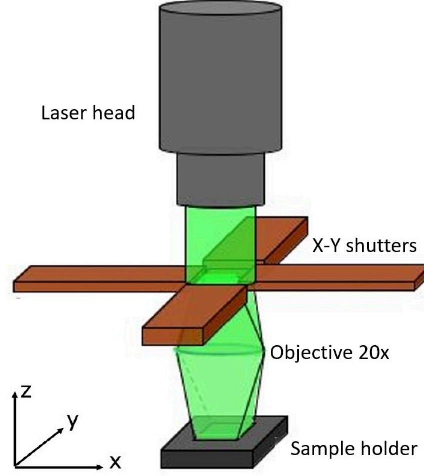

Figure 4.33: Schematic view of the EzLaze3 Laser Cutting System used to develop the local annealing protocol for activating the G centers in silicon.

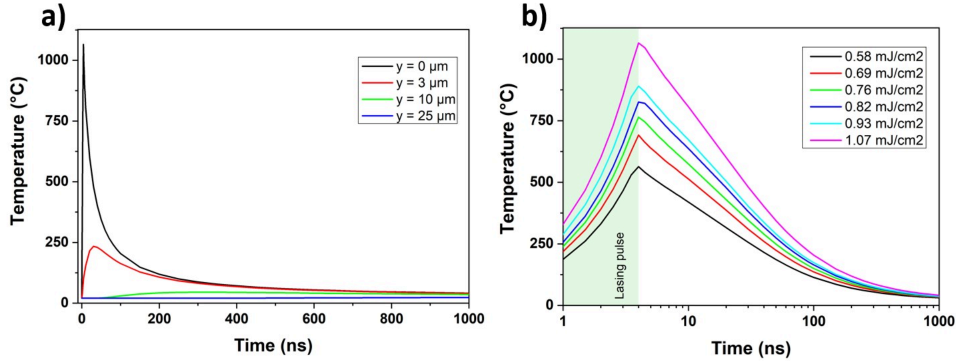

Figure 4.34: Heat transient provided to the silicon substrate upon ns-pulsed laser and simulated with COMSOL 3.5. Plot a) displays the temperature changes at different depths (z = 0 µm, 3 µm, 10 µm, 25 µm) along the symmetry axis of a system (dashed white line in Fig. 4.36), whereas plot b) shows the temperature changes at the surface (z=0 µm) over time for different laser energy densities. A 4 ns long laser pulse is turned on at t=0.

was used to solve the time-dependent equation:

$$\rho \cdot c_{\mathrm{p}} \cdot \frac{\delta T}{\delta t} = \nabla \cdot [K \cdot \nabla T] + S, \tag{4.22}$$

where $\rho = 2330$ Kg·m^3 is the mass density, c_p is the thermal capacitance, K represents the thermal conductivity of isotropic silicon, and S is the source term. Considering x as the propagation direction of the laser beam, the latter describes

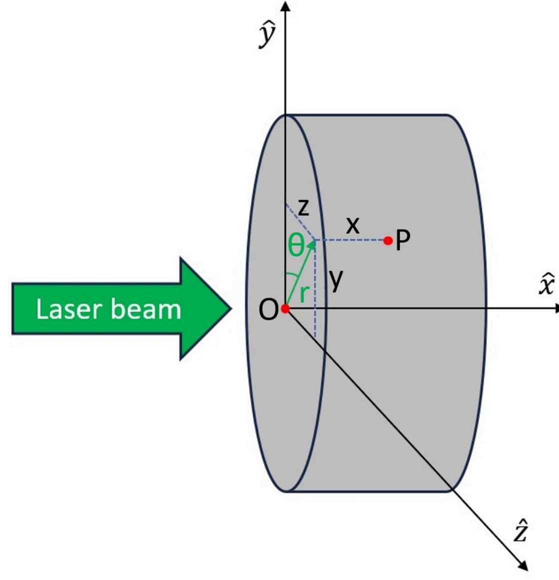

Figure 4.35: The simulation domain used in COMSOL comprises of a cylinder with a radius of 50 micrometers and a thickness of 100 micrometers. The center of the laser spot size corresponds to the origin. Point P can be expressed in Cartesian coordinates (x,y,z) or cylindrical coordinates (x,r,θ).

the heat provided by the lasing pulse, and it is defined as follows:

$$S = D(r) \cdot P(t) \cdot (1 - R) \cdot \alpha \cdot (\alpha - x), \tag{4.23}$$

where D(r) and P(t) are the energy density profile and the temporal profile, respectively. In particular, a Gaussian temporal profile is adopted:

$$P(t) = \frac{1}{\sqrt{2\pi\sigma_{\mathrm{t}}{}^{2}}} exp[-\frac{(t - t_0)}{2\sigma_{\mathrm{t}}{}^{2}}] \tag{4.24}$$

where t_0 is the time instant at which the maximum power is provided (t_0 = 20 ns), and $\sigma_{\mathrm{t}} = \frac{FWHM}{2\sqrt{ln(2)}}$, thus resulting σ_{t} = 1.7 ns. Moreover, the assumed energy density profile is:

$$D(r) = J[\frac{1 - tanh(\frac{r - R_{\mathrm{spot}}}{s})]}{2} \tag{4.25}$$

i.e. a flat profile equal to the J energy density where the multiplied function smoothes the edges of the irradiated regions. Since the beam size is a square with 7 μm side, a circle with area = 49 μm^2 was assumed in the simulations, thus resulting in R_{spot} = 3.95 μm. The initial temperature was fixed to 295.15 K. The thermal capacitance c_p and the thermal conductivity K were set according to reference values [183]. Homogeneous Neumann conditions were applied everywhere except for the

substrate surface, where appropriate boundary conditions were defined to describe thermal convection and irradiation phenomena and to keep the wafer backside at room temperature. The simulated heat propagation dynamics in the silicon substrate offered insight into the quantitative aspects of the off-equilibrium annealing process. Fig. 4.36 reveals the instantaneous temperature maps of the silicon substrate at varying time intervals (4 ns, 40 ns, and 400 ns) following the application of a single 4 ns laser pulse with 1.07 mJ·cm^{-2} energy density. At the end of the pulse

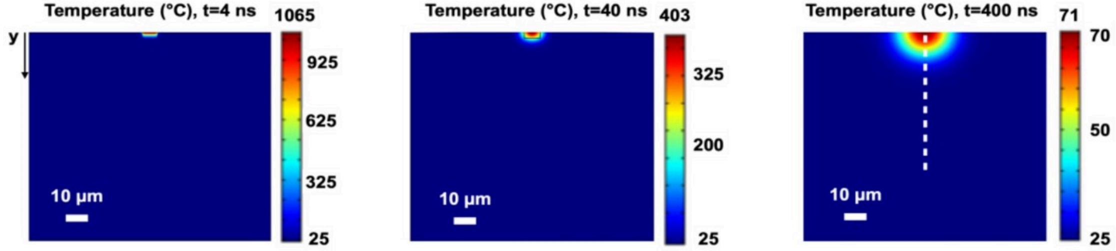

Figure 4.36: Istantaneous temperature maps of the silicon substrate at t=4 ns, t=40 ns and t=400 ns after the 532 nm laser pulse delivery. The heat propagation dynamic has been simulated with finite element simulations in COMSOL 3.5a.

(t=4 ns), the sample surface temperature peaks at 1065°C, which is still well below the melting point of silicon. The laser heating appears confined to the irradiated region, and a sharp temperature gradient extends over a sub-micron scale towards the surrounding environmental conditions. Notably, the annealing effect is strongly limited to the region directly exposed to the laser pulse. Fig. 4.34 a) evidences the localized confinement in depth as well, characterized by a peak temperature of around 250°C for 3 μm depth, which is never exceeded during the whole process. Due to the high absorption coefficient of silicon at 532 nm (i.e., $\sim 10^4$ cm^{-1}) [34], the localization of the heated region extends indeed for the first few hundreds of nm of the material. Finally, the process does not involve local silicon recrystallization, as seen in Fig. 4.34 b), where the temperature peaks are shown for the whole range of energy density values. As highlighted by the latter, of particular relevance is the sub-μs time scale of the entire thermal treatment within the silicon substrate returns to the environmental conditions, thus allowing to consider each lasing pulse with a frequency of 5 Hz as fully independent thermal processing. Up to 1 MHz, the laser annealing can indeed be reiterated until a satisfactory activation of the optical active defects is reached.

Optical characterization

To access the physical properties of the processed sample, the carbon implanted regions exposed to the laser processing were investigated upon PL spectroscopy using the cryogenic confocal microscope optimized for telecom wavelengths and

discussed in Chapter 3. All the measurements were acquired at 10 K and upon continuous wave laser excitation at 488 nm. In this case, a combination of a 700 nm long-pass dichroic mirror and an 800 nm long-pass PL filter enables the radiation collection in the interested spectral range. A typical PL map of the processed sample is reported in Fig. 4.37. The latter displays a low-luminescence background

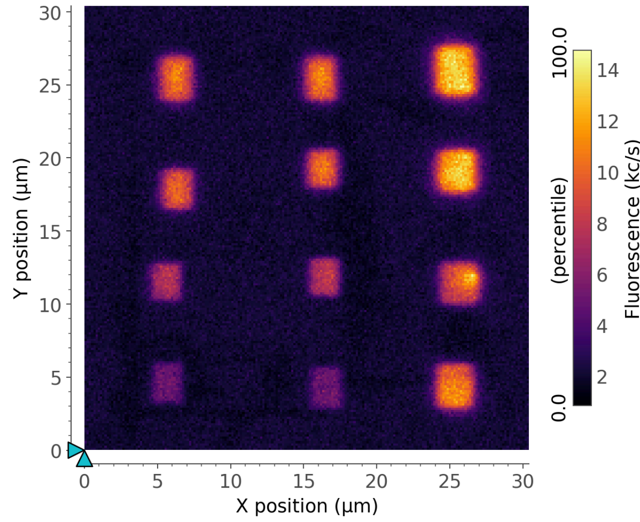

Figure 4.37: Typical PL map of the laser-treated carbon-implanted silicon sample. Each bright square corresponds to a 7x7μm^2 region exposed to the high-power laser with different treatment parameters. The PL map was acquired by raster scanning the sample surface with a CW 488 nm excitation laser at 10 K. $P_{laser} = 200\ \mu W$.

in correspondence with the "as-implanted" region, along with a series of bright squares where the silicon has been laser-treated. Afterward, the spectral analysis in correspondence with the laser-processed regions reveals the spectral features of both the W center (ZPL at 1218 nm) and the carbon-based G complex defect (ZPL at 1279 nm), whose activation was not successful using the same float zone silicon substrate and the same C implantation process upon RTA treatment. In Fig. 4.38, two subsets of spectra have been reported and divided into two plots to appreciate the relative intensities of the different spectral features corresponding to different laser energy density regimes. For low pulse energy density (Fig. 4.38.a), the intensity of the G centers is maximized, and the zero-phonon line (ZPL) overall increases as a function of lasing energy density; conversely, the W center ZPL shows a clear intensity maximum for the process performed at 0.69 mJ·cm^{-2}, while it completely anneals out if the pulse energy density is further increased (Fig. 4.38.b). Going to higher pulse energy density, corresponding to estimated temperatures higher than 800°C, a constant PL intensity of the G ZPL is observed. For better visualization, the ZPL dependence on the pulse energy density is displayed in Fig. 4.39 for both G and W centers. The values were obtained by integrating the

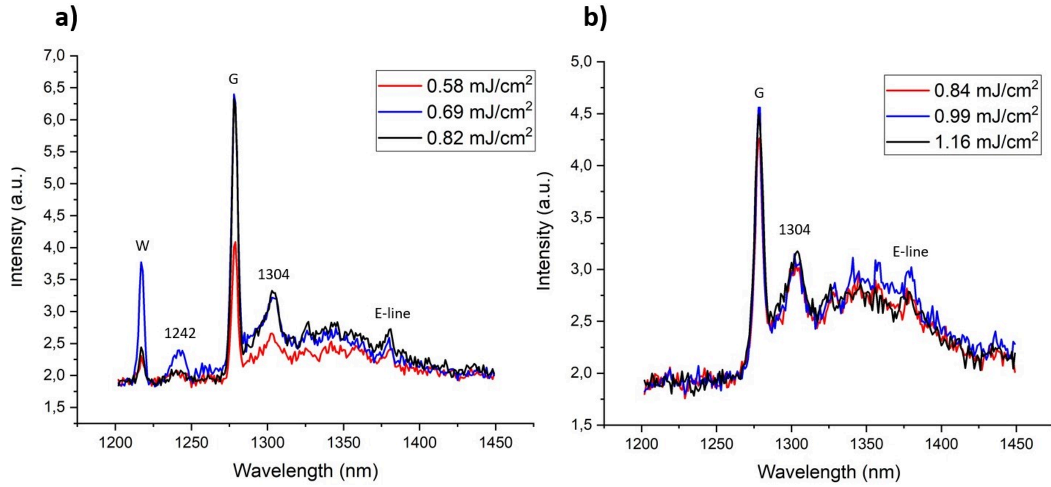

Figure 4.38: PL spectra acquired upon 488 nm CW excitation from the regions laser annealed with energy density in the 0.58-0.82 mJ·cm^{-2} range (a) and in the 0.84-1.16 mJ·cm^2 range (b) All the measurements were performed at 10 K and normalized to the excitation power.

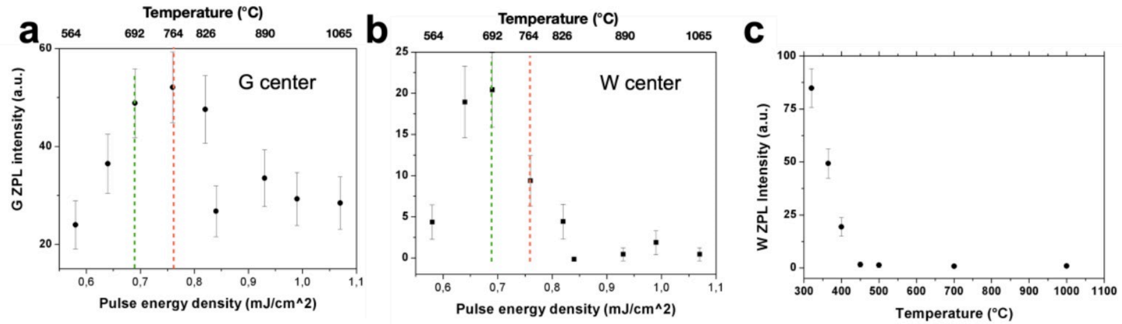

Figure 4.39: ZPL of a) the G and b) W center as a function of the lasing pulse energy density. The temperatures reported on the upper horizontal axis were estimated through the finite element analysis for each experimental energy pulse density. For the sake of comparison, in c), the intensity of the W ZPL line as a function of the annealing temperature upon RTA treatment (20 s duration) is reported.

PL signal in the (1270-1284) and (1210-1218) nm ranges, respectively. The PL signal initially increases for both the G and the W emitter, reaching a maximum in correspondence of 0.76 mJ·cm^{-2} (764°C estimated), emphasised by the green dashed line, and 0.86 mJ·cm^{-2} (826°C estimated), red dashed line, respectively. Higher lasing energy density causes a decrease in both the G and W PL intensity. However, while a PL signal from an ensemble of G centers is still detectable after the laser processing and at the highest energy densities, i.e. > 1 mJ·cm^{-2} reaches

a plateau value, the PL signal related to radiation-induced W defects becomes negligible. The latter can be interpreted as a full recovery of the crystal matrix with the consequent recombination of the interstitial silicon atoms that are not involved in the formation process of the G centers with the vacancies generated during the ion implantation process. Since the temperature range (500-1100 °C) covered with the experimentally adopted lasing parameters (0.58–1.07 mJ·cm^{-2}) overlaps with the set of temperatures achieved by RTA treatments, it is worth noting that the annealing out of the W emitters is verified for higher temperature with respect to the RTA thermal treatment (Fig. 4.39.c), thus indicating, on one hand, a poorer efficiency in dissociating such defects and on the other side corroborating the strong non-stationarity of the illustrated process. Moreover, the W ZPL exhibits only a monotonic signal reduction upon the RTA treatment.

The quality of the created emitters was then verified at the ensemble level, investigating the linewidth, which is a key parameter in integrating quantum emitters into real devices. The expected lifetime-limited linewidth, representing the lower bound on the homogeneous broadening, is $\frac{1}{2\pi\tau} = 8$ MHz (or 33 neV), thus corresponding to an FWHM of 0.04 pm. However, considering the inhomogeneous broadening, recently reported values are FWHM = 0.28 nm for a single G center, limited by the spectral resolution [178] and 0.88 nm for an ensemble [178]. Fig. 4.40 displays the FWHM of the G ZPL as a function of the lasing energy in the 0.58-1.16 mJ·cm^{-2} range. The trend exhibits an increasing linewidth for the adopted parameters, from a minimum of (0.97 ± 0.05) nm (at 0.58 mJ·cm^{-2}) up to a maximum of (1.10 ± 0.05) nm (at 1.16 mJ·cm^{-2}) when the PL signal of the G ZPL is maximized and the W centers completely annealed out. Broader emissions from the fabricated G centers go hand-in-hand with a progressive decrease in the PL intensity, approaching the plateau value. Therefore, the consistency of the reported value with the linewidth individuated in other C-implanted silicon samples both at the ensemble and single-emitter level, processed with Rapid Thermal Annealing (RTA) [180], [86], [178], [184] verifies the suitability of the proposed technique for the fabrication of quantum emitters. Furthermore, the PL intensity dependence on the temperature measurement was investigated in the 10-70 K range, upper limited by the resolution achieved with the monochromator combined with the broadening of the G emission for temperatures higher than 50 K (Fig. 4.41). Fig. 4.42 displays the spectra acquired in a restricted spectral range along with the integrated signal in the 1270-1284 nm range as a function of the sample temperature. Apart from the intense ZPL emission, the emission spectra appear to be quite flat due to the optimization of the experimental configuration in favor of a better spectral resolution but at the detriment of the signal magnitude. However, once more, the observed thermal redshift (~ 0.7 nm) in the investigated 10-70 K temperature range results in quite good agreement with previous works on the fabrication and characterization of G centers ensemble upon C and proton co-implantation combined with RTA annealing [86].

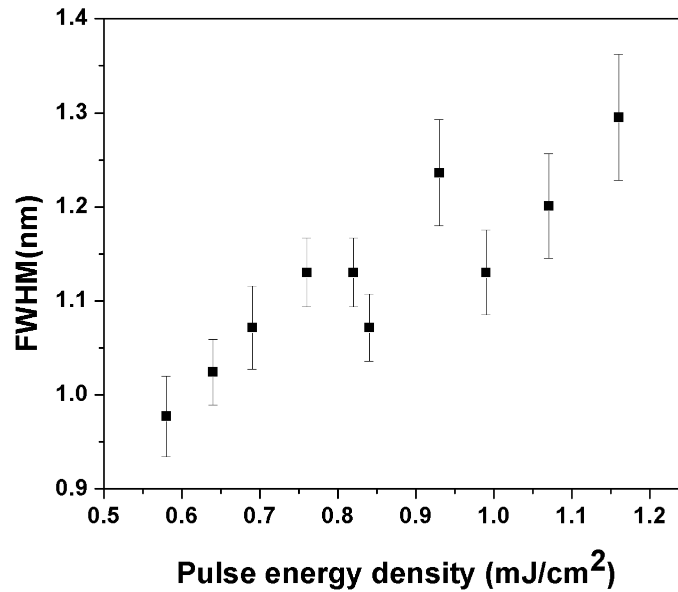

Figure 4.40: FWHM of the G ZPL as a function of the lasing energy density. The error bars result from the Gaussian propagation of the uncertainty of the sigma fitting parameter, which has been squared summed with a semi-dispersion estimated from repeated measurements.

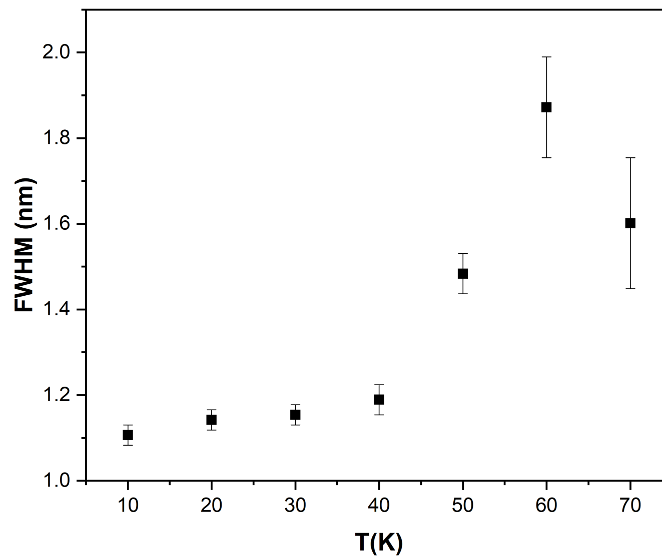

Figure 4.41: Broadening of the G ZPL emission represented by its FWHM as a function of the measurement temperature. The error bars result from the Gaussian propagation of the uncertainty of the sigma fitting parameter, which has been squared summed with a semi-dispersion estimated from repeated measurements.

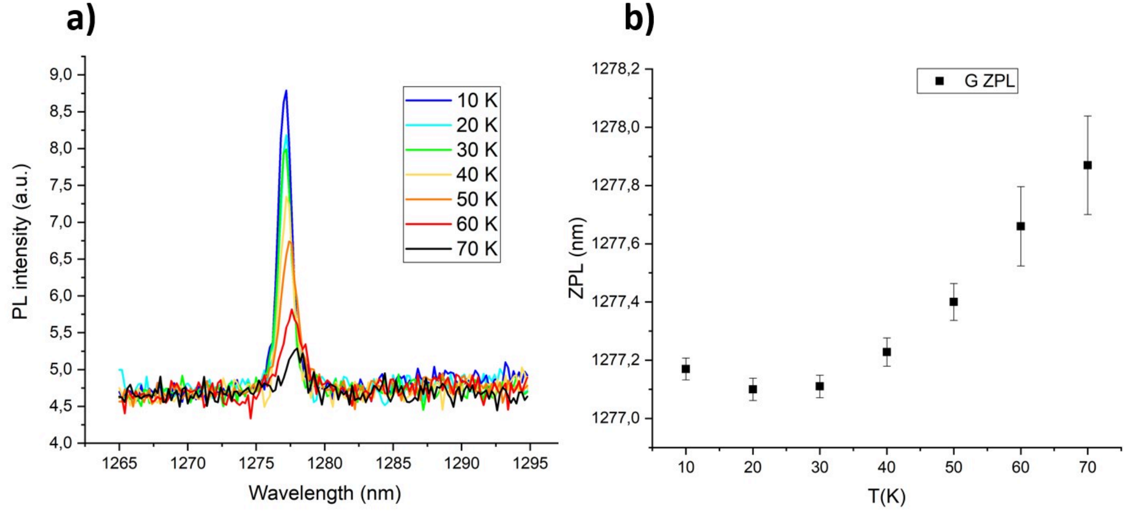

Figure 4.42: ZPL of the G centers as a function of the sample temperature. The measurements have been performed on the ensemble of G centers fabricated with a pulse energy density of 0.76 mJ·cm^{-2} where the signal is maximized. The error bars have been estimated as the squared sum of the uncertainty of the Gaussian centroid fitting parameters and the relative HWHM values.

Furthermore, additional measurements have been performed on a sample based on the same substrate wafer implanted at a different C ion fluence, namely, $8\cdot10^{14}$ cm^{-2} rather than the $2\cdot10^{14}$ cm^{-2}. The same laser processing was performed following the ion implantation. The results on the ZPL intensity are shown in Fig. 4.43 for the G center and the W center, respectively. Compared to those reported in Fig. 4.39, it is apparent a similar trend with a minimal shift in the cutoff value centered at 0.8 mJ·cm^{-2} for the W and 0.85 mJ·cm^{-2} for the G to be compared with the range 0.76-0.82 mJ·cm^{-2} of the sample implanted with $2\cdot10^{14}$ cm^{-2} fluence. However, the latter could be explained in terms of a minimal discrepancy in the focusing conditions of the lasing system. These additional results are instead a confirmation that the energy delivered to the silicon substrate has the sole role of locally increasing the substrate's local temperature. The independence of the cutoff values can be explained by considering that the ion fluence values adopted here are not sufficient to induce any amorphization or phase transition in the material and that the local density of defects produces a negligible change in the absorption coefficient of the material at the considered lasing wavelength.

As the last step, the intensity of the G and W emission lines was investigated in the light of a different number of lasing pulses. Fig. 4.44 reports the intensity of the G center (1279 nm) and W center (1218 nm) against the two relevant parameters, namely the lasing energy pulse density and the number of pulses per burst. As a result, the study does not highlight any particular trend. As a general rule, it can

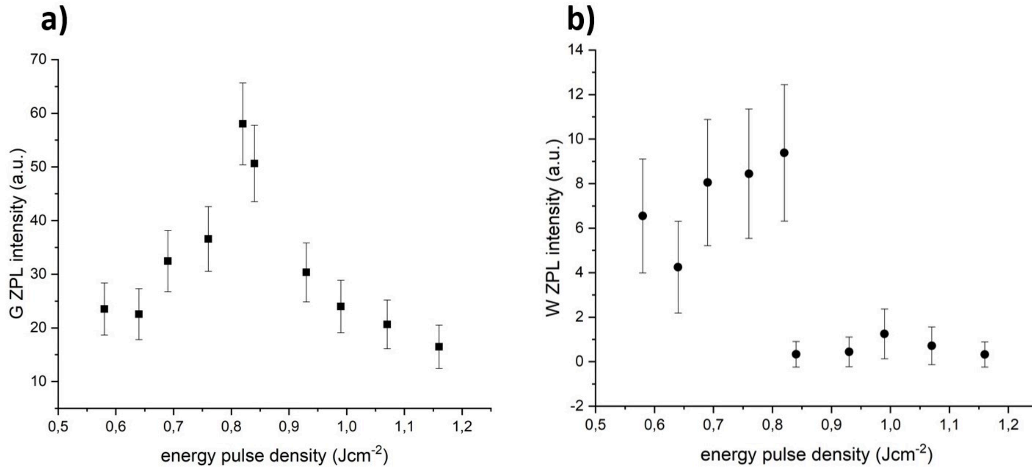

Figure 4.43: ZPL intensity of the G center (1279 nm) and W (1218 m) center as a function of the lasing energy density in a float zone silicon wafer implanted with $8{\cdot}10^{14}$ cm^{-2} C at 36 keV energy. The error bars have been estimated as the squared sum of the uncertainty of the Gaussian centroid fitting parameters and the relative HWHM values.

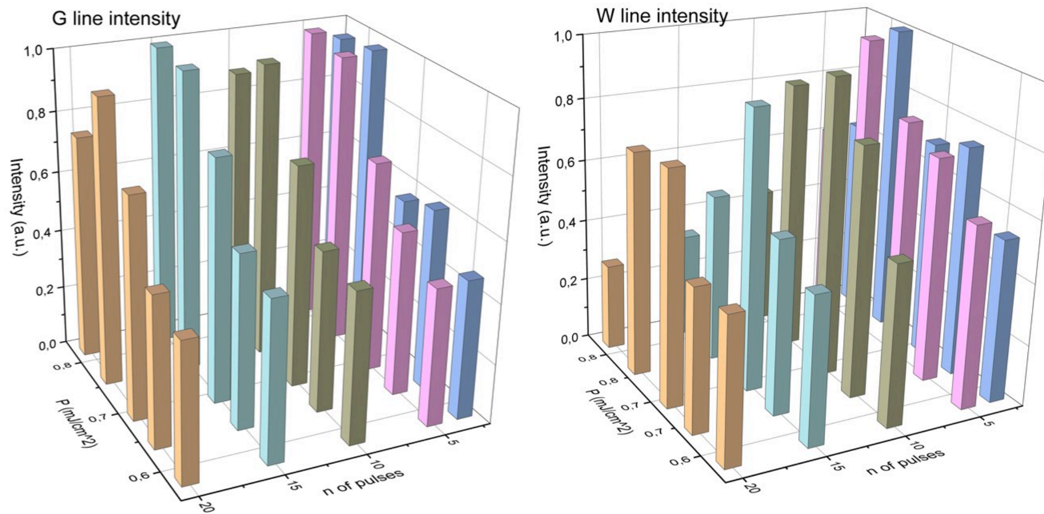

Figure 4.44: ZPL intensity of G and W centers against the lasing energy density and the number of localised ns-pulses. The signal has been measured on a float zone silicon substrate implanted with 36 keV C and a fluence of $2{\cdot}10^{14}$cm^{-2}.

be stated that for a higher number of pulses, assuming the direct proportionality of measured PL intensity from the number of created centers, statistically, a larger number of G centers is created (fig. 4.45.a), thus confirming the repeatability of the process given by the heat dynamics already explored and discussed with the

finite element analysis. On the contrary, the behavior of the W intensity would suggest a decreasing number of created interstitial silicon defects, consistently with the progressive recovery of the crystal matrix and the contribution of the interstitial silicon atoms Si_i to the formation of the G centers (Fig. 4.45.b). A decrease in G and W signals is observed for the highest number of delivered pulses. However, a more detailed investigation is needed to clarify this behavior and understand if some process saturation is reached.

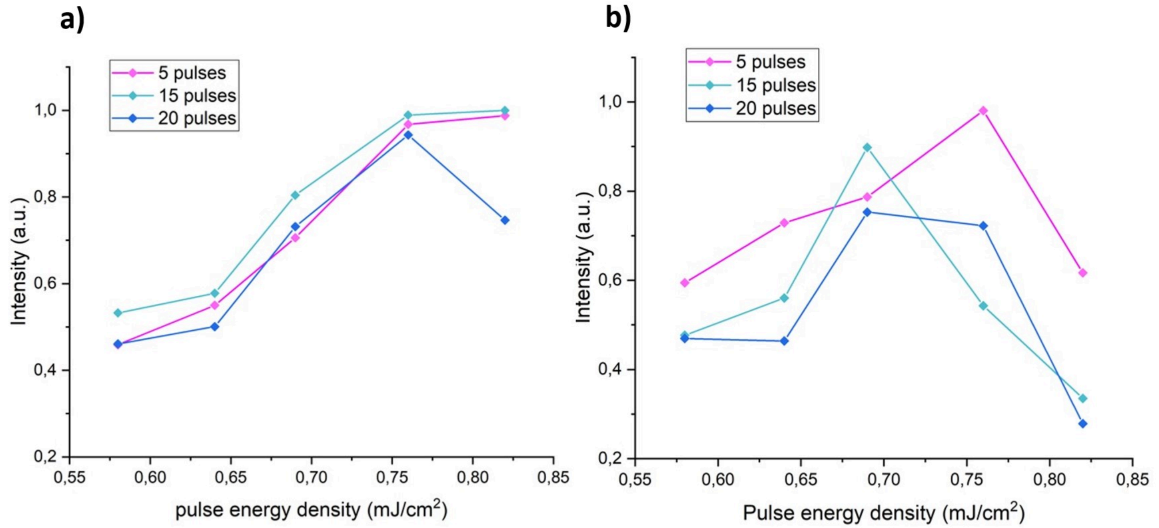

Figure 4.45: ZPL intensity of G and W centers against the lasing energy density for 5 and 15 localized ns-pulses. The signal has been measured on a float zone silicon substrate implanted with 36 keV C and a fluence of $2{\cdot}10^{14}cm^{-2}$.

Outcomes

The following results depict **the first attempt** to explore the **activation of optical dopants in solid-state materials using a nanosecond pulsed laser** [112]. Comparing the outcomes with conventional RTA, which takes a few seconds, it is evident that laser annealing in the nanosecond regime can be a more efficient processing strategy. The approach relies on off-equilibrium temperature transients, leading to **faster and more effective material processing**. However, gaining a full understanding of this phenomenon will require a systematic comparison of silicon substrates synthesised through different methods to optimize defect engineering procedures. Furthermore, the short duration of optical absorption, which provides access to meta-stable defective states in an off-equilibrium procedure, is long enough to prevent the introduction of irreversible structural damage to the crystal lattice structure, thus ensuring **compatibility with the activation of**

color centers embedded in optical structures. In this respect, previous pioneering works by Skolnick et al. have reported the fabrication of G centers using a high-power Q-switched laser inducing the melting and the consequent recrystallisation of the implanted silicon [67]. In the same way, based on recent advancements in laser technology, which have led to the development of new defect engineering methods, research has been conducted on the use of femtosecond laser annealing in silicon, exploiting the melting and subsequent recrystallisation as key mechanisms in the creation of G centers [185]. Conversely, consistent with the illustrated approach, the detection of W centers in an early work where CZ silicon substrates were processed with a broad infrared source and using lasing energy density insufficient to melt the silicon has indeed provided preliminary evidence that the lasing processing can promote the creation of optically active defects by locally supplying the thermal budget [186]. Therefore, by adapting the heat diffusion model to the material-specific thermal boundaries and light absorption waveleghts, the technique can be also applied to **SOI devices, with engaging applications in integrated photonics**.

Chapter 5

Monolithic Active Pixel Sensors (MAPS): a case study for device simulations

Although the simulation activities covered in this section are not strictly related to the tailoring of solid-state target properties, they are intended to remark on the impact a complementary numerical modeling strategy could have in developing a controlled fabrication protocol for the realization of next-generation integrated quantum devices. The depicted scenario is that of the innovative design of Fully Depleted-Monolithic Active Pixel Sensors (FD-MAPS) in the context of the INFN ARCADIA project, which aims to develop Advanced Readout CMOS Architecture with Depleted Integrated Sensors. The discussion relies on the same working principles of the signal formation presented in the previous sections and is based on the already addressed Schokley-Ramo theory. The presented study offers an example of the simulation activities carried out within the PhD project on novel radiation sensors, providing an overview of different simulation tools and a simulation flow routinely adopted for the evaluation of devices' performance. In particular, these simulations refer to the plan of activities of the timing layer working group of the ALICE 3 project, a next-generation multipurpose detector at the Large Hadron Collider (LHC) at CERN, as the follow-up to the present ALICE experiment. The devices under study consist of FD-MAPS designed in the ARCADIA project, i.e., fully depleted sensors where the charge is collected by drift and characterized by low power consumption, low capacitance for a high signal-to-noise ratio, and fast charge collection (in the order of ns [187]). These features provide a promising technology to target the 20 ps time resolution expected in the particle identification via Time-Of-Flight (TOF) of the ALICE 3 upgrade. The simulation study focused on the timing resolution achievable by FD-MAPS, using simulation domains preliminary tuned on experimental data. For this purpose, **Technology Computer-Aided Design (TCAD)** simulations (Synopsis Sentaurus version N-2017.09-SP2) were

combined with **high-statistic Monte Carlo simulations (MC)**, allowing the statistical analysis to estimate the timing resolution of the sensor, starting from **remarkably accurate electric fields and weighting potential maps evaluated with finite element analysis**. The finite element analysis was based on the sensor design developed by Prof. Lucio Pancheri. The device simulations and experimental characterization were the result of close collaboration between Prof. Pancheri's group at the University of Trento, Prof. Angelo Rivetti's group at INFN, and Prof. Stefania Bufalino's group at Politecnico of Torino. This collaboration led to the publication in JINST in 2024 [188]. The evaluation of the device's performance was initially tested by L. DeCilladi. Subsequently, I handled the simulation of the device's electrical characteristics in TCAD to generate the Electric Field maps for the Monte Carlo simulations using Garfield++ and Allpix^2 for analyzing the timing resolution. A systematic investigation on FD-MAPS with large pixel pitch was carried out in collaboration with Chiara Ferrero. Finally, a preliminary study on the convolution of the simulated device's response with the front-end electronics referred to the design of the Front-end electronics by Stefano Durando.

5.1 Time resolution in radiation detectors

A commonly adopted technique for identifying particles in high-energy physics experiments, known as TOF measurements, involves measuring the particle's flight time over a certain distance. This allows the particle's mass to be determined based on its momentum. Consequently, high time resolution (<100 ps [189]) is required to measure the particles' crossing time accurately. In particular, the time resolution σ_t can be described as the result of contributions of different types [174]:

$$\sigma_\mathrm{t}^2 = \sigma_\mathrm{L}^2 + \sigma_\mathrm{D}^2 + \sigma_\mathrm{TW}^2 + \sigma_\mathrm{J}^2 + \sigma_\mathrm{TDC}^2, \tag{5.1}$$

where

- $\boldsymbol{\sigma_\mathrm{L}^2}$ represents the Landau noise, given by the non-uniform ionization and originated from the discrete nature of the generated charge carriers in a fixed thickness of material, whose fluctuations follow the Landau distribution [174];
- $\boldsymbol{\sigma_\mathrm{D}^2}$ represents the distortion term, and it considers the signal distortion caused by both non-saturated drift velocities and non-homogeneous weighting potential. The latter is used to calculate the induced signal through the Schokley-Ramo theorem and is strictly related to the sensor's geometry, with particular attention paid to the width and thickness ratio [190];
- σ_TW^2 is the time walk term and represents the contribution given by the fact that signals with identical shapes and different amplitudes cross the threshold at different times [25]. Appropriate electronic architectures, such as the

Constant Fraction Discriminator (CFD), can minimize the effect; otherwise, it can be corrected using software post-processing algorithms.

- ${\sigma_{\mathrm{J}}}^2$ is the jitter term, determined by the shifting of the firing time of the comparator in the front-end electronics. It is directly proportional to the noise N and inversely proportional to the signal Slew Rate $\frac{dV}{dt}$, meaning the slope of the signal around the discriminator threshold V_{th} [25];
- ${\sigma_{\mathrm{TDC}}}^2$ is the time uncertainty resulting from the signal discriminated by a Time to Digital Converter (TDC), which is affected by the quantization error. However, thanks to the commercially available fine binning TDCs, it can be neglected [174];

Therefore, the first two terms relate to the intrinsic properties of the radiation sensor, while the last three account for the noise contribution from the front-end electronics; as will be discussed in the following sections, the design efforts have been primarily focused on minimizing the intrinsic contributions without convoluting the signal with the front-end electronics.

5.2 The ARCADIA technology

Silicon sensors are nowadays largely employed in modern particle physics experiments where they constitute essential components to retrieve information on particle trajectory and type. A silicon pixel detector is a sensing diode matrix connected to readout electronics. Nowadays, two leading technologies have been used to create these devices [25]. Hybrid detectors represent the first type, where the readout circuitry is integrated on a separate die from the active silicon substrate, and each pixel is connected to the readout circuitry via bump bonding. The second type involves monolithic detectors, where the readout electronics is integrated into the same Si active substrate, thus significantly reducing material budget and production costs [191]. CMOS Monolithic Pixel sensors have particularly proved to ensure their operation in high radiation environments (up to 9 kGy's) [192], thus representing the preferred choice for numerous applications in radiation detection experiments [193], [194]. Among the best examples is the Inner Tracking System of the ALICE experiment at CERN, representing the first silicon tracker with a large area of $\sim 10\ \mathrm{m}^2$ working with CMOS MAPS technology [195]. The innovative design used in developing ARCADIA MAPS is based on a customized 110 nm CMOS process in collaboration with LFoundry [196]. The pixelated sensor is reported in Fig. 5.1, showing the high-resistivity float zone n-type substrate (2 $\mathrm{k\Omega cm^{-2}}$, [196]), fully depleted by applying a negative voltage at the p+ boron-doped backside electrode, thus taking advantage of a limited diffusion of the charge carriers originated by the impinging particle [191]. The depletion hereby starts from the

back of the sensor. In parallel, low-bias voltages are supplied from the top, where n-type implantation defines the sensor nodes, which are entirely isolated only after the complete depletion of the substrate. The full integration of CMOS electronics is enabled by p-well and n-well for nMOSFETs and pMOSFETs transistors, respectively, with additional deep p wells to isolate the n wells of the pMOSFETs, avoiding competitive charge collection. Additionally, an n-doped epilayer with lower resistivity controls the potential below the p wells, shifting the voltage corresponding to the exponential increase of the hole current between the backside p+ electrode and the top p regions, known as punch-through voltage, towards higher values. The visible termination structures with multiple guard rings are essential to avoid early breakdown of the p+/n-substrate junction.

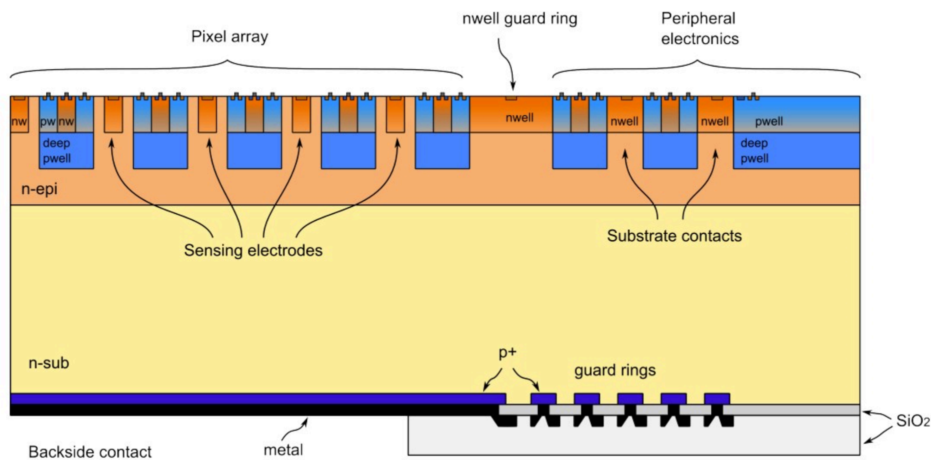

Figure 5.1: Schematic representation of the section of the pixelated sensor designed in the ARCADIA project and based on the modified 110 nm CMOS process in collaboration with LFoundry [196].

5.2.1 MAPS without gain

The study presented in this section will specifically explore how the geometry affects the timing resolution in the ARCADIA MAPS design. Preliminary analysis on the ARCADIA main demonstrator characterized by a 25 μm pixel pitch and a small collecting electrode (2.5x2.5 μm^2), [196], [197] resulted in the non-uniformity of the weighting potential, thus limiting the time resolution to 80-100 ps; hereby based on promising results with a 50 μm pixel pitch, capable of reaching Landau noise component in the 25-30 ps range, **the timing performance of large pad diodes** with pixel pitches ranging from 100 μm up to 200 μm and different

thicknesses forseen for the production run, namely 25 μm, 35 μm, 50 μm was explored **as a function of the weighting field uniformity**. Figure 5.2 displays the TCAD three-dimensional pixel matrix simulation domain. For all the simulations, the temperature was set to 300 K. The foundry provided the doping profile, which was encoded on the color scale and protected under a non-disclosure agreement. The characteristics of the epilayer have been tailored so that the nodes can be biased at 3.3 V MOS transistors. After the proof-of-concepts productions [191], comprehensive and in-depth optimization of the pixel design has been carried out in Technology Computer Aided Design simulations to investigate the sensor's behavior in different environments and to target small pixel capacitance to guarantee low electronics noise, maximum signal-to-noise ratio, and high charge collection efficiencies within the shortest possible time to handle high particle rates [192]. The optimization for fast timing allowed the definition of general considerations, such as the faster collection charge in pixel corners for smaller deep pwells, along with the increasing capacitance for larger gaps, to the detriment of the signal-to-noise ratio [192]. Consequently, the optimized structure resulted in the one reported in Fig. 5.2, where additional details on the design elements and sizes can be found. Fig. 5.3 provides a visualization of the adopted approach for the time performance estimation of the previously illustrated CMOS sensors. In particular, the investigation has been carried out by combining the three-dimensional TCAD with advanced MC simulation frameworks, such as Allpix^2 [198]. In this way, the electrical characteristics of the sensors have been evaluated through the finite element analysis, eventually optimizing the design, and accurate electric fields and weighting potential maps are supplied for implementing high statistics MC simulations based on the Shockley-Ramo theorem for the estimation of the induced current signals. The ensemble of I-t curves at the output of the MC simulations finally enabled the estimation of the timing resolution according to detailed data analysis. In particular, Allpix^2 offers the possibility to accurately treat the response of silicon sensors when crossed by an impinging particle, allowing the simulation of stochastic energy deposition on the basis of the toolkit Geant4, which is an object-oriented platform developed by the international Geant4Collaboration for handling useful aspects such as geometry, tracking, detector response, visualization, in high energy physics, nuclear experiments and accelerator studies [199]. Among the main advantages of this simulation strategy is the relatively manageable computational time, especially compared to the time required for a single event in advanced TCAD transient simulations. Conversely, in MC simulations, a simplified algorithm is used, precluding any considerations on some secondary effects, such as the shielding of the electric fields from the generated electron clouds.

Since low power consumption is targeted in the ARCADIA design concept (<20 mW·cm^{-2} [192]), as already anticipated, the maximum applicable voltage is limited by the onset of the punch-through current between the shallow p-doped backside region and the top pwells, which is responsible for excessive power consumption

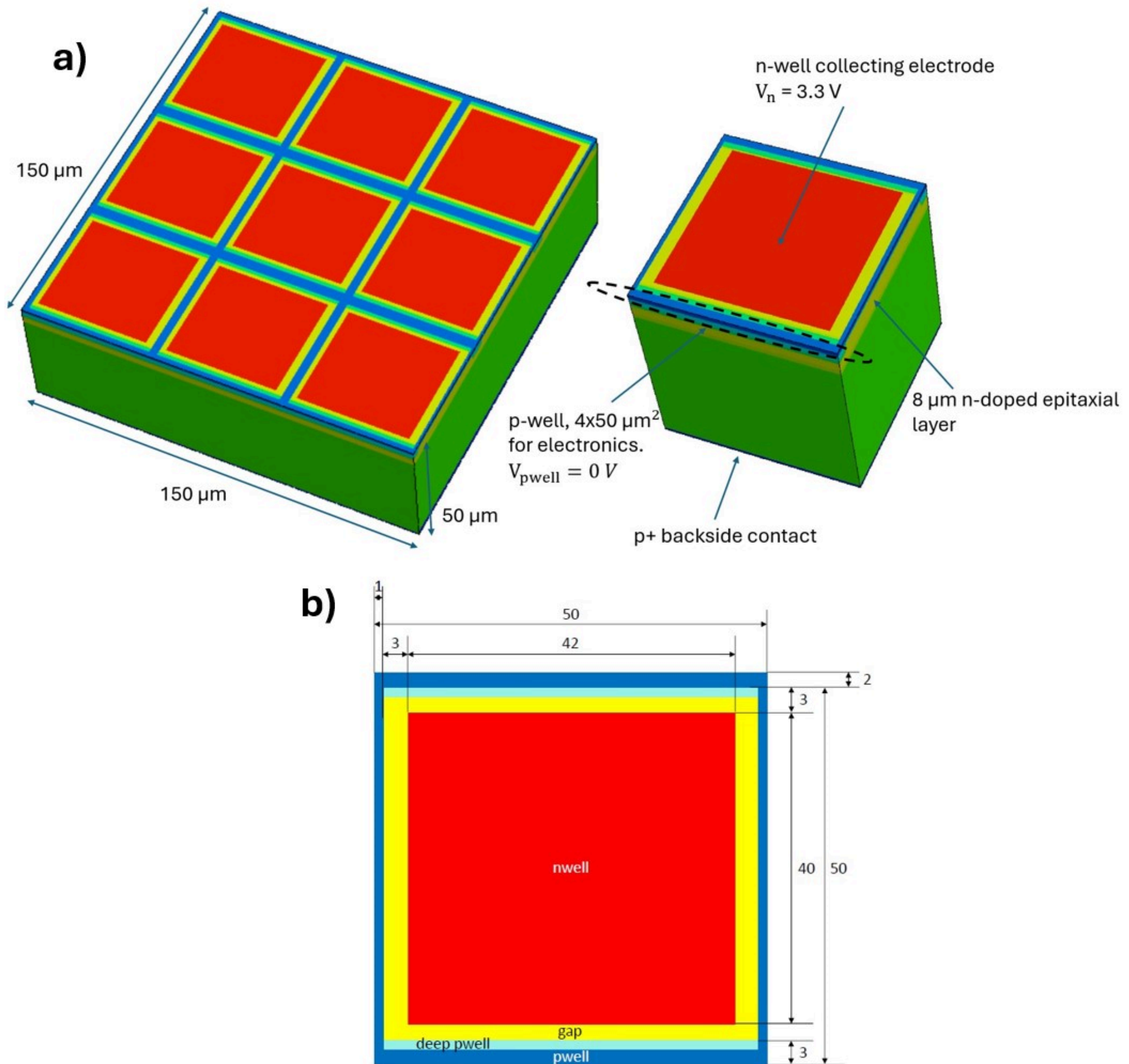

Figure 5.2: a) TCAD three-dimensional simulation domain showing a 3x3 pixel matrix and a single pixel with a 50 μm pixel pitch based on the ARCADIA design [196]. The sensor thickness, in this case, is 50 μm. The color scale encodes the doping concentration (red and blu are the maximum donor and acceptor concentrations, respectively). b) Top view of the single pixel with details on design size. Values are in μm. Assuming the electrical characteristics of the sensor are not remarkably affected by the n-well for the integration of pMOSFETs, their simulation is neglected.

[200]. For this reason, the punch-through current has been evaluated for each flavor of the analyzed pixel sensor to identify a good operating backside bias voltage,

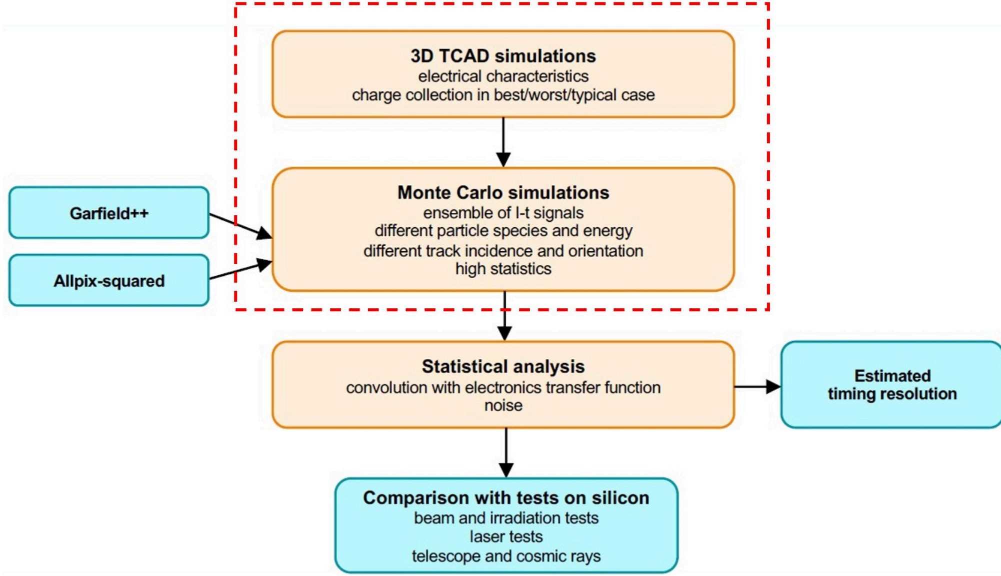

Figure 5.3: Schematic representation of the adopted approach for estimating the suitability of the CMOS sensors based on the ARCADIA manufacturing process in timing application for the ALICE3 experiment. From the online CERN monolithic sensor simulation meeting on 22$^{\text{nd}}$ March 2021, L. deCilladi et al. The red dashed square specifies the main focus of the simulation results covered in this section.

representing a good trade-off between the power consumption and the fastest possible drift mechanism with a drift velocity tending to the saturation one. The IV curves reported in Figure 5.4 show the absolute value of the simulated current evaluated at the top p-well as a function of the backside voltage (V_{back}). The dip of each curve corresponds to the sign inversion point and defines the punch-through voltage V_{pt} [200]. Figure 5.4.a depicts the IV curve for different pixel pitches and a fixed sensor thickness of 50 μm; a slight shift towards higher values is observed in V_{pt} for larger pad diodes. Additionally, the plot reported in Fig. 5.4.b highlights the earlier onset of the punch-through for thinner sensors. The pixel pitch has been set to 50 μm in the latter. In order to choose the operating back bias voltage, the dissipated power density is defined as:

$$P_{\text{d}} = \frac{I_{\text{pwell}} \cdot V_{\text{back}}}{A_{\text{pixel}}} \tag{5.2}$$

where I_{pwell} is the current flowing at the top pwell and A_{pixel} is the pixel's surface area. Considering the target of the sensor design, a maximum acceptable value has been fixed at 10 mWcm^{-2}(dashed red line in fig. 5.5). Therefore, referring to the corresponding back bias voltage as V_{pw}, this implies that $|V_{\text{pw}}|>|V_{\text{pt}}|$. Notably, even though a small variation has been observed for punch-through voltages at larger pixel pitches, the bigger area allows for easier power dissipation and higher

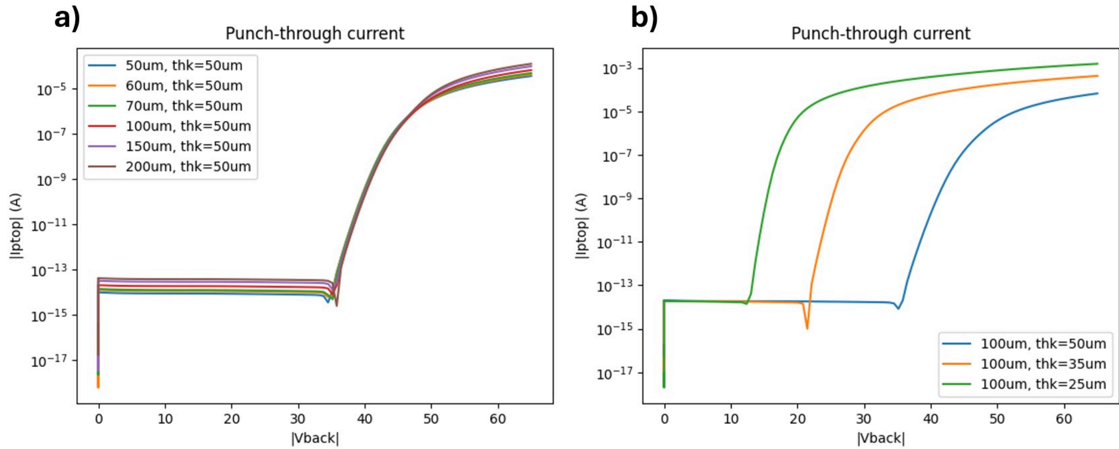

Figure 5.4: I-V curves extracted from TCAD simulation showing the dependence of the current flowing at the top pwell (I_{pwell}) on the backside bias voltage for different pixel pitches (a) and different thicknesses (b). The sensor thickness in figure (a) and the pixel pitch in figure (b) have been respectively fixed at 50 μm. The inversion sign point defines the punch through voltage V_{pt}.

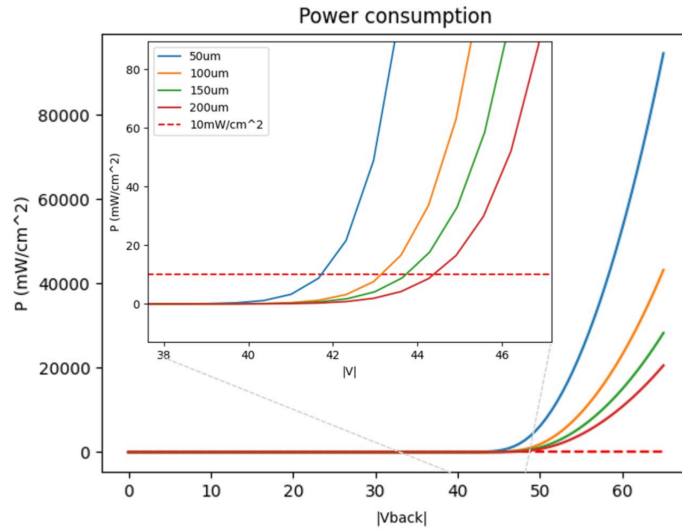

Figure 5.5: Typical P-V curves reporting the dissipated power density as a function of the backside bias voltage for different pixel pitches. The senor thickness is 50 μm. The dashed line represents the maximum power consumption of 10mWcm^{-2} according to the target within the ARCADIA design.

back bias voltages with respect to small pixel pitches. The voltage settings used in the TCAD simulation campaign are then summarised in table 5.2.1 for different pixel pitches and thicknesses.

pitch(μm)	thickness(μm)	V_{pt} (V)	V_{pw}(V)
50	50	34.5	41.7
50	35	20.8	26.2
50	25	12.4	16.3
100	50	35.2	43.1
100	35	21.5	26.9
100	25	12.4	16.8
150	50	35.2	43.7
150	35	22.1	27.9
150	25	12.4	17.1
200	50	35.8	44.4
200	35	22.6	29.0
200	25	13.0	17.5

Table 5.1: Voltage settings of the TCAD simulation campaign.

AC coupled simulations with 10kHz frequency were performed in TCAD using the same sensor domain (Fig. 5.2) to evaluate the C-V curves reported in figure 5.6. The top electrode bias has been fixed at $V_n = 3.3$ V. The sensor capacitance represents, indeed, the input capacitance seen by the front-end electronics, and since it can limit the speed and the noise figures of the system[25], it plays an important role in defining its performance. Moreover, low capacitance implies low analog power [201]. Although in modern front-end electronics, the charge-to-voltage conversion is part of the high gain amplification stage through a circuit element of the feedback path, the sensor capacitance is still a benchmark parameter in classifying the needed "effort" to obtain a good signal-to-noise ratio [25]. For this reason, figure 5.6 reports the C-V curve for different pixel pitch sizes where the pixel capacitance has been evaluated as the capacitive coupling between the n-top electrode and all the other electrodes as a function of the back bias voltage. The capacitance is evaluated for $V = V_{pt}$, which does not correspond to the minimum capacitance since the presence of the low-doped epitaxial layer, which shifts the complete depletion of the substrate, thus the isolation of neighboring collecting electrodes, for slightly higher voltage. In particular, the pixels under study resulted in larger capacitance in the 75-200 fF range with respect to the $\sim$ 35 fF for the 50 μm pitch. Considering a slightly different design, the values align with the scientific literature for the same technology and pixel size [202], [203]. However, a relaxed power consumption requirement would be needed in favor of a more homogeneous electric field ensured by the larger pixel structure, and a more accurate study, which is beyond the scope of this discussion, could provide a more precise estimation of the power required for the electronics.

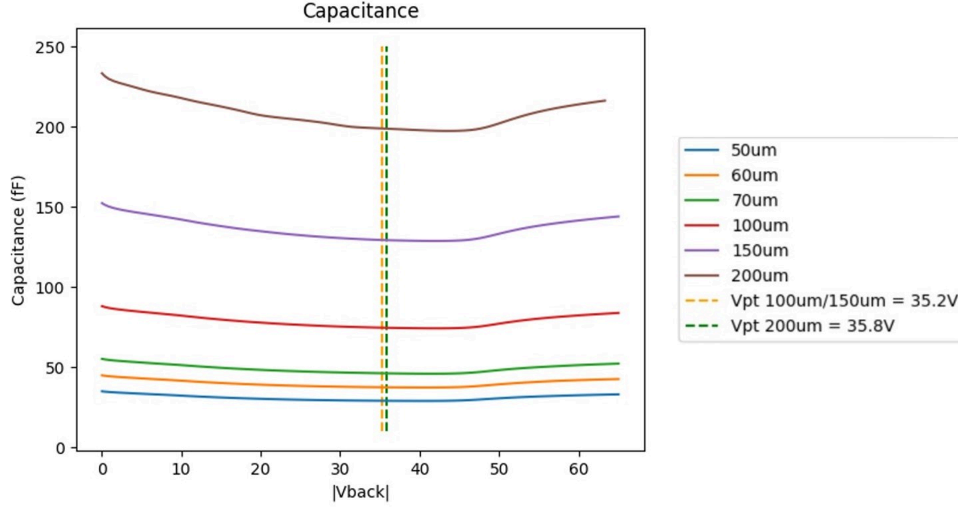

Figure 5.6: Simulated C-V curves where the capacitance between n-electrodes is reported as a function of the backside bias voltage. The dashed lines represent the V_{pt} for the 100, 150 and 200 μm pixel pitch.

Electric field maps have been exported from the finite element analysis to encode the sensor geometry along with the sensor's electrical characteristics in the MC simulations. In particular, the weighting potential has been evaluated as an approximation of the incremental ratio of eq. 4.7; two TCAD quasi-stationary simulations have been performed by varying the bias of the collecting electrode to a slightly different voltage, equal to 1% of the applied bias, while holding the back bias voltage at V_{pw}. Therefore, the weighting potential is defined as follows:

$$W_{\mathrm{P}} = \frac{E_{\mathrm{pot}}(V_{\mathrm{el}} + \Delta V) - E_{\mathrm{pot}}(V_{\mathrm{el}})}{\Delta V} \tag{5.3}$$

where E_{pot} is the electrostatic potential, V_{el} the bias configuration when the collecting electrode is held at the nominal value, and ΔV the voltage difference added to the collecting electrode in the second quasi-stationary simulation. Finally, a converter tool provided with the Allpix^2 framework to convert the TCAD adaptive meshes [198] produces regularly spaced field maps reported in Fig. 5.7. In this way, the sensor's geometry encoded in the electric field map can be imported together with its electric characteristics in the Allpix^2 MC simulation, and the induced current can be calculated based on weighting potential differences. To investigate the impact of the sensor geometry on the timing performance, the weighting potential of a 3x3 pixel matrix has been simulated for different pixel pitches, namely 50, 100, and 150 μm, under the same bias configuration. Fig. 5.8 reports the weighting potential maps estimated as in 5.2 from the TCAD quasi-stationary simulations, where the vertical pink lines identify the single pixel boundaries for each pixel pitch.

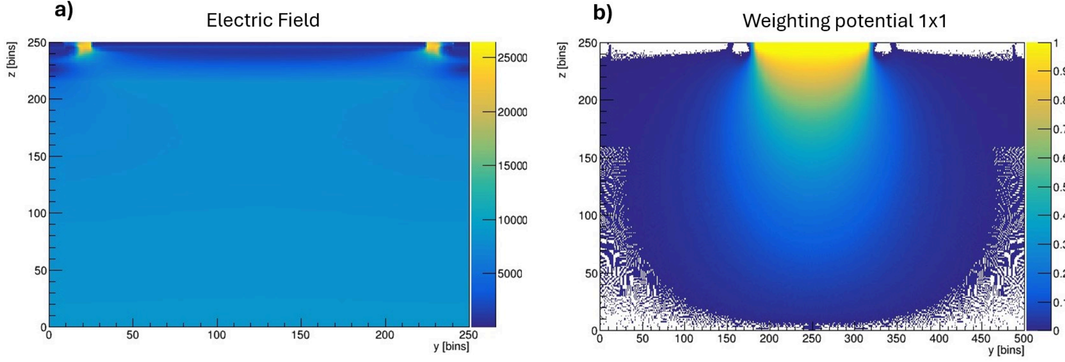

Figure 5.7: (a)Electric Field of a 50 μm thick single pixel with 50 μm pixel pitch exported from TCAD simulation and converted in a regularly spaced map with a mesh element dimension of 0.2x0.2x0.2 μm^3. (b) The relative weighting potential is displayed.

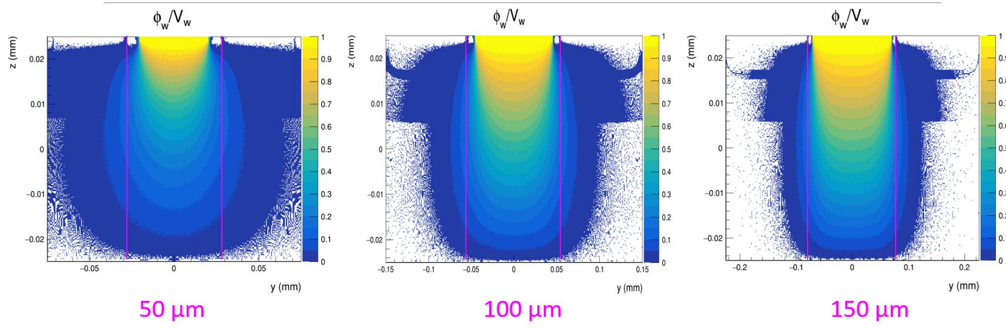

Figure 5.8: 3x3 pixel matrix Weighting potential evaluated from the two TCAD quasi-stationary simulations and converted into a regularly spaced mesh with the Allpix^2 mesh converter for the 50, 100 and 150 μm pixel pitch. The vertical pink lines highlighted the boundaries of the single pixel. The sensor thickness is 50 μm, and the three sensors have the same bias configuration.

From a qualitative point of view, it is already evident that the weighting potential map beneath the largest pixel pitch closely resembles the ideal weighting potential for two infinite parallel plates. This means that particles hitting the active area encounter a more uniform field, mitigating edge effects regardless of their point of impact.

In figure 5.9, the horizontal profiles along the y direction of the weighting potential maps computed for a 3x3 pixel matrix domain are depicted for each pixel pitch at three different sensor depths. Consistently with the maps reported in figure 5.8, the larger the pixel size, the more planar the weighting potential along the horizontal direction, suggesting a time evolution of the induced current almost

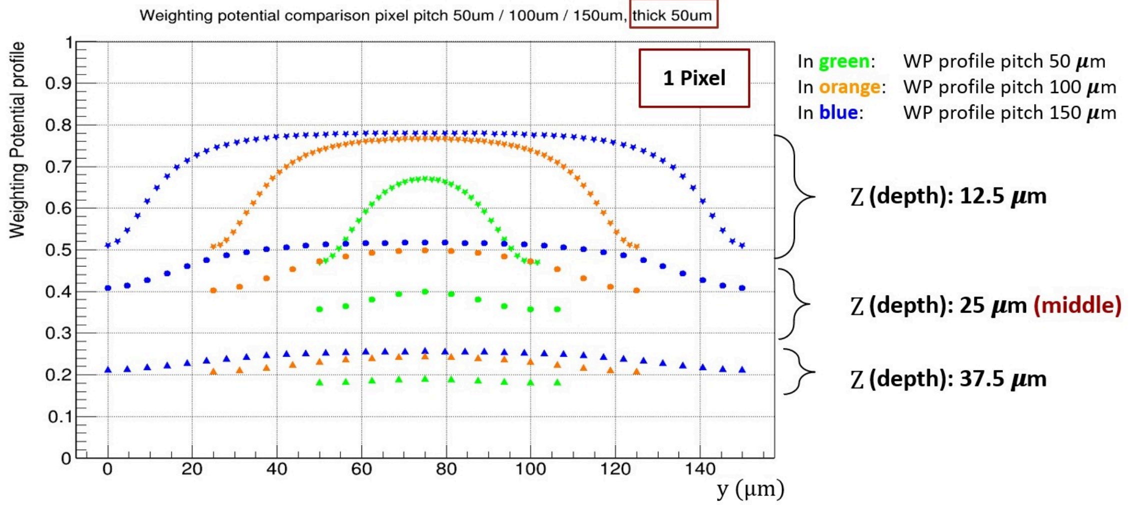

Figure 5.9: Lateral profiles of the weighting potential at three different sensor depths of a 3x3 pixel matrix domain for a 50 μm thick sensor with 50, 100, and 150 μm pixel pitch. The y coordinate represents the horizontal position of the pixel.

independent from the particle incident position and consequently narrower crossing time distributions in the evaluation of the sensor time resolution. The same trend is also visible in figure 5.10 showing the vertical profiles of the weighting potential maps in figure 5.8 along the Z direction at the center of a 3x3 simulation domain. The visible bending of the equipotential lines in Fig. 5.8 results in a non-linear profile for the 50μm pixel pitch; conversely, the almost overlapping linear profiles for the 100 and 150 μm pixel pitch confirm the limited edge effects in the timing performance. The same study has been carried out for a 25 μm thick pixel sensor (figure 5.11), pointing out a more emphasized effect. The latter is probably attributable to the different ratio between the sensor width (w) and the sensor thickness (d), which, according to detailed studies [204], plays an important role in defining the distortion term ($\sigma_D{}^2$) of the time resolution relation 5.1. For an ideal sensor with 50μm thickness, the best $\frac{w}{d}$ ratio is estimated to be $\sim$ 1.1; however, for a 25 μm thickness sensor the $\sigma_D{}^2$ results in a suboptimal range for all the pixel pitches explored [204].

The charge deposited in silicon by a Minimum Ionizing Particle is then simulated with a 200 MeV muon impinging in a random incident point of the surface area of the pixel sensor. The number of created electron/hole pairs is calculated using the mean pair creation [205], and the Fano factor is used to model the fluctuations, assuming Gaussian statistics [206]. This time, since the particle does not stop in the sensor, as discussed in the Ion Beam Induced Charge case, the response varies around a distribution's peak, with a high probability of higher signals, giving rise to an asymmetric density probability distribution. The latter was theoretically described

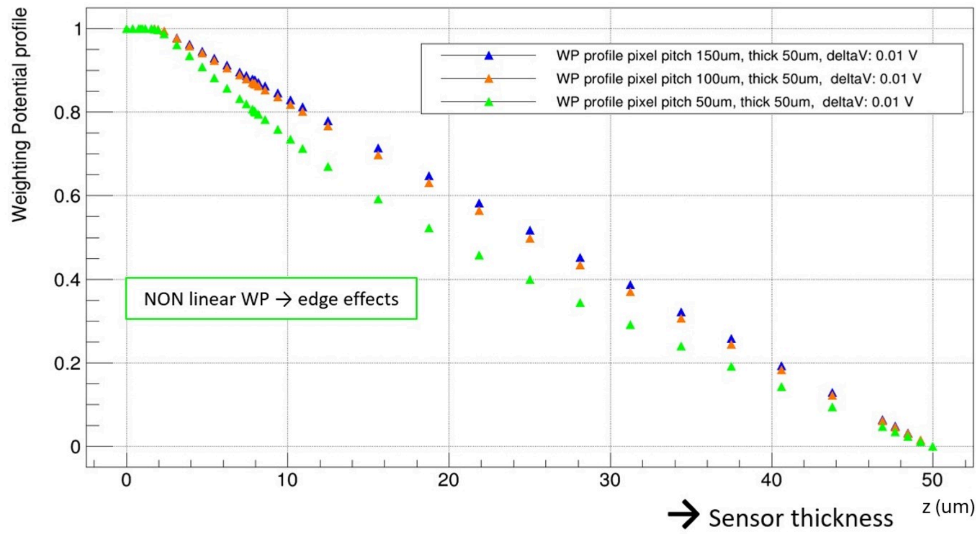

Figure 5.10: Vertical profiles of the weighting potential at the center of a 3x3 pixel matrix domain for a 50 μm thick sensor with 50, 100, 150 μm pixel pitch. The z coordinate represents the sensor depth.

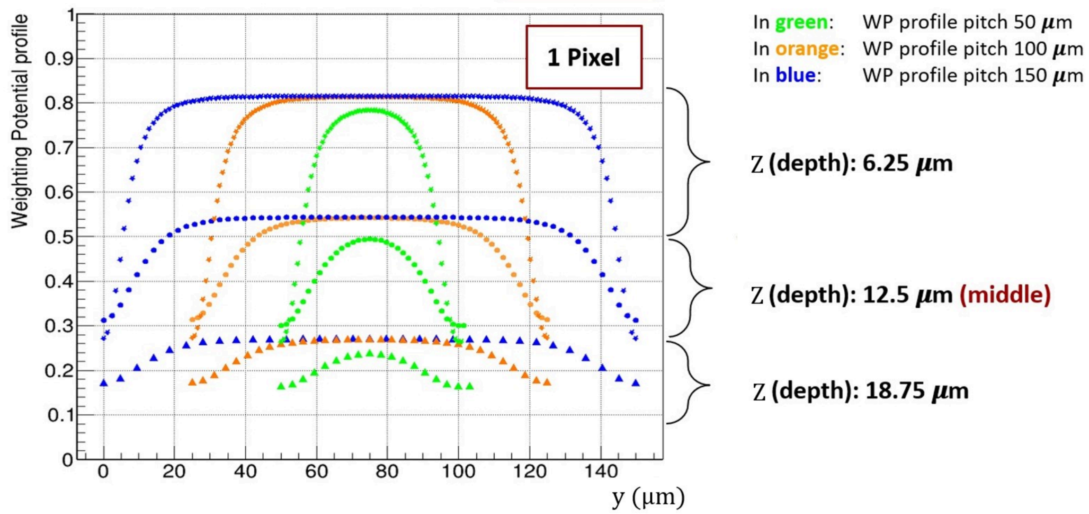

Figure 5.11: Lateral profiles of the weighting potential at three different sensor depths of a 3x3 pixel matrix domain for a 25 μm thick sensor with 50, 100, 150 μm pixel pitch. The y coordinate represents the horizontal position of the pixel.

by Landau and illustrates the fluctuations of energy losses by ionizing charged particles in a thin material layer [207]. Figure 5.12.a reports the distribution of deposited electrons in a 50 μm thick sensor with a Most Probable Value (MPV) $\sim$ 3200 electrons, meaning $\sim$ 65e$^{-}/um$, confirming the expected behavior in a thin

silicon sensor for a minimum ionizing particle [208] and consequently the accuracy of the simulation. The propagation of the charge carriers involves a combination

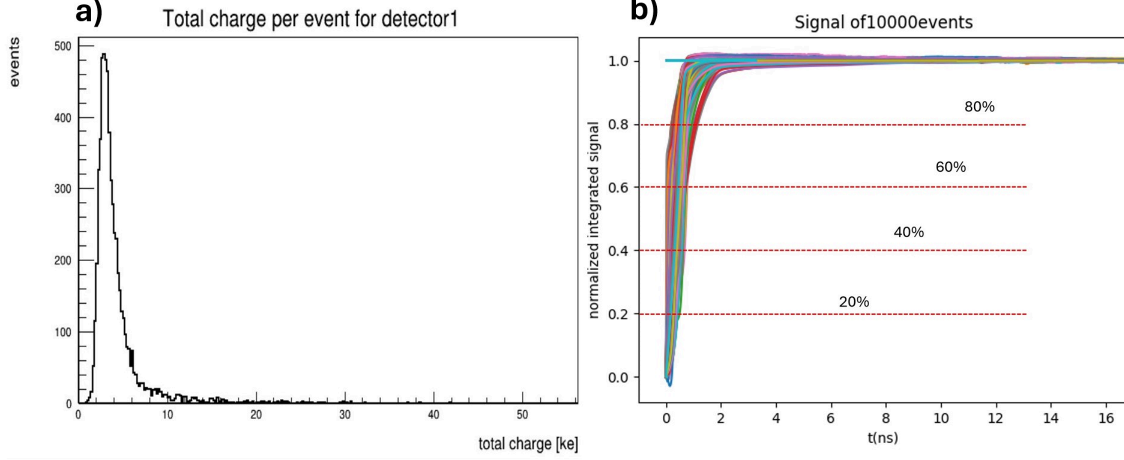

Figure 5.12: a) Landau distribution of the deposited charge by a 200 MeV muon impinging on a 50 μm thick sensor (50 μm pixel pitch). 10k events have been simulated. b) The normalized integrated signal, i.e., the normalized collected charge, is reported as a function of the time for each simulated event. Red dashed lines indicate the thresholds used for evaluating the root-mean-square of the crossing time distributions. The time interval covered provides an indication of the width of the relative time distributions.

of drift and diffusion simulations. The drift is calculated using the charge carrier velocity derived from the charge carrier mobility and the magnetic field, computed using the Lorentz drift [198]. The particle propagation in the electric and magnetic fields is integrated using a fourth-order Runge-Kutta-Fehlberg method [209]. After each drift step, diffusion is taken into account by applying an offset drawn from a Gaussian distribution calculated from the Einstein relation $\sigma = \sqrt{\frac{2k_{\mathrm{b}}T}{e}\mu t}$, where k_{B} is the Boltzmann constant, T is the temperature, μ the mobility, t the time step. Based on the previously shown WP maps, the charge carriers generated by the passing particle are then drifted towards (electrons) or away (holes) to or from the electrode. The charge transport parameters within the medium are determined according to the Masetti-Canali model [210], [211]. To estimate the sensor timing resolution, the root-mean-square of the time distributions was evaluated per each chosen constant fraction of the total collected charge as reported in figure 5.12.b.

It is essential to mention that these results reflect the contribution of the two intrinsic terms in the overall time resolution of the sensor, i.e., the Landau term ($\sigma_{\mathrm{L}}{}^2$) and the distortion term ($\sigma_{\mathrm{D}}{}^2$), while the contribution to the jitter related to the intrinsic noise of the front-end electronics is not included so far. As a general rule, at least for a fixed threshold <70%, it can be stated that for a larger pixel

pitch, a better time resolution is achieved, closely approaching the target $\sigma_{\mathrm{t}} < 20$ ps. Moreover, for thinner sensors (35 μm and 25μm), **the time resolution is upper limited at 20 ps for almost half of the collected charge**. Finally, figure 5.13 displays the resulting time resolution for different pixel pitches and sensor thicknesses. The better resolution can be attributed to a smaller Landau contribution (${\sigma_{\mathrm{L}}}^2$, see relation 5.1) in defining the overall time resolution due to the reduced number of generated charge carriers in the active sensor thickness. This result also underlines a more significant impact of the latter term with respect to the distortion contribution (${\sigma_{\mathrm{L}}}^2$, see relation 5.1), which conversely favors thicker sensors (see figures 5.9 and 5.11).

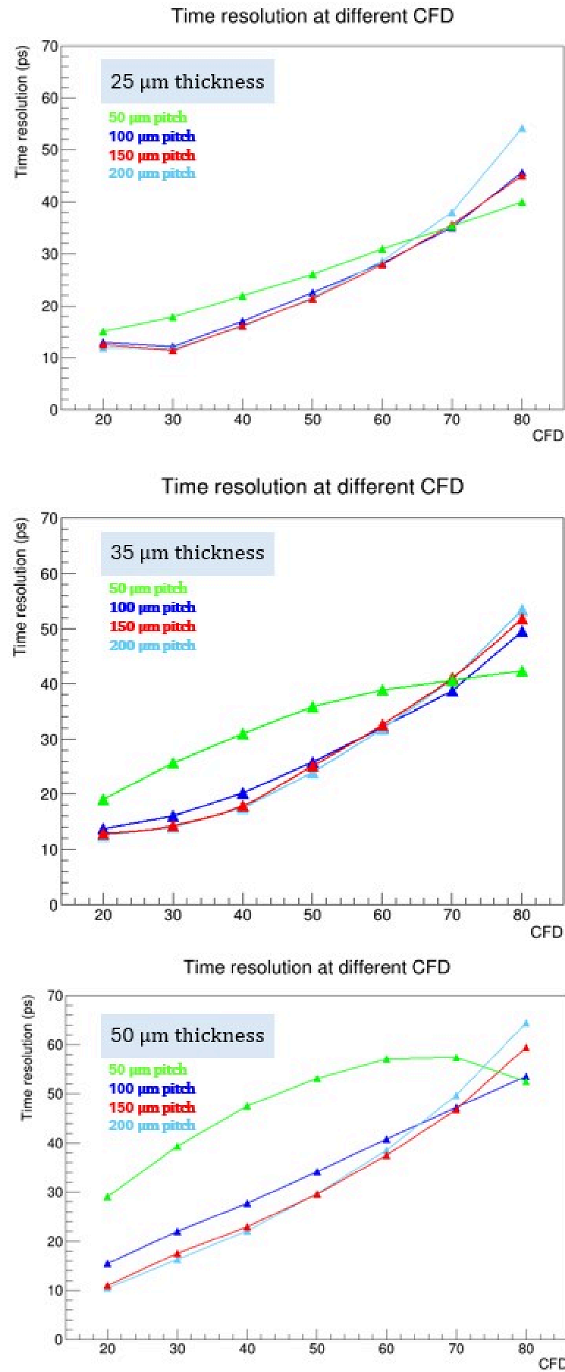

Figure 5.13: Estimated time resolution for fully-depleted MAPS with 50, 100, 150, 200 μm pixel pitch and 25, 35, 50 μm thickness. The results were obtained by simulating 10k events with a 200 MeV muon incident on the pixel sensor surface at a random position.

Additionally, it can be noticed that for thinner sensors (35 μm and 25μm), the curves are overlapping in the case of larger pads; this trend can be explained by taking into consideration the role of the width/thickness ratio ($\frac{w}{d}$) in defining the time performance of the sensor [204] which, given the values of the explored pixel pitches, cannot be further exploited for improving the time resolution in the case of thinner sensors.

To conclude, the time performance of MAPS with a pixel pitch of 100 μm has been briefly explored in the case of different bias conditions (fig. 5.14). In particular, the backside electrode has been biased at the punch-through voltage of the 50 μm pixel pitch corresponding to negligible power consumption ($I_{\text{punch-through}} \cdot V_{\text{back}}$) for the larger pixel pitch since $|V_{\text{back}}| < |V_{\text{pt}}|$ (see figure 5.5). The resulting time resolution does not highlight any particular difference between the two configurations, thus **suggesting the possibility of even reducing the sensor power consumption to negligible values while preserving the same timing performance**.

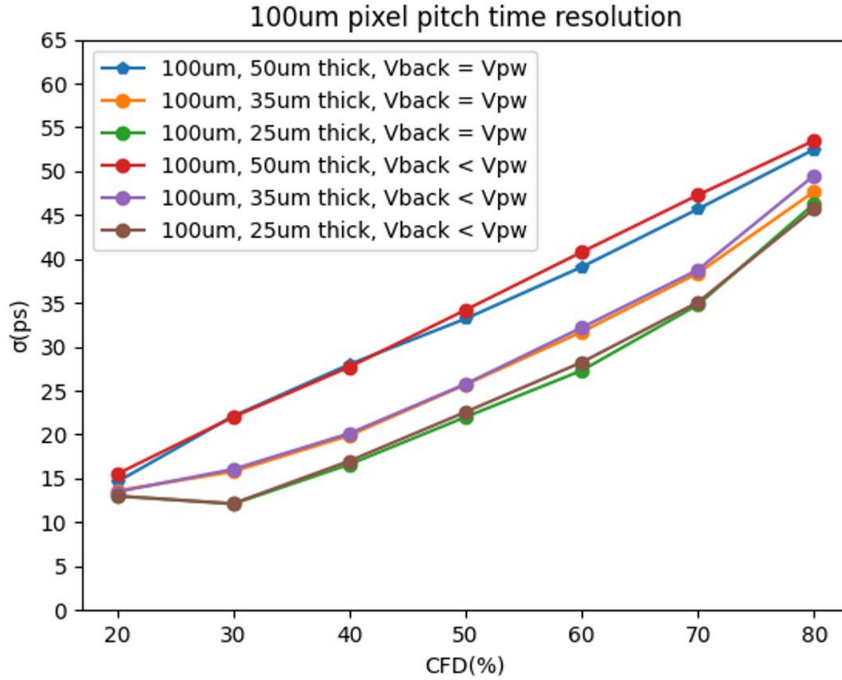

Figure 5.14: Estimated time resolution for fully-depleted MAPS with 100 μm pixel pitch and 25, 35, 50 μm thickness for different bias conditions. The results were obtained by simulating 10k events with a 200 MeV muon incident on the pixel sensor surface at a random position.

5.2.2 MAPS with gain

However, the limits imposed to the power consumption of the front-end electronics, related to the material budget and cooling of the detector, do not allow to explore sub-ns time resolution with standard monolithic CMOS sensors. For this reason, with outstanding predicted and measured time resolution [212], Low Gain Avalanche Detectors (LGADs) are currently the most well-established technology in silicon sensors for TOF measurements. They consist of PiN diodes with an additional highly doped p-type layer that can generate a very high electric field, which triggers an avalanche process. Therefore, with the aim of reducing the electronics jitter, an in-pixel gain layer has been added to the technology developed in the ARCADIA project, as reported in figure 5.15. The sensor must be reverse biased

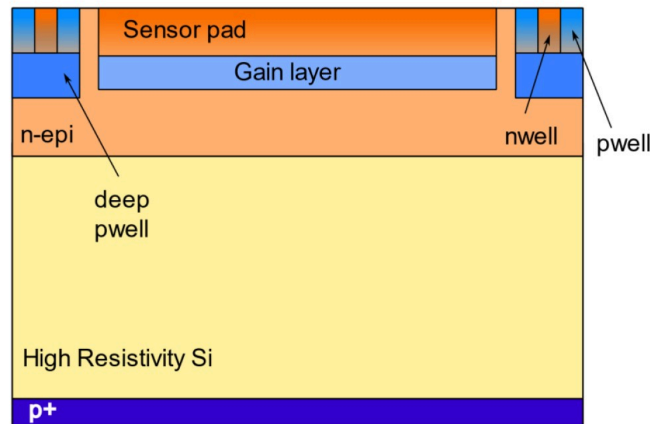

Figure 5.15: The monolithic ARCADIA pixel sensor with the gain layer placed underneath the collecting electrode.From Lucio Pancheri's talk at the 3rd ALICE Upgrade Week (CERN 9th May 2023).

at the back (approximately -30 V) to define the drift field in the sensor, while a positive bias (approximately 35/40 V) is applied to the n-type electrode, which defines the sensor's gain. This time, the MC raw signals have been preliminary convoluted with the transfer function of an integrated amplifier designed by Stefano Durando, whose circuit simulation has been reported in figure 5.16 (blu curve). To do so, the MC simulations have been computed using a toolkit for the detailed simulation of particle detectors based on ionisation measurement in gases and semiconductors named Garfield ++ and developed at CERN. The latter allows to model the signal processing by the front-end electronics using a pre-defined expression representing either a unipolar or bipolar shaper whose parameters have been appropriately determined by fitting the original curve with the following expression (red curve in

fig. 5.16):

$$f(t) = g \cdot e^{n} \left(\frac{t}{t_{\mathrm{n}}} \right) e^{-} t/\tau \tag{5.4}$$

where $\mathrm{t_p} = \mathrm{n}\tau$, g is the gain, n is the order of the shaper, and τ is the time constant. In particular, a gain of 50 was used, and n and τ were set to 2.5 ns and 1.5 ns, respectively. The time resolution has been then estimated using the root-mean-square of the time distributions obtained with fixed thresholds at constant fractions of the maximum amplitude of each signal.

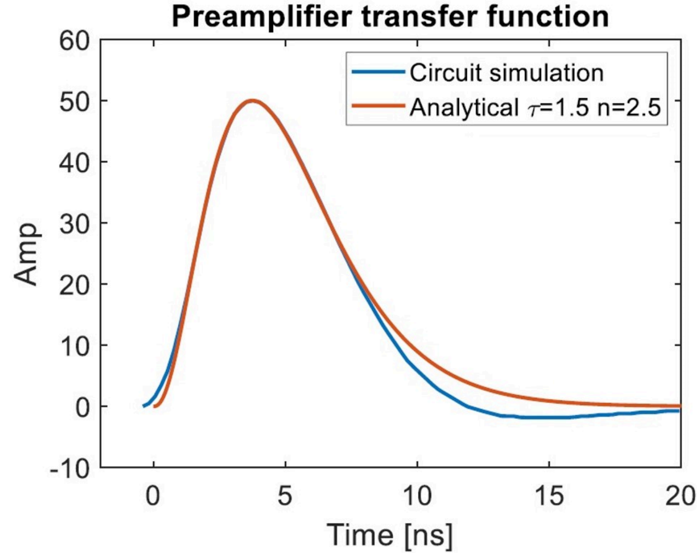

Figure 5.16: Preamplifier transfer function obtained with circuit simulation (blu curve) and the analytical expression defined in Garfield ++ for the signal convolution (red curve). From Lucio Pancheri's talk at the 3rd ALICE Upgrade Week (CERN 9$^{\mathrm{th}}$ May 2023).

Fig. 5.17 shows the electric field profile that reaches a peak value of $\sim$ 480 kV/cm in correspondence with the gain layer and the weighting potential field of the 2D adopted simulation domain obtained from the normalised maps subtraction 5.3 using the two TCAD quasi-stationary simulations where ΔV = 0.01 mV. In this case, Garfield ++ does not require the conversion of the maps from the adaptive to the regular meshes. Moreover, the program handled the charge deposition with Heed program [213], which implements the photo-absorption ionisation (PAI) model. The same charge transport parameters of Allpix^2 according to the Masetti-Canali model [210], [211] were used. Additionally, the van Overstraeten and de Man model rules the avalanche ionisation of the medium [214]. Fig. 5.18 shows an example of the simulated induced signal resulting from the average of 10 k events in a 50 μm thick and 80 μm wide pixel sensor after the convolution of the raw signal with the electronic transfer function defined through the shaper

object. In addition, a noise of 150 ENC (Equivalent Noise Charge) was added to the simulation based on an estimation from the circuit simulation.

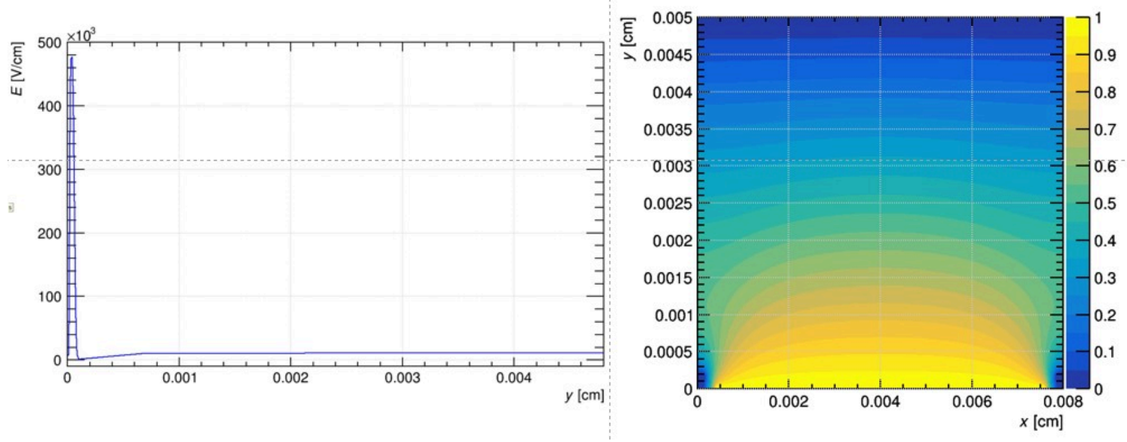

Figure 5.17: (a) Electric field of the ACADIA pixel sensor with the gain layer placed underneath the collecting electrode. (b) The weighting potential of the sensor was estimated from TCAD quasi-stationary simulations. The y coordinate identifies the depth of the sensor.

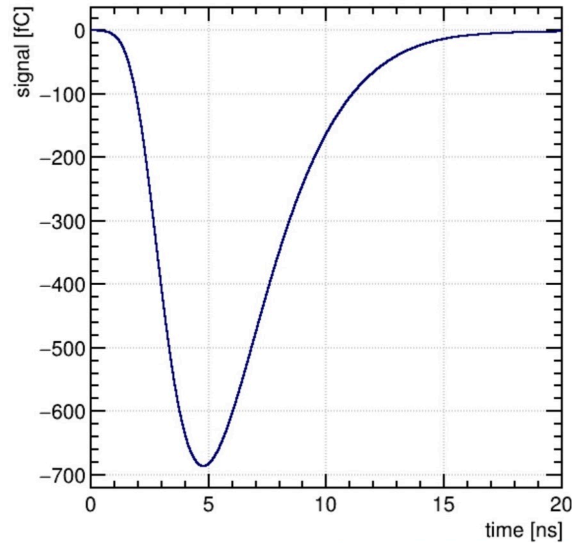

Figure 5.18: Simulated induced charge signal after the convolution with the integrated amplifier obtained as the average of 10k events where the mip particle was impinging perpendicularly in the sensor's center. To model the electronic processing, the shaper object identified by the function 5.4 has been used, setting g=50, n = 2.5 ns, τ = 1.5 ns.

The MC simulations were conducted into two different phases. First, 1D simulations have been carried out. The electric field profile has been extracted along a vertical cross section in the sensor center, and a uniform domain in x and y was defined by homogeneously extending the field for an entire 2D volume in the MC simulations, thus providing a completely flat weighting potential. The gain has been estimated by comparing the Landau distributions' two MPVs with and without the activation of the avalanche. By doing so, a preliminary insight into the time resolution as a function of the sensor thickness and the sensor width was possible. Afterward, 2D electric field maps were exported from Synopsis TCAD into Garfield ++ to properly include the effects of the border of the sensor. Figure 5.19 displays the estimated time resolution of the ARCADIA pixel in the case of a 40 μm width structure with 50, 25, and 15 μm thickness. The nearly overlapping curves of the 50 μm thick sensor indicate that the sensor has reached its intrinsic resolution. No differences can be observed indeed with or without simulated electronic noise. For the thinner sensors, the estimated time resolution resulted in $<$ 30 ps, suggesting that further thickness reduction is required, compatibly with electronics jitter. The same study has been performed for a wider structure (80 μm), exhibiting a moderately worsened performance for the 50 μm thick sensor, while confirming the $<$ 20 ps time resolution of the 15μm thickness. For this reason, the suitability of the 15μm has been explored, varying the electronic noise, figure 5.20. Finally, figure 5.21 compares 2D and 1D simulations for the case of a 50 and 15 μm sensor thickness under different bias conditions for the top electrodes. In this way, the time resolution estimated in the case of the 1D simulation domain provides a term of comparison for a better understanding of the signal distortion caused by the non-uniform weighting potential at the sensor edges and visible in the 2D simulation domain (see fig. 5.17). Due to an unfavourable width/thickness ratio, the latter even emphasises passing from the 1D to the 2D domain in the 35 V biased sensor case. In conclusion, figure 5.22 illustrates the position-dependent timing resolution for a 15 μm pixel pitch sensor. This confirms that with thinner sensors, achieving a time resolution of **$<$ 30 ps is possible even in the worst-case scenario**, considering edge effects due to the non-homogeneity of the weighting potential. Therefore, based on the simulation campaign, adding a gain layer to the ARCADIA process **effectively aligns with the targeted time measurements**. However, a **careful trade-off between active thickness, gain, and electronics power consumption would be needed**. Moreover, further refinement of the estimated electronic noise and 3D simulations is still necessary for a comprehensive understanding and full control of the developed technology.

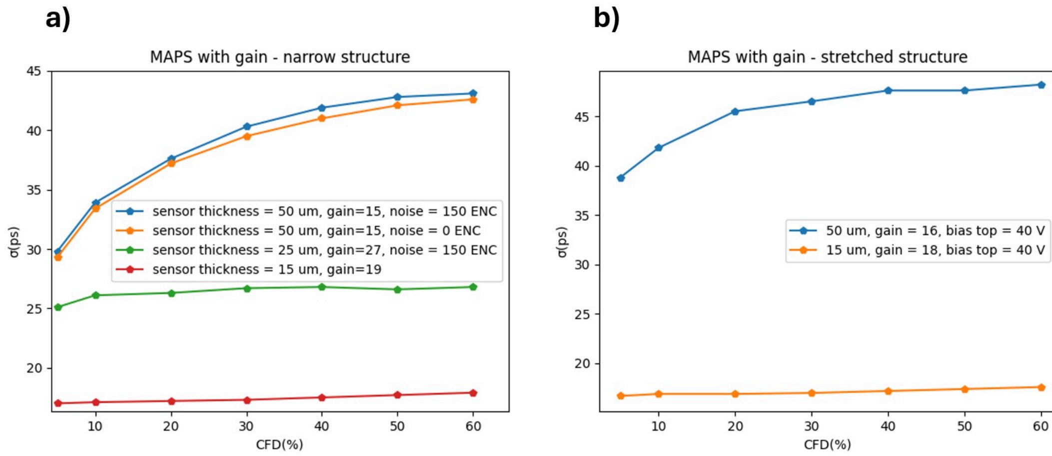

Figure 5.19: Time resolution of ARCADIA MAPS with gain as a function of the sensor thickness and width resulting from 1D simulations. (a) Time resolution of a 40 μm wide sensor with 50, 25 and 15 μm thickness. The orange curve shows the sensor's intrinsic resolution for 50 μm thickness. (b) Time resolution of an 80 μm wide sensor with 50, 15 μm thickness.

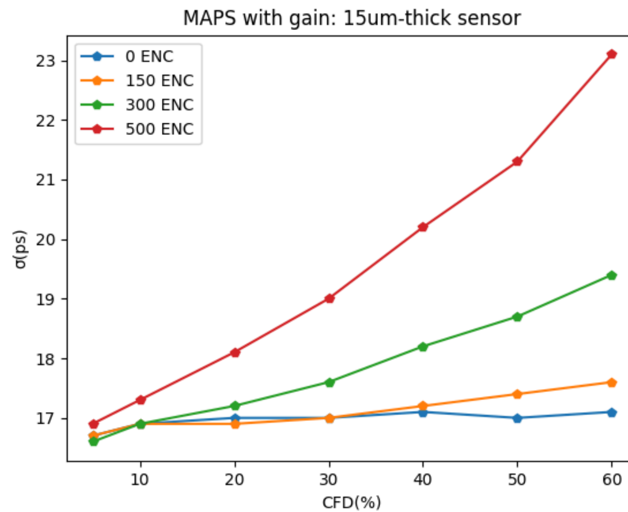

Figure 5.20: Time resolution resulting from 1D simulations of 10k events of ARCADIA MAPS with gain as a function of the simulated electronic noise for a 15 μm thick sensor with 80 μm pixel pitch.

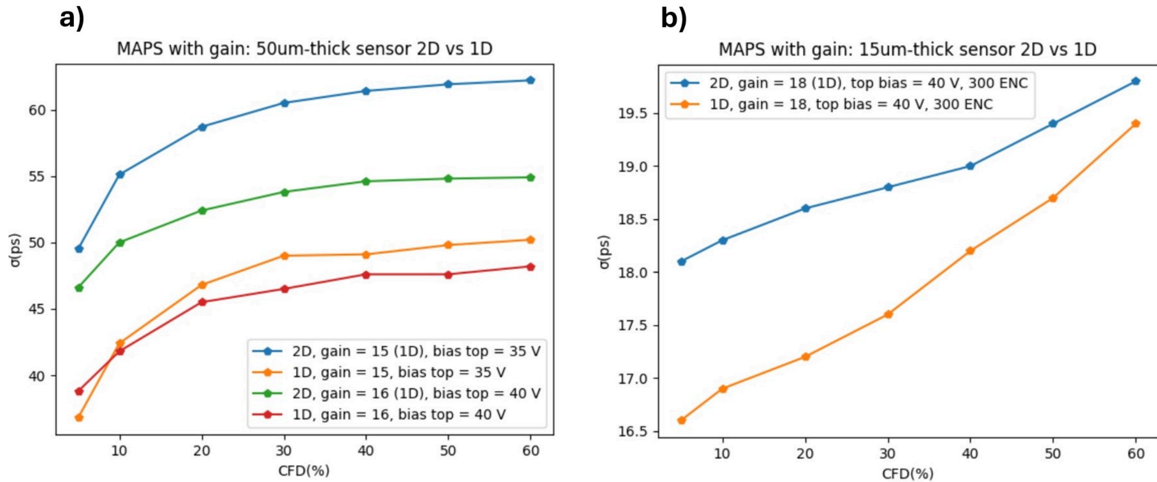

Figure 5.21: (a) Comparison of the time resolution of ARCADIA MAPS resulting from 1D and 2D simulations of 10k events for a 50 μm thick and 80 μm wide sensor under different bias conditions. The significant difference between the blue and the green curves highlights a sub-optimal width/thickness ratio [204]. (b) Comparison of the time resolution resulting from 1D and 2D simulations for a 15 μm thick and 80 μm wide sensor.

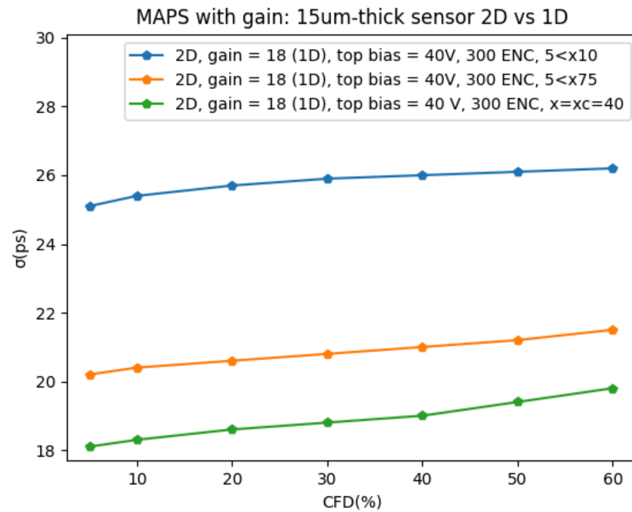

Figure 5.22: Position-dependent time resolution of ARCADIA MAPS resulting from 2D simulations of 10 k events in the case of a 15 μm thick sensor with 80 μm pixel pitch. The x coordinate identifies the position of the impinging particle, where x = 40 μm represents the sensor's center. The impinging position is randomly distributed in each of the provided ranges.

Conclusion

Discussion of results

In my dissertation, I discussed novel approaches to facing the main fabrication limitations in realizing silicon-based single-photon emitters. The developed solutions relied on the different encountered scientific challenges, and they are tackled in the interdisciplinarity nature of the presented activity, including io-matter interaction processes, laser physics, cryogenic quantum optics, and the simulation of electrical characteristics of state-of-the-art devices. The investigations have been mainly focused on float zone silicon substrates, characterized by limited oxygen and carbon native concentrations ($<10^{16}$ cm^{-3}), offering a low-defective environment for embedding telecom quantum sources, thus enabling a **higher level of control in their number and position**. As discussed in the investigation of silicon properties in Chapter 2, contamination and intrinsic impurities can indeed provide effective nucleation points and affect the diffusion of other introduced impurities for tailoring either the electrical or optical properties, thus introducing a large number of additional processes that, competing with the color center formation, limit the manufacturing to a purely statistical approach. Since the single-photon emission in silicon has been demonstrated only at cryogenic temperature, **the implementation of a single-photon sensitive cryogenic** experimental setup has been extensively carried out. The adopted approach is represented by **confocal microscopy**, as described in Chapter 3, allowing the imaging of silicon samples at the ultimate diffraction limit. Specific vacuum and **cryo-compatible instrumentations**, such as nanopositioners, temperature sensors, and optical elements, have been accurately incorporated into the experimental apparatus. The latter has been entirely validated through a case study on the optical characterization of MgV centers in artificial diamond. The results provided a consistent investigation with systematic measurement campaigns carried out at room temperature, **revealing unusual and counterintuitive additional insights into the optical activity** of these quantum systems that were not previously reported in the literature and that, most importantly supported the theoretically predicted potential application of MgV centers for quantum-enhanced sensing protocols based on their high tunable emission properties. Being ion implantation a reliable and

industry-compatible technique at the core of the manufacturing process for the realization of solid-state quantum sources, part of the activities described in Chapter 4 aimed to investigate the implantation damage effects to understand how to properly deal with the radiation-induced modified optical properties. In particular, the possibility to fabricate a large ensemble of color centers, thus increasing the sensibility in quantum-enhanced sensing protocols, allowing the introduction of a number of impurities above the graphitization threshold of diamond was demonstrated in hot diamond substrate implantations. Not only the graphitization threshold has been evidently verified to increase due to the dynamic reconstruction of the crystal matrix during the implantation process, but the results show an increase in the creation efficiency of nitrogen-vacancy centers upon N hot implantation. On the other side, the radiation damage introduced upon keV ion implantation effectively promotes the formation of tri-interstitial telecom quantum sources in silicon, named W centers, often investigated in the scientific literature upon self-implantation processes. Here, it is demonstrated that the introduction of extrinsic ion species in the silicon lattice, combined with conventional thermal treatments, represents a **reliable method to induce the formation of self-interstitial single-photon sources in silicon** as well. Moreover, the quality of the fabricated emitters is consistent with what has already been reported in the scientific literature upon Si implantation. Additionally, the poor creation efficiency of carbon-related defects (G centers) upon carbon implantation and conventional Rapid Thermal Annealing (RTA) treatments in float zone silicon has triggered a **detailed study on the assessment of the proper thermodynamic pathway for the fabrication of carbon-based quantum emitters through off-equilibrium thermal treatments**. The activity resulted in the **first attempt to develop a localized and non-invasive method for the activation of optical dopants in solid-state materials**, thus paving the way for radically novel defect engineering capabilities. For instance, since, according to the simulations reported in Chapter 4, the heat dissipation does not induce a detectable temperature increase at the wafer level besides the local effects vanishing within a few micrometers from the lasing spot, the laser annealing could be straightforwardly integrated into the cryogenic setup, without perturbing the stability of the cryogenic system keeping since the ns-long duration of the process. Besides this, the non-destructive nature of the developed approach, upon the assessment of the diffusion length of C ions under ns temperature transients and high-resolution implantation, ensures compatibility with the activation of color centers embedded in optical structures for the realization of silicon-integrated photonic circuits. Additionally, in the perspective of the deterministic delivery of single impurities in the silicon lattice, an Ion Beam Induced Charge (IBIC) experiment carried out on a Si p-n junction for the **in-situ measurement of the ion beam resolution** is discussed along with finite element analysis for a comprehensive description of the phenomena involved. The observed results provide a powerful protocol for determining the spatial resolution of ion

microbeams in deterministic ion implantation, micro-radio dosimetry, or micro ion lithography, which require in situ monitoring with high positional accuracy, avoiding the need for a separate reference standard. Finally, Chapter 5 remarks on the **impact that complementary numerical modeling strategies**, such as Technology Computer-Aided Design combined with Monte Carlo simulation tools could have in handling the design optimization of a dedicated radiation sensor for the realization of next-generation integrated quantum devices. In this regard, the case study reported discusses the PhD activities carried out within the INFN ARCADIA project.

Future perspectives

The experiments discussed in my Dissertation are examples of adopted techniques for the development of a **consolidated fabrication protocol in the realization of quantum emitters in silicon**. The latter, is certainly the most mature material in terms of synthesis and device manufacturing, as it relies on decades of expertise in research and industry. Conversely, as discussed in Chapter 2 the classes of color centers identified so far exhibit a molecular lattice structure substantially different from the simpler impurity–vacancy configurations found in diamond and SiC. This was also confirmed by the evident drawbacks in the effective activation of these color centers and accompanying the silicon manufacturing opportunities. Although an efficient activation protocol has been effectively proposed and verified, the development of an all-silicon integrated solution requires an all-deterministic manufacturing process involving controlled manufacturing strategies for the **repeatable fabrication of individual color centers** by means of standard fabrication techniques such as ion implantation. Therefore in the context of a scientific synergic effort aiming at the uptake of second-quantum revolution devices, the development and implementation of a complete silicon photonics integrated circuit would, for instance, enormously benefit from the coordinated effort in the field of ion beam-based nano-engineering; the nanopositioning of impurities at the nanoscale could be addressed in the future according to the combination of the **controlled implantation dose and targeted positioning with a sub-micrometer resolution**, such as Focus Ion Beam (FIB) Technology, and the above-illustrated non-invasive and localized activation treatment. Arrays of implantation spots with sub-micrometer precision and an average number of implanted ions per implantation spot could be appropriately chosen to enable the controllable creation of single-photon emitters in the telecom band and exploit the symmetry of the produced patterns to provide a quantitative estimation of the process uniformity and the creation efficiency compared to conventional longer thermal treatment. In this regard, **dual beam implantation and co-implantation of carbon and silicon** would be an effective strategy in further deepening the atomic dynamics

involved in the creation of the G center, enabling **additional information on the temporal evolution** of the lattice damage, the incorporation of the carbon atoms and their mutual influence. Moreover, in light of the microscopic mechanisms described in Chapter 2, involving both intrinsic and extrinsic impurities in the silicon lattice, a **systematic comparison between different silicon substrates** characterized by different impurities content and synthesized by different methods would be a key requirement for a full understanding of the phenomena involved in the G center formation, thus consequently enabling the optimization of defect engineering procedures. In fact, the evidence of the formation of G centers ensembles in silicon samples characterized by a substantially higher content of substitutional carbon and upon the same implantation and RTA processing parameters adopted in this work has highlighted the strong impact of the present contamination impurities in the formation process of optically active defect complexes. Additionally, **suitable parameters** must be investigated for the adoption of the same novel protocol with **silicon-on-insulator (SOI) substrates** distinguished by higher carbon native concentration and representing the commonly adopted technology for silicon photonics integrated circuits. The emission wavelength requirements imposed by the integration of these silicon single-photon sources in commercial systems adopting commercial optical fibers could be addressed with an in-depth investigation of the role of oxygen impurities in accordance with recent theoretical studies which have uncovered the potential application of carbon- and oxygen-related radiation damage defects emitting in the L band and called C centers (covered in Chapter 2) in implementing optically readable quantum memories in case of single-photon emission experimental evidence. Finally, the developed IBIC experiment for the assessment of the ion beam resolution and its potential scalability with keV ion implantation as described in Chapter 4, set the stage for the controlled delivery of individual impurities for the creation of individual color centers by means of ion implantation which could be directly performed at INFN laboratories by taking advantage of **single-ion detection techniques to be implemented at the end station of the already operative irradiation beamline** described in Chapter 3.

Bibliography

[1] I. Aharonovich et al. «Diamond-based single-photon emitters». In: *Reports on Progress in Physics* 74 (2011).

[2] S. T. Alsid et al. «Solid-State Microwave Magnetometer with Picotesla-Level Sensitivity». In: *Science* 19 (5 2023).

[3] J. Wrachtrup and F. Jelezko. «Processing quantum information in diamond». In: *Journal of Physics: Condensed Matter* 18.21 (2006).

[4] E. I. Rosenthal et al. «Microwave Spin Control of a Tin-Vacancy Qubit in Diamond». In: *Physical Review X* 13.031022 (2023).

[5] M. Esmann, S. C. Wein, and C. Antón-Solana. «Solid-State Single-Photon Sources: Recent Advances forNovel Quantum Materials». In: *Advanced Functional Material* Online Version of Record before inclusion in an issue (2024).

[6] X. Xue et al. «CMOS-based cryogenic control of silicon quantum circuits». In: *nature* 593 (2021).

[7] Jacopo Forneris. «Physics PhD course: Experimental implementation of quantum devices». Lecture Notes, University of Turin, Department of Physics. 2021.

[8] I. Aharonovich, D. Englund, and M. Toth. «Solid-state single-photon emitters». In: *nature photonics* 10 (2016).

[9] S. Tanzilli et al. «PPLN Waveguide for Quantum Communication». In: *The European Physical Journal D - Atomic, Molecular, Optical and Plasma Physics* 18 (2002).

[10] Mark Fox. *Quantum Optics, An Introduction.* Oxford University Press, 2006.

[11] C. Bradac et al. «Quantum nanophotonics with group IV defects in diamond». In: *Nature Communications* 10.5625 (2019).

[12] J. Forneris et al. «Electrical stimulation of non classical photon emission from diamond color centers by means of sub-superficial graphitic electrodes». In: *Scientific Reports* 5.15901 (2015).

[13] J. R. Maze et al. «Properties of nitrogen-vacancy centers in diamond: the group theoretic approach». In: *New Journal of Physics* 13.025025 (2011).

[14] P. Siyushev et al. «Low-temperature optical characterization of a near-infrared single-photon emitter in nanodiamonds». In: *New Journal of Physics* 11 (2009).

[15] E. Corte et al. «Magnesium-Vacancy Optical Centers in Diamond». In: *ACS Photonics* 10 (1 2023).

[16] D. Gatto Monticone et al. «Native NIR-emitting single colour centres in CVD diamond». In: *New Journal of Physics* 16 (2014).

[17] M. Radulaski et al. «Scalable Quantum Photonics with Single Color Centers in Silicon Carbide». In: *Nano Letters* 17 (3 2017).

[18] F. Sardi et al. «Scalable production of solid-immersion lenses for quantum emitters in silicon carbide». In: *Applied Physics Letters* 117 (2 2020).

[19] W. Redjem et al. «All-silicon quantum light source by embedding an atomic emissive center in a nanophotonic cavity». In: *nature communications* 14.3321 (2023).

[20] D. Phillips et al. «Time Correlated Single-Photon Counting (Tcspc) Using Laser Excitation». In: *Instrumentation Science and Technology* 14 (3-4 195).

[21] Swabian Instruments. URL: https://www.swabianinstruments.com/time-tagger/.

[22] Michael Wahl. *Time-Correlated Single Photon Counting*. Tech. rep. PicoQuant GmbH, 2014.

[23] Edinburgh Instruments. URL: https://www.edinst.com/blog/what-is-tcspc/.

[24] R. C. Newman. «Defects in silicon». In: *Reports on Progress in Physics* 45.10 (1982), pp. 1163–1210.

[25] Angelo Rivetti. *CMOS Front-end electronics for radiation sensors*. CRC Press, 2015.

[26] Simon Sze and Knok Knok Ng. *Physics of Semiconductor Devices*. Wiley, 1969.

[27] G. Davies. «The optical properties of luminescent centres in silicon». In: *Physics Reports* 176 (1989), pp. 83–188.

[28] K. Uchinokura, T Sekine, and E. Matsuura. «Critical-point analysis of the two-phonon Raman spectrum of silicon». In: *Journal of Physics and Chemistry of Solids* 35.1 (1974), pp. 171–180.

[29] D. Gray, A. McCaughan, and B. Mookerji. «Crystal Structure of Graphite, Graphene and Silicon». Lecture Notes, West Virginia University, 6.730, Physics for Solid State Applications. 2009.

[30] A. D. Zdetis. «Parallel Born-Von Karman study of diamond and the diamond type crystals». In: *Chemical Physics* 40.3 (1979), pp. 345–357.

[31] Efthimios Kaxiras. «Atomic and Electronic structure of Solids». In: Cambridge University Press, 2010. Chap. 4.

[32] Gordon Davies. «Semiconductors and Semimetals». In: vol. 51. B. Elsevier, 1999. Chap. 1.

[33] Ivan Pelant and Jan Valenta. «Luminescence Spectroscopy of Semiconductors». In: Oxford University Press, 2012. Chap. 7.

[34] G. E. Jellison, Jr. Modine, and F. A. Modine. «Optical absorption of silicon between 1.6 and 4.7 e Vat elevated temperatures». In: *Applied Physics Letters* 41 (1982), pp. 180–182.

[35] H. H. Li. «Refractive Index of Silicon and Germanium and Its Wavelength and Temperature Derivatives». In: *Journal of Physical and Chemical Reference Data* 9.3 (1980), pp. 561–658.

[36] H. R. Philipp and H. Ehrenreich. «Optical properties of semiconductors». In: *Physical Review* 129.4 (1963), pp. 180–182.

[37] W Redjem et al. «Single artificial atoms in silicon emitting at telecom wavelengths». In: *nature electronics* 3 (2020), pp. 738–743.

[38] W Redjem et al. «All-silicon quantum light source by embedding an atomic emissive center in a nanophotonic cavity». In: *Nature Communications* 14.3321 (2023).

[39] A. Gritsch, A. Ulanowski, and Reiserer A. «Purcell enhancement of single photon emitters in silicon». In: *Optica* 10 (2023), pp. 783–789.

[40] Bernard Pajot and Bernard Clerjaud. *Optical Absorption of Impurities and Defects in Semiconducting Crystals*. Springer Series in solid-state sciences, 2012.

[41] R.W. Series and K.G. Barracloijgh. «Carbon contamination during growth of Czocharlski silicon». In: *Journal of Crystal Growth* 60 (1982), pp. 212–218.

[42] W. von Ammon and G. Sattler A. Kissinger. «Springer Handbook of Electronic and Photonic Materials». In: Springer Handbooks book series (SHB), 2017. Chap. 5.

[43] Joel K. Kearns. «Single Crystals of Electronic Materials». In: Woodhead Publishing Series in Electronic and Optical Materials, 2019. Chap. 2.

[44] Masayasu Miyake and Mitsutoshi Takahash. «Defects Induced by Deep Preamorphization and Their Effects on Metal Oxide Semiconductor Device Characteristics». In: *Journal of The Electrochemical Society* 144.7 (1997), pp. 1020–1024.

[45] J. LIU, M. E. Law, and K. S. Jones. «Evolution of dislocation loops in silicon in an inert ambient—I». In: *Solid State Electronics* 38 (1995), pp. 1305–1312.

[46] George D. Watkins. «Negative-U properties for defects in solids». In: Advances in Solid State Physics, Springer, 1984, pp. 163–189.

[47] George D. Watkins. «Intrinsic defects in silicon». In: *Materials Science in Semiconductor Processing* 3 (2000), pp. 227–235.

[48] J. L. Hastings and S. K. Estreicher. «Vacancy aggregates in silicon». In: *Physical Review B* 56.16 (1997), pp. 10215–10220.

[49] P. K. Giri. «Photoluminescence signature of silicon interstitial cluster evolution from compact to extended structures in ion-implanted silicon». In: *Semiconductor Science and Technology* 20 (2005), pp. 638–644.

[50] Y. Baron et al. «Optimization of photoluminescence from W centers in silicon-on-insulator». In: *ACS Photonics* 9.7 (2022), pp. 2337–2345.

[51] M. Aboy et al. «W and X Photoluminescence Centers in Crystalline Si: Chasing Candidates at Atomic Level Through Multiscale Simulations». In: *Journal of Electronic Materials* 47 (2018), pp. 5045–5049.

[52] L. W. Song et al. «Bistable interstitial-carbon—substitutional-carbon pair in silicon». In: *Physical Review B* 42.9 (1990), pp. 5765–5783.

[53] J. Paloheimo. «Handbook of silicon based MEMS materials and technologies». In: Elsevier, 2010. Chap. 3.

[54] R. C. Newman. «Oxygen in silicon: thermal donors, intrinsic defects and contamination». In: *Vacuum* 42.5 (1991), pp. 379–382.

[55] E. Irion et al. «Photoluminescence Study of Acceptor-Carbon Complexes in Irradiated Silicon: Aluminum-Related Defects». In: *Applied Physics A* 48 (1989), pp. 25–30.

[56] R. C. Newman and J. Wakefield. «The diffusivity of carbon in silicon». In: *Journal of Physics and Chemistry of Solids* 19.3/4 (1961), pp. 230–234.

[57] A. R. Bean and R. C. Newman. «The solubility of carbon in pulled silicon crystals». In: *Journal of Physics and Chemistry of Solids* 32.6 (1971), pp. 1211–1219.

[58] A. R. Bean and R. C. Newman. «The effect of carbon on thermal donor formation in heat treated pulled silicon crystals». In: *Journal of Physics and Chemistry of Solids* 33.2 (1972), pp. 255–268.

[59] L. I. Khirunenko et al. «Formation of interstitial carbon–interstitial oxygen complexes in silicon: Local vibrational mode spectroscopy and density functional theory». In: *Physical Review B* 78 (2008).

[60] D. J. Backlund and S. K. Estreicher. «Theoretical study of the C_iO_i and $I_{si}C_iO_i$ defects in S_i». In: *Physica B: Condensed Matter* 401-402 (2007).

[61] P. Werner et al. «The effect of carbon on thermal donor formation in heat treated pulled silicon crystals». In: *Journal of Physics and Chemistry of Solids* 73.17 (1998), pp. 255–268.

[62] L. W. Song and G. D. Watkins. «EPR identification of the single-acceptor state of interstitial carbon in silicon». In: *Physical Review B* 42.9 (1990), pp. 5759–5764.

[63] R. B. Capaz, A. Dal Pino Jr., and J. D. Joannopoulos. «Identification of the migration path of interstitial carbon in silicon». In: *Physical Review B* 50.11 (1994), pp. 7439–7442.

[64] H. Wang et al. «Carbon related defects in irradiated silicon revisited». In: *Scientific Reports* 4.4909 (2014).

[65] M.S. Skolnick, A.G. Cullis, and H.C. Webber. «Optimization of photoluminescence from W centers in silicon-on-insulator». In: *Optics Express* 28.11 (2020), pp. 16057–16072.

[66] *Some new photoluminescence features of W line for neutron-irradiated MCz-Si and FZ-Si* (Dresden, Germany). IEEE, Oct. 2008. ISBN: 1082-3654.

[67] M.S. Skolnick, A.G. Cullis, and H.C. Webber. «Defect photoluminescence from Si laser annealed over a wide temperature range». In: *Journal of Luminescence* 24-25.1 (1981), pp. 39–42.

[68] M. Nakamura and S. Nagai. «Influence of high-energy electron irradiation on the formation and annihilation of the photoluminescence W center and the center's origin in a proton-implanted silicon crystal». In: *Physical Review B* 66.155204 (2002).

[69] G. Davies, E.C. Lightowlers, and Z. E. Ciechanowska. «The 1018 meV (W or I1) vibronic band in silicon». In: *Journal of Physics C: Solid State Physics* 20 (1987), pp. 191–205.

[70] D. A. Richie et al. «Complexity of Small Silicon Self-Interstitial Defects». In: *Physical Review Letters* 92.4 (2004).

[71] A. Carvalho, R. Jones, and P. R. Coutinho J. Briddon. «Density-functional study of small interstitial clusters in Si: Comparison with experiments». In: *Physical Review B* 72.155208 (2005), pp. 532–534.

[72] M. Gharaibeh, S. K. Estreicher, and P. A. Fedders. «Molecular-dynamics studies of self-interstitial aggregates in Si». In: *Physica B: Condensed Matter* 273-274 (1999), pp. 532–534.

[73] S. M. Buckley et al. «Optimization of photoluminescence from W centers in silicon-on-insulator». In: *Optics Express* 28.11 (2020), pp. 16057–16072.

[74] S. Buckley et al. «All-silicon light-emitting diodes waveguide-integrated with superconducting single-photon detectors». In: *Applied Physics Letters* 111.14 (2017), p. 141101.

[75] A. N. Tait et al. «Microring resonator-coupled photoluminescence from silicon W centers». In: *Journal of Physics: Photonics* 2.4 (2020), p. 045001.

[76] P. Udvarhelyi et al. «An L-band emitter with quantum memory in silicon». In: *npj Computational Materials* 8.263 (2022).

[77] K. Thonke, G. D. Watkins, and R. Sauer. «Carbon and oxygen isotope effects in the 0.79 eV defect photoluminescence spectrum in irradiated silicon». In: *Solid State Communications* 51.3 (1984), pp. 127, 130.

[78] K. Thonke, G. D. Watkins, and R. Sauer. «Carbon and oxygen isotope effects in the 0.79 eV defect photoluminescence spectrum in irradiated silicon». In: *Solid State Communications* 51.3 (1984), pp. 127, 130.

[79] G. Davies et al. «Temperature, stress, and annealing effects on the luminescence from electronirradiated silicon». In: *Journal of Applied Physics* 44.12 (1973), pp. 5402–5410.

[80] G. Davies et al. «Carbon-related radiation damage centres in Czochralski silicon». In: *Journal of Physics C: Solid State Physics* 19 (1986), pp. 841–855.

[81] A. R. Bean, R. C. Newman, and R. S. Smith. «Electron irradiation damage in silicon containing carbon and oxygen». In: *Physical Review B* 31.4 (1970), pp. 739–751.

[82] C. C. Chartrand et al. «Highly enriched 28Si reveals remarkable optical linewidths and fine structure for well-known damage centers». In: *Physical Review B* 98.195201 (2018).

[83] K. Thonke et al. «0.79 eV (C line) defect in irradiated oxygen-rich silicon: excited state structure, internal strain and luminescence decay time». In: *Journal of Physics C: Solid State Physics* 18.4 (1985), pp. L795–L801.

[84] T. Ishikawa et al. «Photoluminescence from triplet states of isoelectronic bound excitons at interstitial carbon-intersititial oxygen defects in silicon». In: *Physica B* 404.23-24 (2009), pp. 4552–4554.

[85] K. Thonke et al. «New model of the irradiation-induced 0.97-eV (G) line in silicon: A Cs-Si* complex». In: *Physical Review B* 24.10 (1981), pp. 5874–5886.

[86] C. Beaufils et al. «Optical properties of an ensemble of G-centers in silicon». In: *Physical Review B* 97.035303 (2018).

[87] P. Deák et al. «The kinetics of carbon pair formation in silicon prohibits reaching thermal equilibrium». In: *nature communications* 14.361 (2023).

[88] C. Beaufils et al. «Identification of a Telecom Wavelength Single Photon Emitter in Silicon». In: *Physical Review Letters* 127.196402 (2018).

[89] K. M. L. Lee et al. «Optical Detection of Magnetic Resonance for a Deep-Level Defect in Silicon». In: *Physical Review Letters* 48.37 (1982).

[90] M. Hollenbach et al. «Wafer-scale nanofabrication of telecom single-photon emitters in silicon». In: *nature communications* 16.7683 (1982).

[91] M. Prabhu1 et al. «Individually addressable and spectrally programmable artificial atoms in silicon photonics». In: *nature communications* 14.2380 (2023).

[92] C. M. Lee et al. «High-Efficiency Single Photon Emission from a Silicon T-Center in a Nanobeam». In: *ACS Photonics* 10.11 (2023), pp. 3844–3849.

[93] D. Dhaliah et al. «First-principles study of the T centre in silicon». In: *physical review materilas* 6.L053201 (2022).

[94] A. N. Safonov and E.C. Lightowlers. «Photoluminescence characterisation of hydrogen-related centres in silicon». In: 58.1-2 (1999), pp. 39–47.

[95] D. B. Higginbottom et al. «Optical observation of single spins in silicon». In: *Nature* 607 (2022), pp. 266–270.

[96] L. Bergeron et al. «Silicon-Integrated Telecommunications Photon-Spin Interface». In: *PRX Quantum* 1.020301 (2020).

[97] Fatima A. Merchant et al. *Handbook of Image and Video Processing (Second Edition)*. Academic Press, 2005.

[98] Steven Prawer and Igor Aharonovich. *Quantum Information Processing with diamond*. Cambridge, UK: Woodhead Publishing, 2014.

[99] Timothy R. Corle and Gordon S. Kino. *Confocal Scanning Optical Microscopy and Related Imaging Systems*. Academic Press, 1996.

[100] C. Shepard. «Encyclopedia of Optical Engineering». In: Dekker, 2003, pp. 2525–2544. ISBN: 0-8247-4258-3.

[101] Horiba. URL: ttps://static.horiba.com/fileadmin/Horiba/Products/Scientific/Optical_Components_and_OEM/iHR_Series/iHR_Series_Brochure.pdf.

[102] Micro Photon Devices (MPD). URL: http://www.micro-photon-devices.com/MPD/media/UserManuals/PDM-IR_usermanual.pdf.

[103] National Instruments. URL: https://www.ni.com/pdf/manuals/377874a.pdf.

[104] J. M. Binder et al. «Qudi: A modular python suite for experiment control and data processing». In: *SoftwareX* 6 (2017), pp. 85–90.

[105] Montana Instruments. URL: https://www.montanainstruments.com/products/s100.

[106] T. Lühmann et al. «Screening and engineering of colour centres in diamond». In: *Journal of Physics D: Applied Physics* 51 (2018).

[107] A. Pershin et al. «Highly tunable magneto-optical response from magnesium-vacancy color centers in diamond». In: *npj Quantum Information* 7.99 (2021).

[108] S. Ditalia Tchernij et al. «Single-Photon-Emitting Optical Centers in Diamond Fabricated upon Sn Implantation». In: *ACS Photonics* 4 (10 2017).

[109] R. Middleton. «A versatile high intensity negative ion source». In: *Nuclear Instruments and Methods in Physics Research* 214 (2-3 1983).

[110] E. Nieto Hernandez et al. «Efficient fabrication of high-density ensembles of color centers via ion implantation on a hot diamond substrate». In: arXiv:2310.19526 (2023).

[111] *Study of W centers formation in silicon upon ion implantation and rapid thermal annealing* (Sicily, Italy). IEEE, June 2023. ISBN: 979-8-3503-4720-3.

[112] G. Andrini et al. «Activation of telecom emitters in silicon upon ion implantation and ns pulsed laser annealing». In: *communication materials* 5.47 (2024).

[113] G. Andrini et al. «An ion beam spot size monitor based on a nano-machined Si photodiode probed by means of the ion beam induced charge technique». In: *Vacuum* 203 (2022).

[114] M. Nastasi, J. Mayer, and J. K. Hirvonen. «Ion Solid Interactions». In: Cambridge University Press, 2010. Chap. 4.

[115] M. B. H. Breese and P. J. C. Jamieson D. N. and King. *Materials Analysis using a Nuclear Microprobe*. Wiley, 1996.

[116] G. F. Knoll. *Radiation Detection and Measurements, fourth edition*. Wiley, 2010.

[117] M.D. Ziegler J. F. Ziegler and J. P. Biersack. «SRIM – The stopping and range of ions in matter (2010)». In: *Nuclear Instruments and Methods in Physics Research Section B: Beam Interactions with Materials and Atoms* 268.11-12 (2010), pp. 1818–1823.

[118] M. T. Robinson. «Computer simulation studies of high-energy collision cascades». In: *Nuclear Instruments and Methods in Physics Research Section B: Beam Interactions with Materials and Atoms* 67.1-4 (1992), pp. 396–400.

[119] M.T. Robinson and I. M. Torrens. «Computer simulation of atomic-displacement cascades in solids in the binary-collision approximation». In: *Physical Review B* 9.5008 (1974).

[120] R. Smith. *Atomic and Ion Collisions in Solids and at Surfaces*. Cambridge University Press, 2009.

[121] *MARLOWE Simulation of High Energy Ions into Single Crystalline Silicon Substrates* (Würzburg, Germany). IEEE, 2018. ISBN: 978-1-5386-6829-0.

[122] Peter Sigmund. *Particle Penetration and Radiation Effects*. Springer Series in Solid State Science, 2006.

[123] D.K. Avasthi and G. K. Mehta. «Swift Heavy Ions for Materials Engineering and Nanostructuring». In: Springer, 2011. Chap. 2.

[124] E. J. Kobetich and Robert K. «Energy Deposition by Electron Beams and *δRays*». In: *Physical Review* 170.391 (1968).

[125] R. Schirhagl et al. «Nitrogen-vacancy centers in diamond: nanoscale sensors for physics and biology». In: *Annual Review of Physical Chemistry* 65 (2014), pp. 83–105.

[126] M. Schukraft et al. «Invited Article: Precision nanoimplantation of nitrogen vacancy centers into diamond photonic crystal cavities and waveguides». In: *APL Photonics* 1.020801 (2016).

[127] M. Vićentijević, M. Jakšić, and T. Suligoj. «Implantation site design for large area diamond quantum device fabrication». In: *Scientific Reports* 13.13483 (2023).

[128] J. L. Pacheco et al. «Ion implantation for deterministic single atom devices». In: *Review of Scientific Instruments* 88.123301 (2017).

[129] M. S. Dresselhaus and R. Kalish. *Ion Implantation in Diamond, Graphite and related materials*. Springer Verlag, 1992.

[130] D. Saada, J. Adler, and R. Kalish. «Transformation of diamond (sp^3) to graphite (sp^2) bonds by ion-impact». In: *International Journal of Modern Physics C* 9.1 (1998), pp. 61–69.

[131] D. Saada, J. Adler, and R. Kalish. «Computer simulation of damage in diamond due to ion impact and its annealing». In: *Physical Review B* 59.10 (1998).

[132] E. Nieto Hernández et al. «Efficiency Optimization of Ge-V Quantum Emitters in Single-Crystal Diamond upon Ion Implantation and HPHT Annealing». In: *Advanced Quantum Technologies* 6.2300010 (8 2023).

[133] J. Görlitz et al. «Coherence of a charge stabilised tin-vacancy spin in diamond». In: *npj Quantum Information* 8.45 (2022).

[134] P. Wang et al. «Low-Temperature Spectroscopic Investigation of Lead-Vacancy Centers in Diamond Fabricated by High-Pressure and High-Temperature Treatment». In: *ACS Photonics* 8 (10 2021), pp. 2947–2954.

[135] T. Wolf et al. «Subpicotesla Diamond Magnetometry». In: *Physical Review X* 5.041001 (2015).

[136] F. Picollo et al. «Fabrication and electrical characterization of threedimensional graphitic microchannels in single crystal diamond». In: *New Journal of Physics* 14.053011 (2012).

[137] F. Bosia et al. «Direct measurement and modelling of internal strains in ion-implanted diamond». In: *Journal of Physics: Condensed Matter* 25.38 (2013).

[138] C. Uzan-Saguy et al. «Damage threshold for ion-beam induced graphitization of diamond». In: *Applied Physics Letters* 67.9 (1995).

[139] P. Olivero et al. «Characterization of three-dimensional microstructures in single-crystal diamond». In: *Diamond and related materials* 15 (2006).

[140] J. R. Maze et al. «Properties of nitrogen-vacancy centers in diamond: the group theoretic approach». In: *New Journal of Physics* 13 (2011).

[141] M. W. Doherty et al. «The nitrogen-vacancy colour centre in diamond». In: *Physics Reports* 528 (1 2013), pp. 1, 45.

[142] J. Forneris et al. «Mapping the Local Spatial Charge in Defective Diamond by Means of N-V Sensors—A Self-Diagnostic Concept». In: *Physical Review Applied* 10 (1 2018).

[143] M. Lesik et al. «Magnetic measurements on micrometer-sized samples under high pressure using designed NV centers». In: *Science* 366 (6471 2019), pp. 1359–1362.

[144] J. Forneris et al. «Electrical control of deep NV centers in diamond by means of sub-superficial graphitic micro-electrodes». In: *Carbon* 113 (2017), pp. 76–86.

[145] S Pezzagna et al. «Creation efficiency of nitrogen vacancy centres in diamond». In: *New Journal of Physics* 12 (2010).

[146] F.C. Waldermann et al. «Creating diamond color centers for quantum optical applications». In: *Diamond and related materials* 16 (11 2007).

[147] J. Schwartz et al. «In situ optimization of co-implantation and substrate temperature conditions for nitrogen-vacancy center formation in single-crystal diamonds». In: *New Journal of Physics* 13.48 (2011).

[148] A. M. Edmonds et al. «Production of oriented nitrogen-vacancy color centers in synthetic diamond». In: *Physics Review B* 86 (3 2012).

[149] A. Durand et al. «Broad Diversity of Near-Infrared Single-Photon Emitters in Silicon». In: *Physical Review Letters* 126 (8 2021).

[150] P. J. Schultz, T. D. Thompson, and R. G. Elliman. «Activation energy for the photoluminescence W center in silicon». In: *Applied Physics Letters* 60 (1 1992), pp. 59–61.

[151] A. M. Flatae et al. «Silicon-vacancy color centers in phosphorus-doped diamond». In: *Diamond and Related Materials* 105.107797 (2020).

[152] M. B. H. Breese, D. N. Jamieson, and P. J. C. King. *Materials Analysis Using a Nuclear Microprobe*. Wiley-VCH, 1996.

[153] E. Vittone et al. «Evaluation of the diffusion length in silicon diodes by means of the lateral IBIC technique». In: *Nuclear Instruments and Methods in Physics Research B* 158 (1-4 1999).

[154] H. Schone et al. «Time-resolved ion beam induced charge collection (TRIBICC) in micro-electronics». In: *Nuclear Instruments and Methods in Physics Research B* 158 (1-4 1999).

[155] G. H. Döhler and H. Heyszenau. «Conduction in the relaxation regime». In: *Physical Review B* 12 (2 1975).

[156] T. H. Prettyman. «Conduction in the relaxation regime». In: *Physical Review B* 12.2 (1974).

[157] W. Shockley. «Currents to Conductors Induced by a Moving Point Charge». In: *Journal of Applied Physics* 9.10 (1938).

[158] *Currents Induced by Electron Motion*. Vol. 27. IEEE, 1939.

[159] J. B. Gunn. «A general expression for electrostatic induction and its application to semiconductor devices». In: *Solid-State Electronics* 7 (10 1964).

[160] G. Cavalleri et al. «Extension of Ramo's theorem as applied to induced charge in semiconductor detectors». In: *Nuclear Instruments and Methods* 92 (1 1971).

[161] E. Vittone. «Theory of ion beam induced charge measurement in semiconductor devices based on the Gunn's theorem». In: *Nuclear Instruments and Methods in Physics Research B* 219-220 (2004).

[162] Siegfried Selberherr. *Analysis and Simulation of Semiconductor Devices*. Springer Vienna, 1984.

[163] J. S. Laird et al. «The role of high-injection effects on the transient ion beam induced current response of high-speed photodetectorsm». In: *Nuclear Instruments and Methods in Physics Research B* (2004).

[164] M. Ferrero et al. «An Introduction to Ultra-Fast Silicon Detectors». In: CRC Press, 2021. Chap. 3.

[165] D. N. Jamieson et al. «Deterministic doping». In: *Material Science in Semiconductor Processing* 62 (2017).

[166] F. Picollo et al. «Fabrication of monolithic microfluidic channels in diamond with ion beam lithography». In: *Nuclear Instruments and Methods in Physics Research B* 404 (1 2017).

[167] J. E. Manuel et al. *Note: Performance of a novel electrostatic quadrupole doublet for nuclear microprobe application.* 2018.

[168] Technical Reports Series. *Guidelines for the Determination of Standardized Semiconductor Radiation Hardness Parameters.* Tech. rep. International Atomic Energy Agency, 2021.

[169] A. Lo Giudice et al. «Angle resolved IBIC analysis of 4H-SiC Schottky diodes». In: *Nuclear Instruments and Methods in Physics Research Section B: Beam Interactions with Materials and Atoms* 249 (1-2 2006).

[170] D. Cosic, M. Bogovac, and M. Jakšić. «Data acquisition and control system for an evolving nuclear microprobe». In: *Nuclear Instruments and Methods in Physics Research Section B: Beam Interactions with Materials and Atoms* 451 (2019).

[171] A. Morello et al. «Single-shot readout of an electron spin in silicon». In: *nature* 467 (2010).

[172] M. Schukraft et al. «Invited Article: Precision nanoimplantation of nitrogen vacancy centers into diamond photonic crystal cavities and waveguides». In: *APL Phtonics* 1 (2 2016).

[173] S. Achilli et al. «Position-Controlled Functionalization of Vacancies in Silicon by Single-Ion Implanted Germanium Atoms». In: *Advanced functional material* 31 (21 2021).

[174] M. Ferrero et al. «An Introduction to Ultra-Fast Silicon Detectors». In: CRC Press, 2021. Chap. 2.

[175] G. Vizklethy. «Simulation of ion beam induced current in radiation detectors and microelectronic devices». In: *Nuclear Instruments and Methods in Physics Research B* 269 (2011).

[176] T. H. Prettyman. «Theoretical framework for mapping pulse shapes in semiconductor radiation detectors». In: *Nuclear Instruments and Methods in Physics Research Section A: Accelerators, Spectrometers, Detectors and Associated Equipment* 428 (1 1999).

[177] T. H. Prettyman. «Method for mapping charge pulses in semiconductor radiation detectors». In: *Nuclear Instruments and Methods in Physics Research Section A: Accelerators, Spectrometers, Detectors and Associated Equipment* 422 (1-3 1999).

[178] Y. Zhiyenbayev et al. «Scalable manufacturing of quantum light emitters in silicon under rapid thermal annealing». In: *Optics Express* 31 (8352-8362 2023), pp. 59–61.

[179] Y. Baron et al. «Single G centers in silicon fabricated by co-implantation with carbon and proton». In: *Applied Physics Letters* 121 (8 2022).

[180] M. Hollenbach et al. «Engineering telecom single photon emitters in silicon for scalable quantum photonics». In: *Optics Express* 28 (18 2020), pp. 26111–26121.

[181] W. Redjem et al. «Defect engineering of silicon with ion pulses from laser acceleration». In: *Communication Materials* 4.22 (2023).

[182] K. Murata et al. «High-density G-centers, light-emitting point defects in silicon crystal». In: *AIP Advances* 1 (3 2011).

[183] A. La Magna et al. «A phase-field approach to the simulation of the excimer laser annealing process in Si». In: *Journal of Applied Physics* 95 (9 2004).

[184] W. Liu et al. «Quantum Emitter Formation Dynamics and Probing of Radiation-Induced Atomic Disorder in Silicon». In: *Physical Review Applied* 20 (1 2023).

[185] H. Quard et al. «Femtosecond laser-induced creation of G and W-centers in silicon-on-insulator substrates». In: *arXiv:2304.03551* (2023).

[186] G. Götz et al. «Photoluminescence investigation of defects after ion-implantation and laser annealing». In: *Applied Physics Letters* 2 (1-3 1984).

[187] C. Neubüser et al. «Fully Depleted MAPS in 110-nm CMOS Process With 100–300-m Active Substrates». In: *IEEE Transactions on Electron Devices* 67.6 (2020).

[188] T. Corradino et al. «Simulation and first characterization of MAPS test structures with gain for timing applications». In: *Journal of Instrumentation* 19.C02036 (2024).

[189] W. Klempt. «Review of particle identification by time of flight techniques». In: *Nuclear Instruments and Methods in Physics Research Section A: Accelerators, Spectrometers, Detectors and Associated Equipment* 433 (1-2 1999).

[190] W. Riegler and G. Aglieri Rinella. «Time resolution of silicon pixel sensors». In: *Journal of Intrumentations* 12 (2017).

[191] L. Pancheri et al. «Fully Depleted MAPS in 110-nm CMOS Process With 100–300-μm Active Substrates». In: *IEEE Transactions on Electron Devices* 67.6 (2020).

[192] C. Neubüser et al. «Sensor design optimization of innovative low-power, large area MAPS for HEP and applied science». In: *Frontiers in Physics* 9 (2021).

[193] C. B. Wunderer et al. «The PERCIVAL soft X-ray imager». In: *Journal of Instrumentations* 9.3 (2014).

[194] R: Turchetta et al. «Monolithic active pixel sensors (MAPS) in a VLSI CMOS technology». In: *Nuclear Instruments and Methods in Physics Research Section A: Accelerators, Spectrometers, Detectors and Associated Equipment* 501 (1 2003).

[195] M. On behalf of the ALICE Collaboration Mager. «ALPIDE, the Monolithic Active Pixel Sensor for the ALICE ITS upgrade». In: *Nuclear Instruments and Methods in Physics Research Section A: Accelerators, Spectrometers, Detectors and Associated Equipment* 824 (2016), pp. 434–438.

[196] L. Pancheri et al. «A 110 nm CMOS process for fully-depleted pixel sensors». In: *Journal of Instrumentation* 14 (2019).

[197] *Monte Carlo simulations of Fully Depleted CMOS pixel sensors for radiation detection applications* (Valencia, Spain). IEEE, 2023. ISBN: 979-8-3503-0320-9.

[198] S. Spannagel et al. «Allpix^2:A modular simulation framework for silicon detectors». In: *Nuclear Inst. and Methods in Physics Research, A* 901 (2018), pp. 164–172.

[199] S. et al. Agostinelli. «Geant4—a simulation toolkit». In: *Nuclear Instruments and Methods in Physics Research Section A: Accelerators, Spectrometers, Detectors and Associated Equipment* 506 (3 2003).

[200] L. De Cilladi et al. «Fully Depleted Monolithic Active Microstrip Sensors: TCAD Simulation Study of an Innovative Design Concept». In: *Sensors* 21 (6 2021).

[201] H. Pernegger et al. «First tests of a novel radiation hard CMOS sensor process for Depleted Monolithic Active Pixel Sensors». In: *Journal of Instrumentations* 12 (2017).

[202] F. Guilloux et al. «CAcTμS: High-Voltage CMOS Monolithic Active Pixel Sensor for Tracking and Time Tagging of Charged Particles». In: *Proceedings of Science* 313 (2018).

[203] G. Iacobucci et al. «Efficiency and time resolution of monolithic silicon pixel detectors in SiGe BiCMOS technology». In: *Journal of Instrumentation* 17 (2022).

[204] W. Riegler and G. Aglieri Rinella. «Time resolution of silicon pixel sensors». In: *Journal of Instrumentations* 12 (2017).

[205] J. J. Smithrick and I. T. Myers. «Average Triton Energy Deposited in Silicon per Electron-Hole Pair Produced». In: *Physical Review B* 1 (7 1970).

[206] R. C. Alig, S. Bloom, and C. W. Struck. «Scattering by ionization and phonon emission in semiconductors». In: *Physical Review B* 22 (12-15 1980).

[207] L. D. Landau. «On the energy loss of fast particles by ionisation». In: *Journal of Physics* 8.4 (194).

[208] H. Bichsel. «Straggling in thin silicon detectors». In: *Reviews of Modern Physics* 60 (3 1988).

[209] Erwin Fehlberg. *Low-order classical Runge-Kutta formulas with stepsize control and their application to some heat transfer problems.* Tech. rep. NASA Technical Report NASA-TR-R-315, 1969.

[210] C. Canali et al. «Electron and hole drift velocity measurements in silicon and their empirical relation to electric field and temperature». In: *IEEE Transactions on Electron Devices* 22 (11 1975).

[211] G. Masetti, M. Severi, and S. Solmi. «Modeling of carrier mobility against carrier concentration in arsenic-, phosphorus-, and boron-doped silicon». In: *IEEE Transactions on Electron Devices* 30 (7 1983).

[212] V. Sola et al. «First FBK production of 50 μm ultra-fast silicon detectors». In: *Nuclear Instruments and Methods in Physics Research Section A: Accelerators, Spectrometers, Detectors and Associated Equipment* 924 (2019).

[213] I. B. Smirnov. «Modeling of ionization produced by fast charged particles in gases». In: *Nuclear Instruments and Methods in Physics Research Section A: Accelerators, Spectrometers, Detectors and Associated Equipment* 554 (1-3 2005).

[214] R. H. Van Overstraeten De Man. «Measurement of the ionization rates in diffused silicon p-n junctions». In: *Solid-state Electronics* 13 (5 1970).